CARDIFF UNIVERSITY

Use of Rate of Change of Torque to Detect Damage in Gear Systems

Ben Cahill

A thesis submitted in partial fulfilment for
the degree of Doctor of Philosophy

Tribology and Performance of Machines, Structures and Materials
School of Engineering

2018

Abstract

With the improvement and expansion of technology, systems are becoming more expensive to operate and maintain. In an attempt to reduce these costs structural performance and condition monitoring systems have seen a significant boost in interest as companies try to reduce unplanned down time and extend component life. Whilst vibration monitoring and acoustic emission are the favoured monitoring methods at the moment, they have significant flaws when it comes to their application to rotating machinery.

As an alternative monitoring technique, this thesis investigates the application of a non-contact magnetic technique for monitoring rate of change of torque to gear systems. Using both existing and newly developed novel test rigs, data was captured at realistic conditions allowing for four studies to be undertaken. These studies evaluate the performance of the rate of change of torque technique (ROC) and compare it to an already established monitoring method.

The work showed that fundamentally the ROC technique was capable of successfully detecting very small levels: 2.7µm, of tooth bend damage on test gears under realistic operating conditions. Tests conducted on back-to-back gear testing rigs used sensors positioned both outside the torque loop, measuring ROC in parasitic losses, and inside the torque loop making direct measurements of ROC within the loaded gear pairs. These data have been analysed using a range of metrics and other analysis techniques, largely derived from current practice in vibration analysis. Whilst some techniques have been shown to be more suitable than others, it is clear that further development of ROC-specific analysis methods is required in order to achieve a robust methodology for repeatable and unambiguous detection and characterisation of gear tooth faults based on ROC signals.

A further study examined signals generated during tests conducted whilst a bearing was failing. This bearing was positioned on the drive system of the test rig, external to the torque loop. No evidence was found in the in-loop ROC signals from this bearing failure. This was due to the relative power levels in and out of the torque loop, with the much higher amplitude ROC signals generated by the gear meshes swamping any indications of bearing failure. However, in a realistic application (i.e. a bearing in a torque loop) the work in this thesis, demonstrating the high sensitivity of the ROC technique, gives confidence that it is suitable for damage detection in bearings as well as gears.

The final study compared ROC and vibration signals captured simultaneously during a set of gear tests. Whilst both techniques were found to be capable of detecting larger scale tooth bend defects, ROC was found to be more consistent in general, and more capable of detecting the 2.7 µm bend tested.

The thesis concludes that ROC has the potential to be a highly sensitive and reliable condition monitoring technique for rotating machinery. Due to its novelty, further development is required of enhanced techniques for signal processing and classification.

Declaration of Authorship

This work has not been submitted in substance for any other degree or award at this or any other university or place of learning, nor is being submitted concurrently in candidature for any degree or other award.

Signed ………………………………………………………. Date ……………………………………………
(candidate)

STATEMENT 1

This thesis is being submitted in partial fulfilment of the requirements for the degree of PHD.

Signed ………………………………………………………. Date ……………………………………………
(candidate)

STATEMENT 2

This thesis is the result of my own independent work/investigation, except where otherwise stated, and has not been edited by a third party beyond what is permitted by Cardiff University's Policy on the Use of Third Party Editors by Research Degree Students. Other sources are acknowledged by explicit references. The views expressed are my own.

Signed ………………………………………………………. Date ……………………………………………
(candidate)

STATEMENT 3

I hereby give consent for my thesis, if accepted, to be available online in the University's Open Access repository and for inter-library loan, and for the title and summary to be made available to outside organisations.

Signed ………………………………………………………. Date ……………………………………………
(candidate)

STATEMENT 4

I hereby give consent for my thesis, if accepted, to be available online in the University's Open Access repository and for inter-library loans **after expiry of a bar on access previously approved by the Academic Standards and Quality Committee.**

Signed ………………………………………………………. Date ……………………………………………
(candidate)

“Normal people believe that if it ain’t broke, don’t fix it.

Engineers believe that if it ain’t broke, it doesn’t have enough features yet.”

Scott Adams

Acknowledgements

Over the course of this project I have the received the help and support of many individuals, all of whom I owe a debt of gratitude to and my sincerest thanks as without any of them this would not have been possible.

Firstly, I would like to thank my supervisors Dr Alastair Clarke, Dr Rhys Pullin and Professor Karen Holford for their endless patience with this project as well as their support, guidance, and advice though out. The knowledge and guidance they provided, helped me keep going even in my darkest hour.

I would also like to thank the EPSRC and Mercedes AMG Petronas for supporting this project financially as well as Mercedes and MagCanica for suppling test components, equipment and industrial support. In particular, I wish to express my gratitude to Greg Rapson, James Williams, Scott McDougall and Ryan Walker of Mercedes AMG Petronas and Ryan Kari of MagCanica, who have endured my constant emails and have continuously provided me with their knowledge and experience.

I must also acknowledge the help of, and express my thanks to, the members of the Cardiff University workshops who have worked tirelessly and provided help at every stage of this project, with a special mention to Mal Lyall who has gone above and beyond to help me whenever possible. I would also like to extend this appreciation to the members of the Cardiff University Tribology Group and the Structural Performance Group, who have always been there to lend a hand or provide some guidance when needed.

Throughout my time at Cardiff University I've had the fortune to make many friends, without whom this journey would have been far less interesting and a lot less fun. It would be impossible to list everyone but thank you to all for helping keep me sane over these past four years, with a special mention to the Cardiff University Rifle Club and my those in my research group who have always been there for me and with who I have enjoyed so many laughs and maybe a few too many beers.

Of course, I cannot forget to mention my family who have always been there and supported me through thick and thin. My parents have always encouraged my curious nature and helped fuel it since my childhood. It is needless to say, that without them I would not be the man I am today.

A special mention to DR R Bell, who said I had to mention him, so here you go.

Finally, I'd like to thank Student Finance for their help in making my university journey possible. Having done so much, I'm not sure if I'll ever be able to repay you.

Table of Contents

Abbreviations

Acronym	***Definition***
AC	Alternating current
ACB	Angular contact bearing
AE	Acoustic emission
CGTR	Cardiff gear test rig
DAQ	Data acquisition device
DC	Direct current
EEG	Electroencephalogram
EHL	Elastohydrodynamic lubrication
EMD	Empirical mode decomposition
EO	Energy order
FEM	Finite element method
FFT	Fast Fourier transform
FIA	Federation Internationale De l'Automobile
FIR	Finite impulse response
FM	Figure of merit
FZG	Translated from German: Technical institute for the study of gears and drive mechanisms
HUMS	Health and usage monitoring systems
ICA	Independent component analysis
IES	Instantaneous energy spectrum
IIR	Infinite impulse response
IMF	Intrinsic mode function
ISO	International Organization for Standardization
LMD	Local mean decomposition
MAMG	Mercedes AMG Petronas
NI	National Instruments
ODM	Oil debris monitoring
PHMS	Prognostics and health management systems
RMS	Root mean square
ROC	Rate of change of torque
ROCC	Rate of change of armature current
SERC	Science and Engineering Research Council

SNR	Signal-to-noise ratio
STE	Static transmission error
STFT	Short time Fourier transform
SVM	Single value metric
TRQ	Short hand for torque
TSA	Time synchronous averaging

CHAPTER 1

Introduction

1.1 Background

With the advent of the Digital Revolution, our world has seen an unprecedented leap forward in the availability of technology and our understanding of the world around us. With this understanding and availability, new expectations of the technology around us arise as the previously revolutionary becomes the mundane and industry standard. This perpetual shift in expectations has driven innovation across every field and industry around the globe giving rise to the modern world; where the idea of humanity walking on the moon, real-time global communication, and having access to the complete wealth of human knowledge in our pockets has become common place. So much so that these things are taken for granted and with most preferring to spend their time engaging in other activities than considering the complexity of the world around them.

As the technology in our lives and homes has become more complex and connected, so to do the unseen industries that support it. Just as consumer expectations of their products grow so to do those of the industries and their equipment, as higher complexity leads to higher costs, both in the starting capital required as well as operation and maintenance costs. To this end, condition monitoring has become a subject of great interest in the past few decades, as industries try to reduce maintenance costs and improve reliability thus reducing the amount of downtime.

A central focus of condition monitoring from the start has been rotating machinery (Mitchell, 2007). This is the broad term used to refer to mechanical systems in modern industry and plays a vital role across the engineering spectrum, from automotive to power generation, and aerospace to deep-level mining. None more so than in Formula One and other forms of motorsport, where reliability of the mechanical systems can be the difference between winning a race and winning the championship. The gears and bearings found within F1 cars are subject to incredible punishment when compared to most regular applications. Here gears are designed to be as lightweight as possible while maintaining and often outperforming the efficiency and reliability of those found in less demanding environments. The need for condition monitoring in Formula One was given particular focus after a 2014 rule change. Article 23.5-a of the current regulations stipulates that ‘Each driver may use no more than one gearbox for 6 consecutive events in which his team competes' (FIA, 2018) with 23.5-d going further, explaining that internal components may only be changed if the FIA is supplied with satisfactory evidence of physical damage to the components.

Current Formula One gearboxes are manual gearboxes comprised of 8 forward gear ratios, a reverse, dog clutches and a final drive. Figure 1-1 illustrates the general layout of a Formula One gearbox, where the gearbox receives power from the engine through the input shaft via the clutch, where the layshaft and ratios are powered. Gear selection is made by the selector barrel which controls a set of selector forks engaged with their respective dog rings. When a gear is selected these dog rings engage directly with the gear and power is transmitted through the main shaft to the final drive, from which it is distributed to the wheels.

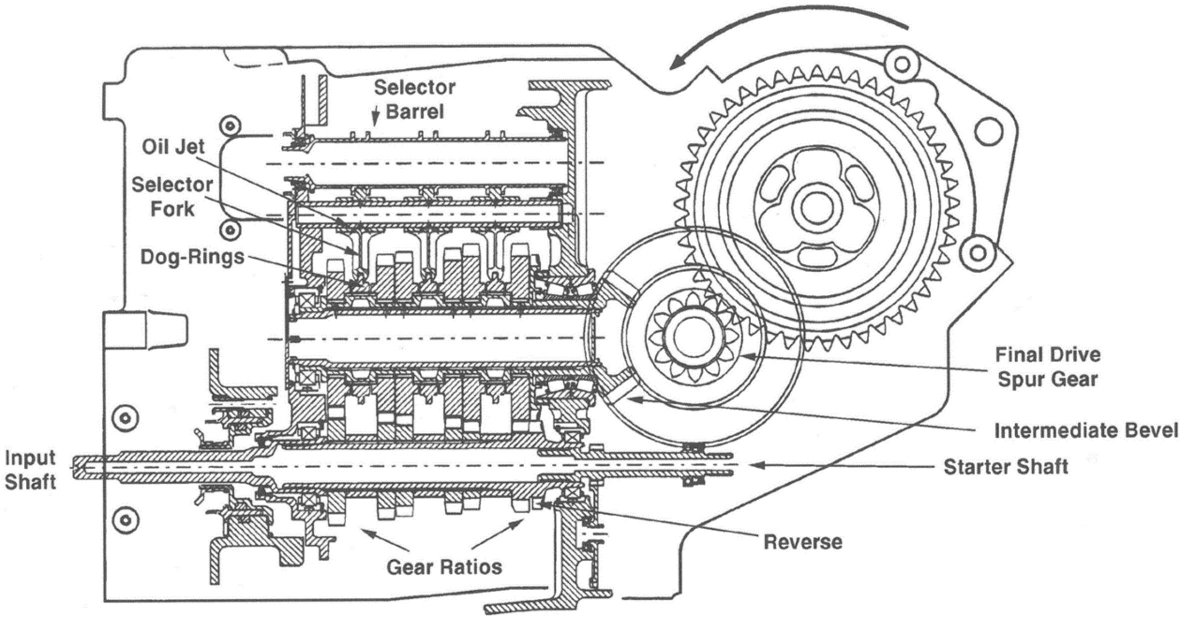

Figure 1-1 – Technical schematic of a high end race gearbox (Clarke, 2017)

As Formula One has little concerns with noise unlike road vehicles and with competition requiring the maximum power transfer with minimal losses, all the gears present are straight cut spur gears. As per Article 9.6.3-a of the FIA Technical Regulations (2017), these gears are required to have a minimum face width as 'no forward gear ratio pair must be less than 12mm wide'. Although it is known by those in the industry that it is possible to achieve a working gearbox with a gear face width less than this, it does provide some advantages. The contact area available for meshing at this width distributes the forces sufficiently that surface defects such as pitting are far less likely to occur, with form defects such as tooth bends and root cracks being more common. These defects directly inhibit the ability of gears to transfer mechanical power and as such cause a reduction in efficiency. At first these defects may not make an appreciable difference but as the damage propagates it can lead to reduction in overall power reaching the wheels, which in a race can make the difference between first and second.

For this reason, new analysis methods and condition monitoring techniques are being researched to accurately detect and monitor gear and bearing faults within powertrains. Whilst vibration and acoustic emission (AE) are well established, with vibration being the primary choice for rotating machinery and AE showing considerable promise in structural performance, both have limitations with potentially far reaching consequences. In an industry where competition is at the very core, anything less than ideal can mean losing the competitive edge.

1.2 Aims and Objectives

From even a brief examination of the literature it quickly becomes clear that the number of analysis methods for a particular monitoring technique are overwhelming. Many methods are designed for monitoring in a very particular set of conditions. Whilst vibration and acoustic emission are currently the most widely used monitoring techniques, they both have limitations that specialised analysis methods are not always capable of overcoming. As a potential competitor to vibration and AE systems, this thesis examines a new monitoring method: Rate of Change of Torque (ROC). This is a novel, non-contact, monitoring method that measures an intrinsic quantity of all rotating machinery.

The main goals of this research were:

- To undertake a series of experiments under real-world conditions to determine the viability of Rate of Change of Torque technology as a condition monitoring system.
- Identify key characteristics of ROC signals with emphasis on allowing detection and characterisation of seeded defects.
- To conduct an investigation into the performance of current condition monitoring techniques with application to ROC signals.
- Determine the sensitivity and damage detection capabilities of ROC technology in comparison to existing techniques.
- Develop a foundation from which research into the application of ROC technology can be expanded and furthered, with the focus of developing a successful ROC based condition monitoring system.

1.3 Contribution to Knowledge

The novelty of the work presented in this thesis can be found in the following areas:

- The design and development of a flexible high-speed gear test apparatus capable of replicating the working environment of a Formula One gearbox.
- An investigation into the capacity of ROC technology to detect form defects using both in-loop and parasitic sources with the examination of the raw waveforms and frequency spectra for both sources.
- An analysis of different filtering techniques with the visualisation of the results that demonstrate the clarity of ROC signals and provide a new level of insight into the torque transfer along the contact path.
- The use of vibration-based damage indicators and advanced frequency methods to successfully detect all damage levels within the experimentation framework, demonstrating the sensitivity of the technique with successful detection of a 2.4 µm (maximum deviation) tooth bend.
- Comparisons of ROC and vibration data for the same test, visualising the fundamental differences in the techniques and how different approaches are necessary to exploit the full capacity of ROC technology.

1.4 Summary of Outputs

The findings of this thesis can be broadly described as follows:

- Design, development, and construction of a novel high-speed gear test apparatus with sufficient scope for future expansion as necessary.
- The use of time synchronous averaging to refine ROC signals to provide a higher degree of clarity and greater level of detection.
- Successful identification of 2.4, 8.7 and 14.7 µm tooth bends within ROC signals with and clear differentiation from both each other and the healthy counterpart within the raw signals.
- Examination of vibration-based statistical and frequency-based detection methods, with successful detection of the damage and the determination that the difference in signal content means that a different approach is required for ROC signals.
- The visualisation of the sensitivity difference between ROC and vibration technology through comparison of data captured simultaneously.

1.5 Thesis Outline

Here an outline summary of each chapter will be provided to aid the reader.

Chapter 2:
Literature Review & Theory

Chapter 2 provides the reader with a background in the basics of gearing relevant to the thesis and a review of the literature surrounding condition monitoring of rotating machinery. An overview is provided of the common defect types found in gear systems as well as the different technologies and applications currently used to detect and monitor them. Finally a discussion of the advantage and disadvantages of these techniques is given and how ROC technology may offer advantages over the established.

Chapter 3:
Preliminary Investigations into the use of Rate of Change of Torque, using a Slow Speed Gear Testing Rig

Chapter 3 examines data captured using an existing slow-speed gear rig with an out-of-loop ROC sensor measuring torque fluctuations within the parasitic losses of the test rig. A basic analysis is undertaken providing preliminary results and a foundation for the future analysis. The chapter concludes that a more representative test is necessary, including ROC measurements taken in a fully loaded section of the system.

Chapter 4:
Design and Development of a Novel and Versatile High-Speed Gear Test Apparatus

Chapter 4 details the specification and design of the new high-speed gear rig which would be used to acquire the majority of the data presented in this thesis. A breakdown of the nature of the test head housings and various subsystems is given along with detailed designs and specification of the selected components.

Chapter 5:
Analysis of the Novel In-Loop Rate of Change of Torque Data

Chapter 5 is concerned with the results and analysis of the new in-loop Rate of Change of Torque data acquired using the new high-speed test rig. A breakdown of the experimental plan is first provided before a range of different techniques are applied with the aim of being able to detect and correctly identify the magnitude of the defect.

Chapter 6:
Comparison of Vibration-based condition monitoring to the Rate of Change of Torque.

Chapter 6 applies similar methods as the previous chapter to vibration data captured alongside the Rate of Change of Torque data on the high-speed test rig. This allows a comparison of the novel Rate of Change of Torque to a well-established and current condition monitoring technique.

Chapter 7:
Discussions, Conclusions and Future Work

Chapter 7 provides a discussion of the overall thesis findings, before concluding these discussions and providing areas of potential interest and recommendations for future research.

CHAPTER 2

Literature Review and Theory

In this chapter, the necessary theory and literature relevant to this thesis are reviewed. To begin a brief introduction to gear geometry and meshing cycles are present to provide a background on the application as well as allowing the reader to understand the nature of ROC technology. Expanding on this, the most relevant types of defects commonly present in gears are discussed and how they affect the operation of gears and overall efficiency.

The reader is then introduced to the field of condition monitoring and the necessity of continued advances and their importance in modern industry. Following this, the most widely used methods are examined with the strengths and weaknesses as well as a comparison to the newly proposed ROC technology.

2.1 Gears

2.1.1 Introduction

The oldest known example of gears can be found in the Antikythera device; an ancient Greek mechanical computer for calculating the lunar and solar calendars (Freeth *et al.*, 2006). Despite being over 2000 years old and the many advancements made across all fields of engineering during this time, gears have remained the primary mechanism for the control and transference of mechanical power.

Whilst similar to their ancient counterparts, advances in our understanding of mathematics, metallurgy, contact mechanics and tribology has allowed significant refinement in the design and manufacture of gears and gearboxes. These developments took time however and while examples of gears have been found throughout history their use was not widely implemented until the centuries before the industrial revolution. As devices such as clocks and more complex machinery requiring mechanical power became more prominent (Watson, 1970), so too did attention to gears and their geometry.

In 1694, French mathematician Phillipe de la Hire discovered involute geometry and its benefits over the then currently used cycloidal curve. These benefits were later confirmed by the famous Swiss mathematician Leonhard Euler in the 18th century, despite this involute geometry would not be implemented into gear design for at least another century. (Watson, 1970)

With the start of the industrial revolution, gear development rapidly grew as scientific principles were no longer left just to theory but were applied to aspects of industry. This saw the adoption of the involute form across nearly all branches of engineering bar a few where the cycloidal form would remain in use. With this growth saw new innovations such as Heinrich Hertz contributions to the field of contact mechanics in the late 19th century and later Wilfred Lewis publishing his methods for calculating bending stresses within gear teeth.

For the purpose of this thesis, only the geometry and technical details of involute spur gears will be discussed.

2.2 Gear Geometry

N.B. This section is a brief summary of fundamental gear theory and contact mechanics. A more in depth explanation can be found in Uicker et al. (2003) and Shigley & Mischke (2001)

For a gear pair to operate efficiently, it is fundamentally required that the ratio of angular velocity between the gears must remain constant. While it is possible for a gear pair to operate without meeting this condition, it is only in primitive applications that it can be tolerated as the adverse effects caused would interfere with the operation of a majority of applications. To achieve a constant angular velocity ratio, modern gear systems almost exclusively use an involute tooth profile.

2.2.1 Involute Profile

An involute curve is a type of spiral that is described as the path drawn by a point on a tightly wound piece of string as it is unwound from a circular profile as shown in Figure 2-1. A more technical description would be that an involute is a curvature of increasing radius, with a radius of zero at the point of contact with the circular profile.

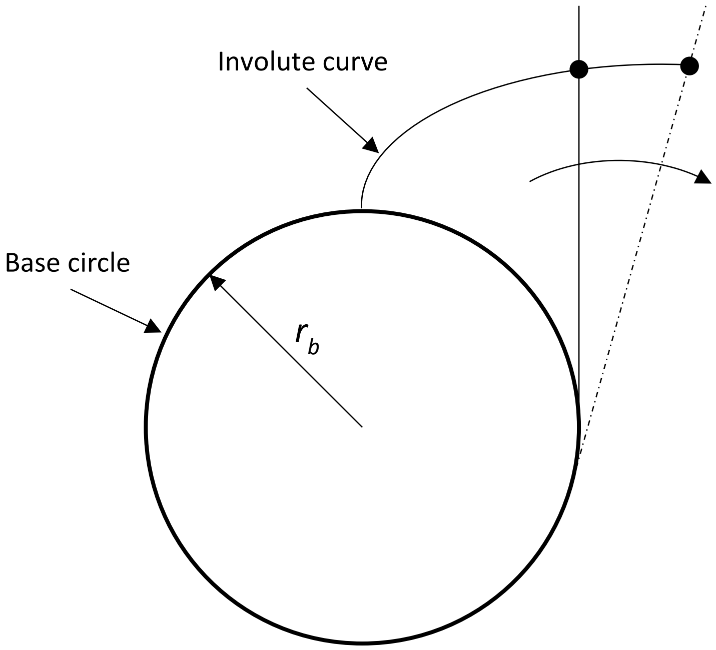

Figure 2-1 – Generation of an involute curve

Figure 2-2 shows the contact between two involute spur gears. The nature of involute geometry means that that path of contact between these gears is defined by the crossing points of the common base tangent (*AB*) and the addendum circles (r_{a1} and r_{a2}). This is indicated as the length *XY*. Given that the upper gear is driving the lower, the point of contact will move along this line from *X* to *Y* as the gear progresses through the meshing cycle.

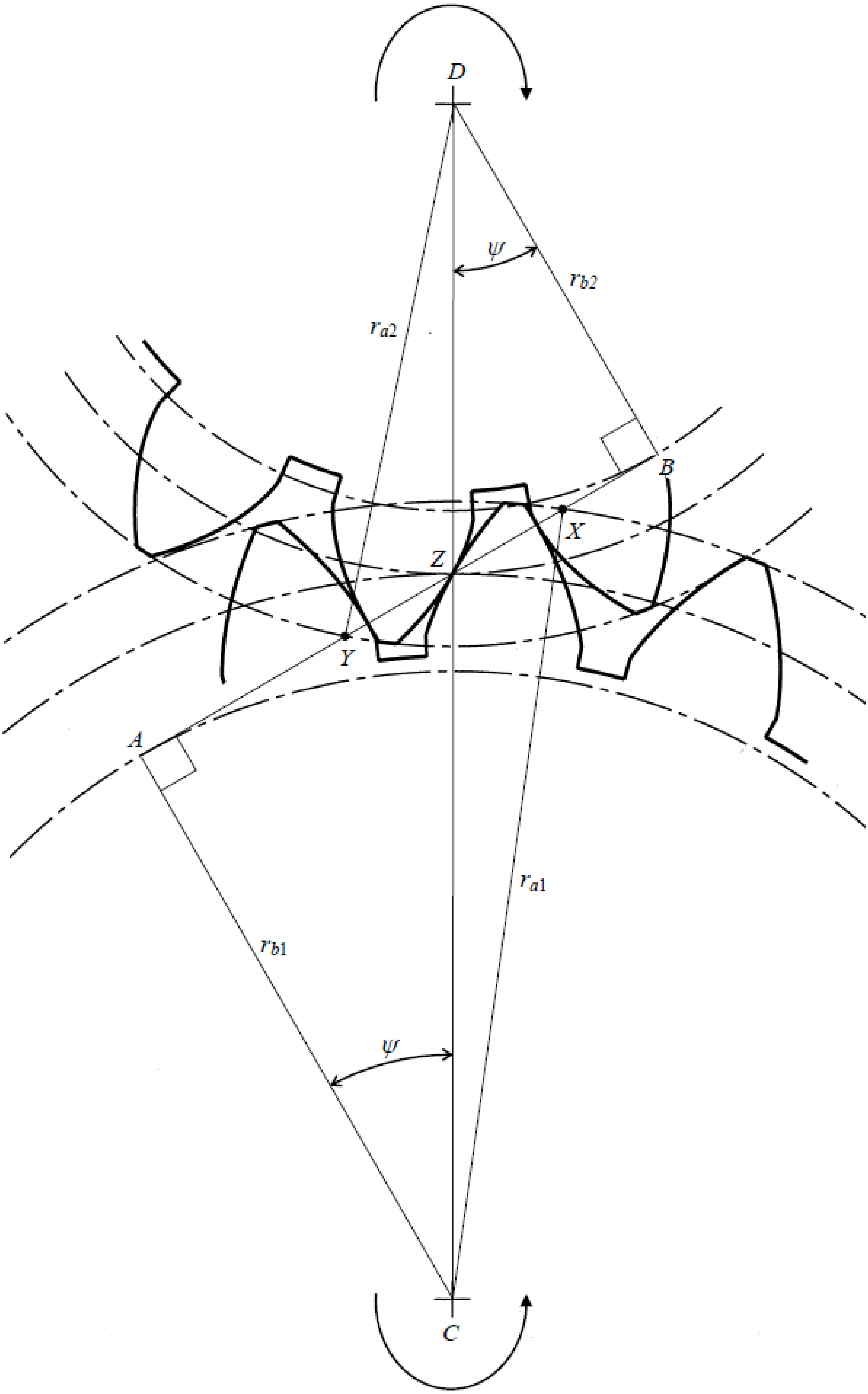

Figure 2-2 – Contact path between two gears.

Figure 2-3 demonstrates this with part 'a' showing the initial contact at the tip of the tooth, part 'b' showing contact at the pitch point i.e. half way through the mesh and finally part 'c' where the tooth is about to leave contact. For the system to produce a continuous and smooth motion, a new pair of teeth must engage before the original have disengaged. This can be observed in Figure 2-3 parts 'a' and 'c', where in front and behind of the teeth of interest (highlighted) respectively, a second pair of teeth can be observed in contact.

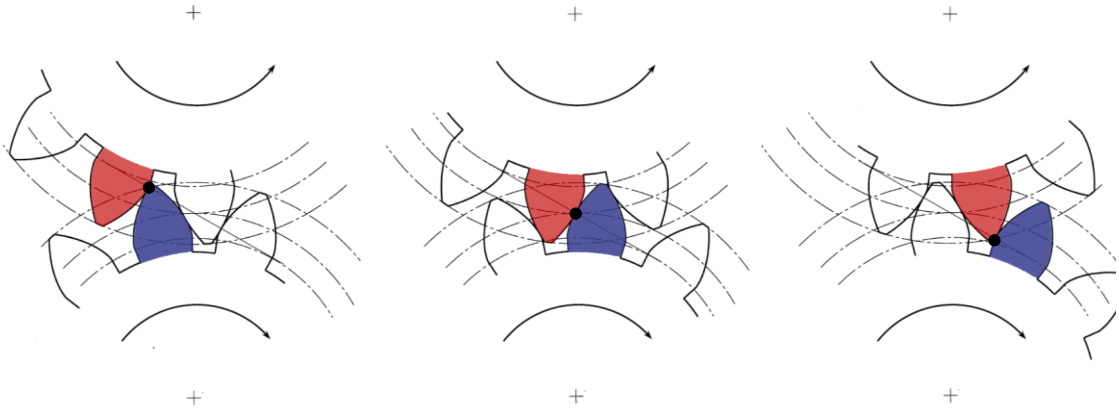

(a) (b) (c)

Figure 2-3 – Involute gears at three stages of the meshing cycle.

For this to occur the base circular pitch (p_b) is required to be less than the length of the contact path. This is characterised by the contact ratio which is defined as:

$$Contact\ Ratio = \frac{p_b}{XY} \tag{2-1}$$

Where:

$$p_b = \frac{2\pi r_b}{z} \tag{2-2}$$

and

$$XY = \left(\sqrt{{r_{a1}}^2 - {r_{b1}}^2} - r_{b1}\tan\psi\right) + \left(\sqrt{{r_{a2}}^2 - {r_{b2}}^2} - r_{b2}\tan\psi\right) \tag{2-3}$$

Given that z is the number of teeth on the gear and ψ is the working pressure angle. The contact ratio is used to define the amount of overlap in the contact path, for a standard gear this will be between 1.3 - 1.8 however high contact ratio gears do exist for particular applications.

2.2.2 Contact Mechanics

Contact between two meshing involute forms occurs in a line along the tooth flank (Figure 2-4). Due to the lack of geometric conformity between the two objects, it is usual to assume that the contact conditions can be obtained through the use of Hertzian line contact theory.

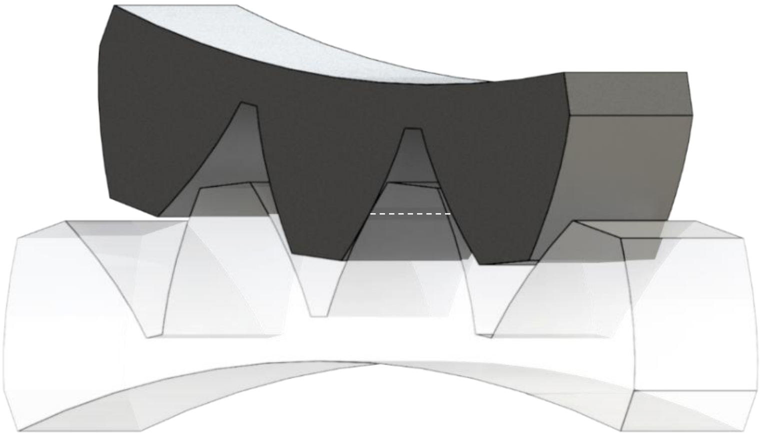

Figure 2-4 – Meshing of involute forms with the contact patch highlighted.

The non-conformity of gear teeth means that are subjected to large stresses over a small contact area. As with all mechanical stress, it is a function on the amount of force that the gear is subject to at any given moment. It is assumed that this load is equally distributed amongst the number of teeth in contact at a given point, this force (F_n) acts tangentially to both base circles i.e. along the path of contact and is equal to:

$$F_n = \frac{T}{nr_b} \tag{2-4}$$

Where T is the torque being transmitted and n is the number of teeth in contact at the current point during the meshing cycle. Before the stress can be calculated the relative geometry at the point of contact must be calculated. At the arbitrary point s on the contact path (where the pitch point marks the origin, implying that s can be both positive and negative), the profile radius of the gear teeth can be represented by two circles of radii R_1 and R_2, where:

$$R_1 = r_{b1} \tan\psi + s \quad \text{and} \quad R_2 = r_{b2} \tan\psi - s \tag{2-5}$$

The radius of relative curvature (R) can then be defined as:

$$\frac{1}{R} = \frac{1}{R_1} + \frac{1}{R_2} \tag{2-6}$$

While contact occurs in a line, this is while the forms are unloaded. When under load, the surfaces deform elastically, and the contact patch becomes rectangular in nature with a width of *2b* and length of t. The force across this contact area can be measured in two forms, the maximum elastic contact pressure (p_0) and the mean contact pressure ($\bar{p}$). The Hertzian equations for both are as follows:

$$p_0 = \left[\frac{W'E'}{2\pi R}\right]^{\frac{1}{2}} \tag{2-7}$$

Where *W′*, load per unit width of tooth is:

$$W' = \frac{F_n}{t} \tag{2-8}$$

And quantity *E′* is:

$$\frac{2}{E'} = \frac{1-{\upsilon_1}^2}{E_1} + \frac{1-{\upsilon_2}^2}{E_2} \tag{2-9}$$

Where *v* and E are the Poisson's ratio and Young's modulus for each gear respectively. Finally, the mean contact pressure is:

$$\bar{p} = \frac{\pi p_0}{4} \tag{2-10}$$

From the equations described here it is possible to better understand the meshing cycle as well find the contact stress at any point in the meshing cycle. By mapping the stress as gears move across the contact path, it allows for better predictions of the conditions involved in a particular application and therefore allows for better material selection and design. This is important as over stressing gears can be problematic and will inevitably result in damage of some varieties and in the worst cases, eventual failure of the gear system. To help prevent this, the causes and effects of the different types of damage are studied to help provide a better understanding and hopefully lead to improved monitoring methods and failure predictions.

2.3 Defects and Damage Mechanisms

In general, gears are robust constructs using high strength steels as well as case hardening techniques to resist contact stresses and preserve the surface finish & roughness of the gear tooth. Provided that there is sufficient lubrication and they are not overly stressed, gears can run indefinitely, however this is unlikely and a gear will eventually suffer deterioration and damage either from prolonged use or changes in the environment, whether natural or by accident, that cause improper running conditions. This deterioration/damage can take many forms, which are generally divided into two categories: surface and form defects.

2.3.1 Surface Defects

Surface defects are, as the name suggests, changes in the surface to the detriment of the gear. These defects can have many different origins, however a majority arise from scenarios where insufficient lubrication has caused metal-on-metal contact causing material loss or corrosion. Another common option is that surface fatigue has occurred leading to material loss. The effect of either of these can have devastating impact on a gear system leading to a large interest in the mechanisms behind them, predictive models and prevention methods.

An example of such a defect is micropitting (Figure 2-5). Micropitting is characterised by the formation of small pits between 10-30μm in diameter and 5-10μm in depth, arising from roughness effects in gears finished by grinding (Snidle and Evans, 2009). The effect of micropitting is that it leads to deviation from the involute profile, this in-turn affects tooth engagement and meshing which results in large, often unacceptable increases in noise. While in some cases these pits maybe thought of as a benign kind of 'running-in', the surface cracks may propagate leading to the formation of deeper cracks and develop into macropitting (Clarke *et al.*, 2015). This large-scale pitting will result in further material loss, which can lead to eventual tooth fracture and gear failure.

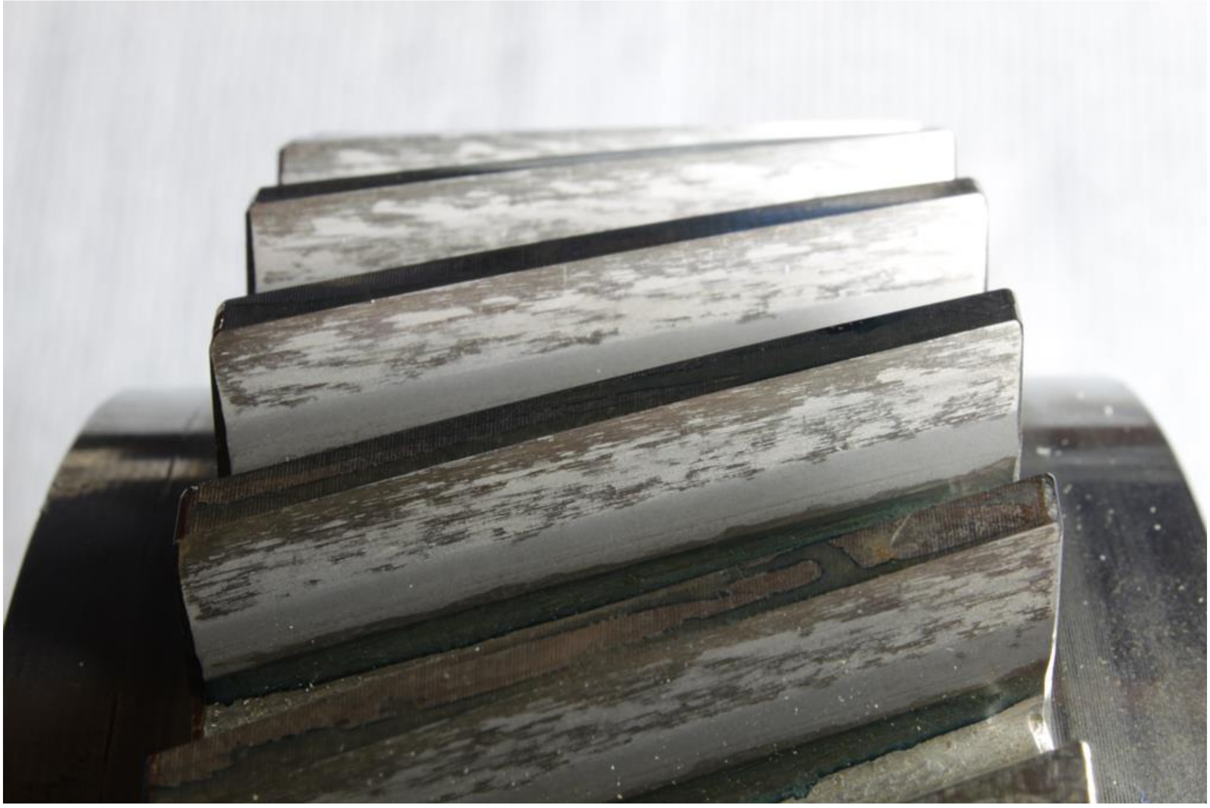

Figure 2-5 – Micropitting damage on the teeth of a helical test gear. (Extracted from Clarke et al. (2015))

Micropitting demonstrates how important the prevention of surface defects is, as while they may originate at the microscopic level, it can be seen from the literature that it is possible to cause significant damage to a gear with the potential to advance to large scale defects potentially causing gear failure entirely.

2.3.2 Form Defects

Form defects, also known as profile defects or errors, are inconsistencies in the involute geometry of a gear. While some deviations are by design and their effects anticipated e.g. tip relief, those that are not can affect the performance and behaviour of a gear pair. It is, of course, impossible to manufacture a gear without some form of deviation. This is demonstrated in Figure 2-6, where teeth profiles from a high precision helical pinion have been measured via the use of Klingelnberg P65 gear checker. While minor in size, these deviations have been seen to affect the how the gear operated as shown by Clarke et al. (2017).

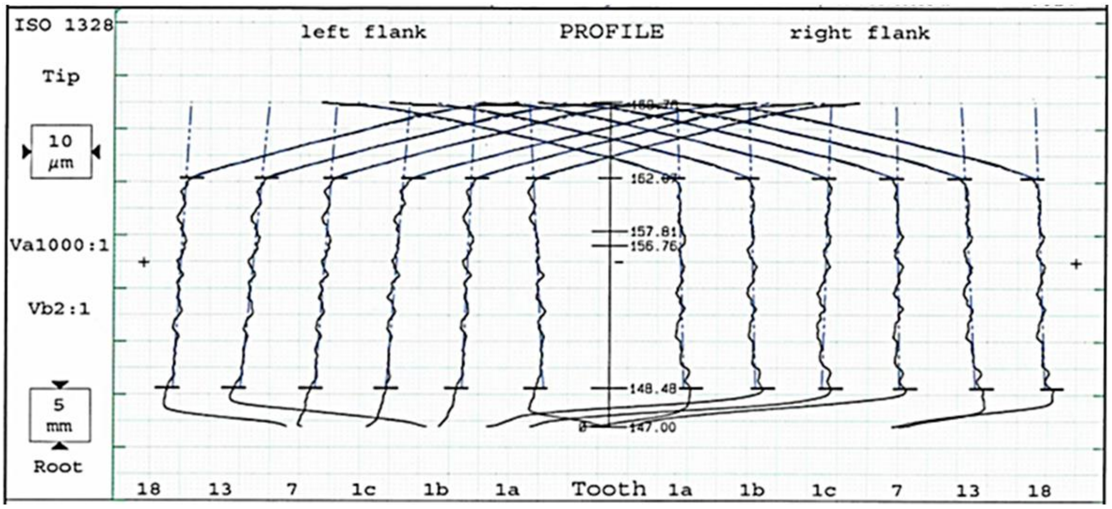

Figure 2-6 – Klingelnberg measurements of the profile deviation from the involute profile of teeth across a helical test gear. (Extracted from Clarke et al. (2017))

The gear in question was used in micropitting fatigue tests, where it was subjected to loads corresponding to a maximum Hertzian pressure of 1.6 GPa. Using data from these experiments, simulations of the elastohydrodynamic lubrication (EHL) were undertaken. Including the error profiles in the analysis; conditions in the contact area were observed to be substantially different from the standard analysis with a much greater contact pressure: increasing from 1.98 GPa to 3.2 GPa and a substantial drop in the minimum film thickness observed. Despite these analyses being theoretical, “the results presented in this contribution suggest that deviations in the profile affect oil film formation to an extent that may not be appreciated” (Clarke *et al.*, 2017). The work undertaken by Clarke et al. is but one example highlighting the importance and necessity for studying and understanding form defects and their effects on gear performance.

One method of quantifying the effect of these deviations is transmission error (TE). Transmission is defined by Munro (1990) as “the deviation in the position of the driven gear relative to the position of that the driven gear would occupy if both gears were geometrically perfect and undeformed.” As such transmission error is a measure of the effect of profile errors from tooth deformation, eccentricity, and manufacturing errors such as surface finish (Ottewill *et al.*, 2009).

There are a number of different types of transmission error that appear in the literature but the most prevalent are static and dynamic. Static TE can be defined as the transmission error of a pair of meshing gears under low loads and low speeds to avoid dynamic effects. Dynamic TE, as the name suggests, takes into account these dynamic effects in the form of a dynamic load factor and is measured at high rotational speeds. TE can be measured in a number of ways but is often measured as a linear displacement at the pitch point in microns (Tharmakulasingam, 2009) along the contact path. As such, TE in a system will alter the meshing cycle and the interactions between the gears at the mesh, potentially leading to increased noise and vibration.

Ottewill et al. (2010) showed how static TE can have a major effect on gear rattle. By generating a static TE function from a mathematical model developed, Ottewell *et al.* were able to prove the relation between profile inconsistencies and gear rattle. Experimental data captured from a 1:1 gear pair driven by servomotor (Ottewill *et al.*, 2009) was then used to derive an static TE function for comparison against that generated from the model, with a remarkable amount of agreement.

In comparison, Li (2007a) studied the effects of form errors on the loading capacity and load sharing of spur gears. For this purpose, Li developed a FEM software for contact analysis with the inclusion of assembly, machining and transmission errors. Comparison of the calculated results from the developed software for lead crowning and assembly errors was made against experimental data originally recorded and published by Rademacher (1968) and data collected by Li himself on a power recirculating gear rig respectively. The author has been unable to obtain a translated version of Rademacher’s original transcript but it was shown by Li (2007b) that the software possessed a high degree of accuracy and reliability in its calculations. As shown Figure 2-7 a & b, the length of the contact patch as calculated by the FEM software is a close approximation to the data measured by Radmacher, even when the position on the contact path is beyond a change point and the load is divided between multiple teeth.

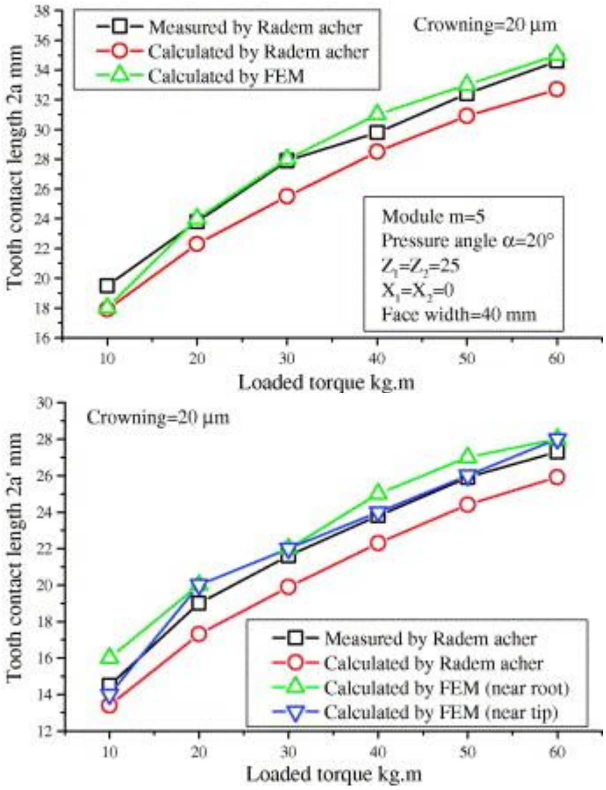

Figure 2-7 - (a) Comparison of tooth contact length in a single tooth contact area. (b) Comparison of tooth contact length in double tooth contact area. (Extracted from Li (2007b))

The accuracy of this simulation is further supported when compared to experimental data collect by Li, where the position of one gear is offset axially to provide misalignment and the root strains recorded using strain gauges at four positions. The results of this are shown in Figure 2-8, where it can be seen that the calculated root strains follow similar trends as those measures and provide a good estimate of the forces involved.

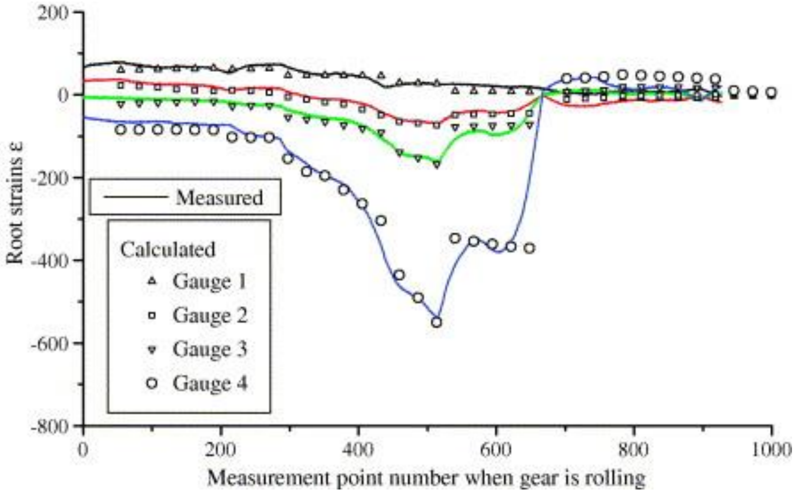

Figure 2-8 – Comparison of calculated and measured root strains at 4 different positions across the tooth root in increments of 10mm. (Extracted from Li (2007b))

While some inconsistencies are clear in both Figure 2-7 and Figure 2-8, the accuracy of the calculations is sufficient enough that merit can be placed on the results of the software. As with all simulations it clearly does not replicate the physical contact exactly and should not be thought as anything but a simulation. The reliability of the results however is enough that the FEM would be sufficient to provide a measure of the contacts and help direct future research efforts.

Li went on to apply the software to investigate the effects of form errors on the contact stress, the root bending stress and the load sharing ratio of gear teeth when multiples are in contact. Though his findings are based entirely off the FEM model, they do suggest evidence that machining errors cause heavy deviation from the predicted contact area with both the contact and bending stress being heavily influenced as a result. This deviation was found to also suggest that the load sharing when more than a single pair of teeth is engaged is not equal as normally assumed and provides an approximate measure of this load sharing. Demonstrated here are some possible consequences of form errors and how they can affect the gear system as a whole. The changes caused by these minor errors, particularly in contact stresses as suggested by Li's model are critical as, if large enough, they can result in more critical defects such as tooth bending.

Tooth bends, as the name implies, are where the tooth is bent away from the involute profile as is shown in Figure 2-9 This bending is caused when the force applied to a tooth exceeds the elastic limit of the gear material and causes plastic deformation. Although small amounts of elastic deformation are not uncommon, as gear teeth under load will experience some form of it routinely during standard operations. Plastic deformation quickly results in efficiency loses and can lead to reciprocating cycle that can generate new damage as well as furthering the initial damage which, if undetected, can lead to catastrophic gear failure.

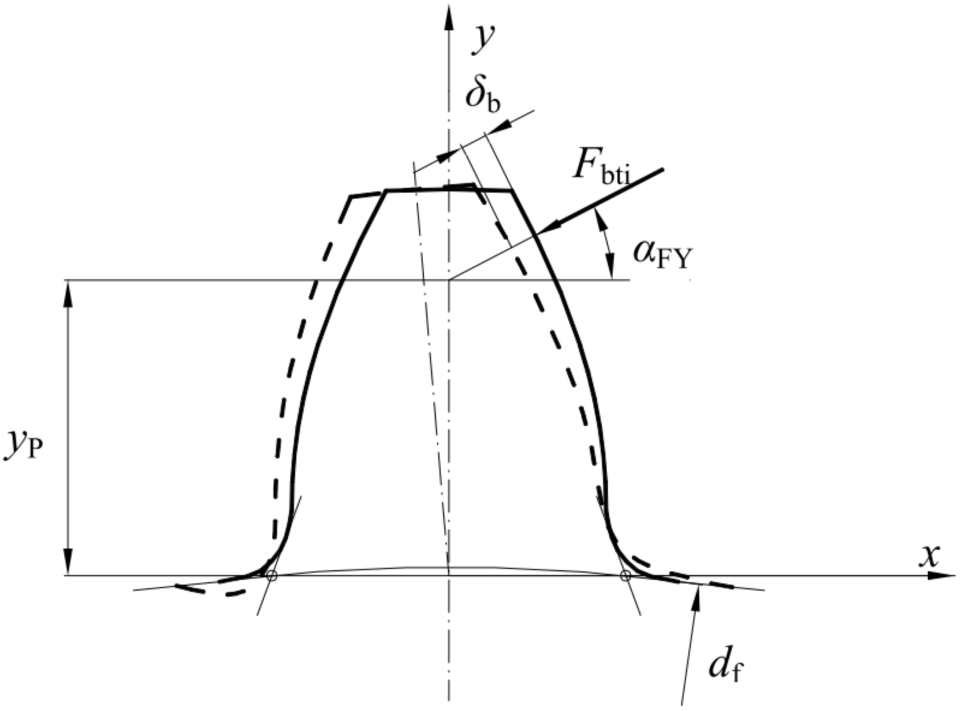

Figure 2-9 – Tooth deflection of a spur gear. (Extracted from Markovic and Fanulovic (2011))

The main reason for concern when looking at tooth bends is their effect on the meshing cycle. As the tip of the gear tooth is no longer evenly spaced with those preceding and following it, the tooth no longer matches the meshing cycle exactly and will engage later than expected, an example of this can be seen in Figure 2-10.

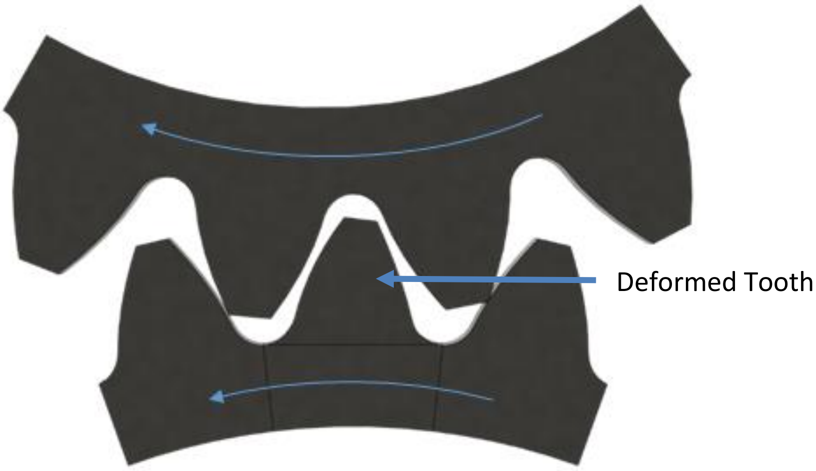

Figure 2-10 – Example of late engagement due to a tooth bend.

This has the same effect as suddenly introducing additional backlash into the system, where the system will try and 'catch up' across this new space. This causes shock loading to occur to the already deformed tooth as well it's mating counterpart.

Whilst tooth bends are a form of deformation, they may also be considered a type of spacing error. These are defined as the circumferential position of the tooth flank with respect to the previous tooth flank. Spacing errors often contribute greatly to transmission error (Inalpolat *et al.*, 2015) and as such can have a variety of effects on the meshing cycle.

This effect was investigated by Padmasolala *et al.* (2000) who studied the effect of profile modification on the dynamic load of gears with tooth spacing errors. Using NASA's DANST code to determine and model the transmission error, it was found that the load factor increases either exponentially with a linear profile modification or linearly with a parabolic profile modification in relation to the size of the tooth spacing error. Implying that tooth spacing errors will result in higher bending and contact stresses.

The increase in both of these quantities, can cause a variety of different effects. The increased contact pressure can alter the lubrication film thickness, producing a change in lubrication regime, which can introduce asperity contact from which surface defects may arise or if violent enough the surface fatigue induced may give rise to tooth chipping. Meanwhile the increase in bending stress can result in increased plastic deformation, propagating the increase in load. With this comes the ever-increasing chance of root crack formation and propagation which given sufficient time will result in complete tooth loss and gear failure.

2.4 Condition Monitoring

With the advent of the Digital Revolution, our world has seen an unprecedented leap forward in terms of both available technology and our understanding of science. As the world around us becomes more complex and connected so too does the unseen industries that supports it. Inevitably with higher complexity comes higher costs, both in the starting capital required as well as operation and maintenance costs. To this end, condition monitoring has become a subject of great interest in the past few decades, as companies try to reduce maintenance costs and improve reliability thus reducing the amount of downtime.

This is key in industries such as energy generation where not only is demand increasing but pressure has been placed on the conversion to renewable energy sources in an attempt to stem climate change. The response to this has seen an increase in the number of offshore windfarms deployed in order to meet the 2020 renewable energy targets. As the number and size of the turbines increase, reducing inspection and maintenance costs has become increasingly important (García Márquez *et al.*, 2012) as due to the harsh operating environments and access challenges presented by offshore wind turbines, they must have higher reliability than their onshore cousins (Yang *et al.*, 2011).

The failure of a mechanical component in a wind turbine is not a small or cheap operation. Not only does it have an effect on the kilowatt-hour costs but it also requires sending engineers to the site and making repairs in-situ or, at worst, having to remove several tons of the structure from the several hundred metre high stanchion (Anon, 2005). By applying condition monitoring in the form of a prognostics and health management system (PHMS), costs for maintenance can be reduced as well as the amount of downtime, both planned and unplanned.

PHMSs can be broken down into 3 areas (Figure 2-11): detection, diagnostics, and prognostics (Martin-del-Campo and Sandin, 2017). These areas are concerned with finding & locating damage, evaluating the severity and type of damage and finally predicting the amount of remaining useful life.

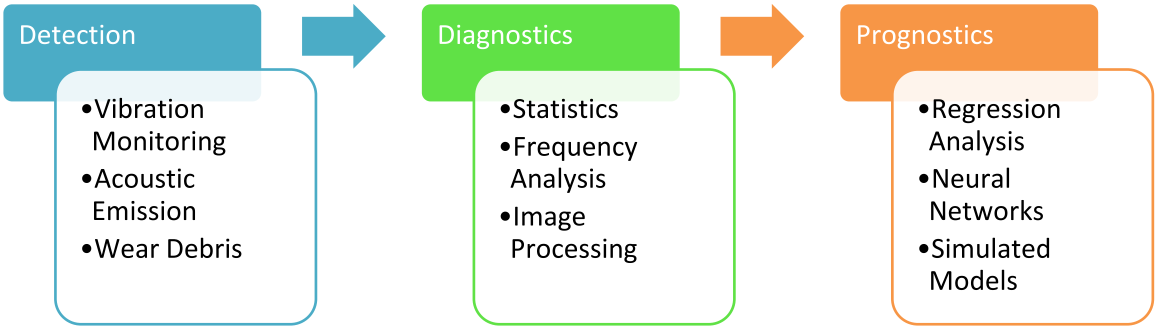

Figure 2-11 – The areas of PHM systems and example methods to achieve each.

While much research has been undertaken and is still ongoing in the individual areas, PHMSs are inherently greater than the sum of their parts. A combination of all three areas allows an image of the overall health of the system to be built. The data produced by a PHMS can highlight areas of weakness within the system. This allows for better product design, by tailoring components for their purpose; further helping to improve reliability. It is inevitable though that the component will deteriorate over time, no matter how good the design is and as such additional actions should be taken.

Using the measure of system health acquired by the PHMS it is possible to shift the maintenance strategy away from corrective and towards the preventative. Initially most industries will have a corrective type plan in place, either reactive or planned. The details of which can be found in Table 2-1. Depending on the importance and nature of the system this maybe the cost effective option, however larger systems such as wind turbines will nearly always benefit from a preventative type strategy.

Table 2-1 - Types of maintenance strategies adapted from Jardine et al. (2006).

Type	Strategy	Description
Corrective	Reactive	Repair or replacement immediately following the failure of the system or components.
	Planned	Routinely scheduled inspections and possible maintenance depending on the condition at time of the checks.
Preventative	Predictive	Planned maintenance based upon the estimation of the system or components remaining useful life, generated from known information of the component.
	Condition Based	By monitoring parameters indicative of the system or components health maintenance actions can be planned accordingly when a pre-determined level of degradation is reached.

Due to the diversity of industries and technologies interested in condition monitoring, a variety of different data acquisition and analysis methods have been developed, some of which are listed in Figure 2-11. This has allowed for data acquisition (DAQ) systems to be customised for their respective application and the refinement of analysis techniques to provide more accurate results. The most common DAQ systems and analysis methods used within gear systems will now be reviewed.

2.4.1 Vibration Analysis

Vibration is present in all machinery as moving elements will inherently generate undesired motion due to minor defects or imperfect weight distribution. While the amount of vibration can be offset through dynamic balancing and well-made designs, engineers must anticipate an amount of vibration to exist within any mechanical system.

With vibration being such an accepted feature of machinery, rotating or not. It is to no surprise it was one of, if not, the first form of condition monitoring. With changes in vibrations capable of being noticed by experienced operators through either touch or sound produced (Mitchell, 2007), the next logical step was to use instrumentation to replicate this ability. This is achieved through the use of accelerometers, which measure the acceleration of a surface or body through the application of Newton's second law of motion.

While many different designs and configurations of accelerometers exist, the majority operate on the configuration illustrated in Figure 2-12, differing only in details (Doebelin, 2004b).

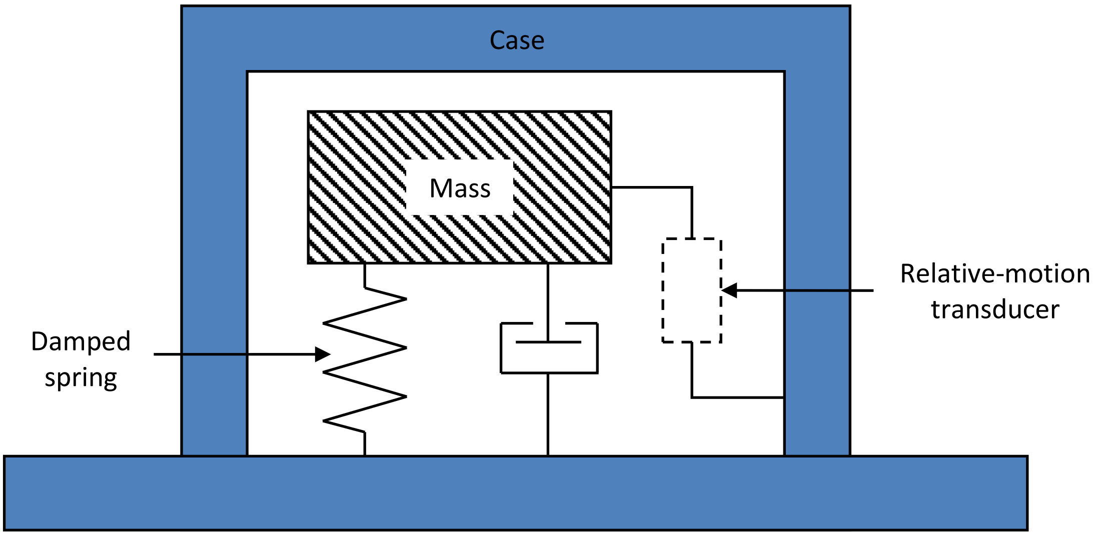

Figure 2-12 - Basic accelerometer configuration reconstructed from Doebelin (2004b)

To convert the mechanical action into an electrical signal, when the case moves relative to the mass a force is induced to the relative-motion transducer. This transducer can vary depending on build and age of the design, a common example being a piezoelectric crystal. These crystals produce an electrical charge when they mechanically deform, which by the law of capacitance:

$$C = \frac{Q}{V} \tag{2-11}$$

A capacitance *(C)* of one farad means that a coulomb of charge *(Q)* creates a voltage *(V)* of one volt across the crystal (Doebelin, 2004a). This voltage is then mathematically converted to a measure of acceleration allowing the formation of a signal representative of the vibration to be constructed.

Diagnosing the early onset of damage through the use of vibration signals heavily depends on the type and complexity of its application. Howard (1994) broke this down into classes of machines depending on the difficulty of bearing fault detection as seen in Table 2-2.

Table 2-2 – Degree of difficulty of bearing fault detection as a function of machine class. (Extracted from Howard (1994))

Class of Machine	Degree of Difficulty for Bearing Fault Detection	Machine Type
Easiest	1	Fans, Electric Motors, Generators
Slightly Complicated	2	Compressors, Pumps
Complicated	4	Industrial Gearboxes
Difficult	5	Turbines including Gas Turbine Engines
More Difficult	7	Helicopter Transmissions
Most Difficult	10	Specialised Rotating Machinery with Extreme Noise Environments

This degree of difficulty is a function of sensor placement and the level of noise to be expected from the environment as well as other components within the machine. While this was specifically defined for bearing analysis, it can be said that gear analysis could be broken down by the same scale as the difficulties that define the different degrees are issues with vibration monitoring universally and not just bearing analysis. Consequently, methods of detection and monitoring using vibration signals can be found applied to multiple areas of rotating machinery throughout the large collection of work now published investigating and expanding the field of condition monitoring.

Although vibration monitoring had been implemented with different degrees of technology and success since the mid-20th century, it was Stewart (1977) that provided the first rigorous investigation into the use of vibration signals for automated monitoring of gear systems. He proposed a series of 'figures-of-merit' applied to a time synchronous average of the raw signal. These descriptive, non-dimensional metrics were designed to allow the detection and the classification of damage within the system, with each one having a specific purpose.

Three of these 'figures-of-merit' were examined both theoretically and empirically, namely FM0, FM2 and FM4. The first of these is FM0 or the zero-order Figure of Merit and is designed to a global indicator of damage. This is to say that it will "react to changes occurring anywhere in the frequency span of the average" (Stewart, 1977). FM0 is defined as:

$$FM0 = \frac{PP_x}{\sum_{n=0}^{H} RMS(P_n)} \tag{2-12}$$

Where PP_x is defined as the maximum peak-to-peak amplitude, P_n is the root mean squared (RMS) of the meshing frequency and its harmonics within the average, H is the number of different meshing components and RMS is defined as:

$$RMS = \sqrt{\frac{1}{N}\left[\sum_{i=1}^{N}(x_i)^2\right]} \tag{2-13}$$

Where x_i is the signal and N is the total number of points within the signal (Randall, 1987). The second metric, FM2, was designed specifically to identify tooth fracture. This is performed by using the Hilbert transform to calculate the envelope of the signal average, this average is then smoothed using a low-pass filter prior to application of a matched filter. The 4th statistical moment: kurtosis is calculated for both the smoothed envelope and that after the application of the matched filter. The ratio of the later over the former is then used to determine tooth breakage. For reference kurtosis is defined as (Samuel and Pines, 2005):

$$Kurtosis = \frac{N\ \sum_{i=1}^{N}(x_i - \bar{x})^4}{[\sum_{i=1}^{N}(x_i - \bar{x})^2]^2} \qquad (2\text{-}14)$$

Finally, FM4 is a "quantifier for unassignable defects", that is those that cannot be detected by the other FM values. The difference between this 'figure-of-merit' and those mentioned prior is the reliance on the use of a residual signal. A signal where the 'regular' components of the signal have been removed i.e. the major gear meshing frequencies and their harmonics. The values of interest are then the standard deviation or kurtosis of this resultant waveform.

Application of these techniques to a gearbox undergoing a full power endurance test until failure, was met with a decent degree of success. Figure 2-13 shows the results of these test for tooth fracture. Stewart reports the success of all methods in detecting tooth fracture though each reacts in a different way and goes on to state that FM0 and FM4 traces indicate a 'clean' break change occurring around the 75 hour mark, lining up with the inspection of the cracked tooth, post-test. Stewart proceeds to explain that the FM2 trace shows a slower, more gradual process of decay with an initial change being detected as early as 30 hrs, the first 'blip' appearing at 75 hours and the final breakage being separated into 2 stage, the first between 99-110 hours and the second from 110 – 130 hours.

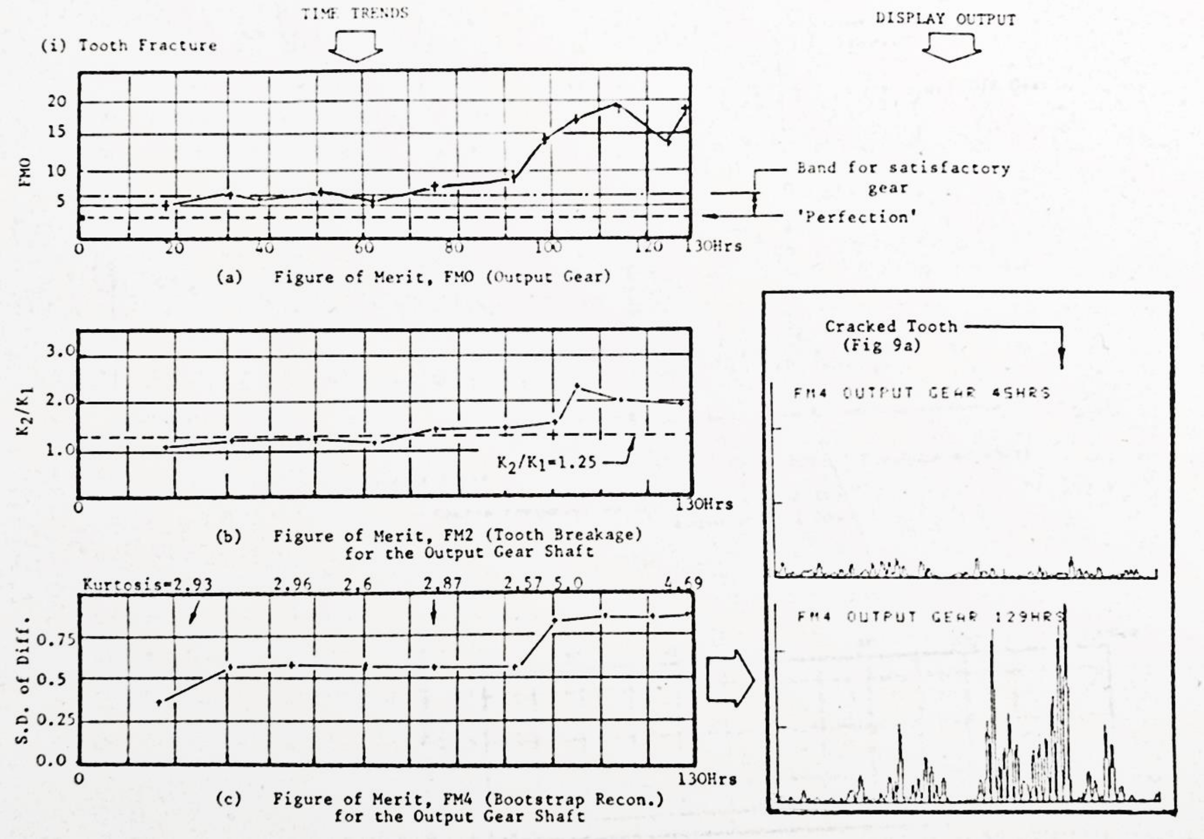

Figure 2-13 - Performance of 'figures of merit' in detecting tooth fracture (extracted from Stewart (1977)).

These results are significant as they clearly show that damage metrics are reliable method of monitoring for damage, especially when considering the use of an automated system. However, it is in the author's opinion that Stewart infers too much from the FM2 trace and is overconfident in the sensitivity of his metrics. While he correctly notes that the FM0 also suggests a more gradual progression of the damage, with an upwards trend seen from 60 hours. This seemingly goes against the physical inspections of the gear which "indicate a fairly a 'clean' break at around 99 hours", suggesting a short duration crack formation and propagation period. Meanwhile, the definition of the first phase of tooth fracture is reportedly between 99 and 110 hours from the FM2 trace. This is unlikely as this comes 10 hours after FM0 and FM4 have already detected the tooth failure, suggesting that any large transient disruption, which would define this phase to be over by this time.

Regarding sensitivity of the 'figures-of-merit', there is a notable lack of any distinct upward trend before the 75 hour point, calling into question Stewart's claim that around the 30 hour mark the condition can be seen going from "bad to worse". Though it can be observed that there is an increase across all the metrics between 20 to 30 hours, most notably in FM4. Without any data prior to the 20 hour mark any claim of detection is unfounded, as the data required is simply not present. The author would suggest it is impossible to accurately accredit any measurement of damage to the findings before the 75 hour mark. With confirmation of this seen from the FM0 and FM2 traces which both contain clear fluctuations before this point with no distinct trend, while FM4 shows no changes bar the aforementioned step increase.

Although FM2 is designed specifically to detect tooth fracture it is clear from this, that it is in fact FM0 and FM4 that showed great promise with Stewart suggesting that FM4 may be a competitor of FM0 in its detection abilities. The conclusions of this were that through effective signal analysis, vibration signals could be distilled into simple values that provide sufficient diagnostic information to allow an automated system to respond.

Continuing the work pioneered by Stewart, McFadden and Smith (1985) investigated the FM4 technique he proposed, specifically the use of the residual signal. The residual signal had by this time become a method for improving the detection capability of vibration data by, as it was claimed, being “due primarily to local variations in the meshing pattern” (McFadden and Smith, 1985). Prior to this no theoretical examination of the residual signal had yet been undertaken. To this end, McFadden and Smith used modulation theory to mathematically derive an envelope function which directly relates to the amplitude and phase modulation present in the original signal.

This proved that the residual signal is the “departure of the actual meshing vibration from the average.” (McFadden, 1987), affirming the prior claim and through the use of a narrowband technique developed by the McFadden highlighting the importance of phase modulation in the early detection of gear faults.

Applying their methodology to the signal from a spiral bevel pinion with a known fatigue root crack, clear evidence of a local defect was found in the envelope (Figure 2-15) despite no visual indication being present in the original vibration signal (Figure 2-14).

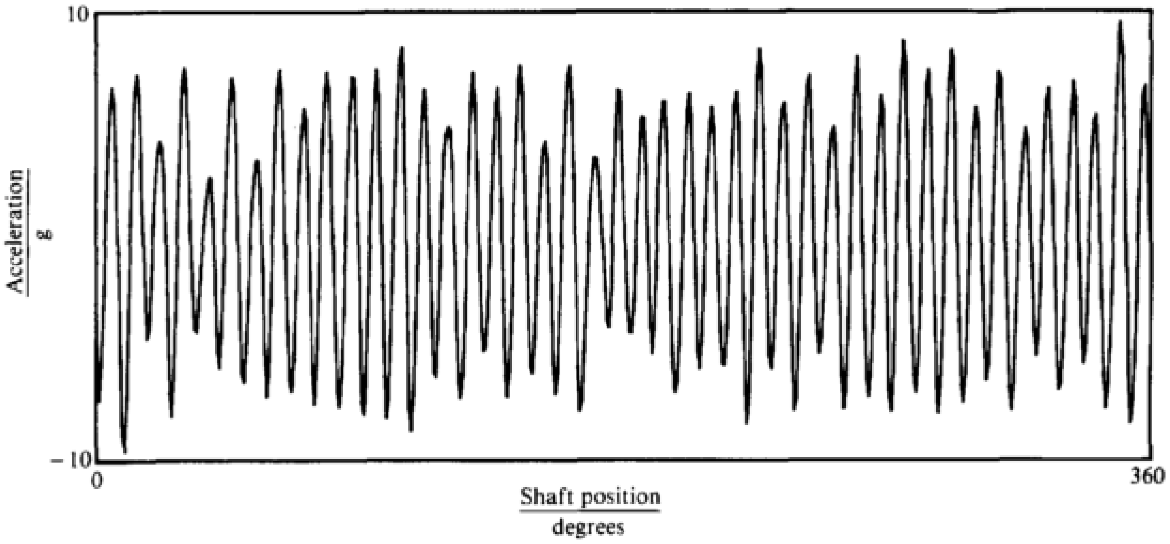

Figure 2-14 – The signal average of the gear vibration (extracted from McFadden and Smith(1985)).

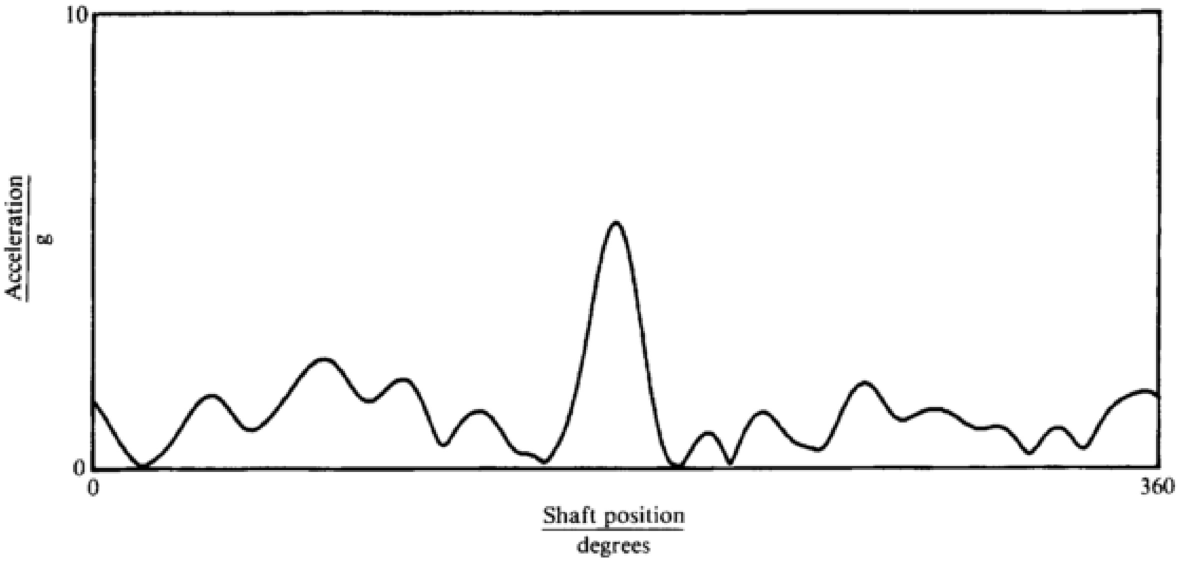

Figure 2-15 – The envelope of the filtered residual signal (extracted from McFadden and Smith (1985)).

Application of the kurtosis to this envelope would then provide a numerical measure of this detection with Figure 2-14 providing a kurtosis of 1.7, heavily implying that the signal is sinusoidal with some Gaussian noise. Figure 2-15 meanwhile produced a value of 9.2, supporting the visual presence of a large peak within the waveform. These findings highlighted the importance of phase modulation in damage detection and how the removal of the dominant meshing frequencies allowed for a clearer and more transparent detection.

McFadden would go on to improve this technique by using the proof seen in McFadden and Smith (1985). By taking the Hilbert transform of the vibration function developed, Mcfadden showed it was possible to generate approximations of the amplitude and phase modulations of the signal. These approximations when plotted provide some insight as to the presence of damage but not enough to be conclusive. This was improved by the application of Kurtosis to the approximations. Whilst some benefit was seen in the amplitude approximation, the most noticeable difference was seen in the phase modulation, where a distinct peak gave a clear indication of damage, as seen in Figure 2-16.

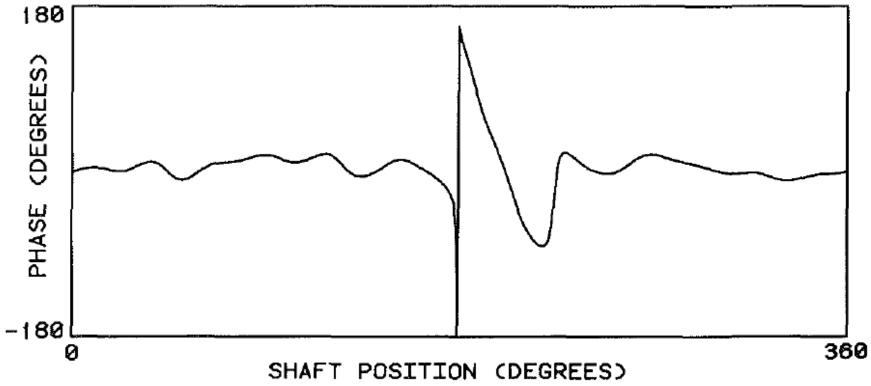

Figure 2-16 – Kurtosis of the approximate phase modulation of the vibration signal. (Extracted from McFadden (1986))

McFadden concluded that a polar representation of both amplitude and phase modulation provided a better visual indication of the progression of damage within a gear.

Zakarjsek *et al.* (1993) used a single pair spur gear fatigue test rig to generate pitting in pairs of test gears. Using accelerometers, they measured the vibration generated over the duration of a number of tests as the gears naturally developed surface defects such as pitting. They applied methods previously developed by Stewart (FM0, FM4), McFadden (Kurtosis of amplitude function) and Martin (1989) who developed M6A and M8A. These are essentially modified versions of FM4 which are designed to be more sensitive to peaks in the difference signal. The authors also presented a new metric, NA4, which was designed to not only detect the onset of damage (as FM4 does) but to continue to evaluate the damage as it progresses and increases in severity. All metrics were found capable, to varying degrees, of detecting initial pitting before the RMS signal level reacted to the damage. Whilst they found that in most cases the new technique, NA4, was a robust indicator of both damage initiation and progression, they noted that not every technique was consistently able to detect damage across all their tests. They therefore recommended that the application of several of different metrics was adopted to allow consistent damage detection.

Later, Zakarjsek (1994) presented further work on fatigue damage of both spur and spiral bevel gears. The previously discussed techniques were applied, as well as a modified form of NA4, called NB4*, which is designed to detect transient load fluctuations generated by a small number of damaged teeth, which are more likely to be visible within the signal envelope. NB4* is conceptually similar to NA4 but uses the envelope of the difference signal calculated using the

Hilbert transform, and is normalised by the variance of a healthy gear time signal as opposed to the variance of the current time signal. They found that NB4* reacted to damage in the majority of tests, in a similar manner to NA4. However, it was also noted than in certain cases, NB4* failed to maintain a warning level despite increasing damage severity.

The metric-based approaches, developed using simple single pair gear test rigs, were applied by Decker and Lewicki (2003) to a full helicopter transmission under test on the NASA Helicopter Transmission Test Stand. The transmission consisted of a spiral bevel input stage driving a planetary second stage, supported by multiple bearing and shaft arrangements. The test stand allows the testing of a real helicopter transmission without the associated difficulties of flight testing using a working helicopter. The test was designed to evaluate the ability of a range of metrics to detect damage under a range of loading conditions. They created a notch in one of the gear teeth, to promote cracking, and monitored the test using accelerometers. Of the metrics tested, Decker and Lewicki concluded that the most effective at detecting damage were M6A*, FM4* and NB4, where the presence of the asterisk indicates normalisation by the variance of a healthy signal rather than the current signal. Unlike the other operators tested, these were found to be load insensitive, and provided indicators of growing damage before traditional inspection methods were able to detect a tooth crack.

As stated by Zakrajsek *et al.* (1995), the availability of growing computer power has led to interest in more complex and computationally intensive techniques such as neural networks and pattern classification techniques, often used to interpret the results of time-frequency analyses.

Wang and McFadden (Wang and McFadden, 1993a) described the fundamentals of the Short Time Fourier Transform (STFT) and the spectrogram which is a visual indication of the STFT presenting a signal simultaneously in both the time and frequency domains, allowing the assessment of the change in frequency content of a signal with time. The spectrogram was found to be highly sensitive to changes of short duration in the signal, such as those caused by local damage to single gear teeth. The paper presents the results of the application of these techniques to the gearbox of a ball mill used for crushing coal in a power station. This can be seen in Figure 2-17 which shows the frequency content of the time signal captured, plotted against angular position of an idler gear.

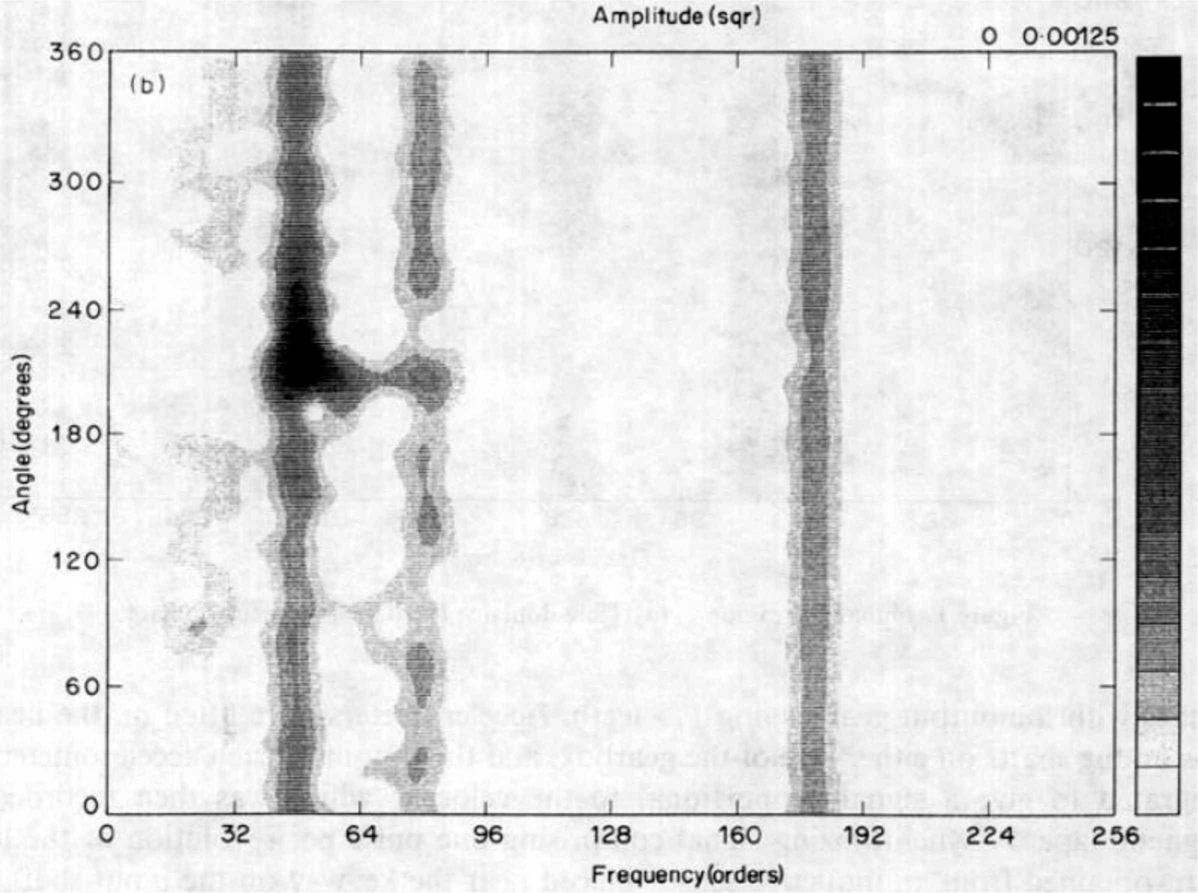

Figure 2-17 – Spectrogram of a gear with a small spall defect on a single tooth face located at approximately 210° (extracted from Wang and McFadden (1993a)).

There is a notable increase in amplitude of expected frequencies and across a wider frequency range at approximately 210° of idler gear rotation. Subsequent inspection of the gear found a small spall located on a single tooth face. This demonstrates the advantages of time frequency analysis and the sensitivity of the spectrogram to early fault detection. As well as the computational overheads however, this method required human interpretation of the spectrograms. Although this may have been feasible for non-critical applications, such human interpretation was clearly unsuited to the developing PHM systems. As these systems were designed to be autonomous and capable of indicating the presence and progression of damage without human intervention, there was a clear need for a computer-based method of interpreting the clearly powerful spectrogram results.

For this purpose, Wang and McFadden (Wang and McFadden, 1993b) treated the spectrogram as an image, and used image processing techniques to identify patterns within the image in order to automatically interpret the information presented visually by the spectrogram. They used early image processing techniques such as segmentation, connectivity analysis and feature extraction to analyse spectrograms of vibration gear obtained at particular points in time over the duration of a 31 hour helicopter transmission fatigue test. By using the image processing methods to quantify the area and intensity of regions of high amplitude within the spectrograms, they were able to detect automatically the increase in frequencies excited and the energy level at those frequencies as a fatigue crack grew within a gear. This simplified the interpretation of the spectrogram to the point where it could be incorporated in an automatic PHM system to raise warning without requiring human intervention. The recent explosion in available computing power has led to the use of more complex and powerful image processing techniques, with a corresponding increase in interest in the use of these techniques for feature extraction from signals for condition monitoring.

By taking the concepts of multiscale and local statistics, both originally developed for image processing, Loutroudis (2008) introduced multiscale local statistics for feature extraction of vibration signals recorded on a single pair spur gear test rig. This saw the application of the first four statistical moments (mean, variance, skewness and kurtosis) in multiscale local form. He found that the evaluation of statistical moments at multiple scales allowed a balance to be obtained between noise-rejection but lack of sensitivity (using larger scales) and localisation but noise sensitivity (using smaller scales). Higher moments such as kurtosis were found to be more sensitive to damage but applying them in a localized and scaled environment leads to the possibility of false positives as the moment becomes reactive to noise at smaller scales. Loutroudis concluded that the technique was potentially more sensitive and less susceptible to noise than well-established wavelet transform based techniques.

Prior to his development of multiscale local statistics, Loutroudis (2004) applied empirical mode decomposition techniques (EMD) to gear vibration data. This technique was originally developed by Huang *et al.* (1998) for the analysis of tide and tsunami data. The method decomposes the original signal into a series of self-selecting Intrinsic Mode Functions (IMFs), which can describe complex signals using a relatively low number of mode functions. Each IMF contains information about the content of a signal within a specific frequency range. Loutroudis tested a series of gears with different severities of artificially induced cracks. By decomposing the vibration signals, he found that the second IMF, in this example, isolated frequencies which were particularly sensitive to root crack size. By then analysing the energy present within the second IMF, he clearly showed the presence of a crack, and that the energy with the second IMF was strongly correlated with the crack size.

Smith (2005) introduced a similar technique to EMD, called Local Mean Decomposition (LMD), which retained more of the amplitude and frequency information from the original signal than was the case for EMD due to its use of the Hilbert transform. Whilst Smith applied this to the analysis of medical (EEG) signals, Wang *et al.* (2010) compared LMD and EMD techniques applied to the vibration monitoring of steam turbines. They found that LMD better captured the signal characteristics and offered earlier fault detection and better identification than EMD.

Whilst the techniques discussed have been applied to vibration monitoring of gears and other rotating machines, the fundamental analysis techniques deal with the identification of features within signals caused by anomalies. Other condition monitoring techniques, including acoustic emission, have also been applied to damage detection in rotating machinery, and are now discussed in turn.

2.4.2 Acoustic Emission (AE)

The phenomenon of AE has been understood since the 1960s where it was discovered that it could be used to detect cracks in pressure vessels. It could be argued that knowledge of AE was around earlier though not yet applied as the principles on which it operates and detection is made are the same as for earthquakes. Defined as the transient elastic waves generated by the rapid release of energy from localised sources within a material (Miller and McIntire, 1987). AE can be generated from a number of sources including but not limited to the movement of dislocations, crack growth, cyclic fatigue and cavitation. These waves then propagate across the surface of the material and the displacement generated is measured by a sensor, not dissimilar in function to that described in the antecedent section. The main difference between AE sensors and the vibration sensors described previously is their frequency response, accelerometers will, in general, produce a flat frequency response and only operate between 0 – 50 kHz as demonstrated by Figure 2-18.

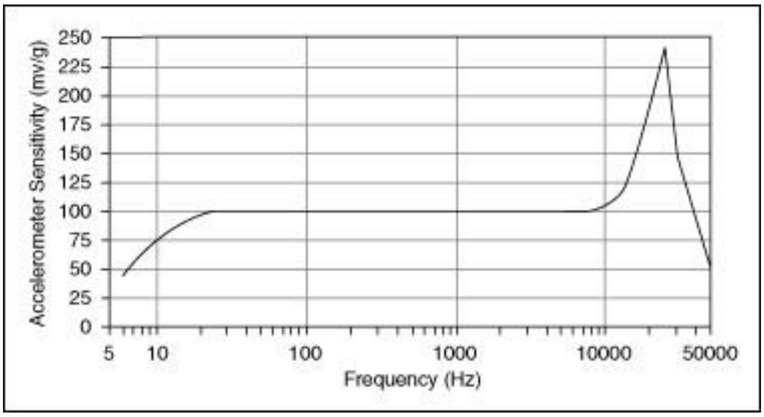

Figure 2-18 – Example of a flat frequency response produced by an accelerometer with a resonant frequency of 25 kHz (Extracted from National Instruments, 2019).

AE sensors however produce much less consistent frequency responses and commonly designed for much higher frequencies, commonly, between 100 kHz and 1 MHz. An example of such a sensor can be seen in Figure 2-19Figure 2-19, where the frequency response for a Physical

Acoustics can be seen. While these frequency responses are less consistent, the sensors themselves can still be used across a range of applications, though using a sensor with a resonant frequency close to the frequencies expected from the application is always preferable.

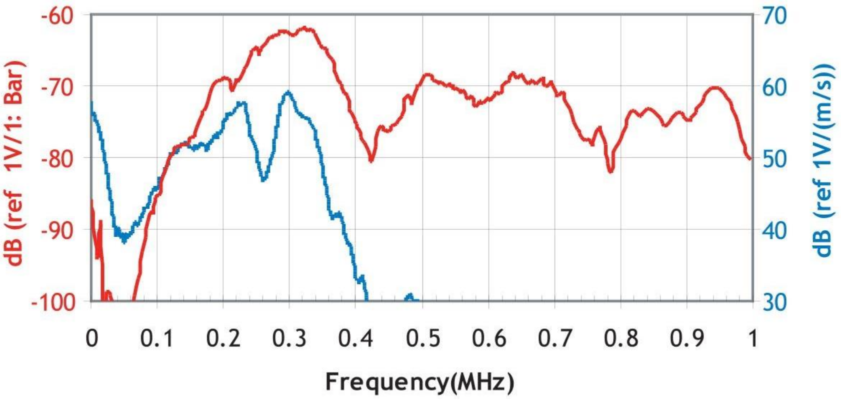

Figure 2-19 – Frequency response for Physical Acoustics R30A general purpose AE sensor (Physical Acoustics, 2019).

AE can offer a number of advantages to other modes of condition monitoring:

- *AE waves are high frequency.*

To quantify this, Miller and McIntire (1987) describe the most common frequency range for AE testing as “100 to 300 kHz” placing AE signals considerably out of range of any mechanical background noise which is broadly located below 20 kHz (Tan *et al.*, 2007). Preventing interference that may obscure results from lower frequency-based methods.

- *Sources of AE are microscopic.*

By nature, the size of a wave is related to the size of its source with larger waveforms e.g. vibration, requiring larger sources to trigger a response. The scale at which AE is generated provides the opportunity for detection of damage at the earliest stages of formation and has successfully been proven to be possible by Scheer *et al.* (2007), who through the application of wavelet analysis found that it was possible to detect both crack and pitting initiation and propagation. Whilst Hase *et al.* (2016) noted significant frequency shifts and increases in the RMS values indicating wear and seizure in journal bearings.

- *Non-directional.*

Unlike vibration that requires multiple accelerometers to measure the components of the three axes, a singular AE sensor will detect any emitting AE source within range no matter the location (Tan *et al.*, 2007). By using multiple sensors, it is therefore possible to triangulate the source of the signal and locate the damage, however it should be noted this rarely has application in rotating machinery due to the motion present.

Despite these advantages and the time passed since the inception of AE as a condition monitoring process, the technology has been used almost exclusively for structural performance and only expanded into rotating machinery in the past 30 years. During this time, AE has seen wide application across the fields of both tribology and condition monitoring to different degrees of success.

Miettinen and Siekkinen (1995), studied the use of AE to monitor the behaviour of sliding contacts, specifically leakage and dry running. This was achieved by mounting an AE sensor on the fastening ring for a double acting face seal and monitoring the RMS of the resultant AE voltage. Miettinen and Siekkinen found that on average that a leaking seal would generate an AE RMS of approximately 25% less amplitude compared to its regular counterpart. Whilst the resultant temperature increase from dry running correlated with the increase in AE activity.

In contrast, Sentoku (1998) investigated how AE would react to surface damage of gear teeth such as pitting. Using a power recirculating rig, Sentoku ran a pair of high frequency hardened gears with an AE sensor mounted on the gear face close to the teeth. These gears were run until pitting was found to have developed. Performing time synchronous averaging on the AE wave forms at periodic intervals Sentoku demonstrated a notable increase in amplitude and AE energy as the test progressed indicating the onset of pitting and its progression, concluding that it was possible to detect pitting at the early stages of its formation.

Various workers have investigated the use of AE to monitor gear systems. Toutountzakis and Mba (2003) investigated the AE from spur gears under test, using sensors mounted on both the rotating gear and on the fixed gear wheel bearing housing. They determined that AE levels (RMS and Energy) for undamaged gears were highly sensitive to operating speed. In a subsequent test, where the gears were inadvertently misaligned, the authors observed changes in the RMS and energy levels of the AE signals. Manual inspection showed evidence of micro and macro-pitting, scuffing and other wear mechanisms in the misaligned gears. Figure 2-20 shows a comparison between RMS signal level for healthy and failing gears.

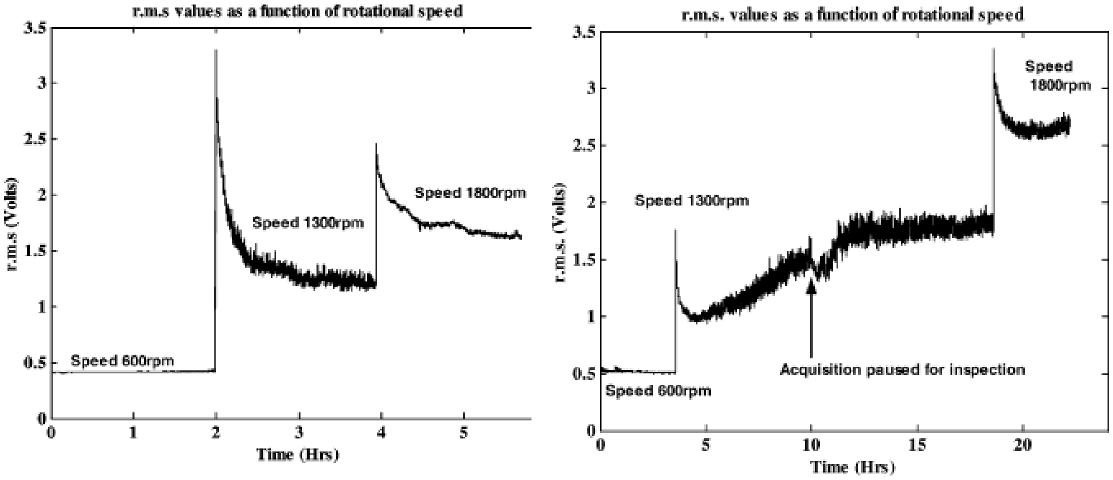

Figure 2-20 – RMS AE levels for healthy (left) and failing (right) gears, recorded using a sensor mounted on the gear wheel. (Extracted from Toutountzakis and Mba (2003))

Toutountzakis *et al.* (2005) went on to investigate AE signals from gears with artificially seeded defects. The teeth of the spur gears were artificially damaged to create small defects using an engraving machine. They found an AE response to the meshing cycle indicating all 16 gear teeth meshing in turn. However, they found that this signal was sensitive to applied torque, as shown in Figure 2-21.

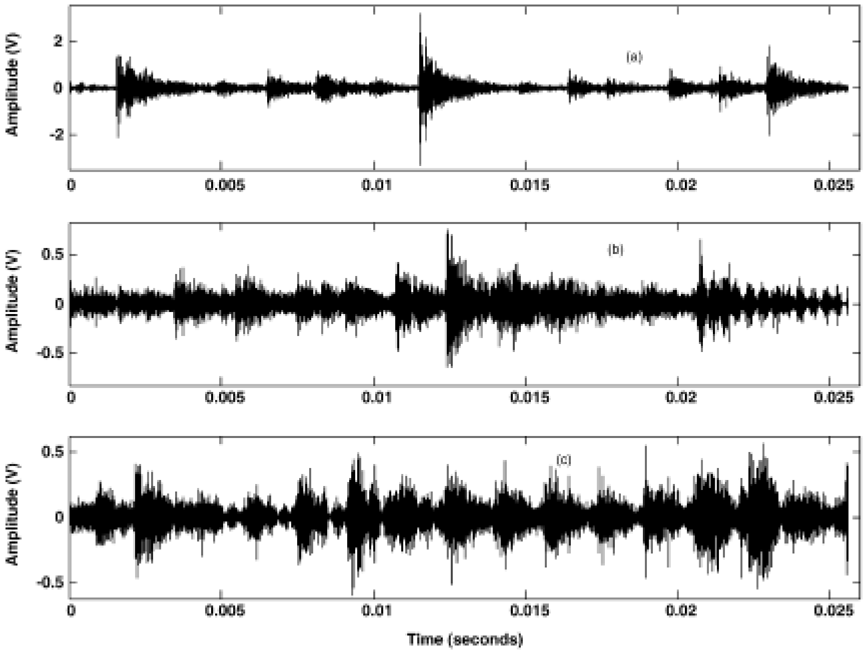

Figure 2-21 – Raw AE signal for a small pitch line defect tested at (from top) 0, 55 and 110 Nm load. (Extracted from Toutountzakis and Mba (2003))

They concluded that, whilst AE showed a change in response related to the defects, the nature of this change was not always predictable. They concluded that sources of AE from seeded defects were not representative of those from naturally occurring defects which form during life tests of gears. For example, during naturally-occurring pit formation, AE will be generated by crack growth and debris over-rolling, neither of which will occur with seeded defects.

Molino Vicuña (2014) and Barrueto Novoa and Molina Vicuña (2016) considered the various potential sources of AE in gears. They demonstrated that typical AE signals from spur gears consisted of transient bursts, spaced at the gear frequency, superimposed on continuous emission, as shown in Figure 2-22.

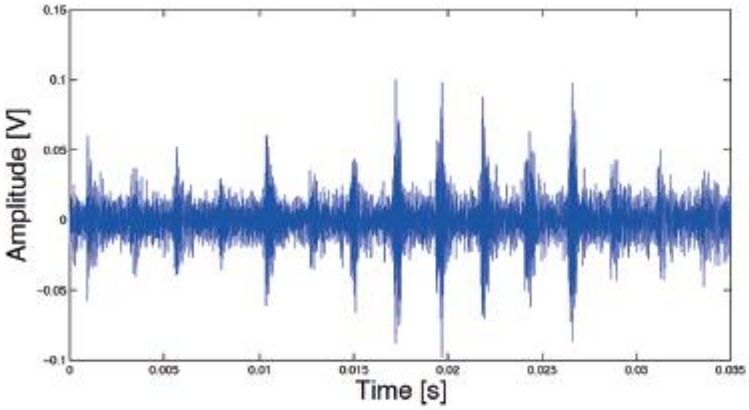

Figure 2-22 – Example AE time signal from single-stage planetary gearbox. (Extracted from Barrueto Novoa and Molina Vicuña (2016))

They hypothesised that the transient bursts were due to either instantaneous pure rolling conditions at the pitch point, by the elastohydrodynamic exit pressure spike or the shock loading caused by tooth engagement. In the author's view, the latter seems the most plausible explanation. They also argued that the continuous emission was related to asperity contact due to the gears operating under mixed lubrication conditions. Their experimental work, using planetary gearboxes, demonstrated the sensitivity of AE to load, speed and lubricant temperature, concluding that changes in AE signals due to speed and temperature (and hence viscosity) changes were primarily due to changes in lubricant film thickness and asperity interaction.

Whilst it is attractive in laboratory tests to mount sensors directly on rotating gears, this is often difficult or impossible to achieve in industrial applications. Therefore, sensors are more typically mounted on gearbox or bearing housings, which means that the signal has to travel along complex transmission paths between source and sensor. Singh *et al.* (1999) used a static tooth breakage rig to investigate the attenuation of AE signals across multiple interfaces such as the gear/shaft interface, and through the multiple race/roller contacts in bearings. The transmission loss across each interface was quantified, and substantial, demonstrating the importance of correct sensor placement for AE monitoring of gears and other rotating machinery.

Much of the literature on the use of AE for gear monitoring is based on simple techniques such as RMS, Energy and wave stream analysis. More recently, authors have used advanced signal processing methods to identify damage-related signal features. For example, Scheer *et al*. (2007) used wavelets to identify both micropitting and tooth root cracks, as shown in Figure 2-23 where a once-per revolution pulse is clearly visible indicating a fatigue crack in a single tooth.

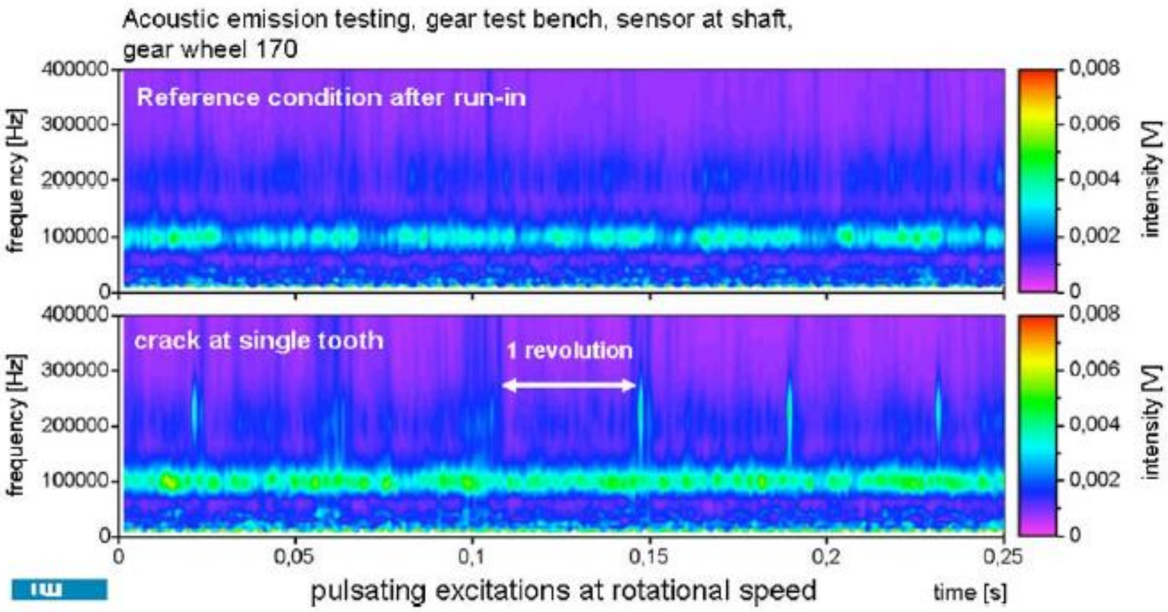

Figure 2-23 – Wavelets of signal from reference gear (top) and gear with crack (bottom). (Extracted from Scheer *et al*. (2007))

Scheer concluded that AE allowed early detection and characterisation of gear faults, run-in effects, and rolling-element bearing faults. Wirtz *et al.* (2016) went on to use similar time-frequency analysis techniques to identify micro and macro-pitting in an FZG gear test rig, with conclusions which supported the findings of Scheer *et al.*

Further advanced techniques for signal processing were used by Crivelli *et al.* (2017) who used image-processing techniques (Chebyshev polynomials) to characterise changes in wave streams recorded over the duration of a gear tooth root fatigue test. They found that the use of Chebyshev descriptors was a computationally inexpensive and efficient way of describing substantial datasets, and could potentially address the issues around the large volumes of data associated with AE monitoring.

2.5 Other Techniques

The previous discussed techniques are currently the most prominent in the field of condition monitoring for rotating machinery. As shown though, these methods are not infallible leading to modern condition monitoring systems to make use of multiple different monitoring methods (Mitchell, 2007). This setup normally comprises of a main system (vibration or AE) supported by one or more ancillary systems. These additional monitoring methods are normally less effective or not as well established, but their inclusion greatly lowers the possibility of false positives and provides subsidiary data to confirm the presence of damage when indicated by the main system. While these methods are numerous and can often be specialised for the application, some of the more common examples are discussed here.

2.5.1 Oil Debris Monitoring

Oil debris monitoring (ODM) is a common method of monitoring and has been well developed in its' own right. Debris present in a lubrication system can be detected in a variety of methods both online and offline. Online methods use sensors built directly into the lubrication system to provide a real-time measurement of the amount of debris in the system. These sensors can a operate in a number of different ways, an example of which is presented by Zakrajsek (1994): As oil passes through a sensing coil, a magnet is energised and de-energised repeatedly. The debris is drawn and collected along the sides of the coil. This leads to a change in the inductance of the sensing coil leading to alterations in the frequency of the output signal, thus indicating the presence of debris. While these sensors have the advantage of the providing data in real-time, they can only indicate the amount of particulates in the system. Offline methods can provide much more data, i.e. the size, shape and material properties of the particulates present. From this, the origin of the particulates can be extrapolated providing an indication as to the state of the system. The major drawback of this is that an oil sample must be removed from the system and the analysis can be time consuming. Implying that further deterioration may occur in an active system before its health can be verified.

Investigating the increased detection capabilities of joint systems, Peng and Kessissoglou (2003) studied the correlation between wear debris analysis (offline) and vibration analysis. This was undertaken using a worm gearbox run in three sets of conditions over 18 weeks with oil samples taken periodically. The first test simulated insufficient lubrication via substitution of the recommend oil for one with approximately one quarter of the viscosity. The second test, was performed with standard operating conditions and the final test had contaminant particles were introduced to the lubrication system. From these experiments, Peng and Kessissoglou found that individually both techniques detected similar wear mechanisms and had their own advantages. Wear debris analysis provided greater insight into the wear rate and the mechanisms for the wear, whilst vibration analysis provided a quick and reliable information as to the state of the system. By comparing the two sets of data however it was concluded that a more reliable assessment of the condition of the system could be gleaned. Where the wear debris analysis indicated signs of increased wear rate, the vibration data provided an indication of a developing bearing fault.

Loutas *et al.* (2011) would expand this concept further by looking at the combined use of vibration, AE and oil debris monitoring (online) as a combined system to provide more effective condition monitoring. Data was collected from a run-to-failure test performed on a single pair gear rig. The total mass and mass rate (*mg/hr*) of the iron content in the system were recorded alongside the vibration and AE. Comparing the oil debris measures directly with post processed vibration and AE results. Oil debris clearly provided an indication that wear, and damage was occurring, although the reaction was delayed compared to the more established techniques. All this data was subsequently fed into an independent component analysis (ICA) algorithm, to extract meaningful information from a variety of sources. This proved effective with Loutas *et al.* showing that the first component of the ICA could be correlated with the oil debris analysis indicating that it can provided a reliable measure for monitoring basic damage modes.

Despite the duration since its inception, many studies are still being undertaken to determine the effectiveness of oil debris monitoring. Kattelus *et al.* (2018) performed a comparative experiment between vibration monitoring and ODM. Running a fatigue test on a power recirculating gear rig, a set of spur gears were ran until macropitting had occurred over 4% of the active tooth face on any single tooth or the test reached 50 million cycles. Visual inspections were undertaken every 2.5 million cycles, with the test being terminated at 10.84 million cycles. Using the visual inspections as guide to the progression of damage, it was found that there was a good correlation between what was the visible stage of the damage and the number of particles being detected by the ODM. The results from the ODM system clearly indicate the start and progression of wear with the cumulative particles present, this is also seen by the number of particles obtained in 2 hour periods, leading Kattelas *et al.* to conclude that on-line monitoring is a promising technique.

A basic vibration analysis was undertaken alongside the ODM and visual inspections. Using a limited number of descriptors being used; namely crest factor, kurtosis and form factor. Different frequency ranges were analysed to identify changes in particular parts of the spectrum. The areas covered the entire spectrum, the meshing frequency and its harmonics, the meshing frequency and its side bands and finally the rotational frequencies. Overall, Kattelus *et al.* concluded that the vibration analysis showed “efficient ways to detect symptoms of a gear fault in the early stage of development”. While the vibration results presented do indicate the damage at the final stage before termination of the test. The consistency of the vibration metrics prior to this can be interpreted as an indicator of early damage onset. As shown in Figure 2-24, stage 2 is among the final hours of the test with oil monitoring showing a sharp increase signifying the rapid increase in macropitting, as confirmed by the visual inspections. This is not represented by any of the vibration metrics shown in Figure 2-25, with stage 2 showing a slight decrease across the board. This may be related to the resolution of the analysis, with the four arbitrarily defined stages not providing enough detail of the vibration signal to allow detection before this point. This highlights the issues with relying on a single detection method and harks back to the conclusions made by others, that a combination of detection methods provided the most effective means to identify the early onset of damage.

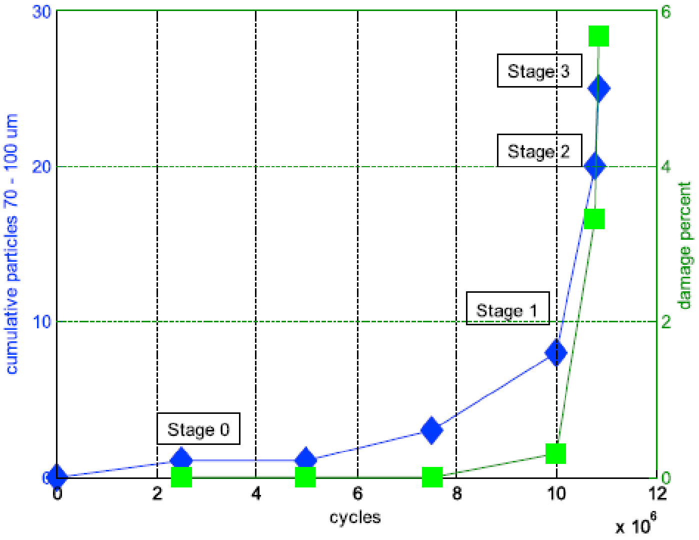

Figure 2-24 – Comparison of gear flank damaged area and the measured particles as a function of load cycles (Extracted from Kattelus *et al.* (2018))

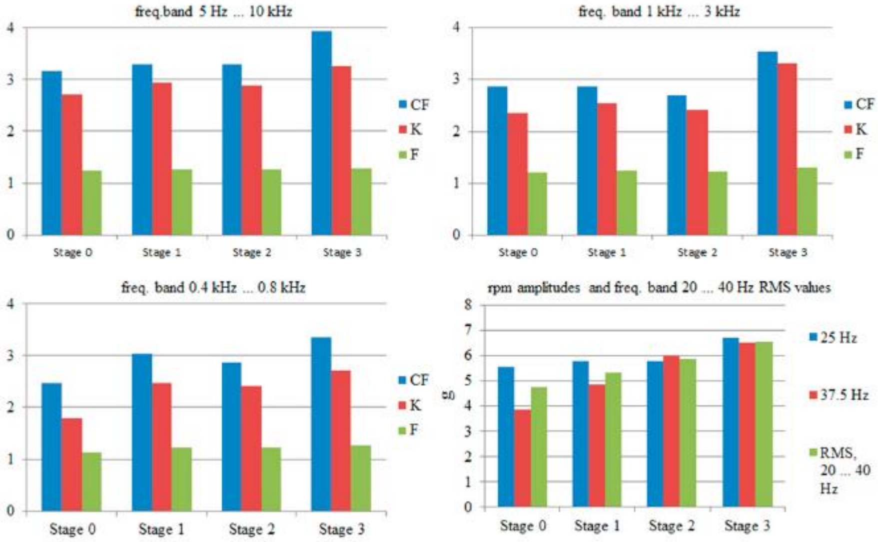

Figure 2-25 – Value of Crest Factor (CF), Kurtosis (k) and Form Factor (F) from vibration measurements at different fault stages. (Extracted from Kattelus *et al.* (2018))

2.5.2 Thermography

Like ODM, thermography or temperature monitoring is a method of damage detection often used to support a main system by providing an additional data source with which to detect and confirm damage. Much like Ronseal™, temperature monitoring does exactly what it says on the tin: by monitoring the temperatures at key locations any increase can be measured. Maintenance engineers perform thermography in the field by making use of thermal imaging cameras to perform quick and easy assessments of the condition of a system (Mohanty and Fatima, 2015). As with all mechanical systems, power loss will occur and a large percentage of this will take the form of heat. Knowing the approximate power loss of each component allows for detection of uncharacteristic fluctuations of increases which then maybe used as a flag to indicate damage or abnormalities in the system.

The most common application of this technology is to bearings as they are often self-contained and generate heat in an even manner. Such an example is Mohanty and Fatima (Mohanty and Fatima, 2015) where the effects of load, speed and shaft misalignment were measured using thermography of the support bearings. The shaft misalignment was successfully detected, though the effect of different degrees of misalignment was not investigated. Gear applications are less common as they introduce difficulties in the monitoring of the temperatures. Placing a sensor at the tooth contact is often not possible and lubrication can interfere with the surface emissivity measured by thermography (Touret *et al.*, 2018).

Despite this, Waqar and Demetgul used thermography in conjunction with vibration and noise measurements to train a neural network. A training set was generated using a worm drive, ran in both healthy and damaged scenarios with the damage artificially generated by removing a tooth from the gear. Whilst the neural network proved to be a highly effective detection and classification method with a success rate of 94%, the thermography results showed promise with areas of interest showing increased temperature despite the monitoring being outside the casing, removing the effects of lubrication but reducing the overall resolution, which can be seen in Figure 2-26.

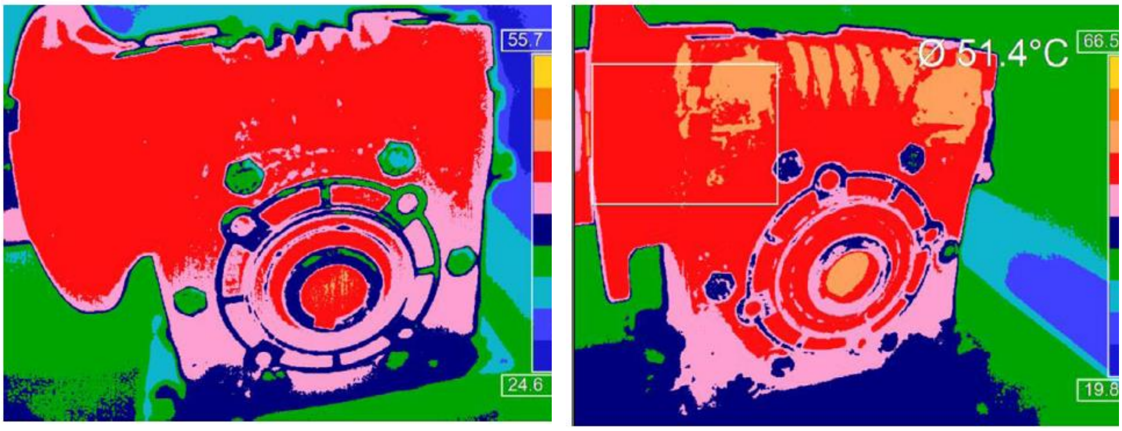

Figure 2-26 – Healthy and damaged thermography images. (Extracted from Waqar and Demetgul (2016))

2.6 Disadvantages of Currently Techniques

As demonstrated in this chapter no method of condition monitoring is without fault. Whilst vibration and AE are clearly well established and can provided excellent detection of faults in the correct setups, the reality of industrial monitoring is that no application will be perfect and flaws in a PHM system will be inevitable. These flaws manifest in different ways depending on the technique used but can be summarised as:

Vibration: The critical flaw with vibration monitoring is that defects must have developed to a scale at which the defect is able to affect the natural vibration of equipment being monitored. By this time, the defect will have often reached a size where it can be detected by routine maintenance. This has the added effect that detection of a defect may only occur at the 11th hour, so to speak. In industry this "last minute" detection may not always be sufficient enough in warning and may lead to logistical difficulties and overly complex PHM systems. Vibration signals are also susceptible to noise as, in general, they occur lower than 20 kHz. This places them in the same area as mechanical background noise and low end electrical interference from 3-phase systems and power supplies.

Acoustic Emission: While AE has been seen to provide the ability to provide very early warning of detection, it has also been seen that this is fraught with difficulties; the greatest of these is attenuation. To compensate for this, many studies directly monitor the AE of gears by attaching the sensor directly to the gear. In industry this is often not possible, and the AE sensors must be carefully located to minimise the loss in signal strength caused by traversing multiple interfaces. While the loss of signal strength through attenuation can be severe on its own, AE has also been shown to be sensitive to speed, temperature and load. In rotating machinery applications, these factors are rarely constant which can lead to uncertainty in AE sources with increased emission originating from a sudden change in operating conditions rather than faults arising from damage.

To help negate some these flaws, PHM systems may be comprised of multiple damage detection methods as previously discussed. While ancillary methods can benefit a system, they also inherently introduce more complexity and cost. While additional monitoring techniques will always be present in PHM systems to help with confirmation and eliminate errors, a more robust principle detection method provides less complexity in systems and the tailoring of the support structure to the application. For this purpose, this thesis is investigating the Rate of Change of Torque.

2.7 Rate of Change of Torque

Rate of Change of Torque (ROC) is a relatively new method of condition monitoring developed by Garshelis *et al.* (2007). ROC was built upon the concept that as torque is an intrinsic component to all rotating machinery, variations in it are ubiquitous. Given that the amplitude, phase, spectrum etc. mirror their causes, monitoring the variations in torque can provide more detailed information than monitoring the total torque. ROC is the characterisation of these fluctuations and continuous monitoring allows for identification of specific events in a torque signal e.g. gear tooth engagement. While a torque signal can be differentiated with respect to time to provide a ROC signal, direct measurement provides greater sensitivity with the ability to capture small transients that maybe lost through a non-direct measurement (Garshelis *et al.*, 2007).

ROC sensors operate on the same magneto-elastic principle that was developed by Garshelis (1992) and Garshelis and Jones (1999) for non-contact torque transducers. For the purposes of this thesis, a brief explanation will be provided, but a full explanation can be found in the aforementioned papers.

A ROC signal is generated by an active band, imbued to a section of a shaft. The active section is defined as the region that has a circumferentially directed remnant magnetisation. Under normal conditions, the magnetisation is a series of circumferential rings where the divergence is zero i.e. no external fields arise from the band, as demonstrated in Figure 2-27 (a).

When the shaft is subject to a torsional load the magnetic field changes from a series of rings to a helical field, inducing an axial flux and increasing the divergence. With a divergence greater than zero an external field to the band arises which can then be detected by the sensor, this can be seen in Figure 2-27 (b).

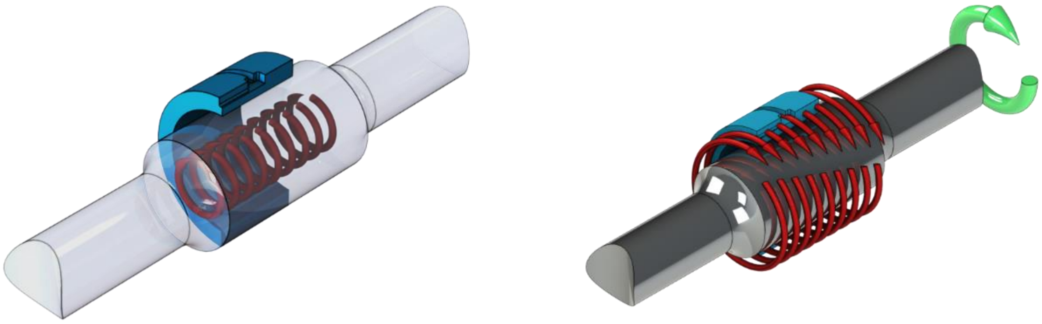

Figure 2-27 – (a) Magnetisation under no load. (b) Magnetisation when subjected to a torsional load.

From this magnetic field the ROC sensor responds to the rate of change of axial flux which is directly proportional to the rate of change of torque. This is achieved through the use one or multiple sense coils, using a singular coil the electromagnetic field (EMF) induced voltage in the coils is proportional to the rate of change of flux. Using multiple coils allows the sensor to be configured for common mode rejection, by having two remanently magnetised circumferential bands applied to the shaft with opposite polarity, a common field applied to both coils can be subtracted and a differential field added (Kari *et al.*, 2011).

The sensitivity of these sensors varies depending on calibration but is generally between 0.5 – 1 µV/(Nm/s), for example the yoke sensor used in Chapter 3 possesses an average sensitivity of 0.9175 µV/(Nm/s) and uses an amplifier with a gain of 100, while the probe sensor used in Chapter 5 and after has a sensitivity of 8.7 µV/(Nm/s) and has an amplifier with a gain of 1000. This calibration of the sensors is performed on a static torsion rig where the ROC sensitivity is determined by applying a near constant rate of change of torque to the shaft during cyclic loading cycles.

Damage detection through the use of ROC signals has an immediate advantage over traditional techniques such as vibration and AE, for a number of reasons: As previously discussed, sensor placement is critical in both vibration and AE to ensure the clearest signal is received and give the greatest changes of detecting damage. Ideally sensors would be placed on the gears themselves, but outside of laboratory conditions this rarely achievable and they must be placed on the casing, leading to attenuation and reduction in sensitivity. ROC sensors avoid these drawbacks by as their operation allows the sensor to be non-contact. This significantly reduces the difficulty of locating the sensor within the system and allows easy incorporation into existing designs. This is further helped as, just as a river must flow from source to sea, torque must flow from engine to wheels or turbine to generator. While torque transfer between components will inherently cause loses, generally these loses will be minor in comparison with the amount of torque being transmitted. This in principle means that a ROC sensor maybe placed anywhere in the torque path and still be sensitive to the variations in the system. While sensor placement will determine what components can be monitored, this allows a great deal of flexibility overall.

Despite these advantages, ROC technology does have its own restrictions as described by Kari *et al.* (2011). The first of these is shaft material, the magnetisation required for ROC means non-ferromagnetic materials cannot be used directly, although it is possible to attach a ferromagnetic band to a such a shaft to achieve the same functionality. Ferromagnetic materials must still 'demonstrate favourable magnetoelastic properties' as well as possessing a Curie's temperature well above 150°C for high temperature requirements limiting the material selection further.

Second to this is the positional containment, i.e. the radial and/or axial position of the shaft to the sensor must be controlled and finally the presence of other magnetic fields in close proximity to either the shaft or the sensor can damage the magnetisation of the shaft, preventing or complicating the data collection process.

To date, little work has been undertaken using ROC technology. Despite this, what has been published presents a promising new method of damage detection in rotating machinery. Garshelis *et al.* (2007) tested the newly developed sensor on an eddy current dynamometer. Running the dyno at a mixture of speeds and loads; the ROC and the rate of change of armature current (ROCC) in the motor were measured. A comparison of the two traces (Figure 2-28) showed that the ROC signal was correctly responding to the torque changes with zero crossings well synchronised, though not exactly. This is important as the armature current controls the motor torque, so a 0 in the ROCC trace implies that the torque is constant.

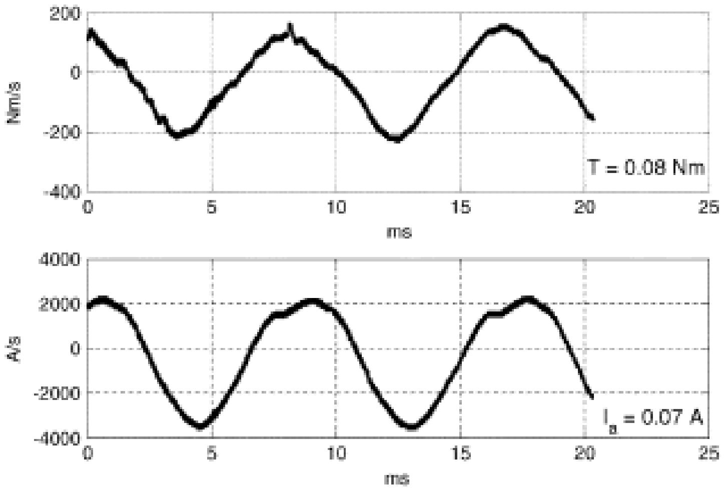

Figure 2-28 – A comparison of ROC (upper) and ROCC (lower) traces at 2000 rpm. (Extracted from Garshelis *et al.* (2007))

Further testing on engine dynamometers was also success with the ROC signal indicating each individual firing event and showed an absence of such event when the tests, included deliberate misfires.

With the initial success of the ROC sensor, Garshelis *et al.* (2008) investigated ROC's ability applied to the operation and condition of a cutting tool on a milling machine. Fitting a ROC sensor over the shank of an end mill between the cutting region and the machine spindle. ROC data was captured over a number of different conditions during active cutting operations. Comparison to a theoretical model, showed that signature features of the model were exhibited by the recorded ROC signal with it staying representative as the number of flutes on the end mill were increased. Further study was undertaken by artificially dulling one of the two cutting edges, this produced Figure 2-29.

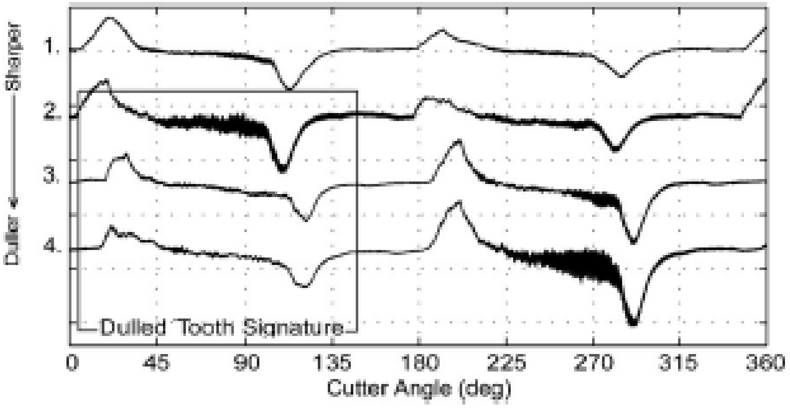

Figure 2-29 – ROC signals with increasing dullness of one tooth of a two flute end mill. (Extracted from Garshelis *et al.* (2008))

From this Garshelis *et al.* notes how the 'how the dulling of the cutting edge upsets the equality of the ROC signals' and how increasing dullness of one tooth causes portions of the signal relating to the dulled tooth to decrease with the following tooth being magnified. With this due to the reduced radius from the dullness decreasing the chip thickness and proceeding tooth picking up the slack. It was concluded that as conditions shifted, the ROC signal changed accordingly providing clear indications as to the condition of the tool and the cutting operations.

Prior to Kari *et al.* (2011), the application of ROC monitoring had been to relatively simple processes. The application of ROC to helicopter power train bearings was the first application of ROC to complex rotating machinery. Using a twin configuration experimental test bed, tests were undertaken where axial load and radial loads were reacted by bearings with artificial raceway defects. Using an envelope frequency analysis, Kari *et al.* compared the ROC spectra with 2-dimensional vibration data. Whilst at higher loads and large defects there was agreement between both ROC and vibration spectra as shown in Figure 2-30, the accelerometer clarity was far less at lower loads and lesser damage levels however (Figure 2-31), with Kari *et al*. concluding that while the technology still required further development the current results suggest a strong potential for helicopter HUMS systems in future.

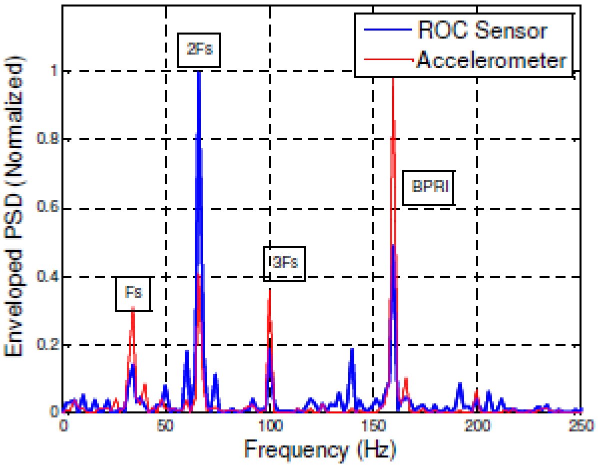

Figure 2-30 – ROC and vibration data for an extensively damaged bearing with high axial load. (Extracted from Kari *et al.* (2011))

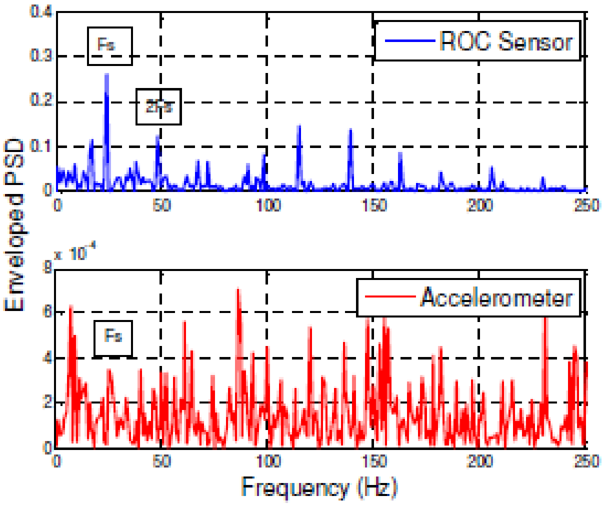

Figure 2-31 – Spectra for a bearing with a 0.4mm hole in the inner race under heavy radial load. (Extracted from Kari *et al.* (2011))

With the positive results present in the literature and ROC technology showing significant potential for health monitoring and fault detection as well as advantages over the existing techniques. This thesis investigates the application to fault find in a reciprocating gear rig.

CHAPTER 3

Preliminary Investigations into the use of Rate of Change of Torque, using a Slow Speed Gear Testing Rig

This chapter describes the initial investigations undertaken using an existing gear test rig, in order to establish the applicability of ROC technology as a condition monitoring tool. The data obtained in these investigations were also used to further identify effective data analysis techniques.

The initial data used during this work was generated through experimentation performed on an adapted gear test rig. Whilst not suited to replicate the complex nature of industrial applications, the single pair test set up provided simplicity and stability with which to perform the first tests and generate data that would allow for the preliminary objective to be achieved.

The challenge comes because condition monitoring within dynamic systems (such as gearboxes) are a complex problem. Relatively basic systems (such as the system used in this chapter) can provide an exhaustive challenge to even seasoned monitoring methods with resultant waveforms comprising of both stationary and transient components. Traditional techniques such as Acoustic Emission (AE) and vibration monitoring, while well-established, provide mixed results depending on the application as demonstrated in Chapter 2. ROC technology however has the potential to provide a new, more precise platform for condition monitoring by directly monitoring a quantity inherent in all mechanical power transmission systems.

3.1 Description of the test rig

The test rig was originally designed and built as part of a SERC-funded project to investigate the scuffing of spur gears and the eventual failure caused by prolonged operation under adverse conditions.

The rig follows the established design of a back-to-back power-recirculating rig, also known as a “four-square” rig. As can be seen from Figure 3-1, the design uses two gear pairs to overcome the lack of a full drive train by inducing an equal but opposite torque in the corresponding shaft thus recirculating the power throughout the system. An outline of the original rig specification can be seen below:

- Gear ratio 3:2 (fixed),
- 75 mm centre distance,
- Maximum input speed of 3000 RPM,
- Adjustable speed via eddy-current variable-speed drive,
- Maximum hydraulic loading pressure of 30 Bar, equivalent to an in-loop torque of 200 Nm on the upper shaft,
- Controllable oil temperature with up to approximately 100 degrees Celsius.

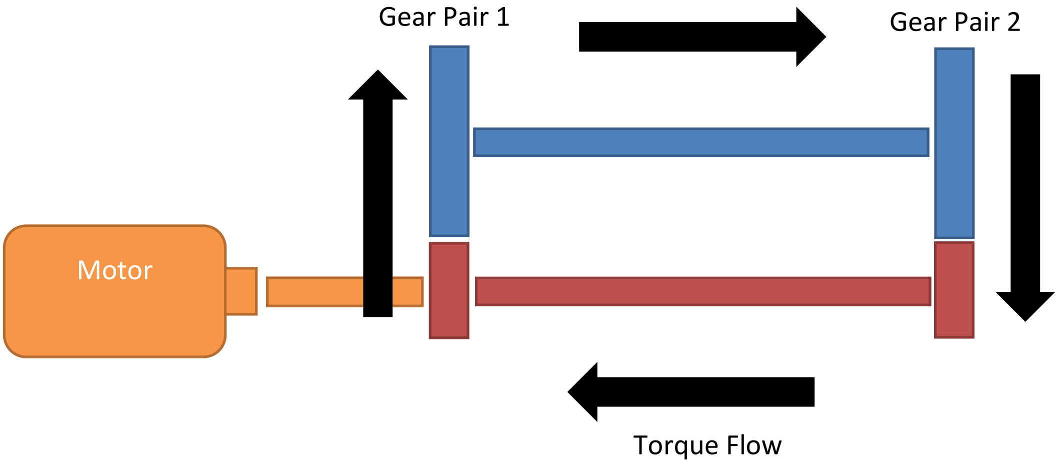

Figure 3-1- Torque Flow Schematic

Following electrical failure of the obsolete eddy-current drive, the rig was fitted with a 4-pole motor combined with a polyvee belt and pulley system to drive the lower shaft, with tension controlled by a horizontal sliding bed upon which the motor is mounted. Whilst lacking variable control, this system allows set changes in speed via alterations to the pulley ratio and eliminates potential electrical noise from a variable-frequency drive. To minimise stress on the system, as a result of the tension, the slave pulley is supported by a bearing block which in turn feeds into the rear housing as shown in Figure 3-2.

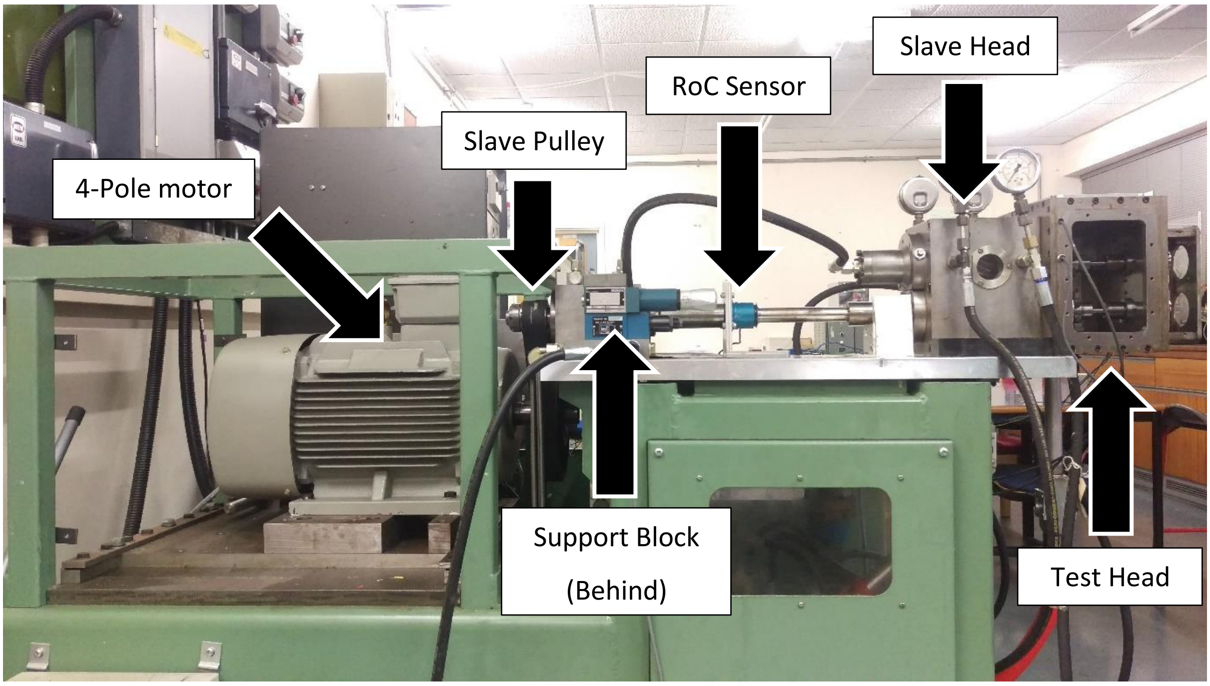

Figure 3-2 - Overview of the test rig.

The rig consists of two housings (the rear, and test housings). A pair of gears in each housing are connected by shafts, as shown in Figure 3-3.

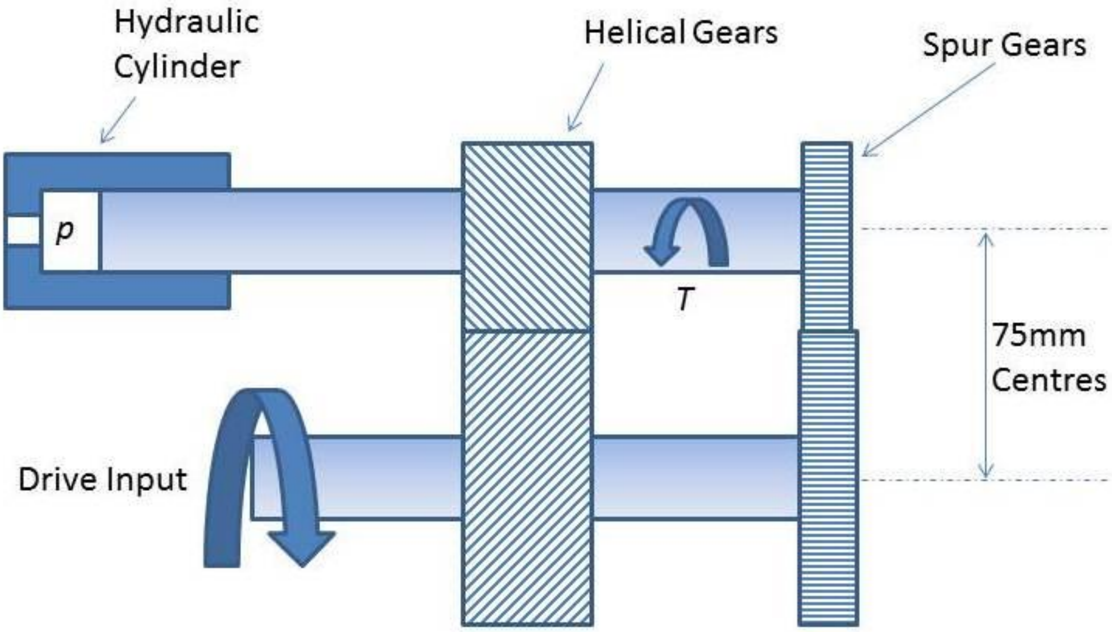

Figure 3-3 - Basic layout of back-to-back test rig.

Within the rear housing are a set of 3:2 ratio helical slave gears which provide the torque generation for the rig through the application of axial load via hydraulic pressure. This is achieved due to the helix angle of the gear teeth. As can be seen Figure 3-4, by applying an axial load to one gear the contact force between the gears is increased. So long as ample lubrication is maintained to prevent metal-on-metal contact and consequently scuffing, increasingly large loads can be applied. The resultant force contains a large tangential component which attempts to rotate the gear further. The restraint provided by the spur test gears on the opposite ends of the shafts (in the test housing) means that a torque is induced within the system. Additional loading at this point can be used to further increase the torque. The helical gears are of a significantly higher face width than the spur gears, and this, combined with the higher load sharing between helical gear teeth, means that any likely failure due to scuffing, tooth fatigue or pitting will occur at the spur test gears.

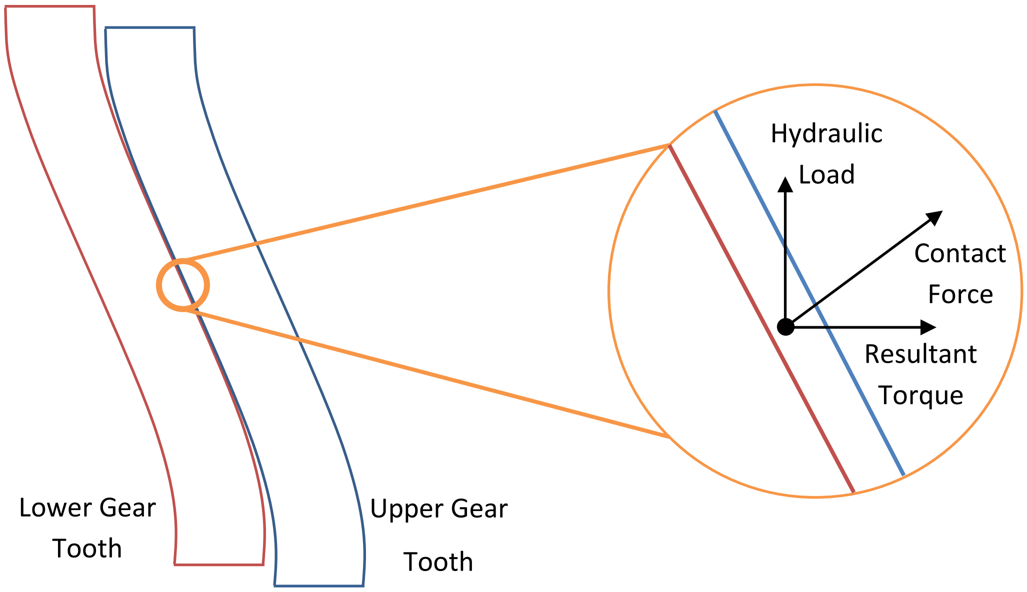

Figure 3-4 - Torque Generation

For this method of torque application to work, the lower shaft must be restrained axially, whilst the upper shaft must be allowed to float axially. The lower shaft is mounted in back to back angular contact spherical ball bearings, which react the axial load. To allow the necessary sliding movement for the upper shaft, it is supported at each end by hydrostatic bearings. These bearing are fed from a dedicated hydraulic system. For the axial load application, the system uses a hydraulic ram. This ram is located at the rear end of the test head and is controlled by a manually operated servo valve, as shown in Figure 3-5. This system is connected to a pressure meter with indicators of the corresponding torque values.

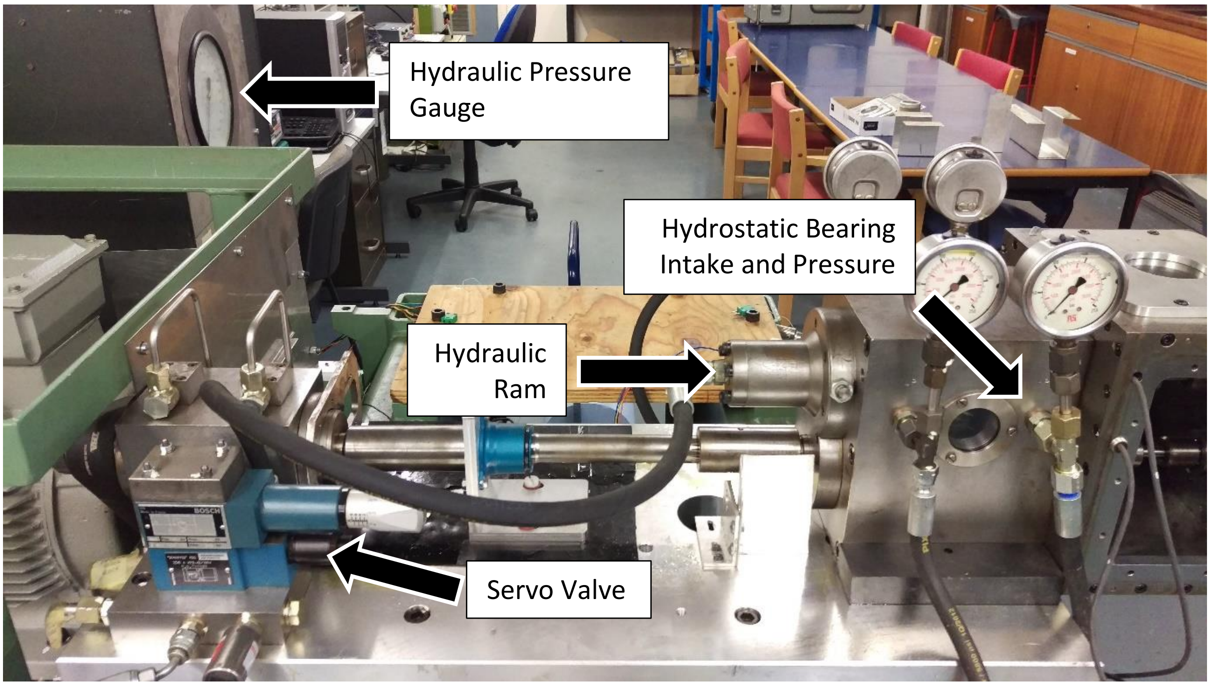

Figure 3-5 - Overview of the torque system.

The front housing (Figure 3-6) contains the test gears, where they are secured to the shafts with a combination of spacers to compensate for the motion of the upper shaft and a set of lock rings to secure everything. The fixed (lower) test gear has a larger face width than the upper gear, which moves axially as the torque is applied. The shafts are directly connected to light gate trigger discs outside of the housing, which have an "N-1" design to give a pulse each time a tooth passes but it also allows the position of the damaged tooth to be tracked via the missing tooth. The setup of this system for testing will be detailed in more depth later.

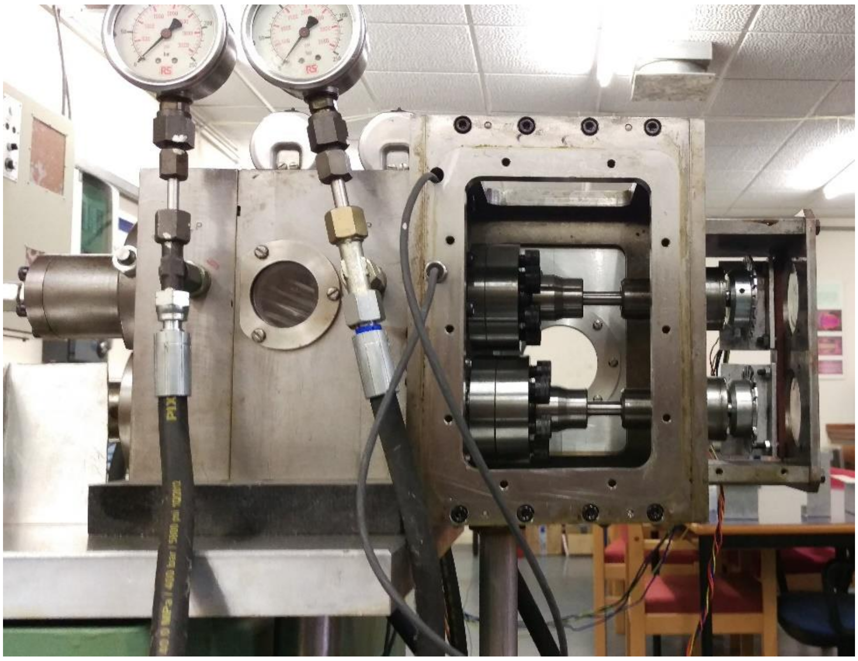

Figure 3-6 - Front housing

3.2 Limitations and Modifications

Following the conclusion of the original project, the rig was largely unused for a number of years. This presented an opportunity to modify it to accommodate the ROC sensor. A gearbox input shaft from the industrial sponsor was fitted to the rig. The shaft was fitted between the drive pulley and the input to the rear (slave) housing, as shown in Figure 3-7. In this position, the ROC sensor will only measure fluctuations in the frictional losses from the rig, limiting this initial work to measuring ROC signals in the frictional torque to provide a straightforward evaluation of the likely suitability of ROC torque measurements for gearbox condition monitoring.

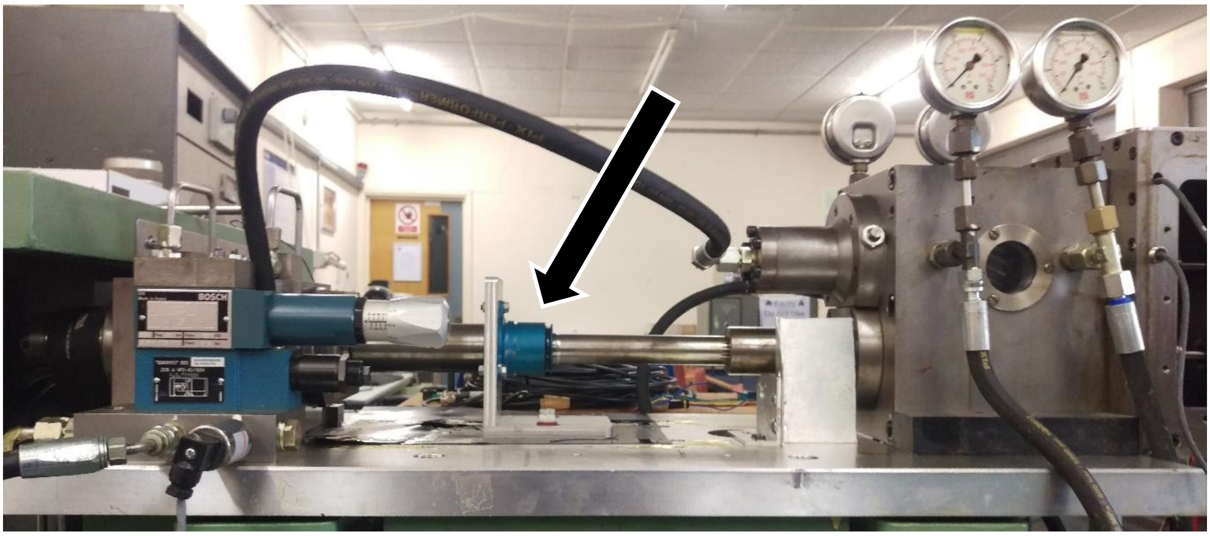

Figure 3-7 - ROC sensor placement

Having been modified for purpose however, the test rig does have limitations. These are listed below:

- 75mm centre distance,
- Fixed 3:2 gear ratio,
- Speed limited by pulleys,
- Torque limited by hydraulic loading,
- ROC sensor outside of the power recirculation loop.

These limitations have profound consequences on the scale and diversity of testing possible. For example, the 75mm centre distance limits the size of the gears. This combined with the locked in 3:2 ratio, means that only gears of 27:18 tooth count can be used if a module representative of the sponsor’s design practice is used. This prevents testing the effects of higher or lower tooth counts upon ROC effectiveness to detect damage. Combined with the maximum load that the rig can apply and the lack of direct simulation of the industrial application, the result is that this rig can only be used for preliminary data collection and not for fully-representative application simulation.

3.3 Control and Functionality

The operation of the test rig is controlled and monitored through an interface (Figure 3-8) built by A. Cockerill in National Instruments' LabVIEW software. The flexibility of LabVIEW allowed the construction of an easy to use interface for data acquisition; the equipment for which was also of National Instruments manufacture.

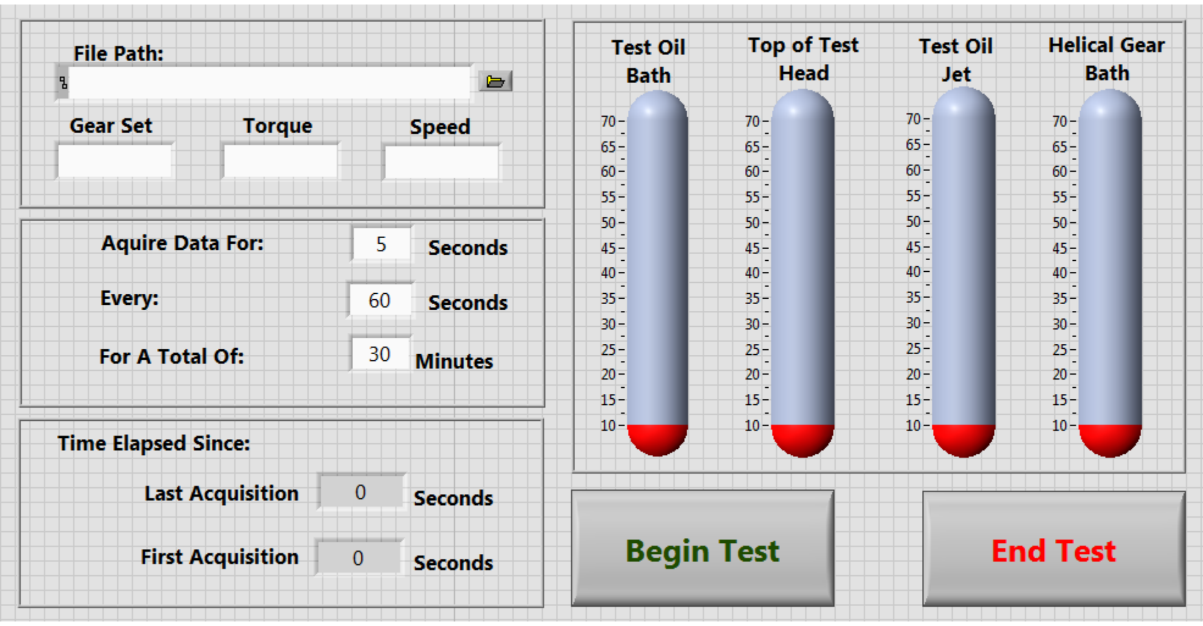

Aquire Data For: 5 Seconds

Every: 60 Seconds

For A Total Of: 30 Minutes

Time Elapsed Since:

Last Acquisition 0 Seconds

First Acquisition 0 Seconds

Figure 3-8 - LabVIEW Front Panel

The control system for the data acquisition system allows the sampling period to be altered between tests and provides visual feedback regarding test progress. It also provides temperature display of the key components of the test rig throughout the operation of the test rig. To date this is the only functionality of the control interface, while further functionality is a possibility, this was a retro fit to an older test rig. This has meant that a full control system was not possible without significant investment required to bring multiple systems up to date and provide them with computer control capabilities. As this was not an option the test rig instead requires multiple operators manning the various pump and motor controls and relies heavily on operator knowledge and visual checks to control the rig effectively.

3.4 Experimental Work

3.4.1 Test specimens

The test specimens were custom manufactured specifically for use with the test rig described in section 3.1 to the following specification:

Table 3-1 – Basic Gear Details

Ratio	27:18
Centre Distance	70mm
Normal Module	3.250
Normal Diametral Pitch	7.815mm
Normal Pressure Angle	22.5°
Transverse Pressure Angle	22.5°
Transverse Working Pressure Angle	25.73°9
Transverse Base Pitch	9.433 mm
Reference Centre Distance	73.125mm
Working Centre distance	75mm

The sponsor provided 8 gear pairs in total: 4 to remain healthy for comparative tests and 4 to be artificially damaged. An example of a pair of test gears can be seen below in

Figure 3-9. These were manufactured to identical standards of material and finish of the gears used by the sponsor. This is to say that the gears are manufactured to class 5 tolerances as set out in the standard DIN 3962. The gears are ground and superfinished to achieve a surface finish with a targeted Ra of 0.05, although the Ra typically achieved is between 0.07-0.09.

Figure 3-9 – Test gear specimens: designation 2.4 (healthy).

Through the use of specially designed loading fixtures and a precision hydraulic load machine, increasing loads were applied to the tip of alternating teeth of a mainshaft gear supported by the 2 teeth either side of the tooth of interest. The deflections generated were then measured using a Klingelnburg precision gear measurement machine, using the applied loads and measured deflections the amount of force required to plastically deform the gear and generate the desired artificial tooth bends could be interpolated. From this, the sponsor was able to generate 3 levels of damage, within the range of interest: 4-16 µm. These deflections were approximated to 4µm, 8µm & 16µm, using a Klingelnberg, tooth spacing measurements were taken and used to confirm the final magnitude as seen in Figure 3-10.

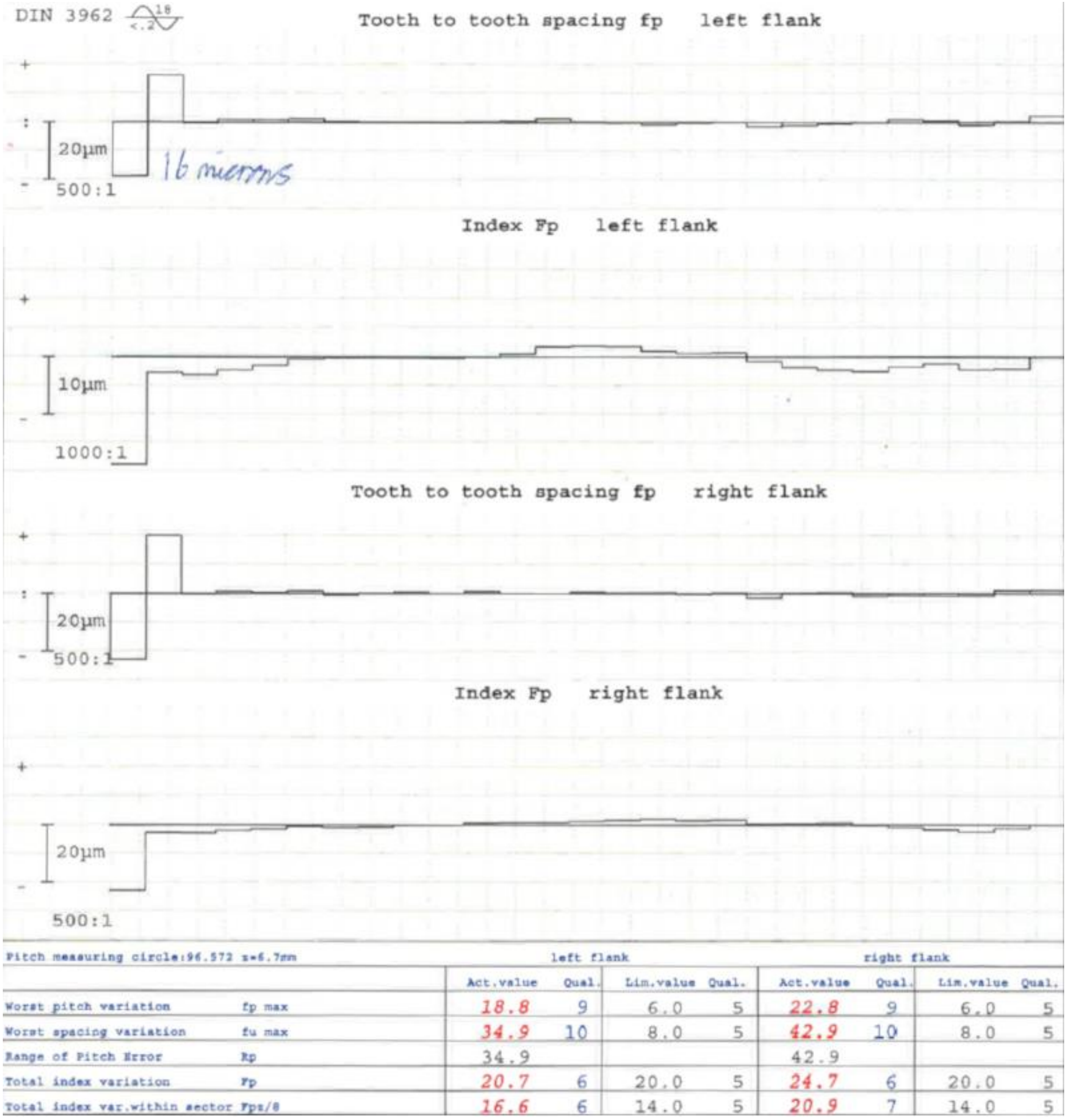

Pitch measuring circle:96.572 z=6.7mm		left flank				right flank			
		Act.value	Qual.	Lim.value	Qual.	Act.value	Qual.	Lim.value	Qual.
Worst pitch variation	fp max	18.8	9	6.0	5	22.8	9	6.0	5
Worst spacing variation	fu max	34.9	10	8.0	5	42.9	10	8.0	5
Range of Pitch Error	Rp	34.9				42.9			
Total index variation	Fp	20.7	6	20.0	5	24.7	6	20.0	5
Total index var.within sector	Fps/8	16.6	6	14.0	5	20.9	7	14.0	5

Figure 3-10 – Spacing errors as presented in a Klingelnburg report for an artificial 16 micron tooth bend in a 27 tooth gear.

3.4.2 Typical Test Sequence

A typical testing sequence can be divided into 3 stages:

- Setup
- Pre-test
- Testing

Setup is the initial stage of testing, which consists primarily of installing the gears. The first step of this process is to confirm that the upper shaft is located axially as far back as possible, thus resetting the hydraulic ram for loading. The upper shaft must then be rotated anticlockwise to remove any backlash now present due to the change in position of the helical teeth. Following this the test gears can be fitted on to the shafts along with the spacers and finally the locknuts; caution must be taken though to correctly position said gears, firstly so that the damaged tooth is top dead centre for light gate alignment and secondly so the gears do not introduce any further backlash. At this point the lock nuts bolts can be tightened up to a torque of 50Nm to secure everything.

Upon successfully installing the gears, the connection hubs can be placed on the end of the shafts and locked in place to link the shafts and the light gates. The light gates are then adjusted so that missing tooth is in the same position as the damaged tooth, at which point the setup phase is complete and the pre-test phase can begin.

To begin the oil heaters and temperature regulation system are started, this is accompanied by the supply pumps which must be warmed alongside the oil to prevent them from stalling due to sudden expansion through rapid temperature increase. With the system started, there are several optics that allow confirmation of the oil flow from the housings, these must be regularly checked both before and throughout the test to confirm that the oil supply is flowing. As the test rig approaches the test temperature of 60 °C the pressure gauges for the hydrostatic bearings begin to settle, with each bearing having a high and low pressure side corresponding to their position in the bearing. These must be confirmed to be stable before proceeding further, at which point the test settings should be confirmed within the LabVIEW control system. With confirmation of continuous oil flow, stable hydrostatic pressure, correct acquisition settings and light gate positions; the main drive motor may be started and the testing stage begun.

Upon start up, the rig will take a few seconds to reach speed and adjust to the new equilibrium, during which period all oil flows etc. should be closely monitored and the rig immediately shut down upon discovery of any anomalies.

When satisfied that the test rig has reached equilibrium the data acquisition process should be started to capture data for the pre-determined period of time. Upon completion, the DAQ system will display a message, informing the rig operators that it has completed its task. It is at this point that the torque may be increased by adjusting hydraulic ram pressure with the servo valve.

From this point on the process is repeated until maximum torque is reached, at which point, torque should be slowly removed until it reaches zero, the motor should be switched off and when it has come to a complete stop the pumps, heaters and temperature control system can be switched off.

The damaged test gears, along with the four healthy specimens, were tested at 3 distinct speeds (1600 RPM, 3000 RPM and 4500 RPM) and at a range of torques at each speed, from 0 Nm – 200 Nm at increments of 50 Nm. This gave a total of 15 different combinations of torque and speed for each gear.

3.5 Analysis & Results

3.5.1 Initial Results

Upon acquisition, an examination of the raw waveforms was undertaken. Using the light gate data to periodically identify the start of each rotation, the data was divided up into individual rotations, and the rotations overlaid. Figure 3-11, shows 85 superimposed rotations of a healthy gear and all degrees of tooth bend damage, this shows that a clear transient could be identified within the larger damaged signals (8 and 16 micron). This was confirmed to be the damaged tooth by scrutinising the light gate position as well as the stacked rotation plot, confirming that the transient was present at the same position in all rotations. While successfully determining damage for 8 and 16 micron defects, identification of damage for the 4 micron bend remained elusive, with the waveform having a high visual correlation with the healthy waveforms.

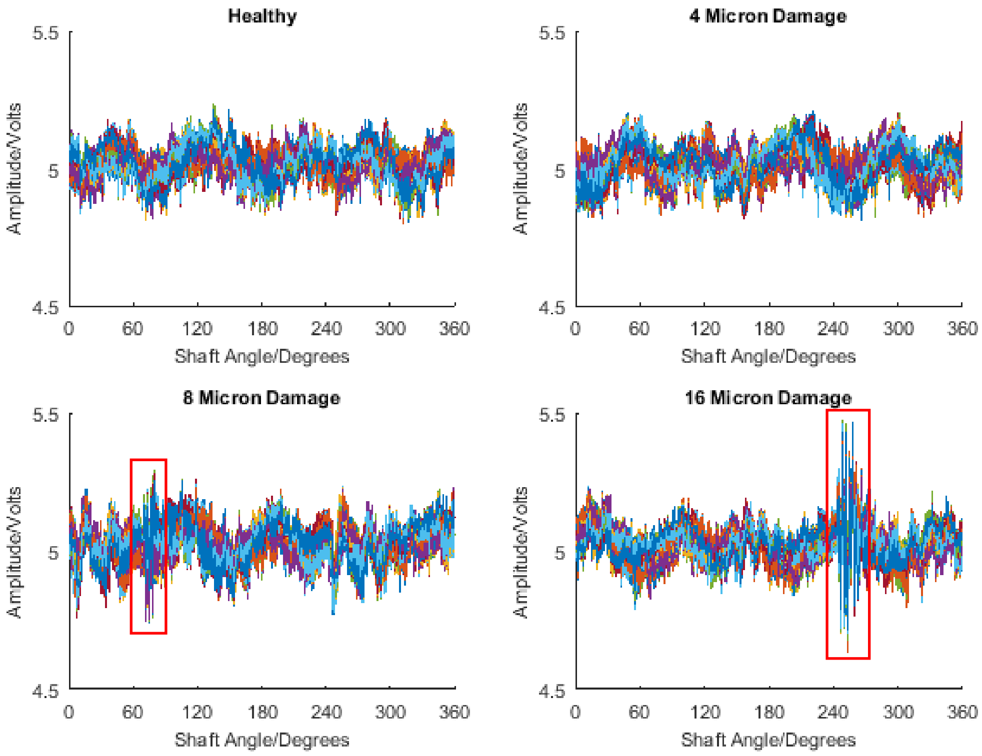

Figure 3-11 – Stacked rotations of the raw waveforms of both healthy and damaged gears at 1600 rpm and 50Nm torque where conversion factor is 0.9175 mV/(Nm/s).

The transient observed is related to the meshing frequency; as discussed in Chapter 2, tooth bends have a significant impact on the meshing cycle due to the late engagement. Figure 3-12 displays the FFTs of the data used to produce Figure 3-11. The initial peaks are the shaft frequency and its harmonics, in this case the first peak is expected to be approximately 26Hz, as well as some electrical noise. The rest of the signal however is dominated by the meshing frequency and its harmonics. There is no noticeable difference in amplitude of the meshing frequency itself or the 1st harmonic over the course of the signal. The 2nd harmonic gains significant amplitude as damage increases as well as the energy present in the sidebands. From this it can be determined that the damage transient is linked directly to the meshing and more specifically has a relationship with the 2nd harmonic.

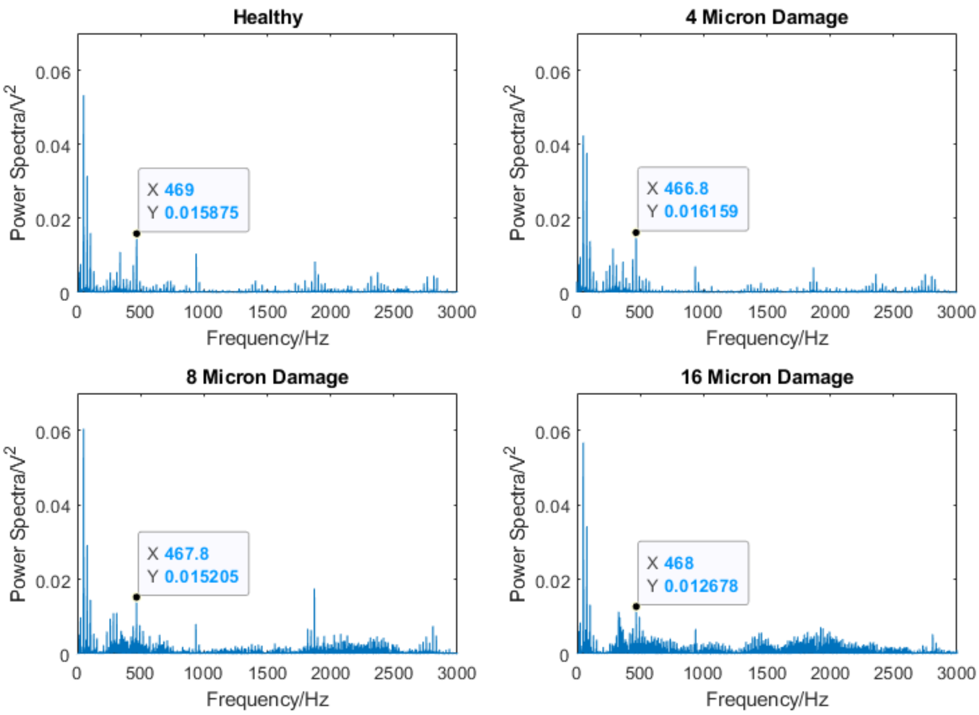

Figure 3-12 – Comparison of the FFTs for the first 3000 Hz of increasing damage signals at 1600 RPM and 50Nm.

The result for the 4-micron defect was to be expected because this defect is of the same order of magnitude as the manufacturing tolerances i.e Class 5 as per DIN 3962 for the gears, suggesting that the defect would make no significant effect on the running of the gears in any scenario. When it is also considered that measuring frictional losses is expected to cause a reduction in signal strength and clarity, as opposed to measurements within the torque loop, this inability to detect 4 microns defects is not unexpected.

Following this initial success, a number of analytical techniques, both statistical and frequency based, were selected to give a quantitative measure of the damage and provide greater clarity.

3.5.2 Signal Clarity

Despite this initial success, a number of inconsistencies were discovered in the data. While some were traced to electrical issues, others were found to be intrinsic to the test rig.

Flat-lining: Attributed to loose wiring, where vibrations cause a disconnect leading to the signal rising quickly to the maximum possible voltage and remains there until the connection is reformed and the sensor output returns to normal. Signals containing this problem were eliminated from subsequent analyses.

Dropouts: This phenomenon is associated with low end 50Hz noise (likely to be from the electrical mains supply). Characterised by a sudden shift in the waveform shape (Figure 3-13), it takes on the appearance of a more classical sinusoidal wave shape with a much lower frequency before the effect 'bleeds out' and the waveform returns to the expected.

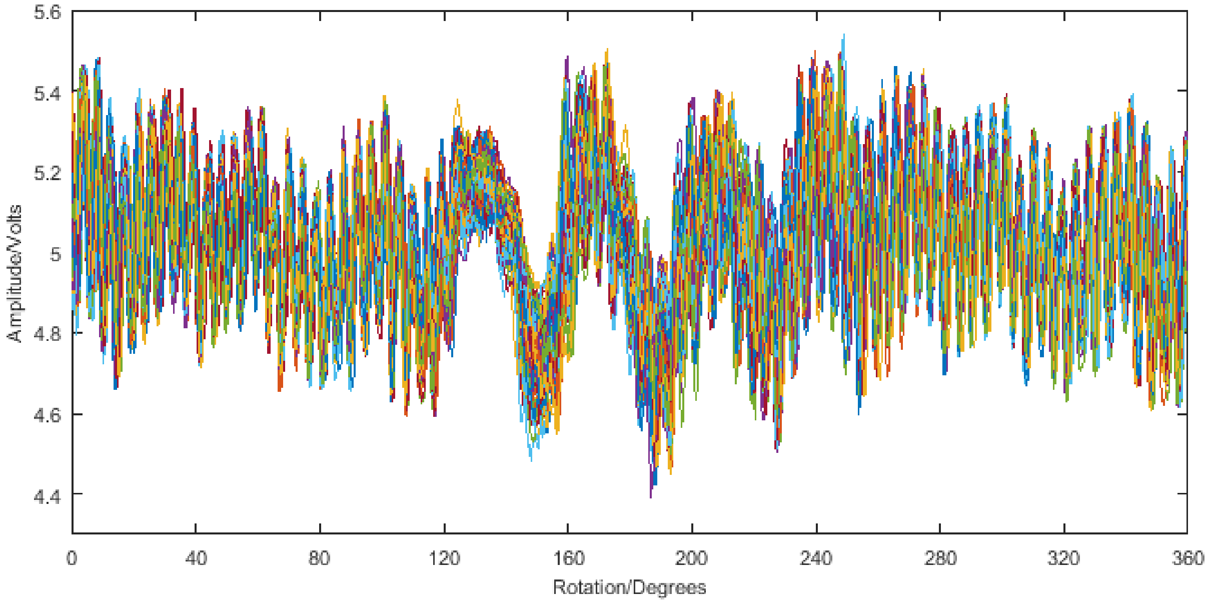

Figure 3-13 - Example of 'dropouts' found within data (conversion factor is 0.9175 mV/(Nm/s)).

Micro Pulses: So called due to their incredibly short duration, these pulses can be seen appearing periodically throughout all waveforms. As seen below in Figure 3-14, the frequency is consistent enough that the pulses align over rotations suggesting that they are caused by a mechanical component. However, the frequencies calculated do not relate to any known part and because little work with ROC technology in this application has been undertaken, the signal content is not greatly understood. It is unclear whether this is a reaction to unknown damage elsewhere within the system.

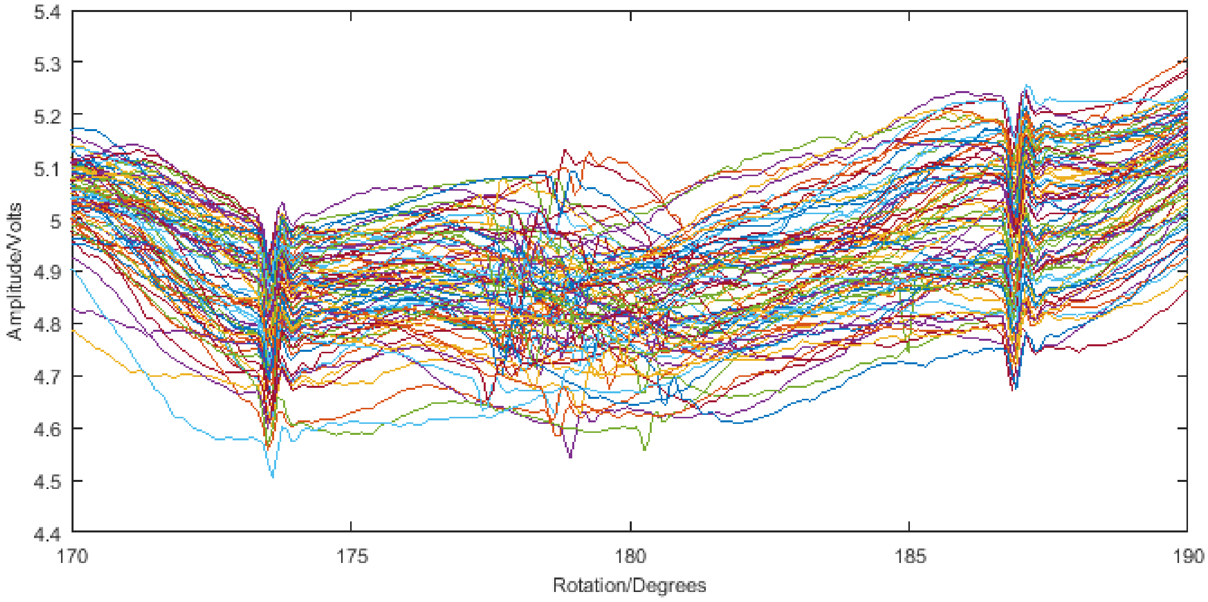

Figure 3-14 - Example of micro pulses (conversion factor is 0.9175 mV/(Nm/s)).

All 3 of these unexpected variations in the signal have had a profound effect on the data analysis. Waveforms that contain a large amount of flat-lining have been removed entirely from the data analysis as they cause unrepresentative increases in the metrics used. Micro pulses have been seen to cause sudden reactions in specific metrics however application of the metrics to window functions can limit this effect, though care must be taken when controlling the size of the window, so that it is an appropriate size to the data being processed.

Aside from this there is also cycle-to-cycle variation in the ROC signal, these variations can be caused by a number of factors such as variations in motor speed changing the amount of energy in the system to once per rotation factors. One such example is if the magnetic field of the ROC sensor is magnetically disturbed it can cause a pulse once per rotation. On top of this there are bearing imperfections and defects to consider, these will affect the bearing fundamental frequencies so deviations may not align consistently throughout rotations depending on the bearing frequencies in question. Whilst hunting ratios of gear teeth can also cause variations, these are unlikely to affect the data presented here as the gears in question do not possess a hunting ratio.

3.5.3 Analytical Techniques

Filtering

To help improve signal clarity and prevent false positives the raw waveforms were filtered before processing. Initially, an Infinite Impulse Response (IIR) Butterworth high-pass filter with a stop band of 450Hz and pass band of 500Hz was used to eliminate background noise and unnecessary low-end frequencies. The result of this was a much clearer signal, with greatly reduced electrical noise (Figure 3-15) and removal of a significant carrier wave. The only disadvantage of this was the loss of data of the first 5 rotations to prevent the step response of the filter influencing the metrics. This loss was negligible in comparison to the total data sampled, however.

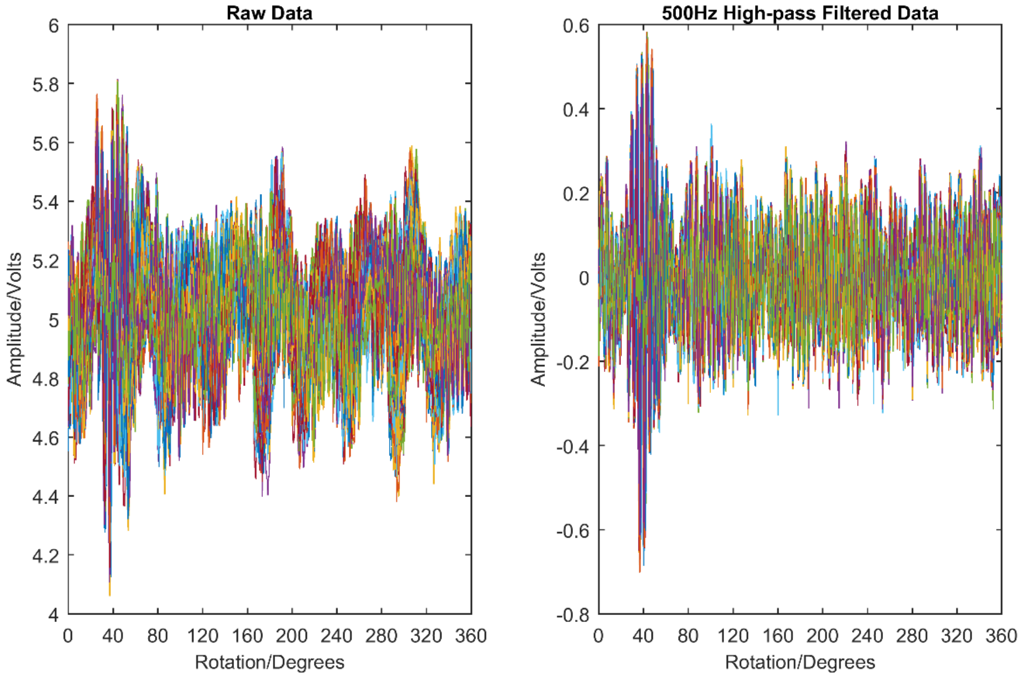

Figure 3-15 – Raw vs. filtered singal comparison of stacked rotations for the 16 micron tooth bend at 3000 RPM and 100 Nm torque (conversion factor is 0.9175 mV/(Nm/s)).

While this filter benefitted the initial work, it was crudely developed and as such further work was undertaken to expand the understanding of the signal and create a more robust filter. For this work IIR type filters were selected over Finite Impulse Response (FIR) filters, while FIR filters have some notable advantages over IIR, the lower orders used by IIR filters means they require significantly less processing time (MathWorks, 2018), a quality that would be necessary to allow all the data collected to be analysed. The faster processing time of IIR and the knowledge that phase information was not required for any of the methods to be applied after filtering made IIR the more reasonable choice.

To begin the 4 types of IIR filters available in MATLAB were compared: Butterworth, Chebyshev Type I, Chebyshev Type II, and Elliptic:

Table 3-2 - Filter descriptions (D'Antona and Ferrero, 2006).

Butterworth:	The Butterworth filter type is a monotonic function, where there are no ripples in both the pass-band and stop-band but require higher orders to do so.
Chebyshev Type I & II:	Unlike the Butterworth, Chebyshev filters possess a degree of ripple allowing for a sharper transition between pass-band and stop-band. Type I Chebyshev filters are characterised by having a ripple in their pass-band only while Type II only experience ripple in the stop-band.
Elliptic:	Elliptic filters allow the ripple in both the pass-band and stop-band allowing a much sharper response as well as reaching the design criteria with the lowest order, making them the computationally efficient.

To visualise the effect that this would have, each high-pass filter of each type was designed with initially 250Hz stop-band and 300Hz pass-band applied to the same section of data. The results of this can be seen in Figure 3-16, where the dotted line indicates the start of the damage pulse. Using this as a reference, there are noticeable time delays and, by association, phase delays present in the Butterworth and, if only small, Chebyshev type-I. The filtering causes no clear indication of time and phase delays in both the Elliptic and Chebyshev type-II filters, with them producing nearly identical results.

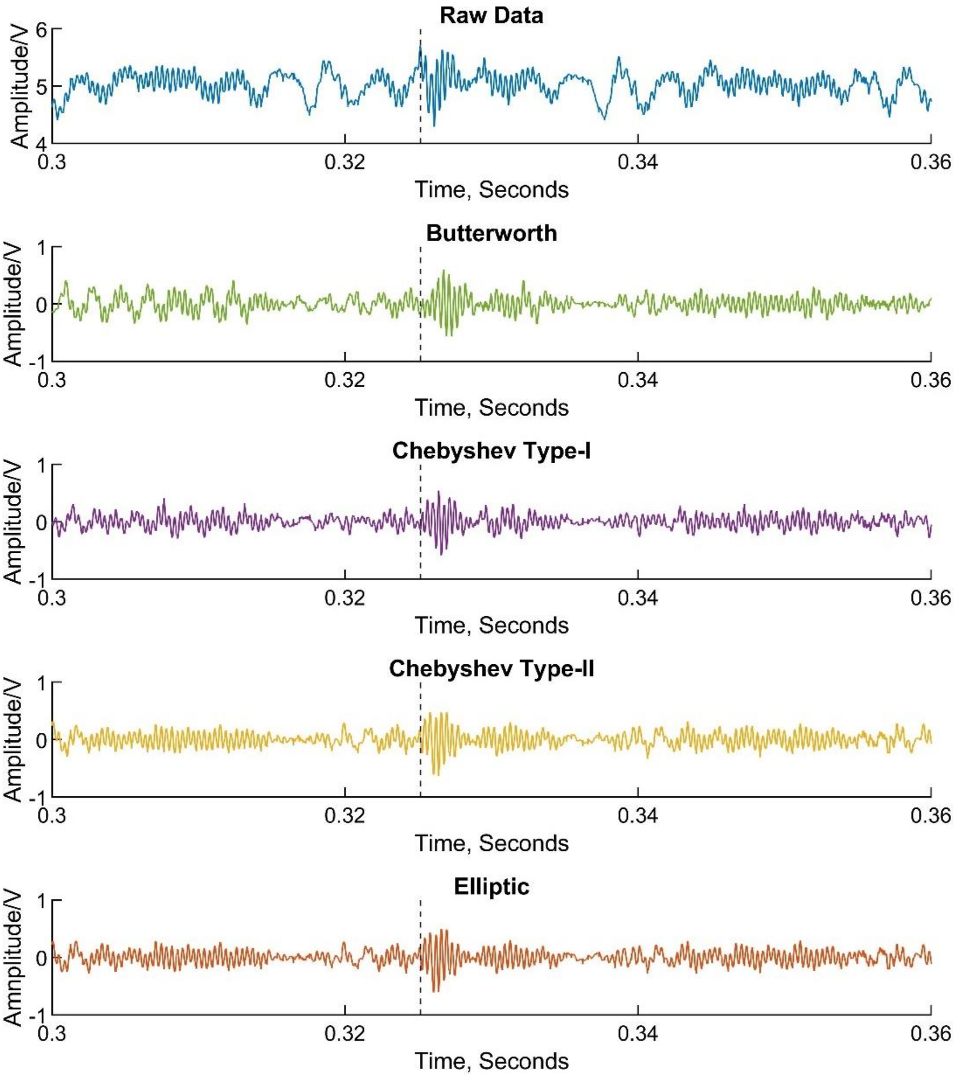

Figure 3-16 – Filter Response Comparison

The Elliptic filter type was selected as while in theory the ripple generated by the filter application, though not visible on the figure due to the X-axis offset, is undesirable, a significantly faster filter response means that the signal is much less likely to be distorted by phase delay.

Using this, a number of filters were designed with different conditions and a selection of 16 micron data was processed. This data was selected as the damage was able to be identified clearly by visual inspection of the raw signal as seen previously in Figure 3-11, and therefore the effect and relative clarity could be more easily identified. The results of these tests are shown in Figure 3-17, Figure 3-18 and Figure 3-19, where 5 rotations have been plotted and are identified by the guide lines.

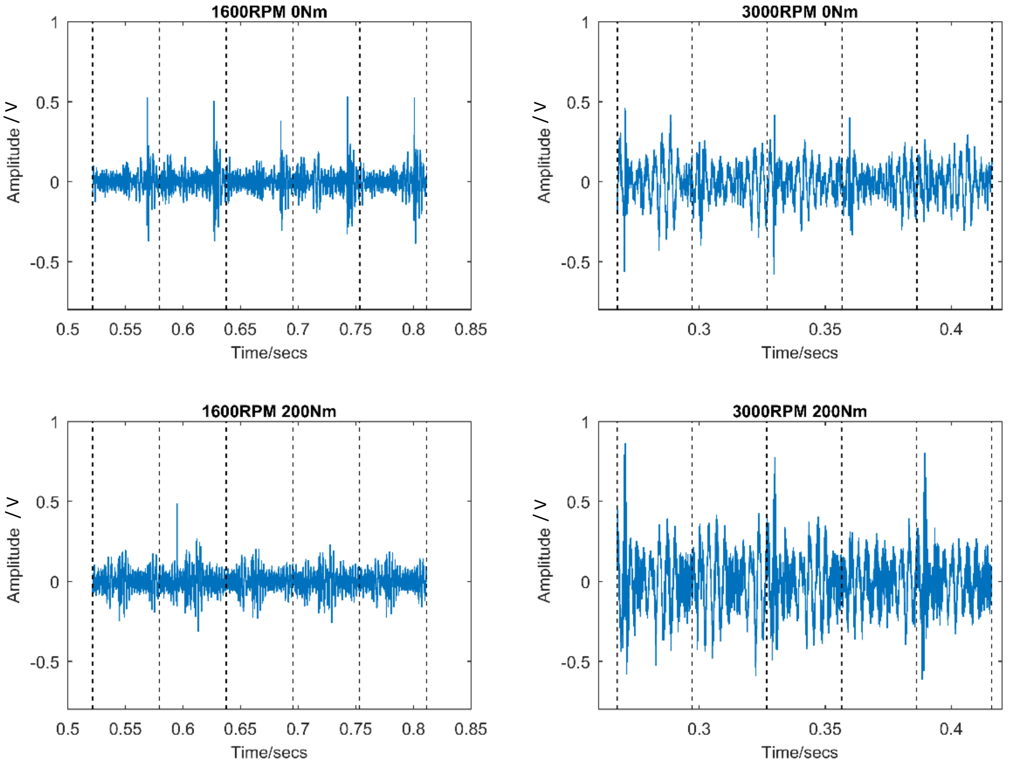

Figure 3-17 – Filtered 16 micron tooth bend data with stop-band: 150 Hz & pass-band: 200Hz (ROC Conversion factor is 0.9175 mV/(Nm/s))

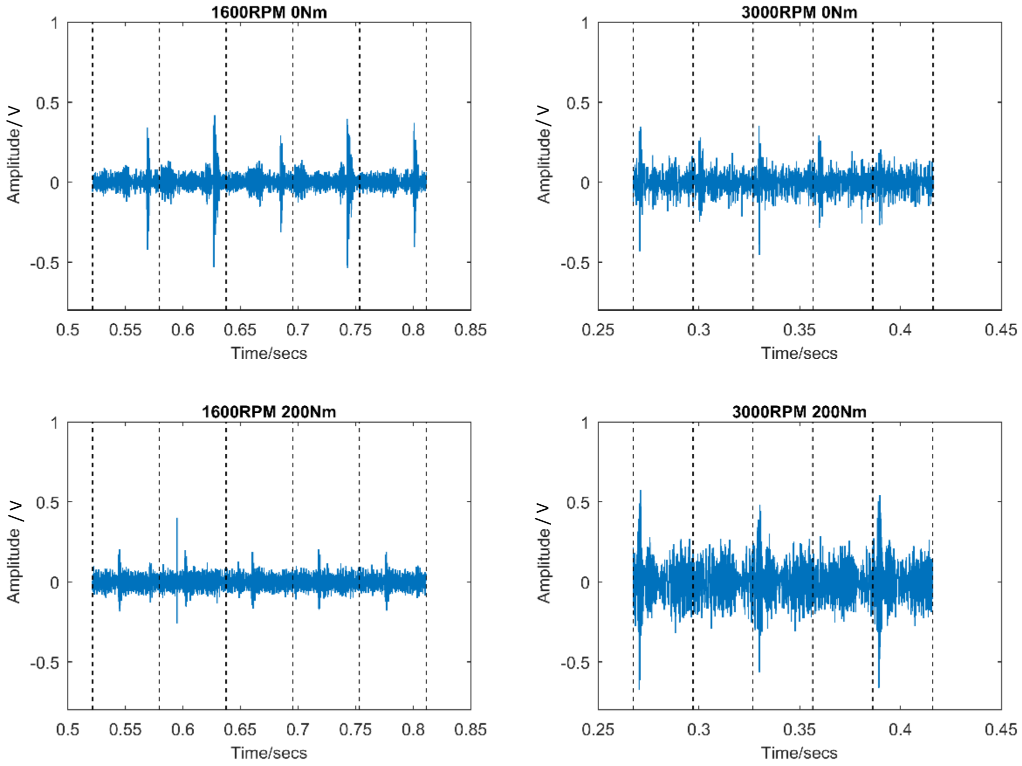

Figure 3-18 – Filtered 16 micron tooth bend data with stop-band: 450 Hz & pass-band: 500Hz (ROC Conversion factor is 0.9175 mV/(Nm/s))

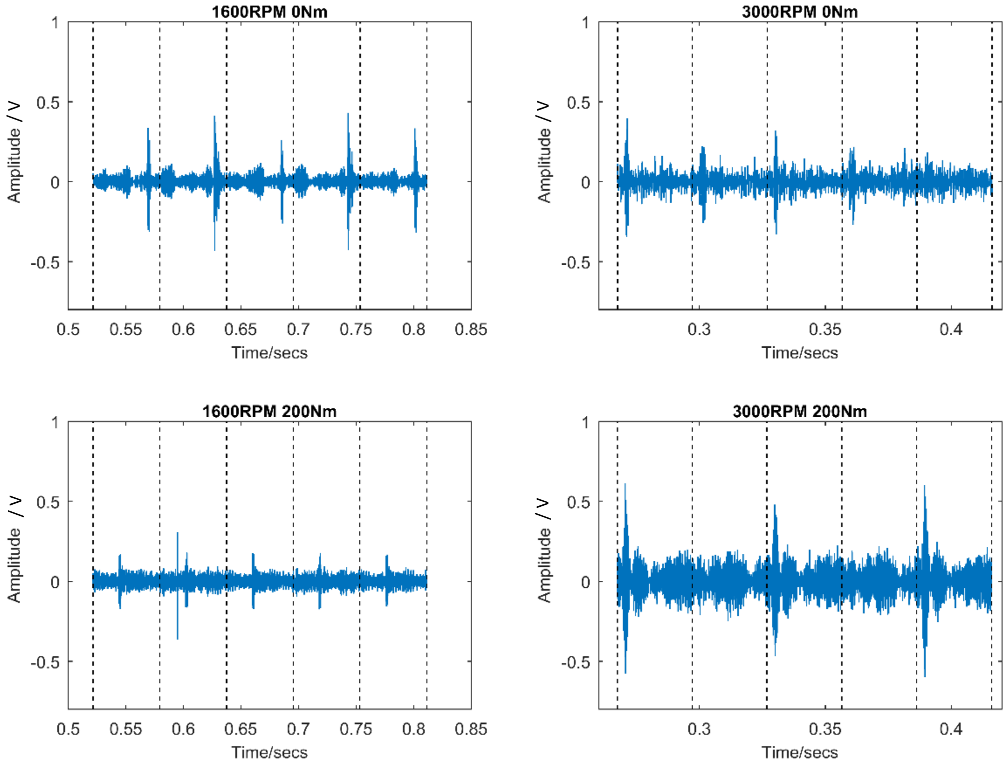

Figure 3-19 – Filtered 16 micron tooth bend data with stop-band: 950 Hz & pass-band: 1000Hz (ROC Conversion factor is 0.9175 mV/(Nm/s))

From Figure 3-17, Figure 3-18, and Figure 3-19, it is noticeable that as the filter parameters increase the amount of noise present in the signal is seen to diminish, whilst the damage signal remains clearly visible. This is most distinctive between the filters of pass-bands: 200Hz & 500Hz, where low frequency sinusoidal carrier waves are removed, producing a much more distinct signal. Despite the significant jump to a 1000Hz pass-band; the final filter had little improvement on the clarity of the signal, other than decreasing the overall amplitude of key features.

It was noted that an increase in torque had a negative relationship with the amplitude of the peaks representing the damage within the signals as seen in Figure 3-19. Where the peak-to-peak amplitude of the damage (at 1600 RPM) is reduced from an average of 0.6695 V to 0.3661 V, a decrease of more than half. Looking at the 3000 RPM tests in Figure 3-19, this decrease is only visible in rotations 2 and 4. With the amplitude increasing in rotations 1, 3, and 5 at 200 Nm instead. The damage in rotations 2 and 4 is clearly no longer detectable though, suggesting that at minimum there are two frequency components to the damage signal, each individually altered by the speed and torque. As the meshing frequency (approximately 900 Hz) has been filtered out in these tests, it can be concluded that the presence of damage within the ROC signal is more reliant on the harmonics then the initial meshing frequency. From a frequency analysis of the signals in Figure 3-20, where the green line indicates the rough position of the meshing frequency and the red lines: the meshing harmonics. They do not illustrate the exact position of the harmonics, rather the theoretical, as the speed changes throughout the test cause considerable frequency shifts. The most notable difference is at 200 Nm where the amplitude of the alternating meshing harmonics i.e. 2nd, 4th, 6th etc are increased over their odd numbered counterparts. The increased amplitude of these harmonics and the increase in the amplitude of the damage suggests that these harmonics have a greater influence on the signal than their alternating counterparts. Though it is not clear if this the harmonic themselves or the high energy sidebands now present. At this point there was no clear indication on what may have prevented the damage from appearing in every other rotation. At first, the unusual activity around 1000 & 2000 Hz was thought to be related to this phenomenon, however confirmation against other tests eliminated this as a possibility.

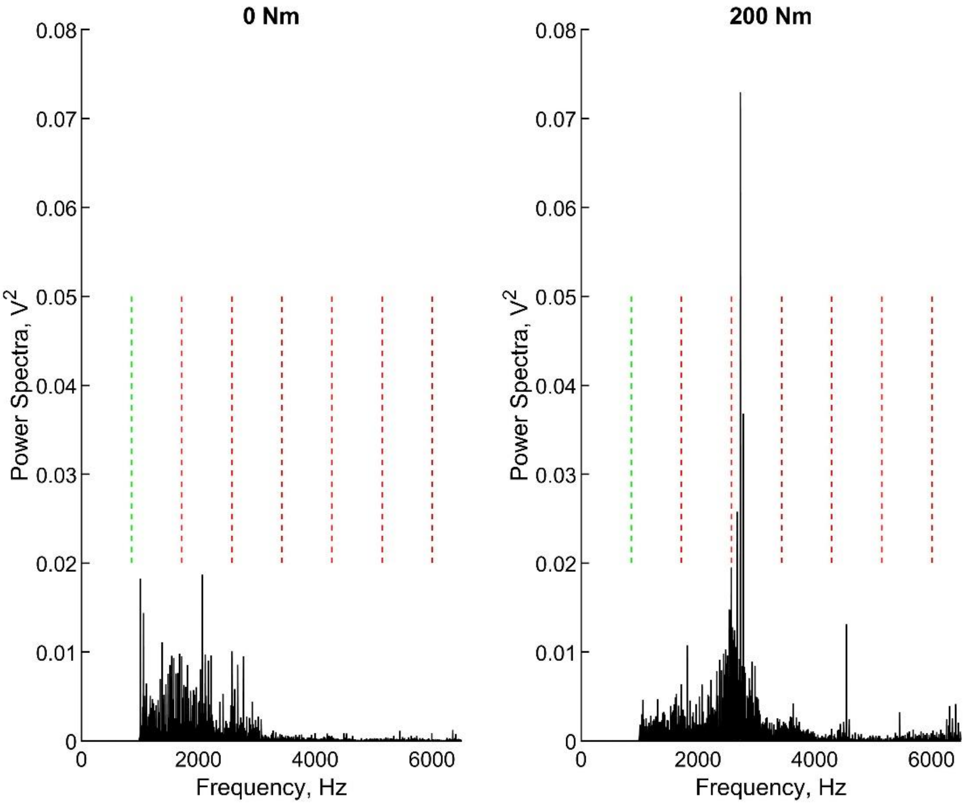

Figure 3-20 – FFT Comparison comparing the amplitudes of the meshing frequency and the first 6 meshing harmonics, indicated by the rede dashed lines, for the 16 micron tooth bend at 3000 RPM.

The combined effect of the 950 Hz pass-band filter and torque suppression would have led to a negative impact on the metrics later used. For this reason, the 500Hz pass-band filter was adopted for further analysis as, although this still eliminated the meshing frequency of the slowest speed, the analysis of the largest filter proved that this effect could be considered small enough that the decrease would not have a significant effect on the usage of future metrics.

The filtered signals were then analysed using a range of statistical techniques and metrics, which are now described in turn.

Root Mean Square

The root mean square (RMS) is the defined as the square root of the average of the sum of the squared values of a signal.

$$RMS_x = \sqrt{\frac{1}{N}\left[\sum_{i=1}^{N}(x_i)^2\right]} \qquad \textbf{(3-1)}$$

Where *x* is signal vector, *N* is the total number of samples and *i* is the current sample number. Using an RMS has benefits over the traditional mean when variables are both positive and negative and sinusoidal in nature. This is characterised best by a typical sine wave where the traditional mean gives a value of 0, while RMS produces a value of 0.707 times the amplitude of the wave (Decker and Lewicki, 2003) as demonstrated in Figure 3-21.

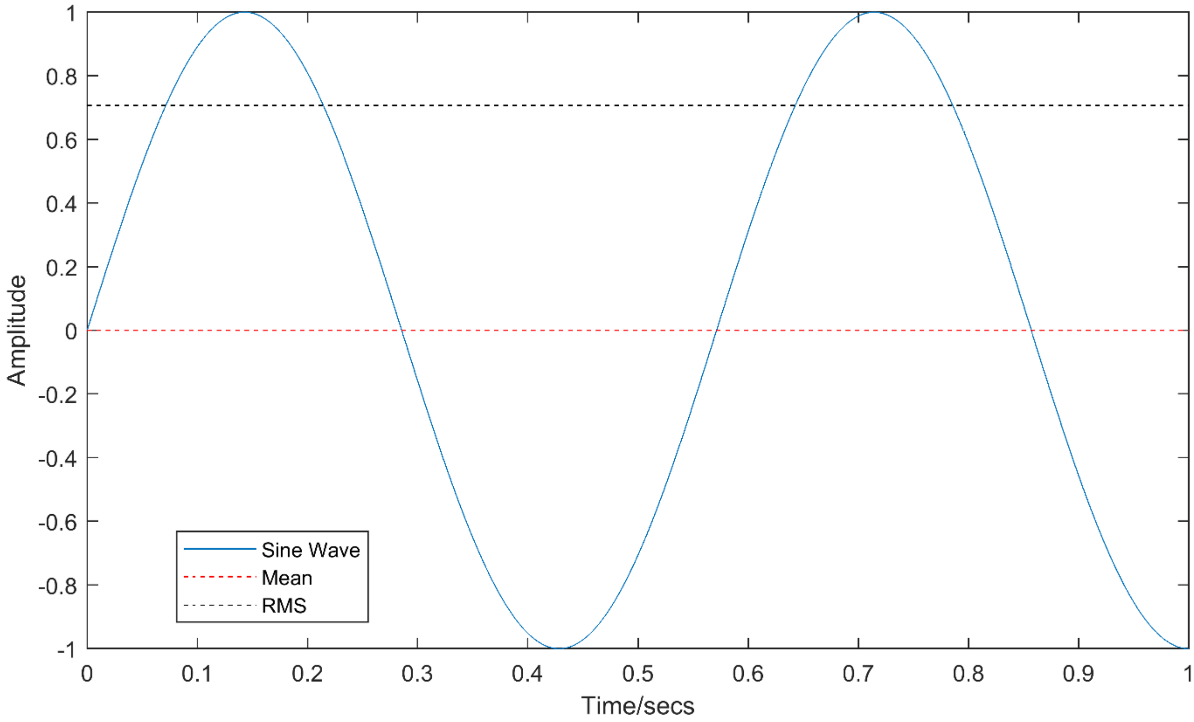

Figure 3-21 - Comparison of Mean and RMS upon a sine wave.

At initial glance this would have little benefit to a ROC signal with a 5V DC offset but after filtering this offset was removed, allowing RMS to work as intended. While normally applied to a full signal, it was found that a singular RMS value provided little information (Table 3-3) to describe the signal with and provided no clear indication of the different levels of damage.

Table 3-3 – Typical RMS Values

Designation	2.1	2.2	2.3	2.4	1.2	1.3	1.4
Status	*Healthy*	*Healthy*	*Healthy*	*Healthy*	*4µm Damage*	*8µm Damage*	*16µm Damage*
RMS / V	0.0827	0.0739	0.0764	0.808	0.0910	0.0723	0.0992

To overcome this, a rectangular moving window was devised to allow for a series of values to be generated. After initial experimentation a window size of 40 degrees of gear rotation (approximately 3 teeth) and shift size of 15 degrees (approximately 1 tooth) was settled upon, providing the best balance of detail and processing speed. This resulted in a series of RMS values being calculated between 0-40, 15-50, 30-60 degrees etc. across the full rotation.

By applying this method and dividing up the resultant waveform into rotations, a much clearer indicator of damage was found. An example of this can be seen below in Figure 3-22, where a region of high intensity is observable at the same area in every rotation. Confirmation was made via the light gate position that this was the area of the damaged tooth.

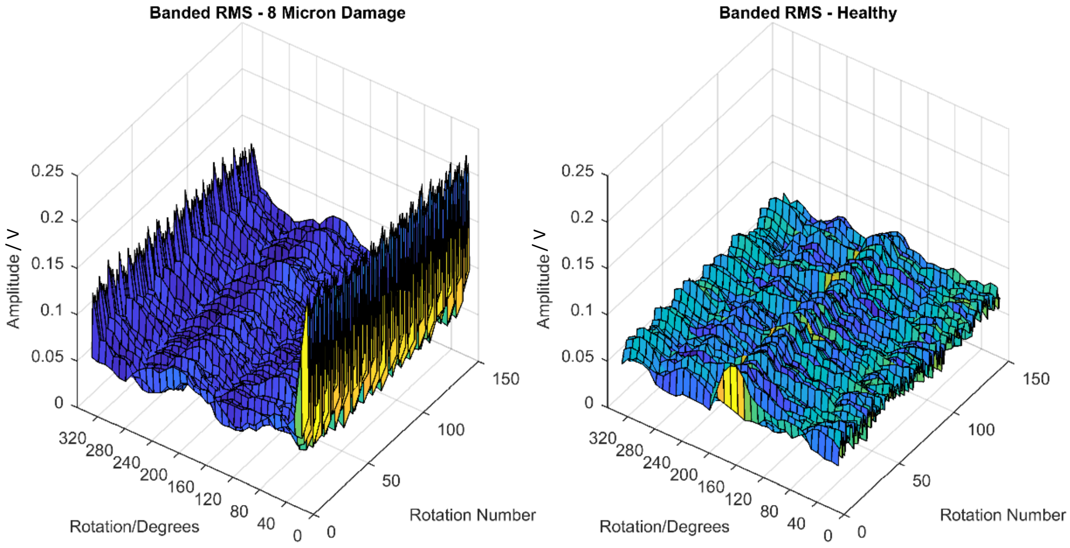

Figure 3-22 - 8 micron damage and healthy windowed RMS plots at 3000 rpm and 50 Nm.

With successful detection the analysis was expanded and (Figure 3-23) saw similar regions being identified throughout both the 8 and 16 micron data. When compared to the healthy signals, a clear distinction could be made, notably from the lack of any abnormally high amplitude regions appearing across the waveforms for the healthy gears. The 4 micron damage remained elusive with the data found to be indiscernible from the healthy gear waveforms, this was anticipated though as mentioned previously due to the low level of the damage compared with gear tolerances.

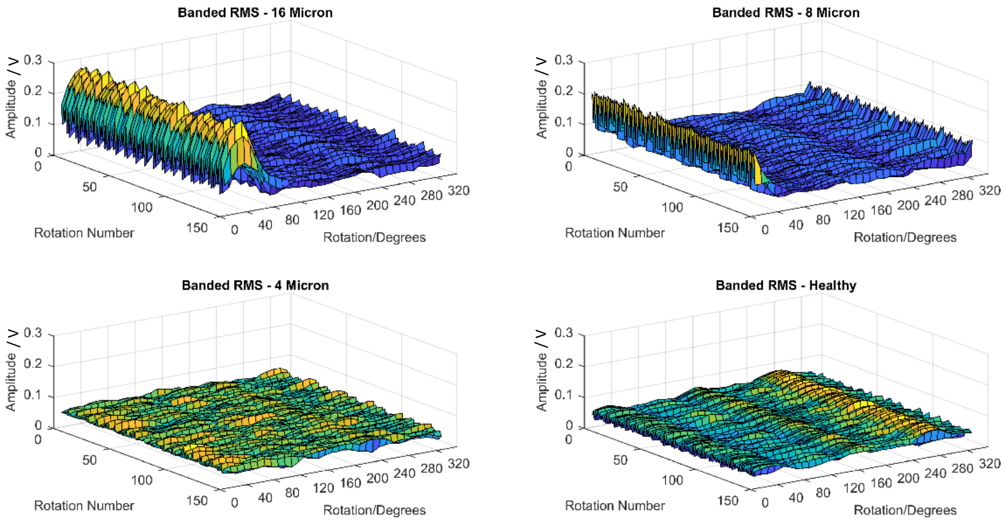

Figure 3-23 - Damage Comparison at 3000 rpm and 50 Nm torque.

Further study confirmed the damage detection is not simply a binary reaction, but has enough distinction between the 16-micron, 8-micron and healthy specimens, to potentially allow for quantification. To demonstrate this the average of the maximum RMS of each rotation were taken, in the case of the healthy gears designated 2.1-2.4, the calculated averages were then averaged again to provide a singular result. From this, it was found that while the RMS values increased in amplitude with torque as presented in Table 3-4.

Table 3-4 – Average RMS values in volts at 3000 rpm.

	50 Nm	**100 Nm**	**150 Nm**	**200 Nm**
16 Micron damage	0.2	0.22	0.2	0.19
8 Micron damage	0.16	0.18	0.15	0.145
Healthy gears	0.07	0.09	0.121	0.149

The healthy average shown here is not truly representative however as it was found that at 150 Nm and 200 Nm, an average for one of the healthy gears provided the same results as the RMS for the 8 micron damage gear and then the 16 micron damage gear. Even with this gear removed from the combined average it was found that the healthy gears approached that level of the 8 micron gear eventually leading to it being obscured.

This effect was seen across all the tests to different degrees. As the load applied to the gears is increased, the response of the RMS signal to the damage is decreased to the point where, in the worst cases, damage is no longer visible at the maximum torque of 200 Nm as demonstrated below. Due to this circumstance, the overall goal of detecting damage in an active F1 gearbox would not be possible so the study was expanded to include other statistical parameters in order to achieve the desired goal.

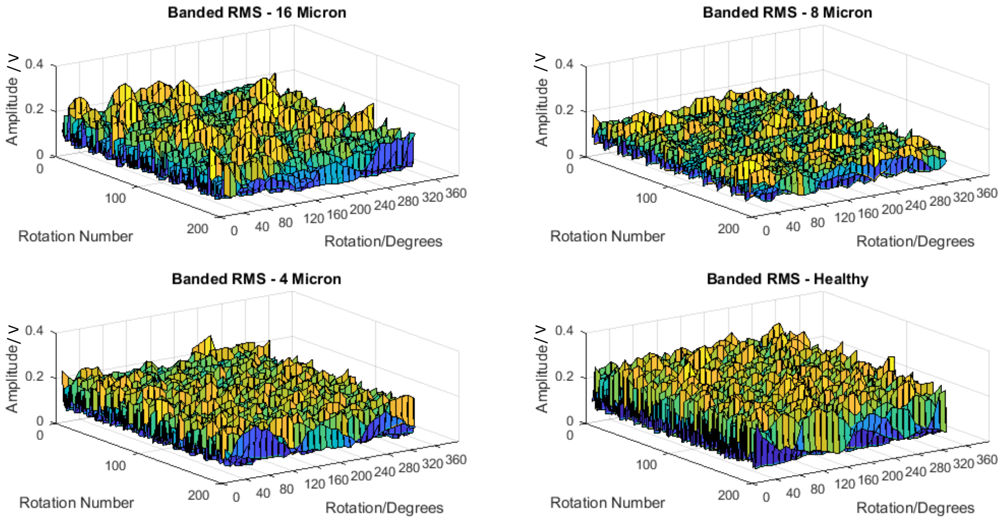

Figure 3-24 – Torque suppression effect seen at 200 Nm and 1600 RPM across all levels of damage.

Statistical Moments

In mathematics, moments are quantitative measures of the shape of a data set, the first of which is the mean and describes the average value. As discussed in the last section, the standard mean was not used but instead the RMS, moving forward the second moment, variance, which describes how far a set of variables vary from their mean was investigated. Variance is mathematically described as:

$$Variance = \frac{\sum_{i=1}^{n}(x - \bar{x})^2}{n} \tag{3-2}$$

Where $\bar{x}$ is the mean of data series x. The variance proved to be highly reminiscent of the RMS, with the noted exception that it appeared to contain less low-level noise. This meant that the signal provided a very clear indicator of the damage as can be seen in Figure 3-25.

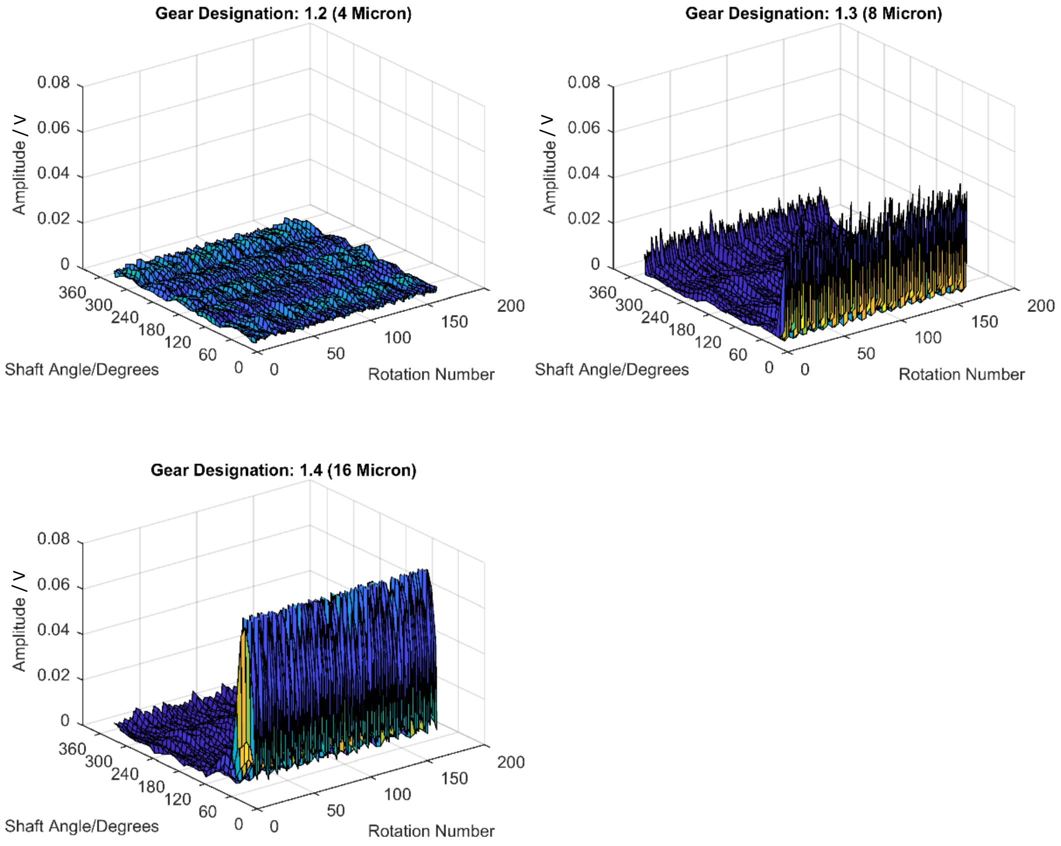

Figure 3-25 – Windowed variance of 4, 8 and 16 micron damage signals at 100 Nm and 3000 RPM.

Despite this clarity at lower loads, it was found that the variance suffered from identical effects as RMS when applied to data with higher torque levels. Average damaged peak amplitudes reached a point of obscurity when compared with healthy data at the same point the RMS did. This is demonstrated below in Figure 3-26, where neither RMS nor variance show any clear indication of the damage.

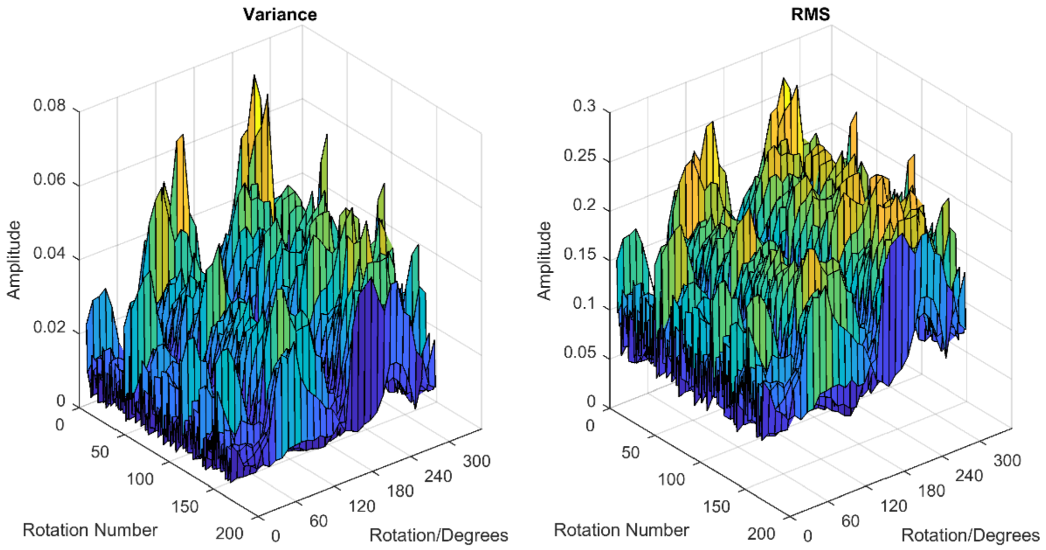

Figure 3-26 – Comparison of the windowed variance and RMS at 3000 rpm and 200 Nm torque for 16µm damage.

The third moment, skewness, was considered and rejected. As a measure of the asymmetry of a distribution it was unlikely to lend itself to the detection of a transient within a signal. To confirm this theory, it was run on a small amount of data known to show clear results with other techniques. An example of this is shown in Figure 3-27, where no clear distinction of any damage can be discerned despite the data producing a clear indication of damage with other methods such as RMS and variance.

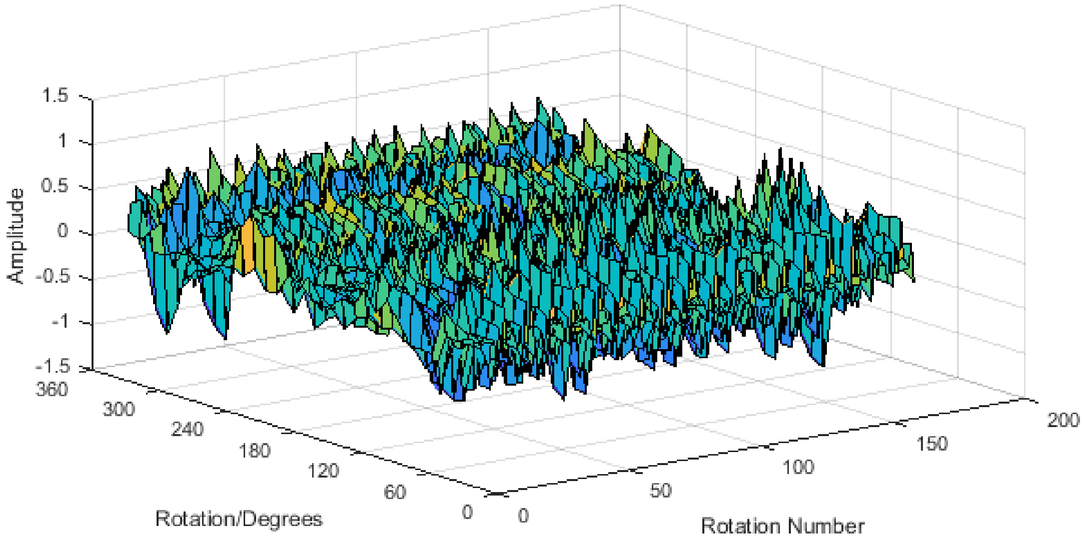

Figure 3-27 Windowed Skewness at 3000 rpm and 100 Nm for 16µm damage.

Kurtosis is the 4th statistical moment following mean, variance, and skewness. It is generally described as a measure of 'tailedness', this is to say it is a measure of the probability of outliers occurring within a probability distribution number with a higher kurtosis resulting from infrequent extreme outliers. Mathematically it is described as:

$$Kurtosis = \frac{n\sum_{i=1}^{n}(x_i - \bar{x})^4}{(\sum_{i=1}^{n}(x_i - \bar{x})^2)^2} \qquad (3\text{-}3)$$

For a purely Gaussian signal, the kurtosis provides a value of 3. As the signal moves away from Gaussian noise, the value increases, making it ideally suited for identifying step changes or high amplitude transients in signals, which are exactly what one might expect as a bent tooth enters the mesh.

As with the RMS, the kurtosis was applied both to the data in its entirety, to generate a single value, and to sequential windowed sections to create a map across the rotation. Application of kurtosis to the complete data sets resulted in mixed findings. Figure 3-28, Figure 3-29, and Figure 3-30 describe the single kurtosis values calculated for each burst of data captured for each gear. These are organised with from left to right from healthy to 16 micron damage in ascending order, separated by dashed lines, the gears are described as per their test designations as per Table 3-3. Moving from left to right, across the figures increase in values from the different gears as damage level increase indicates that kurtosis can respond to, at minimum, the 8 micron damage. This detection is far from guaranteed however as can be seen throughout Figure 3-29 and Figure 3-30, where detection is intermittent or impossible without prior knowledge as well as, at times, none existent.

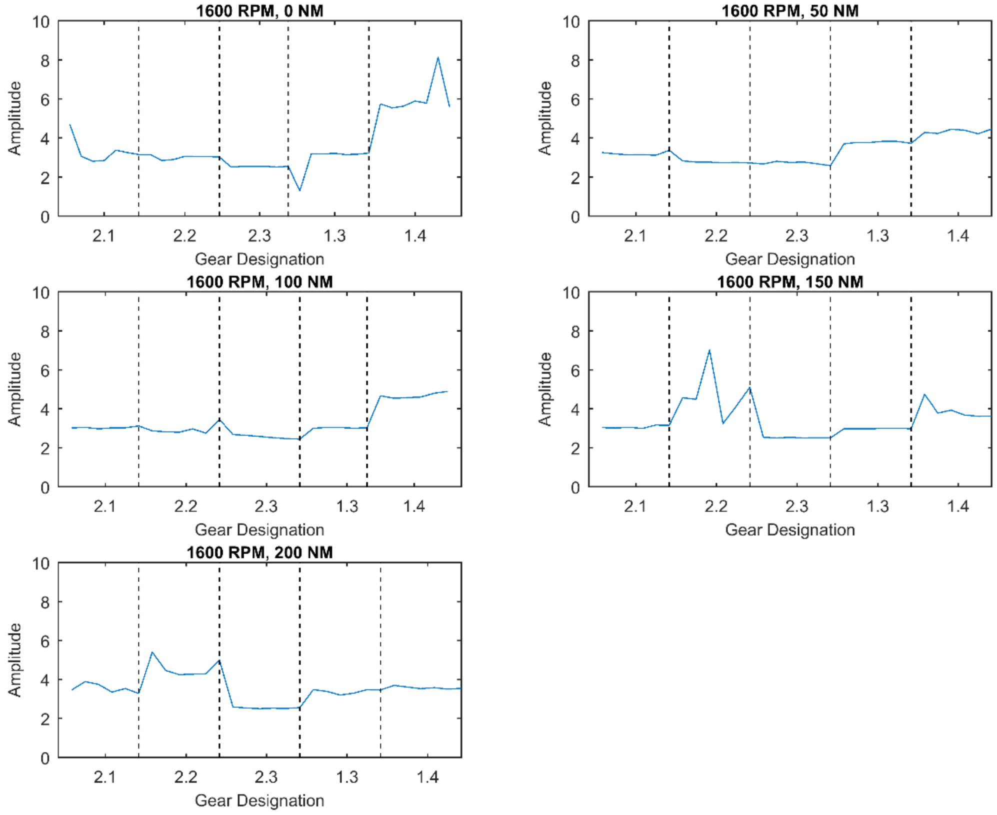

Figure 3-28 – Single value kurtosis for all files logged separated by gear and in order of escalating damage from left to right at 1600 RPM.

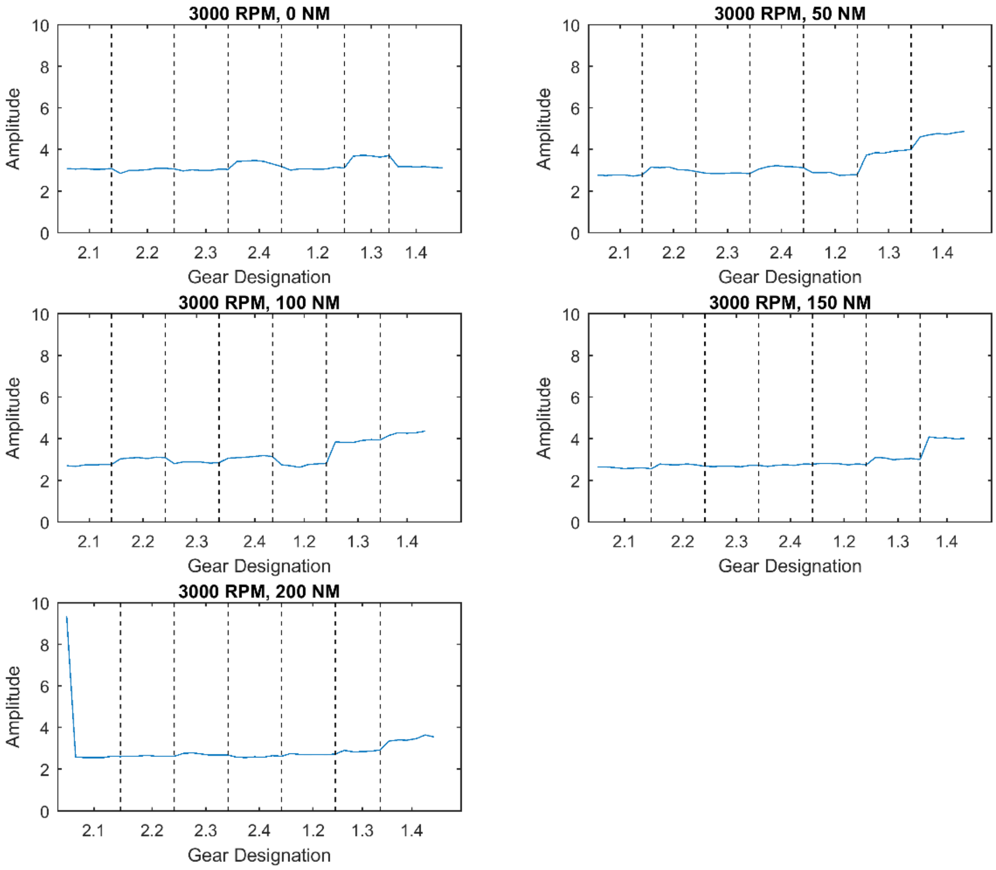

Figure 3-29 - Singular Escalating Damage Kurtosis Values at 3000 RPM (Gear designations as per Table 3-3).

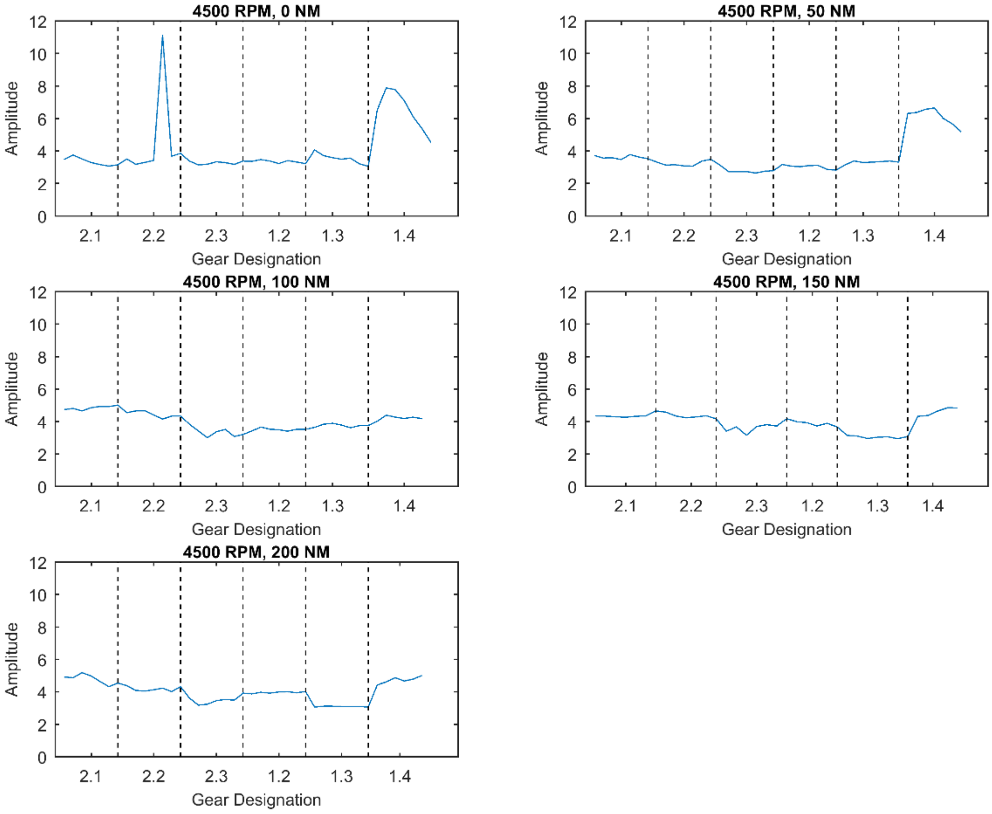

Figure 3-30 - Singular Escalating Damage Kurtosis Values at 4500 RPM (Gear designations as per Table 3-3).

Its reliability is inconsistent however, as seen with the large variations appearing between tests, as highlighted best by the 150Nm tests. The largest outliers can be traced back to errors in the data such as the aforementioned flat-lining. Tailoring the comparison around these “corrupted” sets (as has been done in the Figure 3-28 to Figure 3-30), still provides unclear results. The effectiveness is hindered further by the increasing torque, which again has a suppressing effect on the kurtosis values for the visible damage, making detection impossible at the highest torque values.

Following this, the windowed application performed better, but was subject to the same issues, as can be seen in the Figure 3-31, which shows 3D surface plots of the windowed kurtosis values over every rotation captured across the sampling period. Areas of high noise cause the windowed kurtosis values to peak creating more inconsistency across the data set. At low torques, this did not present an issue as the area of damage had a consistently higher magnitude than the noise. When combined with the suppressing effect of increased torque, the effect is the same as seen previously where the damage-related signal is reduced in amplitude until it is indistinguishable from the rest of the signal.

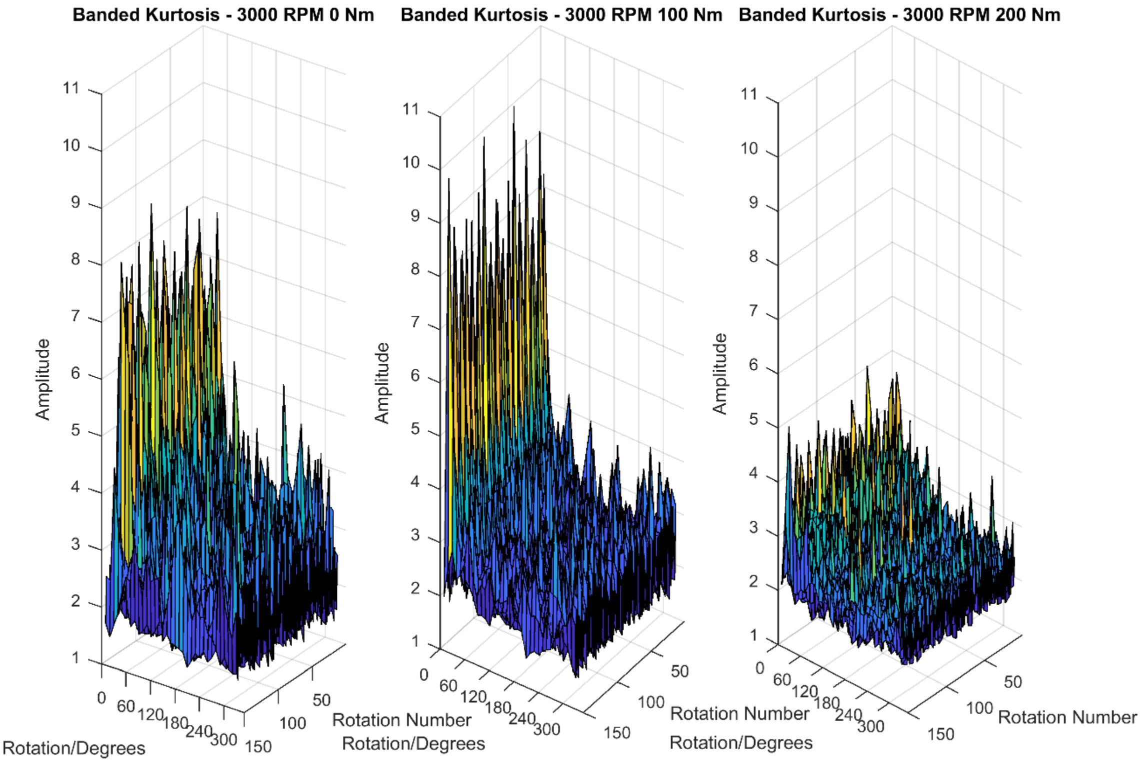

Figure 3-31 – Examples of banded kurtosis across different torques levels for 16 micron damage at 300 RPM.

Gear Metrics

Gear metrics are statistical measures that have been developed to allow for better detection of damage within gearboxes. The metrics presented in this section have all been developed primarily for use with vibration measurements. The 3 metrics covered here are FM0, M6A and M8A.

FM0 was designed by Stewart (1977) as an indicator of major faults in a gear mesh. While shown by Zakarjsek *et al.* in 1993 to be well suited to detecting surface defects, primarily pitting, as a comparison of the maximum peak to peak amplitude of a signal to the sum of the amplitudes of the meshing frequency and it’s harmonics; the design leans towards changes in the gear mesh. This makes it an ideal candidate for use with ROC technology for detecting tooth bends. FM0 is described mathematically as follows:

$$FM0 = \frac{PP_x}{\sum_{n=0}^{H} RMS(P_n)} \tag{3-4}$$

Where PP_x is the peak to peak amplitude, P_n is the amplitude of the n^{th} harmonic and H is the total number of meshing harmonics present within the signal.

Unlike the techniques previously shown, the nature of FM0 does not allow for application to windowed data and as such singular values were the only comparative option, filtering was also not applied to make sure all the necessary frequency data was available.

The results of the FM0 analysis generally show an increasing trend as the damage increases, but the metric proved to be unreliable. As can be seen in Figure 3-32, the results are often obscured by random anomalies. After removing said anomalies (Figure 3-33) a trend can be seen that is representative of damage, but does not always provide enough clarity to allow it to be quantified. Inspecting the individual waveforms and frequency spectra of these anomalies, no clear indication of the reason behind them can be found. This decreases the usability of the technique greatly as while filters maybe designed to limit these anomalies, there is no guarantee that they would not remove high amplitude non-anomalous data as well. It is possible that these outliers are caused by instability in the technique as even among data sets for the same gear, the results are erratic. This potentially is due to the nature of ROC signals and their intrinsic differences from vibration signals however, it may also be attributed to the automated application of the metric. To make data processing more efficient, measuring the amplitude of the meshing frequency harmonics was automated with the user identifying only the meshing frequency. Although the automation was tested prior to mass processing of the large amount of data collected during these tests, errors may have still occurred contributing to the instability of the technique.

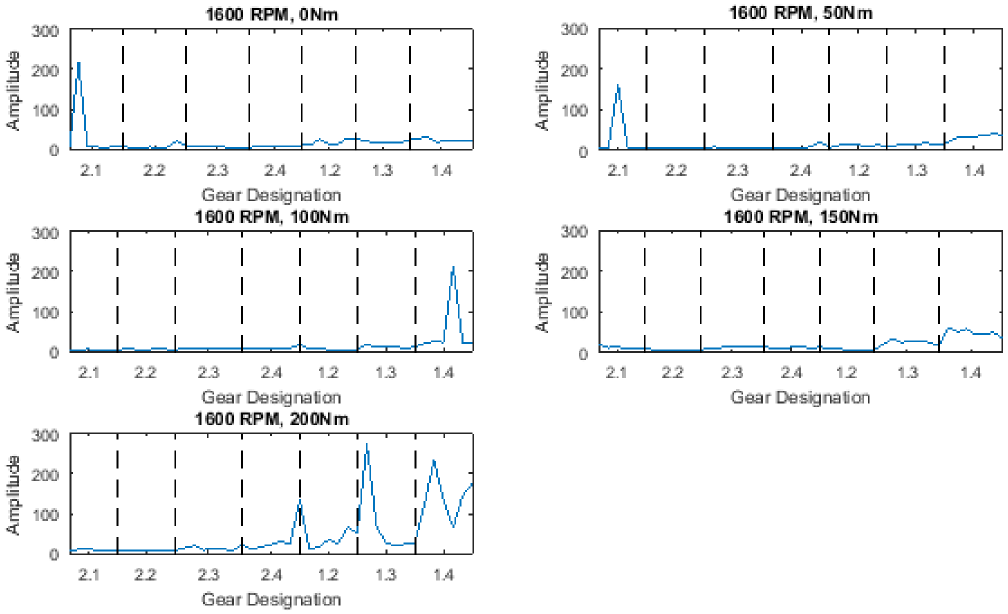

Figure 3-32 – Unfiltered FM0 plots for all gears at 1600 rpm and all load levels (Gear designations as per Table 3-3).

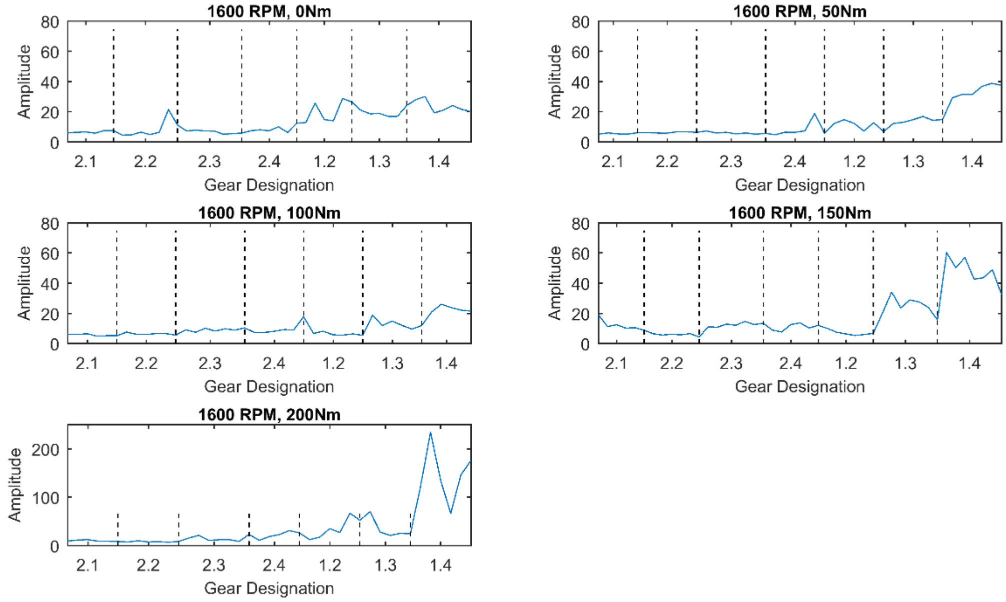

Figure 3-33 – Filtered FM0 results for all gears and torques at 1600 rpm (Gear designations as per Table 3-3).

Despite this, the increase in average amplitude towards the right-hand side of the graphs is a clear response to the 16 micron bend and at times signs of the 8 micron bend are present. With the current noise present and ambiguity in the results, plus the relatively low signal levels associated with measuring ROC in frictional data, it would be difficult to justify the use of FM0 in blind tests as shown in Figure 3-34 there are times when anomalous readings mask any trends or it fails to react entirely.

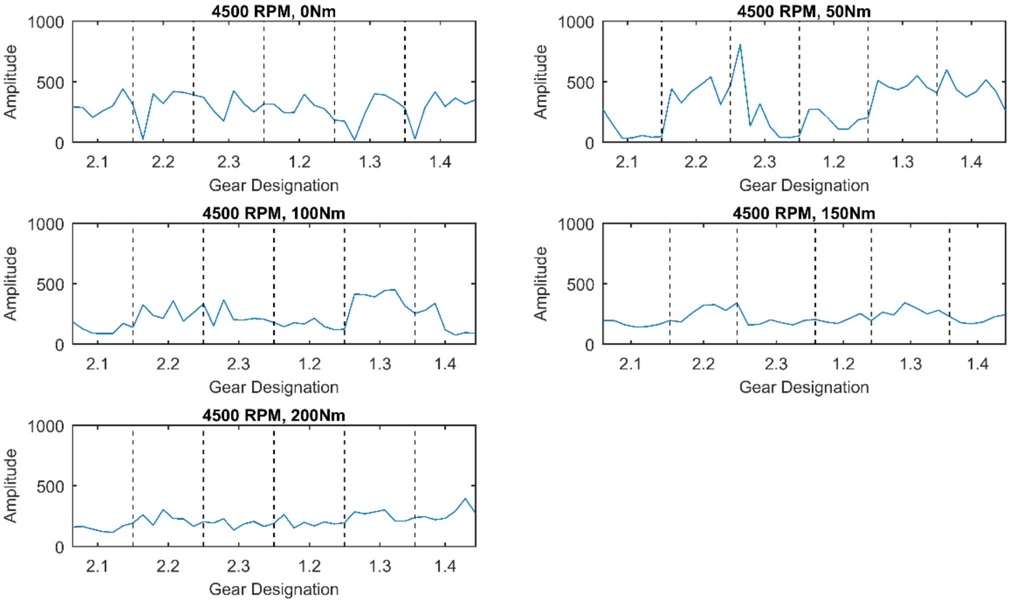

Figure 3-34 – Examples of lack of clarity found within FM0 results at 4500 RPM (Gear designations as per Table 3-3).

Following FM0, M6A and M8A are modified versions of FM4 proposed by Martin (1989). FM4 is mathematically identical to the kurtosis but is distinguished by its application to a difference signal d or residual signal r, both of which describe a vibration signal with the meshing frequencies, their harmonics, and in the case of the difference signal: the first order sidebands removed. These methods are intended to be more sensitive to peaks than the standard FM4 metric, by increasing the orders present to 6 and 8 respectively and normalised by an increased order of the variance (3 and 4 respectively). The formula for M6A and M8A are as follows:

$$M6A = \frac{n^2 \sum_{i=1}^{n} \left(d_i - \bar{d}\right)^6}{\left(\sum_{i=1}^{n} \left(d_i - \bar{d}\right)^2\right)^3} \tag{3-5}$$

$$M8A = \frac{n^3 \sum_{i=1}^{n} \left(d_i - \bar{d}\right)^8}{\left(\sum_{i=1}^{n} \left(d_i - \bar{d}\right)^2\right)^4} \tag{3-6}$$

Initially, it was thought that a more responsive measure meant that the new metrics may better detect damage as their increased sensitivity would lead to a better response to the damage. It was found, however, that the results from both M6A & M8A values varied very little from those provided through the use of kurtosis. When compared side by side (Figure 3-35) it can be seen that the trends from increasing damage are near identical despite the larger amplitudes.

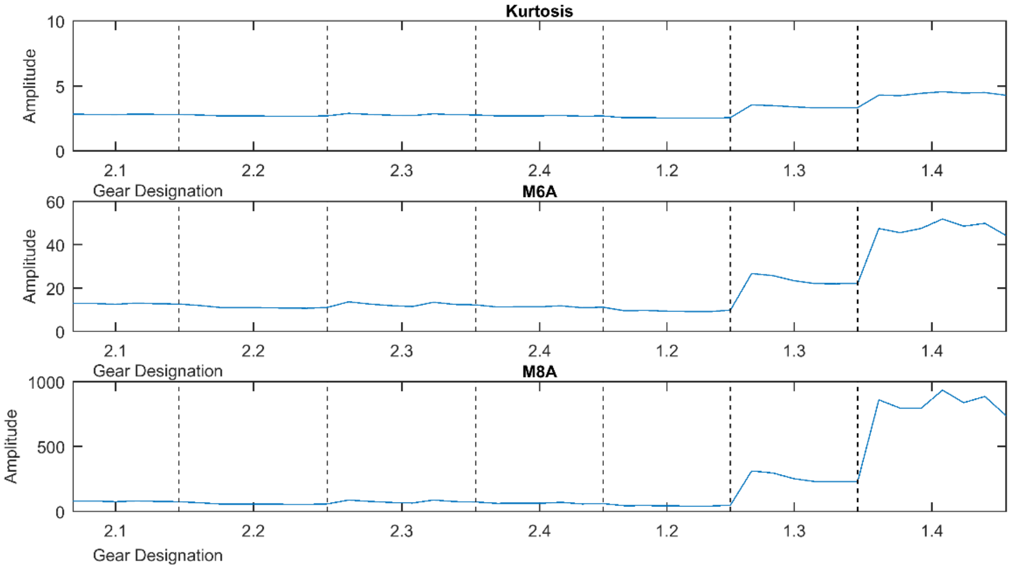

Figure 3-35 - Comparison of Kurtosis, M6A & M8A at 1600RPM & 100Nm Torque (Gear designations as per Table 3-3).

The most noticeable variation between the 3 methods is due to the increased sensitivity, where what were initially found to be small outliers in the kurtosis, have been amplified with the increase in orders of M6A and M8A (Figure 3-36). The concern with the use of these techniques then became that these anomalies were found to scale so greatly that all other trends present became insignificant simply due to the variation in magnitude. This made detecting even the 16 micron damage impossible and making the use of M6A and M8A redundant.

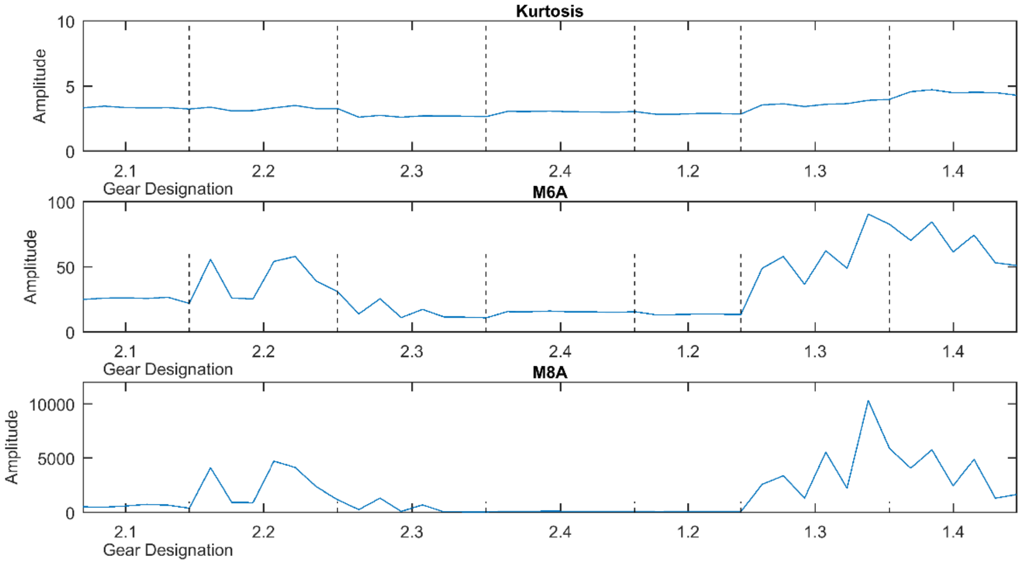

Figure 3-36 – Example of amplification at 3000RPM and 50Nm Torque (Gear designations as per Table 3-3).

3.6 Conclusion

Overall the initial work performed with frictional loss data showed that while work was still required, ROC technology has potential as a new non-contact method of condition monitoring in gear systems. That said, the use of frictional loss data, while moderately successful, may not yield the results necessary to allow ROC technology to be as effective as current techniques such as those presented in Chapter 2.

Raw waveform: The visibility of a large-scale response in the signal at different damage levels backs the idea that there is merit to the basic RoC technique and that detection is possible given the right signal processing approach.

Filtering: The implementation of a high-pass filter of 500Hz helped to significantly improve the clarity of the original signal. This increased clarity allowed the methods applied to have the best chance at detecting all the possible damage levels.

RMS: In conclusion, the RMS was the most successful technique providing a clear go/no go measure of damage through the use of ROC. With 8 and 16 micron bends able to be differentiated at lower loads, higher torques reduced this effect until a point where the damage related signals in most cases could no longer be clearly differentiated from their healthy counterparts. The 4 micron damage was found to be undetectable at all times, though due to manufacturing tolerances this was expected. Overall RMS provides only a limited ability to quantify the damage in frictional ROC measurements, however provides a stable starting platform on which to expand the understandings of ROC technology.

Variance: Whilst variance initially appeared to be improve upon the RMS, as the study continued it was found to provide almost identical results and suffer from the same torque related issues.

Kurtosis: Application of increased torque proved to be the limiting factor for kurtosis. At 0 – 100 Nm of applied torque it provided clear detection of the 16 micron bend and intermittent detection of the 8 micron bend. The higher torques, however, provided little information as the suppression had grown in scale enough to hide all traces of damage.

FM0: The nature of ROC technology and its measurement of such an intrinsic quantity to gearboxes would appear to lend itself to the use of FM0. Combined with frictional loss data however this is not the case where the metric provided some detection of the largest defect, but the variation and instability in the values generated meant that repetitive, accurate detection would not be possible at this time.

M6A & M8A: The higher order modification to kurtosis was found to reduce the effectiveness overall. While able to provide many of the same results as the standard kurtosis, the anomalies and outliers generated values of much greater magnitude masking any trends of much lower amplitude.

That said, many of the anomalies in the data can be attributed to the measurement of fluctuations in relatively small frictional torques. This chapter has identified the fundamental ability of ROC measurements to identify tooth bend defects even under these difficult conditions and gave confidence for the work to proceed to the next stage – the construction of a more representative test rig capable of making ROC torque measurements within the torque loop.

CHAPTER 4

Design and Development of a Novel Versatile High-Speed Gear Testing Apparatus

Following the conclusions presented in Chapter 3, it was clear that ROC technology had potential to detect tooth damage but required further work, particularly with measurements of ROC Torque under loaded conditions, rather than the measurements made in parasitic torque in Chapter 3. With condition monitoring playing an increasingly important role in engineering, whether for fiscal or safety reasons, there was a need to better understand this technology and its application to real, non-laboratory based, environments. This prompted the design and manufacture of a new novel test apparatus. The aim was to develop a test rig that would allow the full capabilities of ROC technology to be explored with a specific focus on the replication of real world conditions. Whilst this project would only be concerned with form defects in gears, it was known that future projects would wish to investigate other areas and so provisions were made to allow expansion of the rig specifications if and when they are required.

4.1 Design Philosophy

With the success of the "slow-speed" gear test rig and the experience gained at Cardiff on the operation and benefits of a recirculating torque design, it was concluded that the new test rig should be based upon the same principle i.e. a back-to-back power recirculating gear test rig. The use of a back-to-back design provides a simple but elegant solution to the lack of endpoint usually present in gear systems e.g. final drive or turbine, allowing large amounts of power to be recirculated whilst the drive motor requirements only have to overcome friction and other parasitic losses.

The nature of this means that the new design is not dissimilar to that which is presented in Chapter 3, where the test head comprises of 2 housings connected by shafts with an integrated loading device.

The general specifications for the rig were:

- Maximum achievable speed of 15,000 RPM on the input shaft.
- Dynamic fast shaft loading to simulate gearbox cycles.
  - Maximum sustainable torque of 600 Nm.
  - Max peak torque of 1000Nm.
- Full gearbox construction including use of car-specification gears.
- Controllable oil temperature.
- Individual flow control of bearing lubrication.

The decision to be able to run the full Mercedes AMG Petronas gearbox was based upon the experience gained from using the ‘slow-speed’ rig, constrained as it is to run a 3:2 ratio only. Simulating the full gearbox allows for an increase in signal complexity that would much more closely resemble what would be seen at the operating conditions of a sensor incorporated into a future powertrain. The specifications for speed, load, and temperature were directed by the current or known future plans for the Mercedes powertrain.

The maximum speed was set at 15,000 RPM, as per rule 5.1.3 of the Formula 1 technical regulations (FIA, 2017) as presented by the FIA. At the time of design, there was no known proposed changes to Formula 1 engines until 2020. Without knowledge of what these changes might be, there was no reason to exceed the current rules and risk unnecessary reductions in component life. From data provided by MAMG, it was known that the maximum peak torque observed during race operations was approximately 1000Nm. This occurs solely during gear changes and for very short periods of time, ignoring these gear changes, the maximum sustained loading was found to be approximately 600Nm. For the purpose of the testing ROC technology, the maximum torque was set at 600Nm as exceeding this represents no clear benefit when trying to establish the abilities during normal operation. To provide context to this figure and the testing capabilities, the mean and maximum gear contact stresses along the contact path for 7th gear are shown in Figure 4-1. As can be seen, the maximum contact stress, particularly for single tooth loading, is incredibly large reflecting how heavily the loading on these gears is. Expanding upon this, the calculated bending stress for the worst case loading i.e. 15000 RPM and 600 Nm torque was found to be: 1.31 GPa. To put this in perspective, the ultimate tensile strength of the gear material is 1.32 GPa before heat treatment, although the case hardening puts distance between these values it demonstrates how close to the limits these gears are run at and by association the extent of the new rig’s test capabilities.

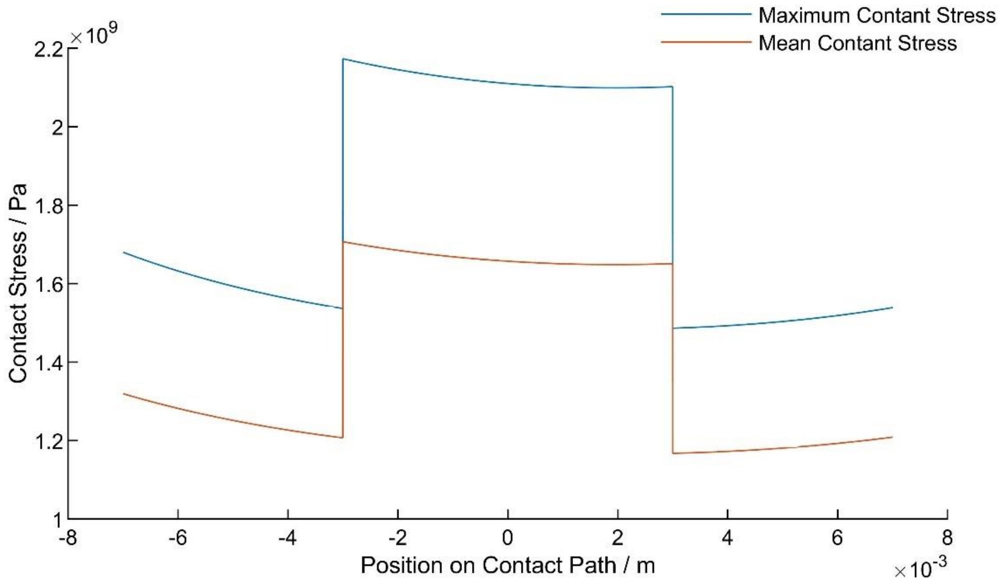

Figure 4-1 – Contact stresses for 7th gear running for 600 Nm torque.

For future work purposes, it was proposed that the maximum torque capable of being run on the rig should be 1000Nm for the purpose of gear fatigue tests. This choice was made with the knowledge that the gears are most susceptible to damage during gear shifts due to the sudden changes in loading and the peak loads associated, therefore replicating such conditions for even a brief period should allow for a gear to be stressed beyond its lifespan.

To allow the test head to operate at these speeds and loads required a lubrication system capable of providing sufficient lubrication to sustain operations for long periods as well as removing additional heat generated. From personal communications with MAMG, the average running temperature of their gearbox was known to be 120°C. To continue to simulate the MAMG running conditions this temperature would be taken as the standard operating temperature. This temperature would be later revised to be 80°C however, with initial run-in tests finding that the oil capacity of the tank and circulation meant the heater could not bring the system to the desired temperature. Plans were made to reduce the capacity of the tank, increase the temperature capacity of the system, but could not implemented in the span of this project. Given this temperature, from preliminary calculations it was suggested that at the maximum speed and loads for standard testing the heat generated by the gear contacts would lead to the overall temperature to continue to increase past the test standard and as such need for a cooling system would also be required to maintain stable testing temperatures.

With these details in place, the ancillary systems and details could then be designed and specified so as to allow the main systems to achieve these set conditions.

4.2 Test Rig Layout

As presented in Figure 4-2, the rig can easily be broken down into 3 distinct sub-assemblies: the test head, drive system, and the ancillary systems.

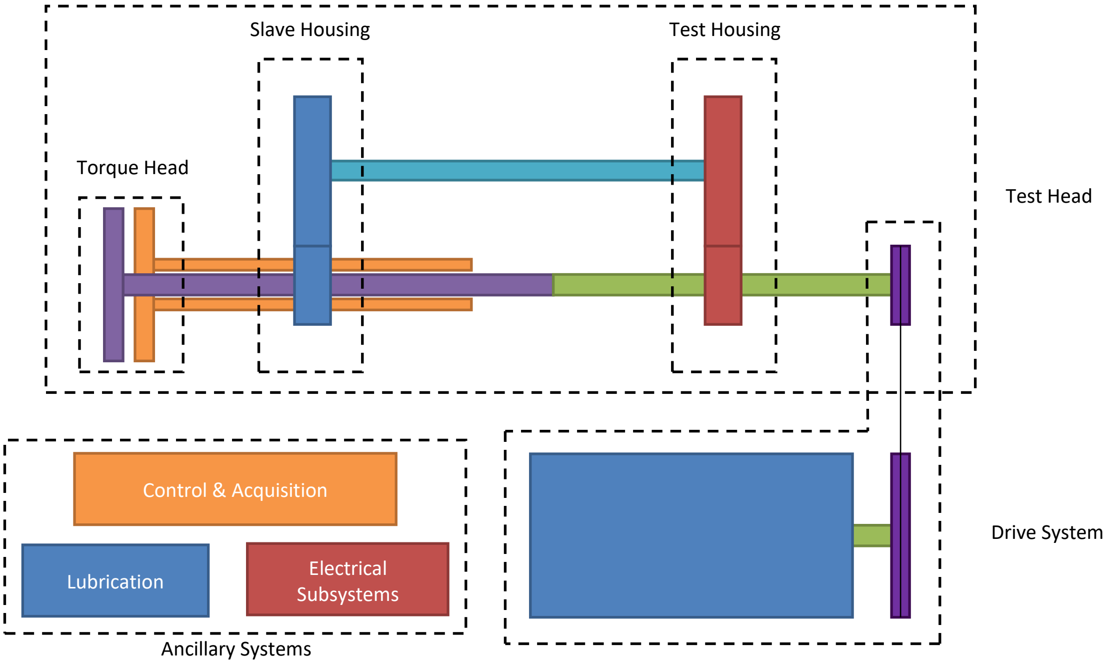

Figure 4-2 – Simplified schematic of the test rig.

As discussed in the antecedent section, the new test rig would be of the recirculating torque type of design. Many of these types of test apparatus found in academia and industry follow the FZG approach, which can be seen in Figure 4-3. Named so for being developed by FZG (translated as the Technical Institute for the Study of Gears and Drive Mechanisms), these rigs provide versatile testing facilities for gears and are often used in combination with FZG testing procedures as defined by the International Organisation for Standardization (ISO). Although highly flexible, these rigs are generally designed for what are comparatively slow speeds and a much wider range of torques. With two examples of FZG rigs having maximum possible loads of 800 and 4000 Nm, but a maximum speed of only 3000 RPM (Institute of Machine Elements, 2016).

Whilst in many ways the rig design under this study can be said to be similar to a FZG rig as seen by the similarities in layout between Figure 4-2 and Figure 4-3, in practice the two differ greatly. This stems from the differences in specification, with the most noticeable differences being the method of loading and how torque is recirculated around the test rig.

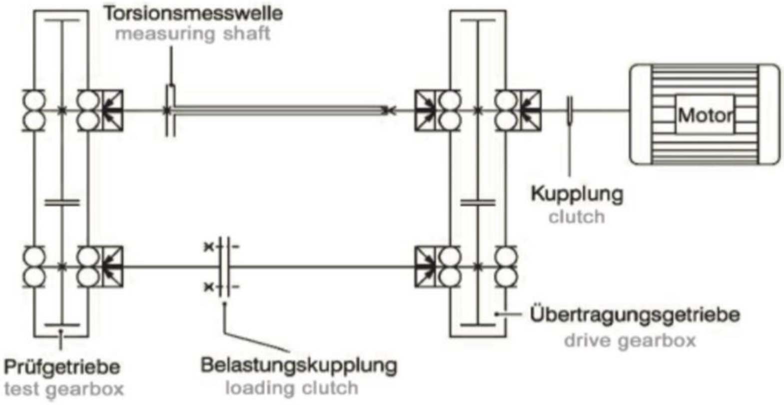

Figure 4-3 – Design layout of an FZG back-to-back gear test rig. (Extracted from Institute of Machine Elements (2016))

Under normal conditions, the MAMG gearbox would have load delivered from the engine via the input shaft and power exits via the final drive. In order to best replicate these conditions, the torque device was positioned to introduce load during the 'input stage'. For the final specification of the rig, a Micromatic rotary vane hydraulic actuator was selected to allow replication of the dynamic conditions in the MAMG gearbox. Although this device was never implemented during the time scale of this project, design of the rig was undertaken to ensure that it could be integrated in future. To this end, the torque head was situated behind the slave housing as can be seen in Figure 4-2. A mechanical torqueing device was designed using the same attachment points as the rotary actuator, allowing for its future integration. The result this meant that the torque loop was no longer rectangular and led to the design that is presented in Figure 4-4.

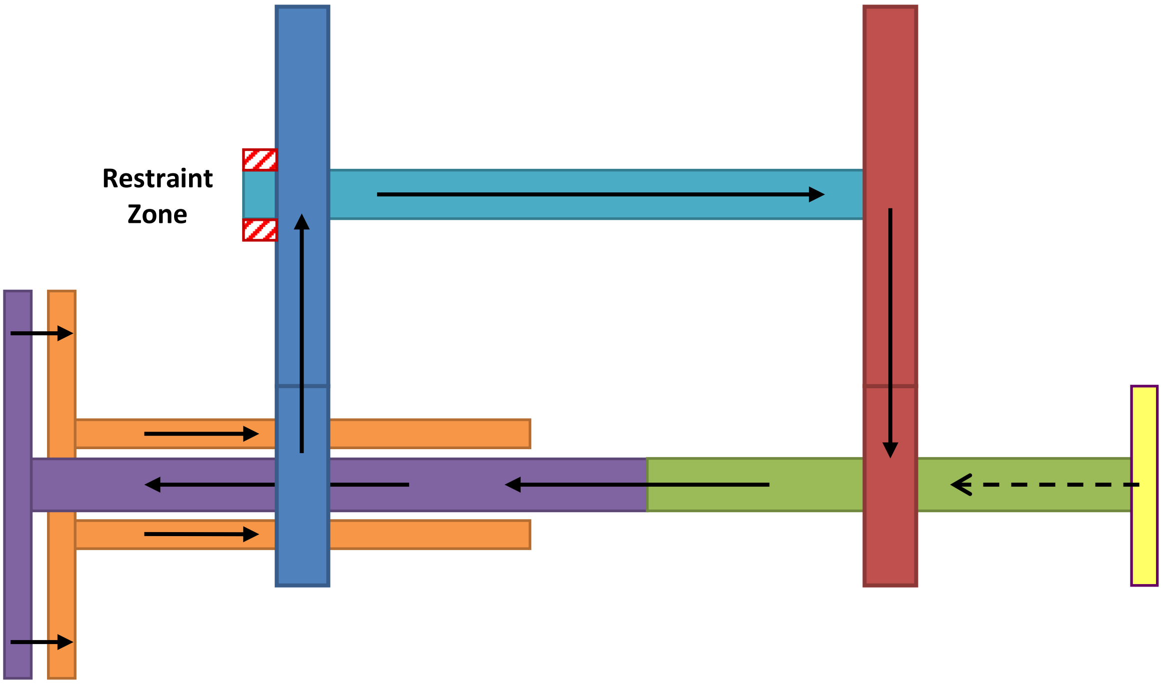

Figure 4-4 – Block diagram of the torque loop.

Static torque is induced via the manual torqueing device. This acts essentially like a clutch by allowing the connection between 2 shafts (shown in orange and purple in Figure 4-4) to be controlled. A torque is induced by disconnecting the ‘clutch’ and restricting movement in the rest of the rig by restraining the upper shaft at one end. By generating a torque along the purple quill shaft, when the ‘clutch’ is closed, this torque is locked in and can no longer be released by the loop. By removing the restraint and providing drive and compensation for frictional torsional loses via the pulley (yellow), it is possible to generate and sustain a controllable level of torque within the system.

4.3 Mechanical Design of Test Head

The test head itself can be broken down into 3 separate assemblies: the test housing, slave housing and torque head.

4.3.1 Test housing

The test housing contains the test gears. The housing was designed, within this study, to accommodate the internal components of the MAMG 2014 gearbox. As shown in Figure 4-5 and Figure 4-6, the gearbox main and layshafts are supported by a series of roller element bearings, each with their own lubrication feeds. The gearbox is designed to run with forward running 8 gear pairs as well as a reverse and a set of trigger discs. As this project required flexibility within its test set up a series of spacers were manufactured to allow the testing of any number of gear pairs at once. While provisions were made for the shifting mechanism to be included, they are currently not included within the test housing. Similarly, additional systems and lubrication requirements were not included in the design at this stage following discussions with the sponsor for the purpose of simplicity and available time.

The housing itself is made up of four aluminium plates that provide the core structure of the housing as well as two end plates that provide support for the bearings and shafts mounted within. Of these four, all except the bottom panel (which provides the drainage port) possess windows with removable covers to allow inspection during tests as visible in Figure 4-6. Upon the end plates for this framework are mounted 3 bearing caps to provide targeted lubrication and sealing, with the lower left bearing (Figure 4-5) having an offset lubrication jet and sealing provided by a MagCanica torque sensor as shown in Figure 4-6.

The assembled housing is mounted on a large aluminium base plate, which is in turn mounted on the speed frame structure of the rig albeit separated by ceramic tiles to reduce heat loss from the test head. To maintain positional accuracy, the separate plates are dowelled together as well as being doweled to the base plate. A full set of technical drawings including full tolerance information was produced for the housing and bearing cap components for the test housing and were supplied to the sponsor for manufacture.

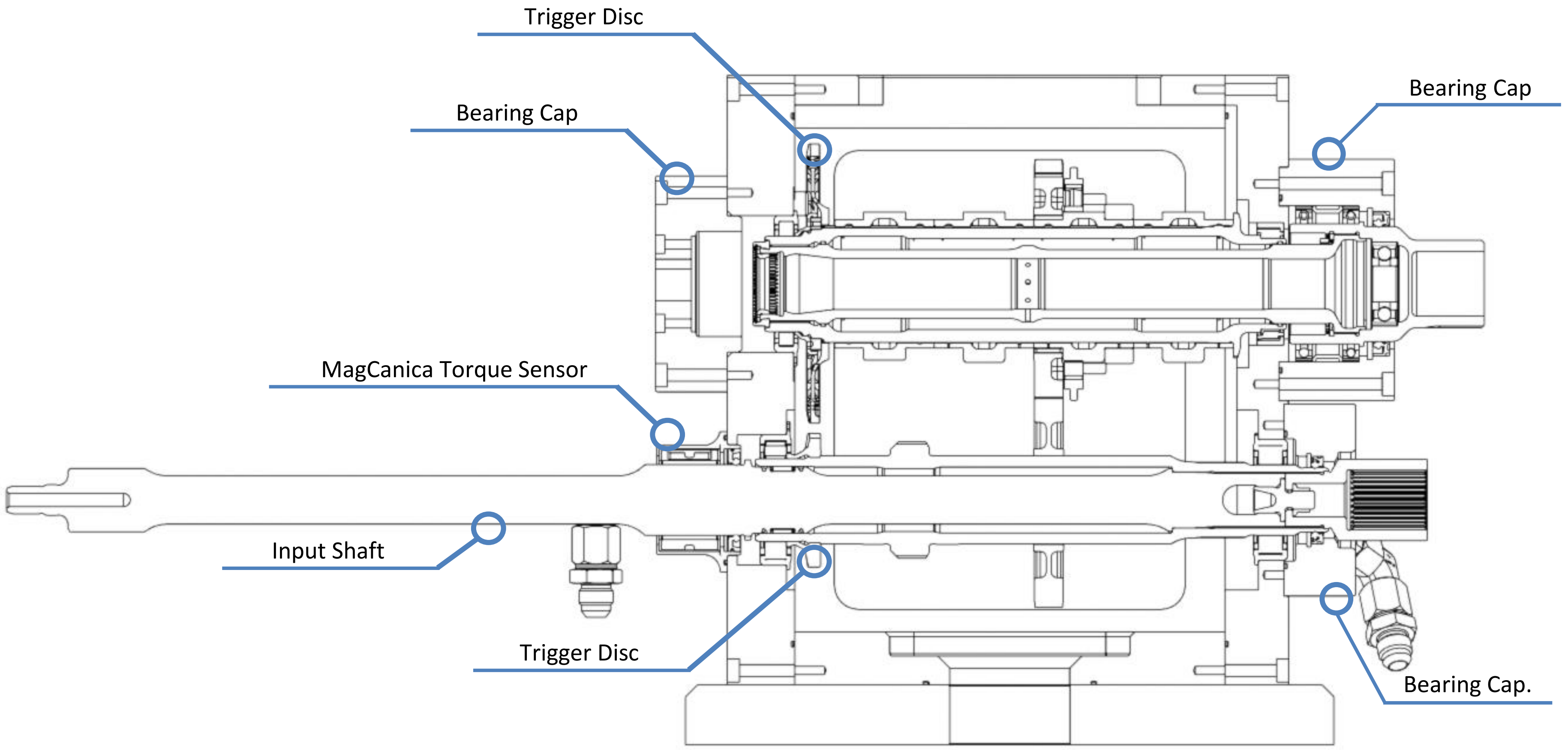

Figure 4-5 – Planar section of the Cardiff gear test rig test housing.

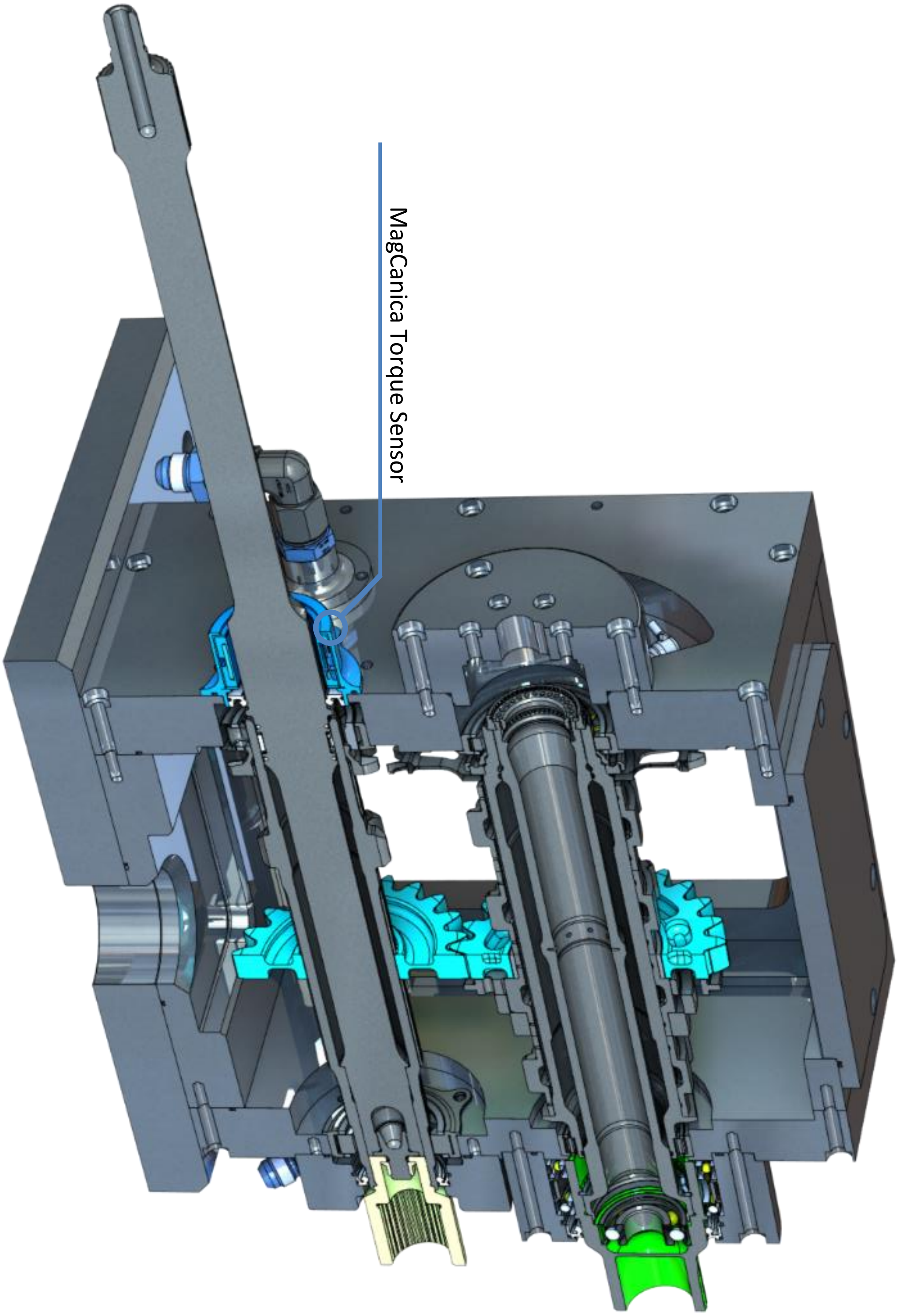

Figure 4-6 – Sectioned Cardiff gear test rig test housing.

4.3.2 Slave housing

Unlike the test housing, the slave housing was entirely designed or specified by the author (omitting gears) and is only intended to allow for one gear pair at a time. As can be seen in both Figure 4-7 and Figure 4-8, the main shaft engages the gear with an artificial dog ring that is a machined feature of the shaft and terminates with a spline allowing connection to the test housing, and a hexagonal feature to allow all motion in the rig to be restrained for the purposes of loading. In order to provide a torque-recirculating pathway through the rig, a quill shaft (Figure 4-8) runs through the lower shaft connecting the test housing to the torque head. This shaft is also important as it houses the remnant magnetic field used by both the torque and the ROC sensors. The larger layshaft encircles the quill shaft but is connected only to the torque head via splines and transmits the torque via the layshaft gear to the rest of the rig.

For these shafts to perform their assigned tasks without failure, the correct material selection had to be made. To this end, an extensive stress analysis was undertaken for every shaft designed with both hand calculations and finite element analysis being used. This analysis looked at multiple materials and the recommended suitable heat treatments for them. Sets of full technical drawings were produced for every component including those of the torque head and test housing and delivered to the sponsor for manufacture. Whirling calculations were also undertaken to confirm that critical speeds for the shafts were not being approached. Prediction of where failure was to occur if it were to happen was found be near the rear of the quill shaft just before the connection between the torque head and the slave housing.

These shafts are supported by a number of bearings. Whilst the bearings differ, both shafts are supported with the same setup of two angular contact ball (ACB) bearings in a back-to-back configuration at one end, and a cylindrical roller bearing at the opposing end. This setup is designed so that while all 3 bearings resist the radial loads, the ACBs will resist a higher proportion and are able to resist any axial load. The roller bearing still provides some radial support but is critical in allowing for axial displacement of the shafts due to thermal expansion during operation. In order to determine that the bearings would not fail prematurely because of the test conditions, the L_{10} life was calculated and compared for each candidate.

The L_{10} life can be defined as the life that 90% of a sufficiently large group of identical bearings will achieve when operating under identical conditions and is described mathematically as:

$$L_{10h} = \frac{10^6}{60\ n} L_{10} \tag{4-1}$$

L_{10h} is the bearing life in hours with n defined as the rotational speed in rotations per min and the bearing life in millions of revolutions, L_{10}, described as:

$$L_{10} = \left(\frac{C}{P}\right)^{p} \tag{4-2}$$

where C is the dynamic load rating in kN, p is the exponent of life given by SKF (SKF, 2017) as 3 for ball bearings and 10/3 for roller bearings. Finally P is equivalent dynamic bearing load in kN which is:

$$P = XF_r + YF_a \tag{4-3}$$

F_r and F_a are the radial and axial bearing forces respectively, while X and Y are the respective load factors for the bearing.

Using the two load scenarios described in the specification i.e. 600 and 1000 Nm and the maximum rotational speed of 15000 RPM, the worst case expected life for both standard operations and fatigue tests could be calculated. For a bearing to be considered suitable for the test rig it had to meet two criteria: a minimum expected life in hours and a minimum bearing safety factor, which is define as the static load rating (C_0) divided by the equivalent static bearing load (P_0). These criteria ensured sufficient amount of run time and that the bearing would not deform under the load while idle. The specified values for these criteria for the two load scenarios can be seen in Table 4-1.

Table 4-1 – Specified minimum bearing safety criteria.

	600 Nm	**1000 Nm**
Minimum Expected Life (hrs)	300	50
Minimum Safety Factor	2	2

Using these values to determine the effectiveness as well as the limiting speed of the bearings, four bearings were selected for the slave housing as listed in Table 4-2.

Table 4-2 – Selected bearing for the slave housing.

Designation:	C/kN	C0/kN	Lim Speed (RPM)	Type	Shaft
MAMG Special	-	-	-	Roller	Lower
NU 1010 ESP	46.8	56	9500	Roller	Upper
7208 CD/P4A	33.8	24.0	34000	ACB	Lower
7210 CD/HCP4A	44.9	34.0	30000	ACB	Upper

It should be noted that the limiting speed, despite its name, is a cautionary limit rather a prohibiting one, however lubrication requirements and tolerances must be adjusted accordingly to prevent ceasing and failure.

These bearings were housed in custom aluminium end plates (Figure 4-7) that were dowelled into a frame similar to that of the test housing, as can be seen in Figure 4-8. This frame was then doweled into a base plate that also supported the torque head. Bearing covers were then designed to provide sealing and directed lubrication for each of the bearing. The bearing covers also served as mounts, notably for the ROC sensor and the locking block to restrain the motion in the test rig.

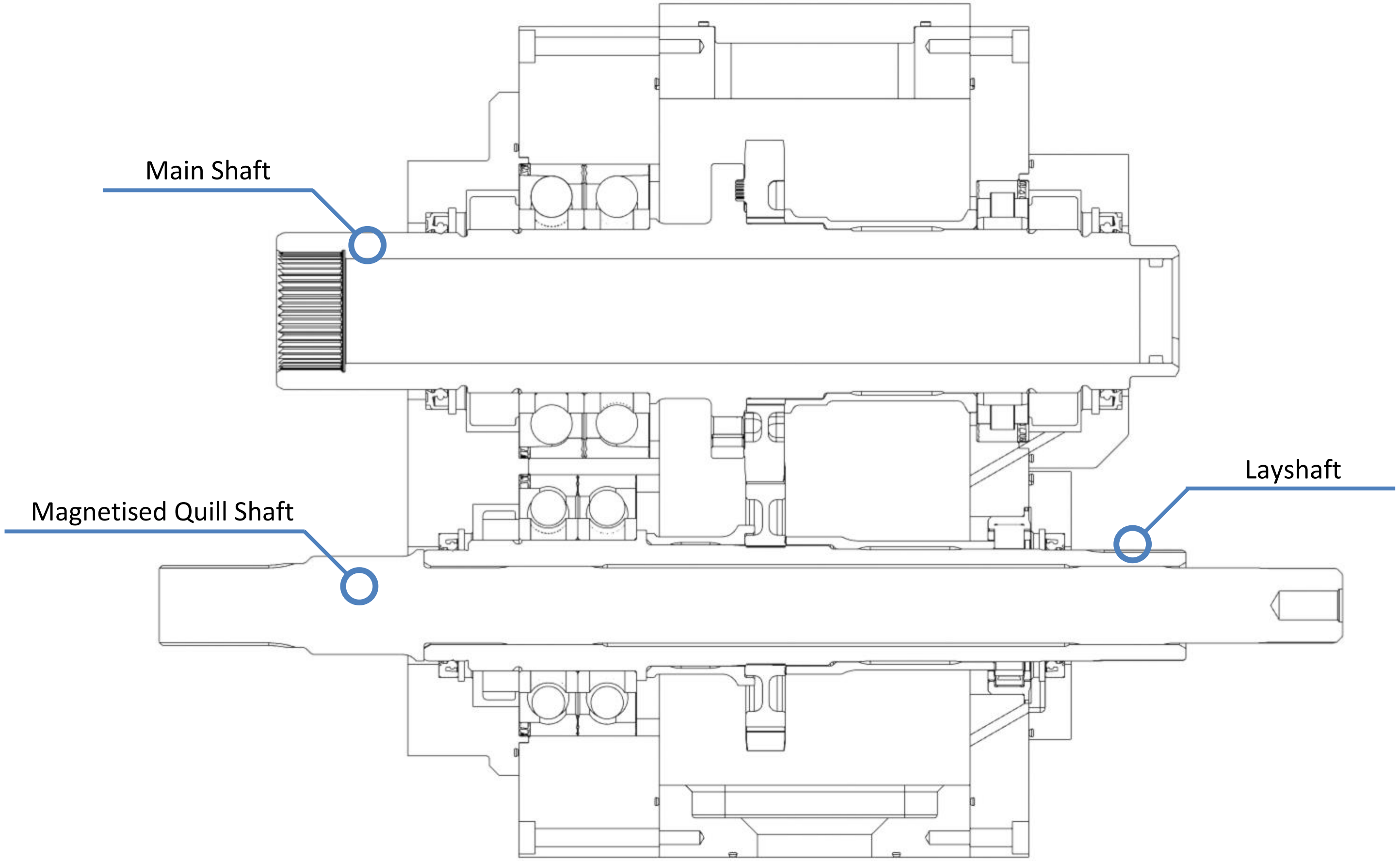

Figure 4-7 - Planar section view of the Cardiff gear test rig slave housing.

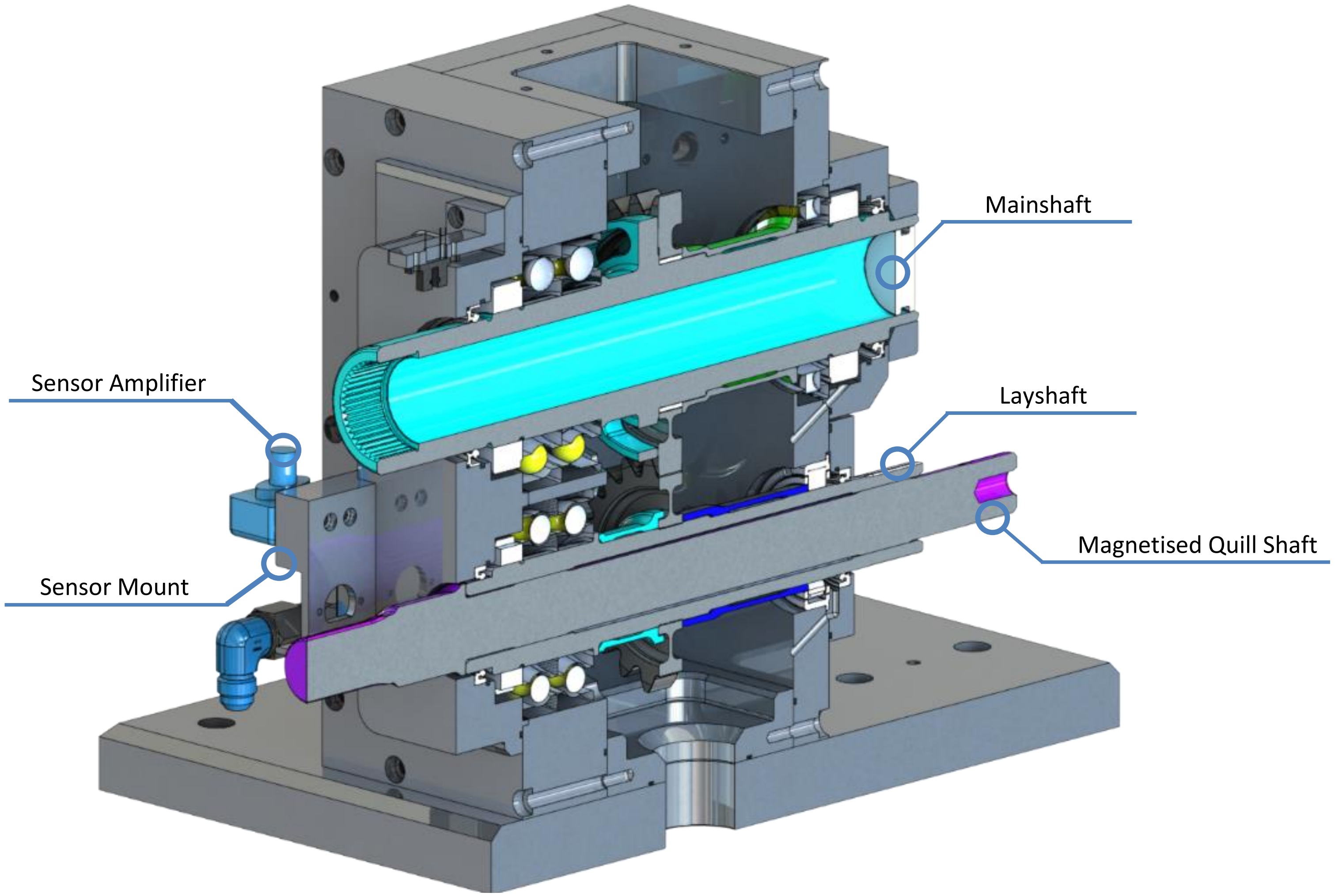

Figure 4-8 –Section view of the slave housing.

4.3.3 Torque head

The torque head as seen in Figure 4-10 and Figure 4-11, is a custom device designed and developed by the author to allow the application of static torque to the test head. It is comprised of 6 major components from left to right (Figure 4-11) of: an input shaft, retaining plate, splined disc, annulus, output shaft and support assembly. As the assembly in Figure 4-10 demonstrates the input and output shafts lie concentrically. They are only restrained by the splined disc and can move independently, once it is removed. The splined disk has external splines which mate with the output shaft (via the annulus), and internal splines which mate with the input shaft. To apply torque, motion in the rig is restricted via the use of a locking block and the hexagonal feature located at the end of the slave housing main shaft. The splined disc is then disengaged from the mating splines, and a loading arm and hanger are attached to the input shaft via the triple square connection at the opposing end, an example of this setup being used is shown in Figure 4-9.

Figure 4-9 - Loading via the manual torqueing process.

Through basic geometry the mass required to apply the desired torque can be calculated, the additional mass required is added to the hanger. The splined disc can then be reinserted to lock in the torque. To always allow the disc to fit between the input shaft and annulus, regardless of the orientation of their splines, the splined disc was designed with a hunting ratio. Once locked in the disc is held in place with a guard to prevent slip during testing.

Just as with the slave housing, the bearings for the torque head were specified by the author. However, unlike the slave and test housings the torque head would not have a lubrication system integrated into it. As such the bearing would have to be self-lubricated with a life span sufficient to not interfere with testing. By using the same analysis as mentioned in the previous section of calculating the L_{10} life the bearing in Table 4-3 was selected.

Table 4-3 – Torque head support bearings.

Designation:	**C/kN**	**C0/kN**	**Lim Speed (RPM)**	**Type**
S71914 ACB/HCP4A	17.4	18.6	19000	ACB

While the duration of the project has only seen the use of static torque applied manually, the acquisition of the aforementioned Micromatic rotary vane actuator meant the design must allow integration to the rig. As such the annulus and the output shaft connect via the same points as the actuator requires. Further to this a coupling has been designed and drawn ready for manufacture at the time of transition. This coupling allow connection between the input to the actuator and the magnetic quill shaft, once the torque head input shaft has been removed.

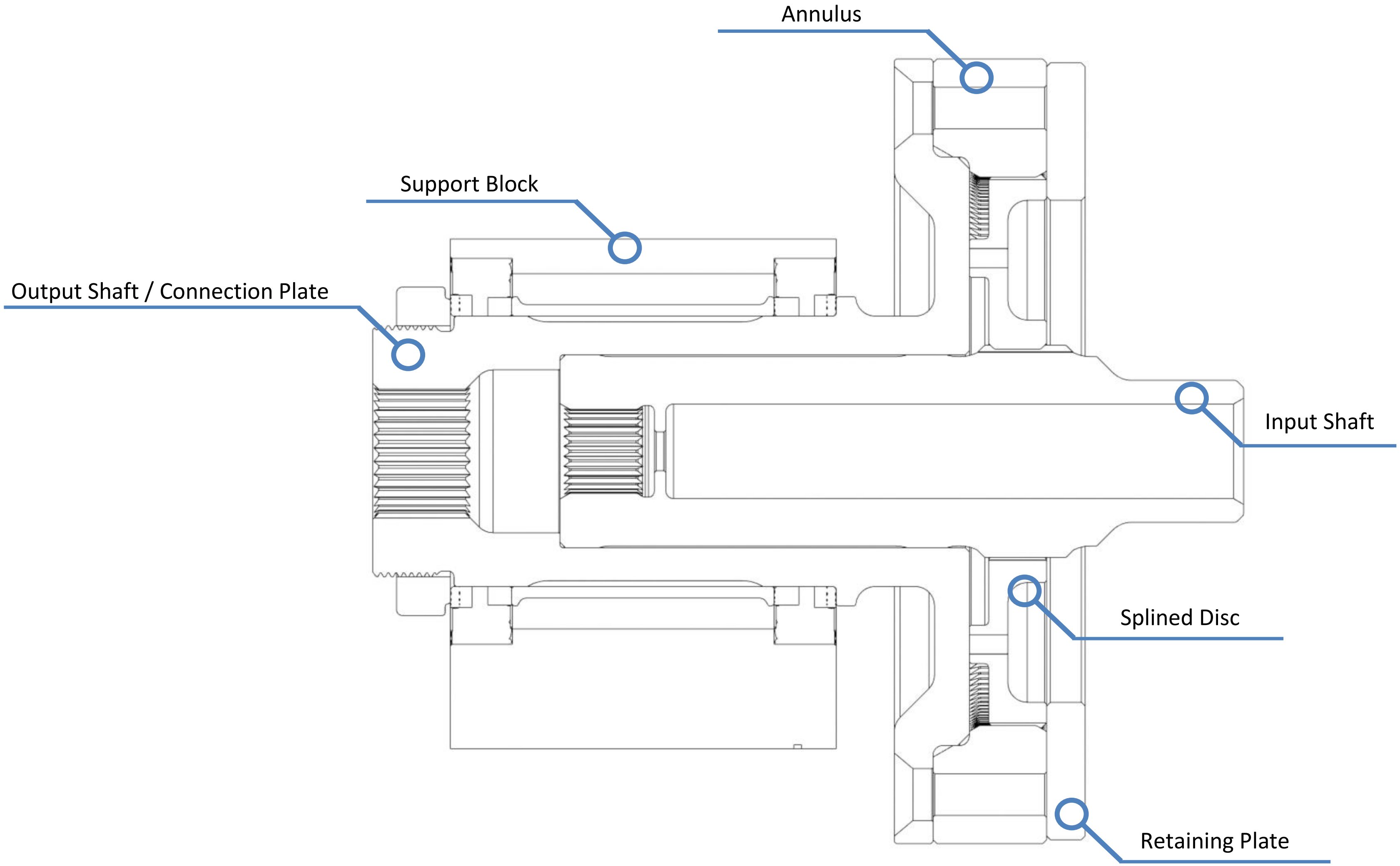

Figure 4-10 – Planar sectioned view of the Cardiff gear test rig torque head.

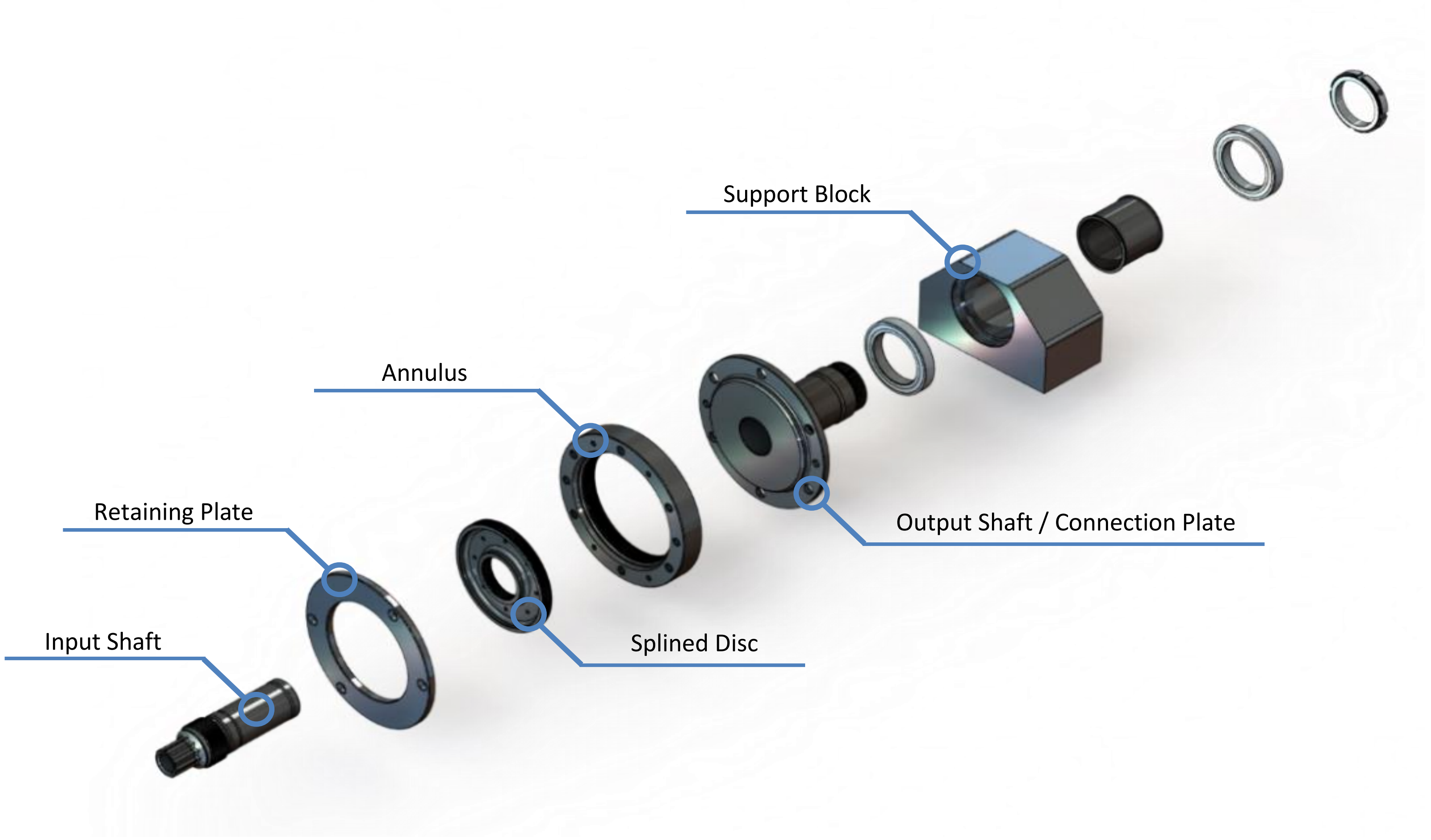

Figure 4-11 - Exploded view of the torque head.

4.4 Drive System

The design of the drive system (Figure 4-12) was inspired by the configuration used in the previous test rig, albeit with modifications to accommodate the new requirements. A 22kW, 2-pole three-phase AC electric motor was selected; while generating less torque than the previous 11kW 4-pole motor, the fewer poles allows for a higher synchronous speed of 2940 rpm. When combined with the new pulley ratio, this allowed the new maximum speed of 15000 rpm to be reached in a single belt stage, allowing the tensioning process to be simplified as idler pulleys were not required and a tilting motor base plate could be used. A 22kW inverter was specified to provide power and speed control. This inverter was subsequently given a manual controller and also connected to the control system to allow for computer control.

Figure 4-12 – Polyvee belt drive system.

The pulley was supported in a block not dissimilar to that seen in the torque head. As shown in Figure 4-13, it comprises of a custom designed shaft supported by two identical back-to-back ACBs (Table 4-4) with the pulley secured rotationally to the shaft by keys. These were selected after a stress analysis and specified for the speeds and forces expected. Finally, lock nuts are used to retrain the axial movement of the shaft and pulley.

Table 4-4 – Pulley support bearing specifications

Designation:	**C/kN**	**C0/kN**	**Lim Speed (RPM)**	**Type**
S71908 ACB/P4A	6.75	6.4	28000	ACB

The pulleys are part of a 16 rib polyvee belt system with a 5.2:1 ratio. This system was selected based on the specified maximum speed and torque requirements. However, it is worth noting that the pulleys had to be manufactured from steel due to the rim speeds being too great for standard iron pulleys to maintain without damage. Finally, the assembly is dowelled and bolted onto an aluminium baseplate to allow connection to the frame.

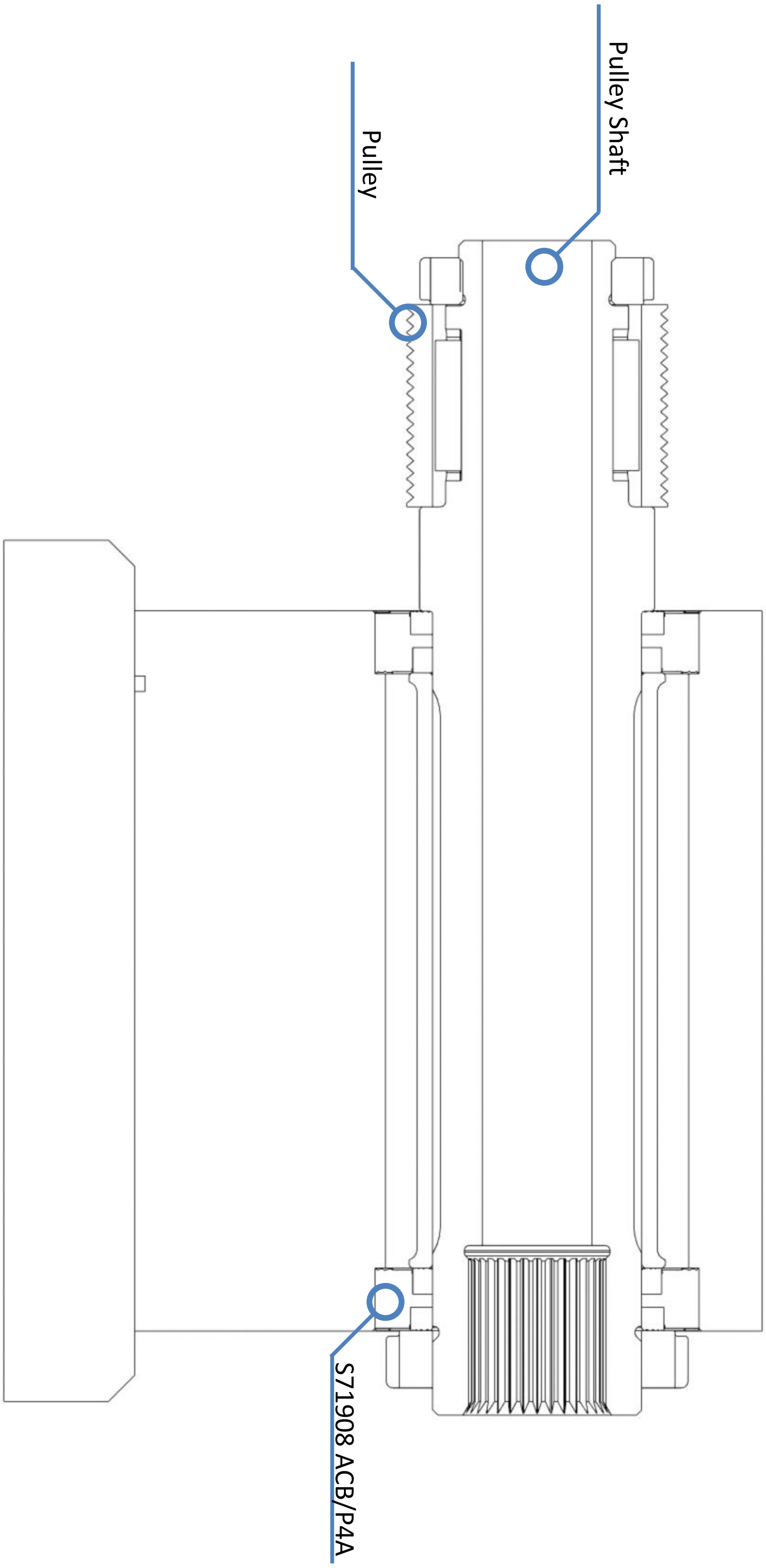

Figure 4-13 – Planar section of the pulley assembly.

4.5 Lubrication System

The lubrication system comprises of 2 distinct circuits connected to an insulated 30 litre tank as can be seen in Figure 4-16. The tank itself is of a custom design to allow better integration into the super structure of the rig. As can be seen in Figure 4-14 the tank is comprised of an inner and outer shell of stainless steel with insulation sandwiched between. Three connection ports are integrated directly into the tank, the two visible in the left wall are reserved for the intake and outlet for the heat exchanger, while the last one supplies the pump that feeds the test head using the static head to reduce the need for suction. The lower port also has a 250 micron wire mesh mounted over the intake acting as a filter to prevent any large debris from entering the pump.

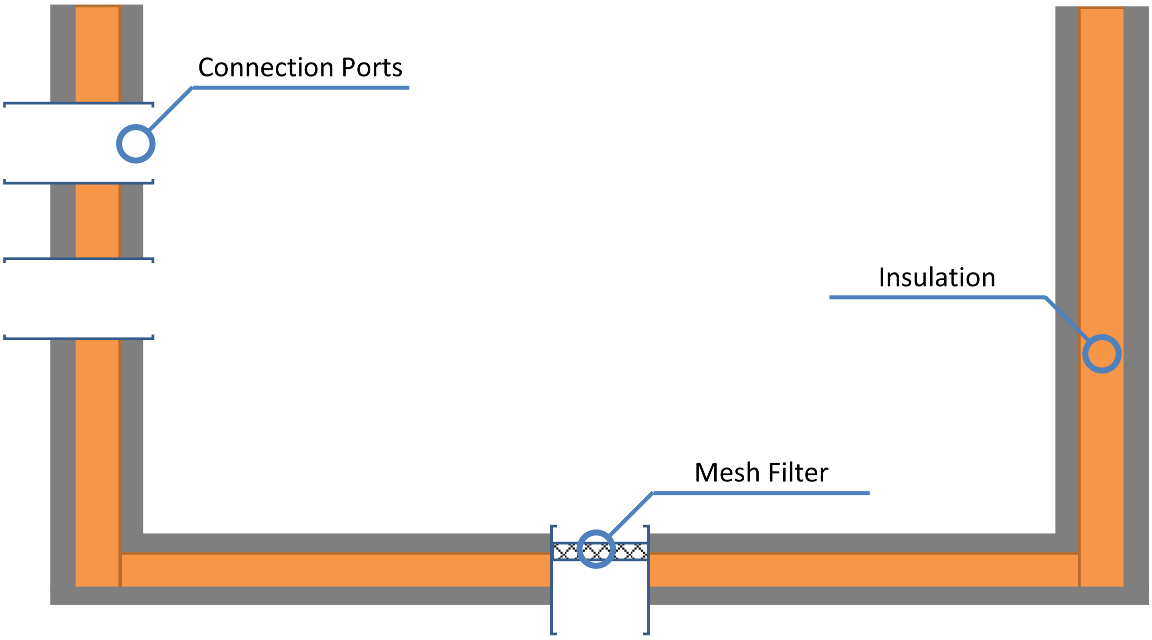

Figure 4-14 – Simple schematic of the insulated oil tank.

The tank has an insulated lid that covers all but the mounting plate. This mounting plate allows for the oil returns from the test heads and the heating unit, and both this and the lid can be observed in Figure 4-15. The heating unit is a Grant Instruments TXF200, which was selected due to its flexibility in both temperature range, control, and mixing. As it can achieve up to 200 °C, it can easily maintain the temperatures required for testing and can be set to either one fixed temperature or a program. This flexibility as well as the possibility of LabVIEW control, ensures that the heater has sufficient scope for future projects as well as meeting the requirements for this one.

Figure 4-15 – Insulated oil tank.

As previously mentioned, the overall lubrication system has two different circuits. Of these, the cooling circuit is by far the simpler. Using a 0.25kW inverter controller gear pump, the oil is circulated through a GDM GDAC 14 heat exchanger, capable of dissipating 16.5 kW at 100°C, before being returned to the tank. This allows for the regulation of oil temperature so that thermal runaway due to frictional heating does not occur.

The second circuit supplies the test head. From Figure 4-16, it can be seen that the circuit to supply the test heat is more complex than the cooling circuit. Using an identical pump to the cooling system, the oil is passed through a 25 micron filter to prevent contamination affecting the operation of the bearings or gears, before it enters the manifold. The manifold (Figure 4-17) is made up of two halves, the first (left) has 6 ports for providing lubrication to the test housing, while the second is dedicated to the slave housing. The purpose of this is that it allows two systems to be isolated from one another. This opens the up the possibility of oil tests and the ability to test the effects of different oils upon the operation of the gearbox. Also seen in Figure 4-17 is that each port has a needle valve and T-joint. Whilst the T-valve allows for connection to the rig and future expansion, the valves allow for fine tuning of the flow rate for each individual bearing and the gear lubrication jet and provide the possibility of oil starvation tests in future.

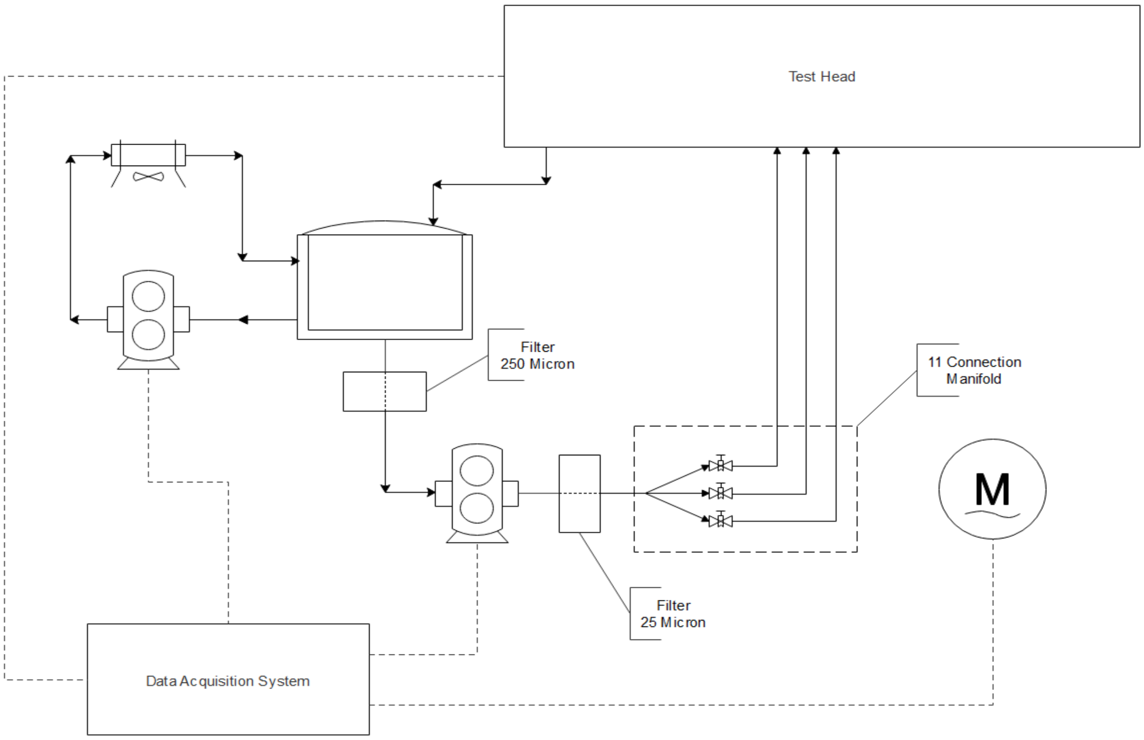

Figure 4-16 – Fluid system and control diagram.

Figure 4-17 – CGTR Manifold

To supplement these systems, optics and inverters were also introduced. The optics are included in the oil returns from the test housing and slave housing as seen in Figure 4-18, this allows the users to manually confirm oil flow from both housings before the drive system is engaged. The inverters were specified to provide the power requirements and allow for variable speed control. Both pumps are controlled by identical Fenner 0.25kW inverters, which were subsequently given manual controllers as well as being connected to the NI DAQ so that LabVIEW control could also be implemented.

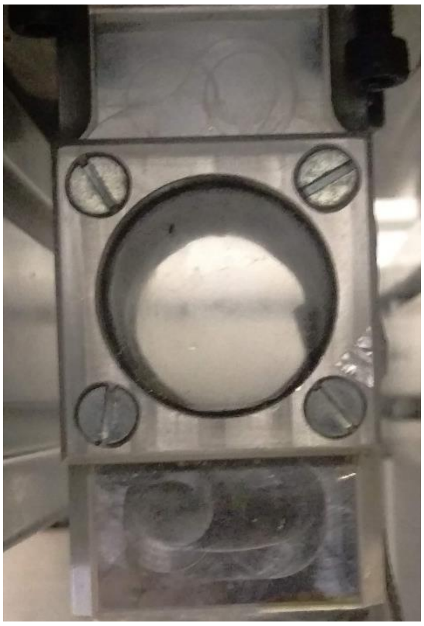

Figure 4-18 – Oil return optic.

4.6 Control and Data Acquisition System

In order for the high speed test rig to fulfil its purpose and provide a stable platform for a plethora of tests for both this project and future projects, it has to be able to capture sufficient, reliable data. To do this a variety of sensors have been incorporated into the test rig and are as follows:

ROC sensor: The ROC sensor is the key part of the high speed test rig. While a more detailed explanation can be found in Chapter 2, the ROC sensor measures the rate of change of torque via magnetic fields. The sensor and shaft are a pair and with the sensor calibrated to the shaft's magnetic field on Cardiff's behalf by the manufacturer MagCanica.

TRQ sensor: To allow for a direct measurement of the torque in the system to help with the setup of a test and the induction of static torque into the system, MagCanica provided a basic torque (TRQ) sensor to be run on the same shaft as the ROC sensor. Unlike the ROC sensor however, the TRQ sensor was not calibrated prior to receipt. This was performed in situ by loading the system statically to generate a known amount of torque and recording the output voltage of the sensor to generate a sensor response graph.

Hall Effect sensors: The test rig has four Hall Effect sensors in total, with two operating on each shaft's trigger disc. Outputting a digital square wave signal, the sensors allow for precise phase measures of the ROC signal as well as an accurate measure of speed whilst the rig is in operation.

Light gate: The light gate is included to provide an indication of the signal and a once per revolution pulse. Aligned so the gap is 180° from the damaged tooth, the light gate generates an analogue signal controlled by a Schmitt trigger to generate a square wave, which can be translated to a digital signal post process.

Thermocouples: To monitor temperatures across the test rig, up to 8 k-type thermocouples can be connected at any one time. The nature of the acquisition system means they require no signal conditioning, linearization or cold-junction compensation as this is done by the thermocouple amplifier module installed in the data acquisition system.

In order to collect the data from the aforementioned sensors and control the test rig, a National Instruments compact DAQ was used, specifically the NI-9178. This 8-slot chassis provided flexibility as it allowed for task specific cards to be selected and in the future upgraded as the capacity of the rig is expanded. The cards installed are as such:

NI 9211 – 4 channel temperature input module.

- Voltage measurement range: ±1.5 V
- Resolution: 24-Bit
- Sample rate: 14 S/s

NI 9215 – 4 channel simultaneous-sampling analogue input module.

- Voltage measurement range: ±10 V
- Resolution: 16-Bit
- Sample rate: 100 kS/s/ch

NI 9269 – 4 channel analogue output module.

- Voltage measurement range: ±10 V
- Resolution: 16-Bit
- Sample rate : 100kS/s/ch

NI 9401 – 8 channel digital input & output module.

- 5 V/TTL
- Update rate: 100 ns

These cards covered all the basic control needs of the test rig as well as data acquisition, a schematic of the overall system can be seen in Figure 4-19.

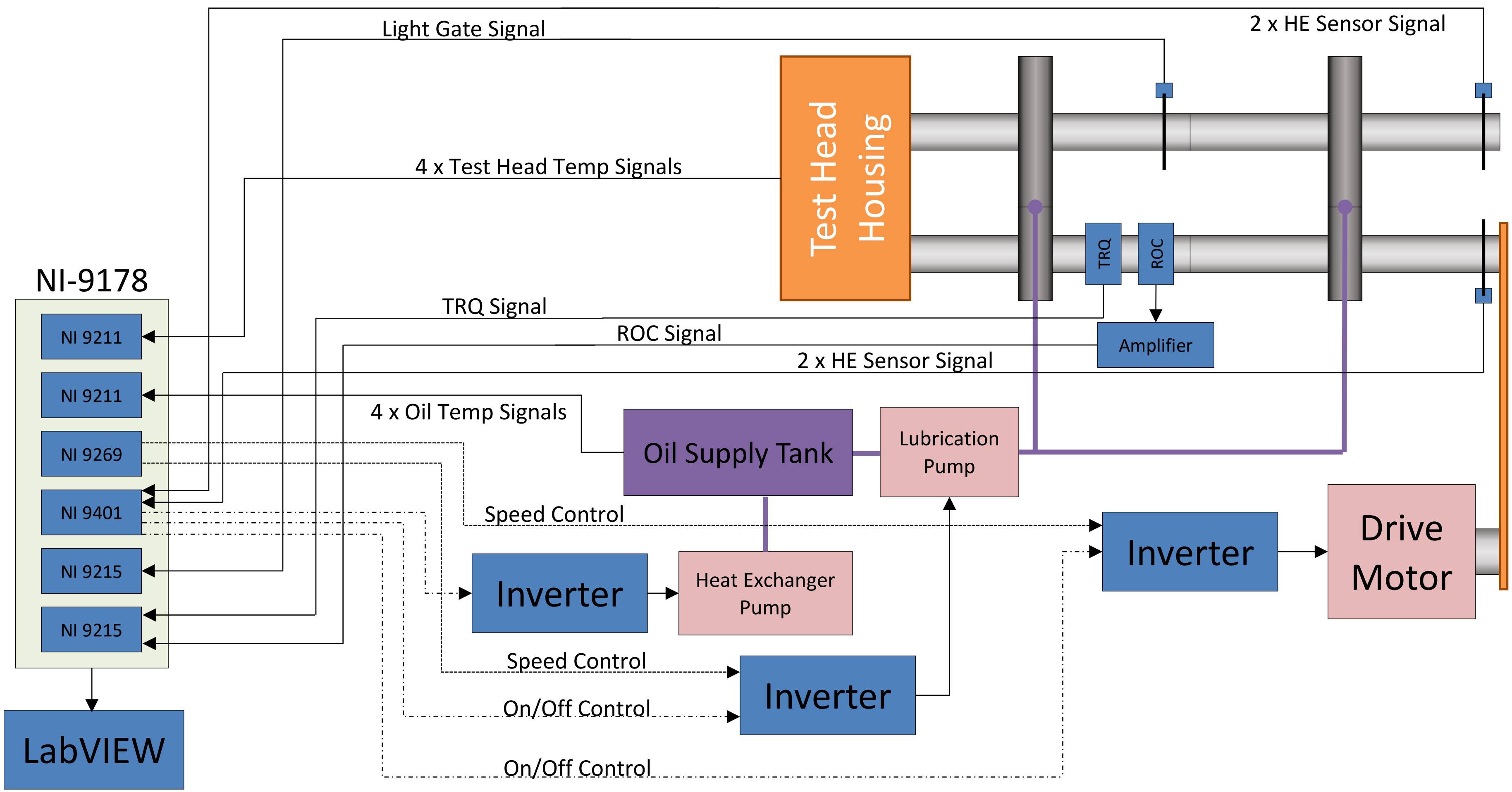

Figure 4-19 – Schematic of the test rig control and data acquisition system.

To allow for a human operator to interact with the rig, an interface was designed in LabVIEW 2014. This interface (Figure 4-20) was designed to allow control over all aspects of the test, as well as the acquisition and logging of data. The initial window provides the facilities required to set up the test i.e. test speeds, operating temperatures, logging destination and all necessary tolerances. It also displays the current torque in the system as read by the torque sensor, to allow the user to correctly load the rig.

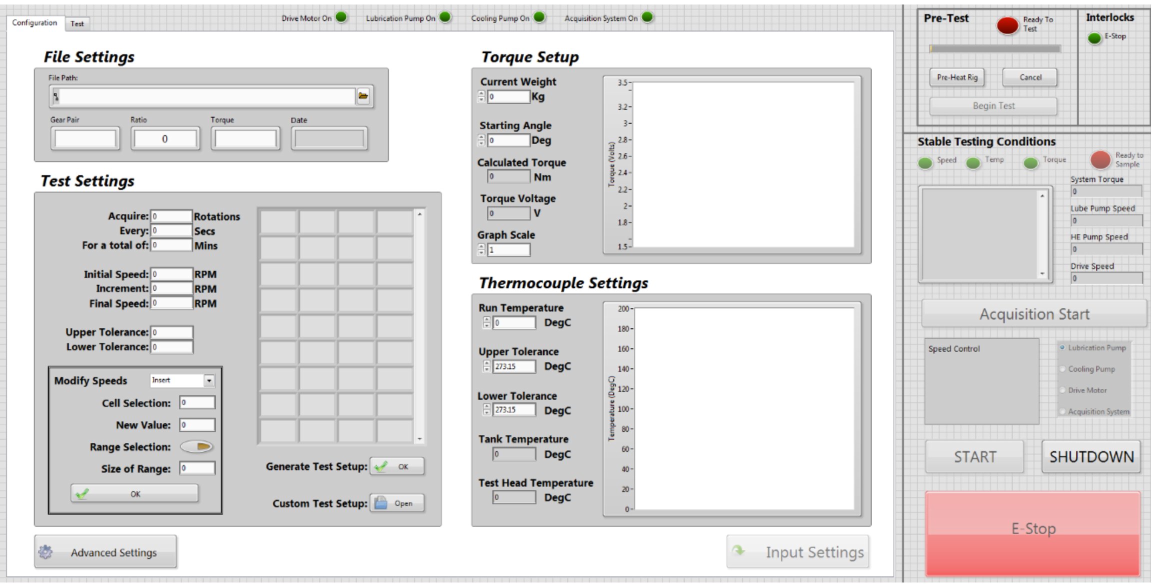

Figure 4-20 – LabVIEW setup panel.

This panel also allowed the user to begin the preheating process as well as accessing the settings menu. The settings menu (Figure 4-21) allowed the configuration of each individual type of input and output e.g. analogue, digital, and temperature to be set up. This configuration is comprised of several components all of which can be seen in Figure 4-21, these are namely the channel on which the input is connected, the sample rate, the maximum and minimum voltages and whether the user wants the system to use the channel or not.

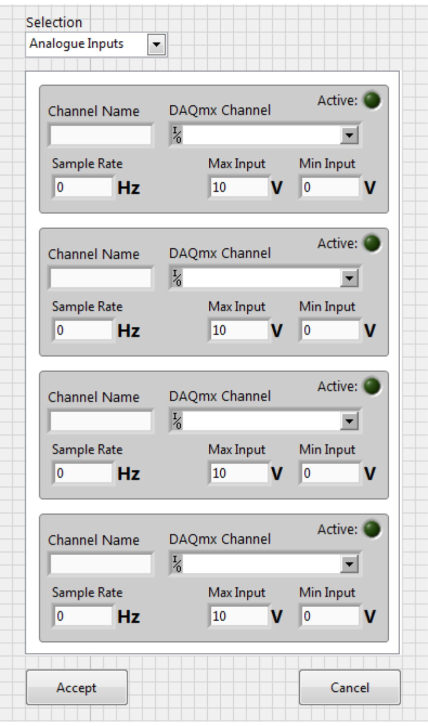
Selection: Analogue Inputs

Channel Name:
DAQmx Channel:
Sample Rate: 0 Hz
Max Input: 10 V
Min Input: 0 V

Channel Name:
DAQmx Channel:
Sample Rate: 0 Hz
Max Input: 10 V
Min Input: 0 V

Channel Name:
DAQmx Channel:
Sample Rate: 0 Hz
Max Input: 10 V
Min Input: 0 V

Channel Name:
DAQmx Channel:
Sample Rate: 0 Hz
Max Input: 10 V
Min Input: 0 V

Figure 4-21 – LabVIEW settings page.

The second window (Figure 4-22) unlocks following the end of the setup phase and the activation of the preheating stage. Initially only the thermocouples are actively displayed here, but upon entering the test phase this is where the test rig's speed can be observed in real time, as well as a preview of the ROC data upon acquisition.

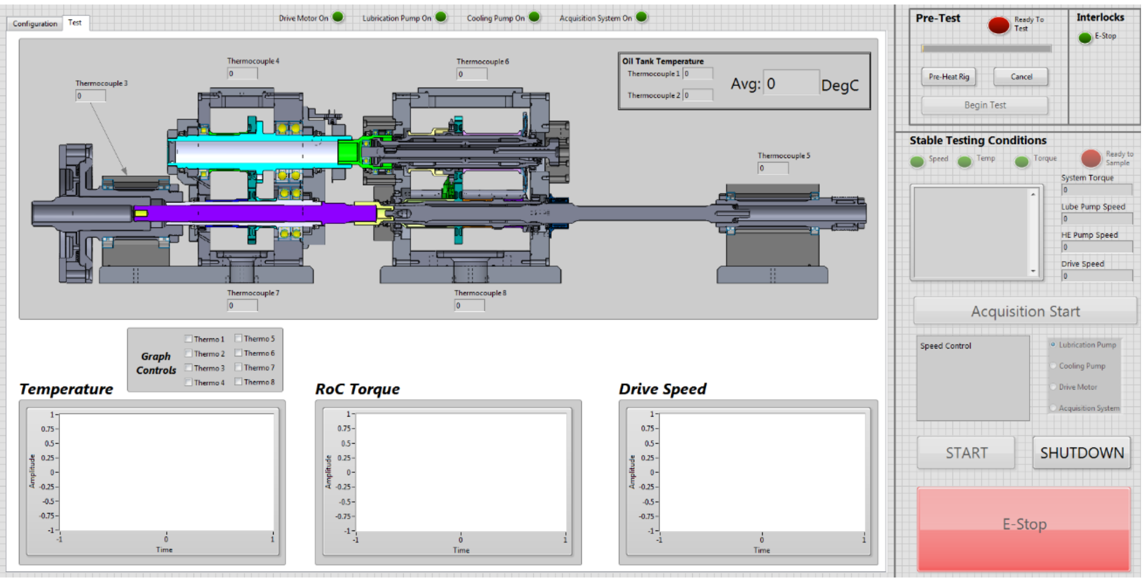
Thermocouple 3: 0
Thermocouple 4: 0
Thermocouple 6: 0
Oil Tank Temperature
Thermocouple 1: 0
Thermocouple 2: 0
Avg: 0 DegC
Thermocouple 5: 0
Thermocouple 7: 0
Thermocouple 8: 0
System Torque: 0
Lube Pump Speed: 0
HE Pump Speed: 0
Drive Speed: 0

Figure 4-22 – LabVIEW test panel.

At this stage, the user now gains control over the main drive as well as the acquisition system and may perform the test. To provide a slightly more detailed look at this process a flow chart of the major steps of the LabVIEW can be seen in Figure 4-23.

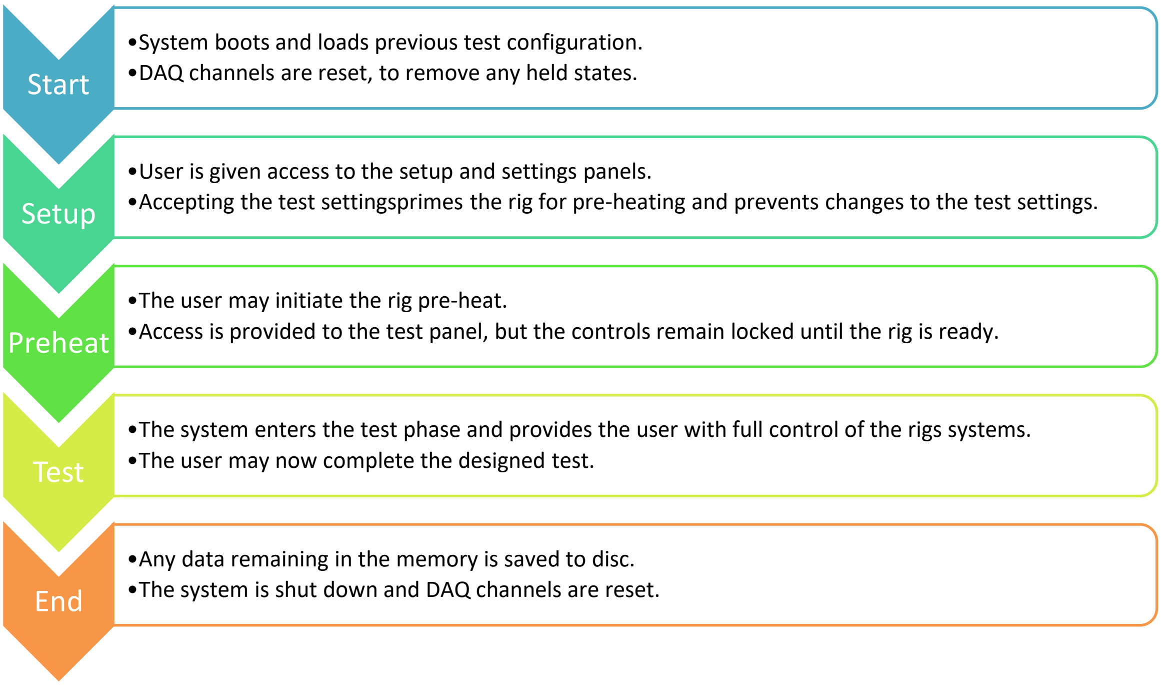

- System boots and loads previous test configuration.
- DAQ channels are reset, to remove any held states.

- User is given access to the setup and settings panels.
- Accepting the test settingsprimes the rig for pre-heating and prevents changes to the test settings.

- The user may initiate the rig pre-heat.
- Access is provided to the test panel, but the controls remain locked until the rig is ready.

- The system enters the test phase and provides the user with full control of the rigs systems.
- The user may now complete the designed test.

- Any data remaining in the memory is saved to disc.
- The system is shut down and DAQ channels are reset.

Figure 4-23 – LabVIEW test process flow chart.

The sample rates and length of each data acquisition are discussed later in Chapter 5 when the experimental procedure and test setup used for this thesis are described.

The LabVIEW code itself based on the queued message handler (QMH) architecture. This architecture is comprised of a series of both parallel and series loops, as demonstrated in Figure 4-24. Upon the user interacting with the UI, the user input generates a 'message' based on this input, which is subsequently passed on that is passed to the message handler loop. This loop reads the message and then decides on the course of action required. Depending on the content of the original message, the message handler loop will generate one or more of its own messages. These messages will contain the information required to allow the subsequent loops to respond appropriately to the users input.

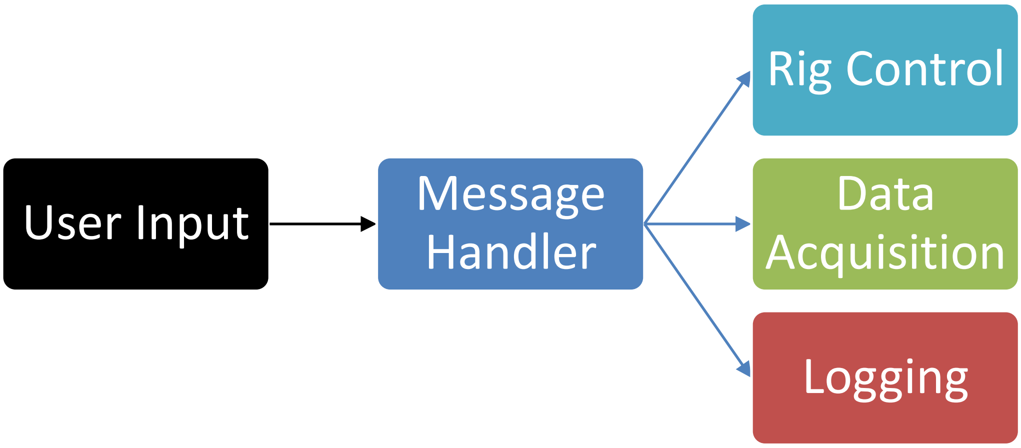

Figure 4-24 – LabVIEW code process flow chart.

To give an example: The user has finished preparing the rig for testing and is ready to acquire data.

1. The user clicks the Acquisition button.
2. The user input loop acknowledges this action and creates a message specifying that the user wishes to start the acquisition and passes it to the message handler loop.
3. Upon receiving the message, the message handler creates 2 messages.
    a. The first is sent to the acquisition loop, telling the loop it may proceed with acquiring data.
    b. The second is sent alongside the first to prepare the logging loop for the incoming data.
4. When all the data necessary has been acquired, the acquisition loop will send a message containing the data and start signal to the logging loop. It will then send a message back to the message handler to confirm it has completed its operation.
5. The logging loop receives the message from the acquisition loop and save the data to file. Upon completion of its task the logging loop will send a message back to the message handler, informing it so.
6. Only when both messages from the loops are received by the message handler will it then inform the user that this process is complete.

This approach allows different loops to operate in parallel while receiving a series of user inputs. As the message handler can only operate on one message at a time, the messages to it must be queued, this means that the order of the inputs is preserved and conflicts do not arise from the parallel loops trying to receive different inputs.

4.7 Test Rig Base and Enclosure

In order to construct the superstructure of the test rig, extruded aluminium section also known as “speed frame” was used. This provided a versatile method of building the test rig as well as the ability to easily mount attachments such as emergency stops and solenoid valves. The overall structure is rather simplistic and cuboidal in nature. The versatile nature of using speed frame allowed the structure to be customised to provide support where it was needed. This can be seen in Figure 4-25 where the support beams for the test head, the motor baseplate and the two shelves to support the pumps and oil tank can be seen.

Figure 4-25 – The Cardiff high speed test rig super structure and enclosure.

In order to isolate the test head from the environment for health and safety reasons, an enclosure was created out of smaller scale speed frame and perforated aluminium and polycarbonate panels, which can be seen in Figure 4-26. The perforated aluminium was used as a ceiling to allow air flow and heat to easily escape for cooling purposes. The enclosure is hinged directly to the superstructure, using hinges provided by the speed frame manufacture to integrate directly with the slots of both sizes. It is secured via a solenoid valve that is connected to the main drive motor electrical system so that when it is engaged during the preheat stage, the enclosure is locked and cannot be opened until the motor has come to a stop.

Secondary to this, there is an interlock that disconnects when the enclosure is open to prevent the rig from being started, this also acts as an emergency stop in the case that the solenoid is bypassed. Other safety features on the rig include an interlock between the drive motor and lubrication pump to prevent the lubrication system being turned off during operation and so the lubrication does not stop until the motor has come to a complete stop. As well as a number of e-stops, located at either end of the rig as seen in Figure 4-26 as well as another next to the PC so that one is always close at hand, no matter the stage of testing.

Figure 4-26 – The Cardiff high speed test rig fully assembled with the enclosure closed.

4.8 Typical Test Sequence

As with the previous test rig, the test sequence for the high speed rig can be broken down into 3 phases: setup, pre-test and testing.

The setup phase begins with the need to decide which gear ratio is to be tested. Unlike the slow-speed rig that was locked at a 3:2 ratio, the new rig can run any ratio so long as the centre distance is not altered and the same ratio is installed in both test and slave housings. For the purpose of this chapter the details on gear installation are not included, although the author developed all the tooling necessary to disassemble the test and slave housings in order to change gears. Once the gears are installed the desired static torque can be locked in. Torque is applied manually through the use of the torque head. Motion in the rig can be locked via the hexagonal shaft end on the upper shaft of the rear assembly as seen in Figure 4-27.

With motion restricted, the guard and the splined disc that locks in the torque can be removed. The loading arm can be attached and making use of the torque sensor, the correct torque can be implemented by loading the carrier attached to the arm. Once the correct load is reached, the outer ring must be rotated as far as possible anti-clockwise to confirm that the gear cannot rotate and release the new torque. The torque head can then be reassembled, and the restraint removed. The test parameters are then input into the labVIEW control system and the pre-test phase begins.

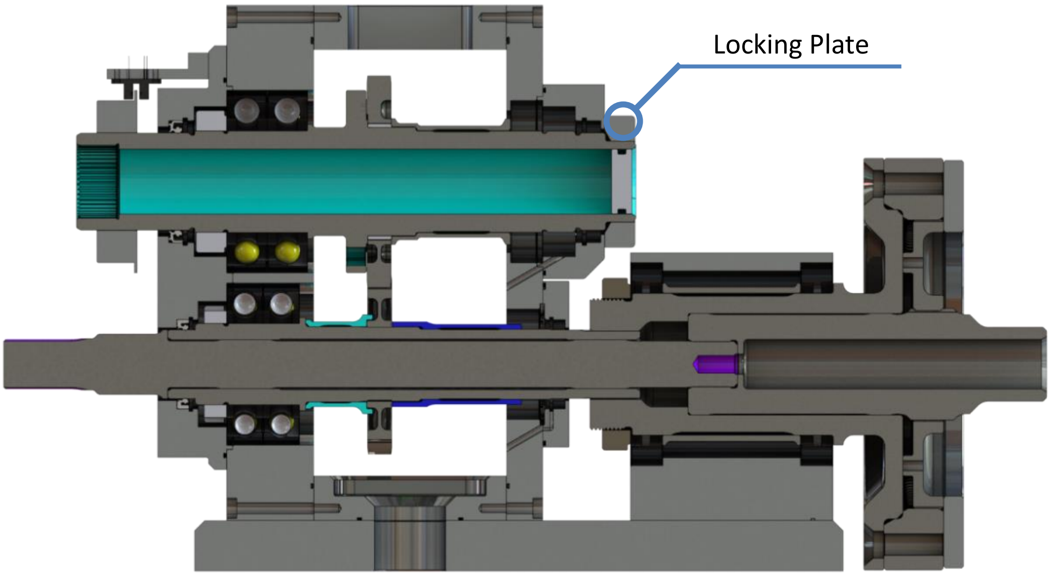

Figure 4-27 - Rear assembly section.

During this phase the rig can be pre-heated, by activating the lubrication pump and tank heater. Due to the size of the oil tank, this is a lengthy process, but the rig requires checks periodically to confirm that the reduction in oil viscosity does not reveal any leaks and that oil is flowing properly from all inlets. Upon reaching the test temperature, the control system can switch into test mode, thus signifying entering the test phase. The main drive can now be switched on and the first test speed selected, at which point the test rig will proceed to ramp up until it is within the set tolerance range of the selected speed. The acquisition system can then be activated, and the first set of data can be captured. Upon completion of the acquisition, this process is repeated until data for all the specified speed steps have been acquired and logged. Once the rig has cooled, the torque or gear pair/ratio can be changed, and the procedure repeated to acquire ROC data at a range of torques, speeds, loads and damage levels.

The next chapter describes the use of this rig to acquire such ROC data, in a much more realistic environment than previously possible with the much simpler rig used previously.

CHAPTER 5

Analysis of the Novel In-Loop Rate of Change of Torque Data

This chapter presents the experimental design used to acquire the data required for this work, using the bespoke test rig described in the previous chapter. The subsequent analysis is then covered, looking at a range of statistical and frequency-based methods to detect and characterise the damage present within the signals.

5.1 Experimental Plan

The experimental design was based on both the abilities of the test rig and the available test specimens. The sponsor provided a total of 13 test gears, these gears formerly used for dynamometer testing but are manufactured to the same quality as race gears. The specification is as such: 12mm face width, 3.6mm nominal module, 25° pressure angle and manufactured to class 5 tolerances as per DIN 3962. The gears are ground and superfinished to achieve a surface finish with a targeted Ra of 0.05, although typically 0.07-0.09 Ra is achieved. After manufacture the gears are measured via the use of Klingelnberg gear measurement machine and the profile, lead and tooth spacing are examined to confirm they are to specification. An example of these measurements can be seen in Figure 5-1.

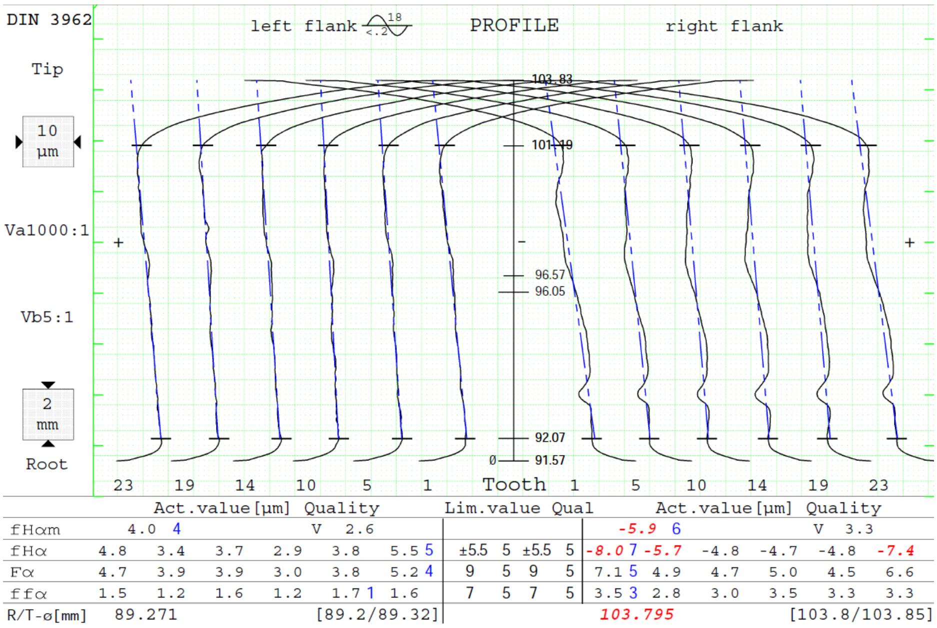

	Act.value [µm]	Quality					Lim.value	Qual			Act.value [µm]	Quality				
fHαm	4.0 4				V 2.6						-5.9 6				V 3.3	
fHα	4.8	3.4	3.7	2.9	3.8	5.5 5	±5.5	5	±5.5	5	-8.0 7	-5.7	-4.8	-4.7	-4.8	-7.4
Fα	4.7	3.9	3.9	3.0	3.8	5.2 4	9	5	9	5	7.1 5	4.9	4.7	5.0	4.5	6.6
ffα	1.5	1.2	1.6	1.2	1.7 1	1.6	7	5	7	5	3.5 3	2.8	3.0	3.5	3.3	3.3
R/T-ø[mm]	89.271				[89.2/89.32]						103.795				[103.8/103.85]	

Figure 5-1 – Profile measurements for a 27 tooth main shaft gear in a healthy condition.

This aligns with the 2015 car specification based upon a specification devised by the author. This specification expanded upon what had been previously available for the slow speed test rig, discussed in Chapter 3, by increasing the number of damage steps and involving more than one ratio. The resulting gears provided by the sponsor can be seen in Table 5-1:

Table 5-1 – Available test gears with damage levels.

Ratio	Designation	Damage Level / *µm*
2nd Gear - 35/13	*L30265*	Healthy
	L30744	1.5
	L30667	6.7
	L30665	8.9
	L30662	12
	L30659	17.1
	L30663	28.9
7th Gear - 27/23	*L30479*	Healthy
	L30496	2.4
	L30826	8.7
	L30473	14.7
	L30475	18.8
	L30482	29.7

Due to the methods and difficulties involved with artificially inducing plastic deformation in gear teeth, the results are rarely exact. Whilst this has no bearing on the testing itself, it does mean that the offset between damage levels is not as well defined, potentially having implications for the characterisation later on.

From the gears provided by the sponsor, only 9 were selected for testing (as highlighted in green in Table 5-1). The reasons for removing 4 gears from the experimental design were based on necessity as well as for health and safety reasons. Previous experience with the slow speed test rig has shown that a 16 micron tooth bend was easily detectable even when only measuring parasitic loses, as described in Chapter 3. This would imply that an in-loop measurement would provide an even clearer indication of the presence of damage, given that from private communications a 16 micron tooth bend is considered by the sponsor to be unacceptably large. Any tooth bend larger than this would have no bearing on the investigation as these gears would be removed from a gearbox before they were capable of reaching such a degree of deformation. Concerns were also raised regarding the sensibility of testing near 30 micron bends, as there is a possibility that the dynamic overloads caused by defects of such magnitude could lead to further damage in both specimens and test rig as well as previous experience dictating that gear whine from such a defect would require a very high-degree of ear protection.

Having selected the gears to be tested, the maximum speed and torque were decided by preliminary run-in tests of the test rig, whilst speed and torque increments were selected based upon the level of detail they would provide but without producing an experimental plan that would be needlessly cumbersome. This resulted in the ranges of speeds and loads seen below in Table 5-2:

Table 5-2 – Tables indicating the range of speeds and torques used as test parameters.

Speed / RPM	1500	3000	4500	6000	7500	9000	10500	12000	13500	15000

Torque / Nm	0	50	100	150	200	250	300

It should be noted that the reason for the reduction of torque from the original design specification of 600 Nm to 300 Nm, was due to the discovery in the preliminary tests that the motor did not possess the torque required to overcome the inertia within the system at loads above 300 Nm.

The nature of the tests to be performed would initially be identical to the original tests performed on the slow speed rig i.e. a single gear pair tested at all speed and torque combinations. With the content of the signal unknown on the new rig, this was deemed to be a safe starting point as it allows direct comparison to the data measuring the parasitic losses.

To begin, the 7th gear ratio would be tested as the damage levels available possessed the most similarity to those previously tested. Following this the 2nd gear ratio would be tested to allow for a comparison of the effect of tooth count on the signal. Finally, the last gear to be tested would be subjected to additional idle pair tests. These tests would be identical in parameters to the singular pairs but would feature increasing numbers of idle gear pairs present in the test head i.e. 2, 4, & 8. This provides the opportunity to measure the influence of the idle gears on the ROC signal as well as measure the effect of any background noise they may introduce. For clarity the experimental design can be seen below in Table 5-3.

Table 5-3 – Experimental Design

	Gear	**Damage Level / *µm***	**Order of tests (→) and the number of gear pairs present.**											
7th Ratio	*L30479*	Healthy	1											
	L30496	2.4		1										
	L30826	8.7			1									
	L30473	14.7				1								
2nd Ratio	*L30265*	Healthy					1							
	L30744	1.5						1						
	L30667	6.7							1					
	L30665	8.9								1				
	L30662	12									1	2	4	8

The acquisition rate for these experiments was set at 100 kHz, the maximum possible with the current DAQ module. To prevent an overabundance of data that could lead to long processing times, the acquisition system was set to capture two bursts, of 50 rotations each, at every speed and torque level. These settings made sure that enough data was available for a solid analysis as well as making sure conditions remained stable across the duration of the test.

Due to unforeseen complications, this plan had to be modified to represent what was realistically possible in the time remaining. These unfortunate circumstances radically reduced the amount of viable testing as use of the 2nd ratio and multiple gear pairs was no longer possible. Highlighted in green in Table 5-3 are the remaining options that were available for testing. The reasons for this reduction in testing are as follows:

1. A bearing failure meant that while a replacement bearing was acquired the rig was inactive reducing the time remaining in which testing would be possible.
2. A design oversight that prevent 2nd gear from being installed in the slave housing.
3. The supply of 2015 gears and hubs, as the rig was designed with the 2014 gearbox in mind, the hubs received caused misalignment when installed on the 2014 shafts and could not fit within the length of the 2014 gearbox.

Though significantly reduced in scope, the testing still allowed for the project goals to be achieved although a greater amount of future work would now be required to establish the full capacity of the technology. In order to compensate for some of the lost tests, the available tests were also repeated with accelerometers mounted on the test rig to provide a comparison to an established technique. This data was processed separately and can be found in the proceeding chapter, while the focus of this chapter is on the capacity of ROC technology.

5.2 Results and Analysis

5.2.1 Raw Signal

A set of typical waveforms for a single rotation of each of the tested specimens is shown in Figure 5-2. The waveforms were deconstructed into individual rotations using the HE sensors, the reliability of the motor meant that variation in signal length for each rotation never varied more than 6 samples. The waveforms differ heavily from those previously present in Chapter 3, presenting more periodic features and no clear indication of a carrier wave, although this not true for all waveforms as is discussed later. The periodicity of the signals is best represented by the 2.4 micron damage waveform, where 54 distinct peaks are clearly identifiable. This is exactly double the number of teeth present on the main shaft gear, leading the author to believe that the twin peak phenomena may be related to timing differences in the meshing cycle between the test and slave housing generated by the torsional deflection in the shaft.

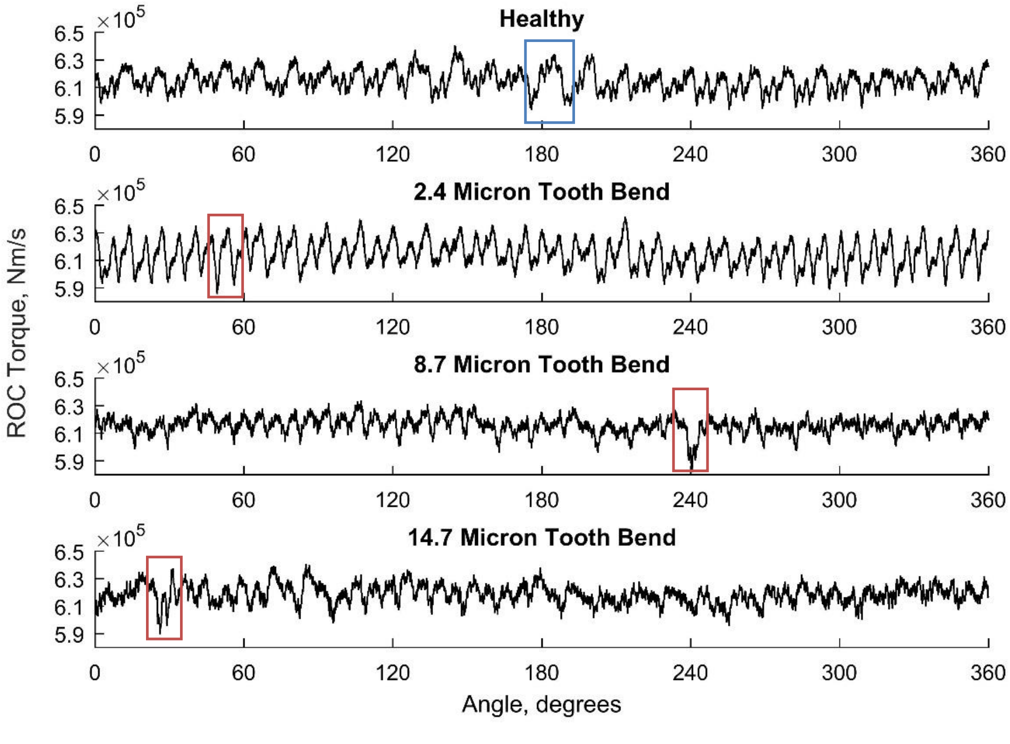

Figure 5-2 – Comparison of the raw signals at 100 Nm torque and 3000 RPM, with red highlights indicating the damage transient and the blue highlight showing an area of relative similarity to the smallest damage.

This is just a hypothesis as the while other waveforms do exhibit similar fluctuations, it is never as clear as the 2.4 micron damage. Fortunately, this had little effect on the visibility of damage, which is seen in all three damage-related waveforms as indicated by the red squares. The 2.4 micron damage is currently the smallest amount of damage detected using ROC technology although visually identifying the transient in the waveform is difficult without prior experience and further confirmation methods. Without these, the damage would likely be overlooked as the damage is reminiscent of characteristics found within the healthy waveform at 180°, highlighted in blue. This is to be expected however as the tooth bends of this magnitude would cause little to no effect and are similar in magnitude to the form and spacing error tolerances for these gears during manufacture. This can be seen in comparison to the higher damage levels, where a clear transient is present at the position of the damaged tooth within the rotation.

As demonstrated in Figure 5-3, a single rotation of the parasitic loss data differs greatly from the in-loop data. Most notably, it is impossible to clearly identify individual teeth in any of the parasitic loss data, other than the damaged tooth. This is likely due to the high efficiency associated with spur gears (at least 99%), as the parasitic losses are generated from frictional contact. The low friction coefficient of a well lubricated gear pair means that minimal losses occur and that the individual tooth signature is not great enough to be observed. The damage is observable however as the changes made to the meshing cycle due to late engagement cause a decline in this efficiency and an increase in the losses. This means that the transient caused by the damage can be seen to have a peak-to-peak amplitude far greater than the average for the waveform. This is quite different to the in-loop data which while the damage is indicated (at the upper levels) by a large amplitude transient, due to the significantly higher amplitude signals caused by the normal meshing cycle it does not standout as clearly as that seen in Figure 5-3.

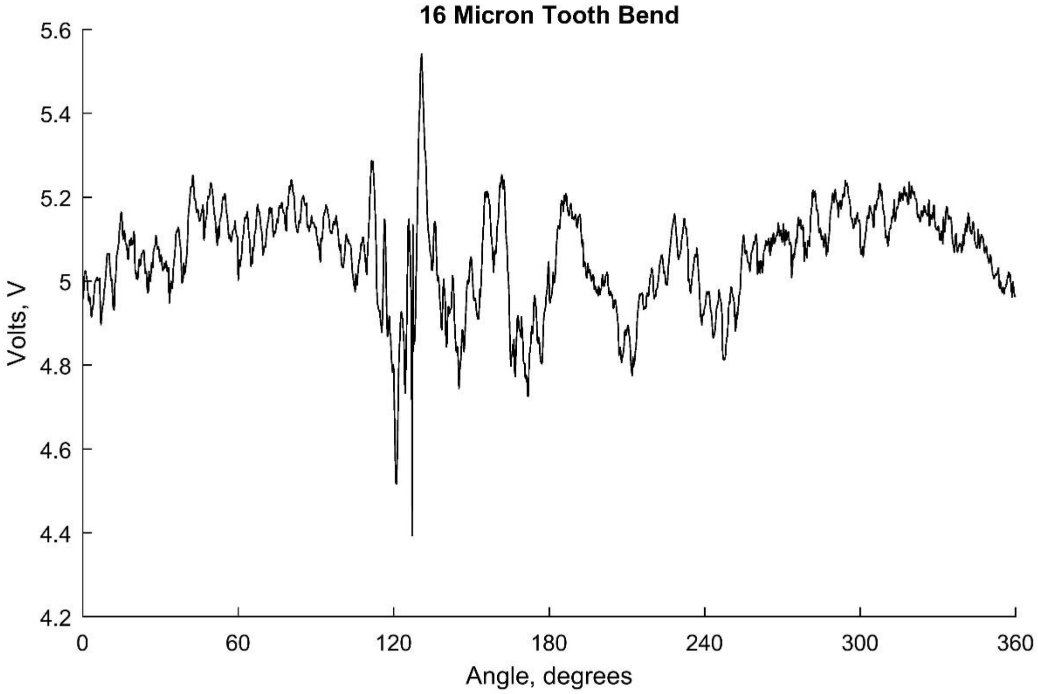

Figure 5-3 – Example of parasitic loss data collected at 100 Nm torque and 3000 RPM.

Looking at the frequency spectra of the data shown in Figure 5-4, these are predominately made up of the meshing frequency and the first 11 harmonics. This was predicted, as seen in Chapter 3 where the FFTs of the parasitic loss data were also comprised of meshing harmonics, although the amplitude of these harmonics rarely exceeds 0.02 V^2 and a lot more background noise was present. In contrast the clarity and number of harmonics present in Figure 5-4 shows that in-loop data provides a more accurate picture of what is present within the torque loop.

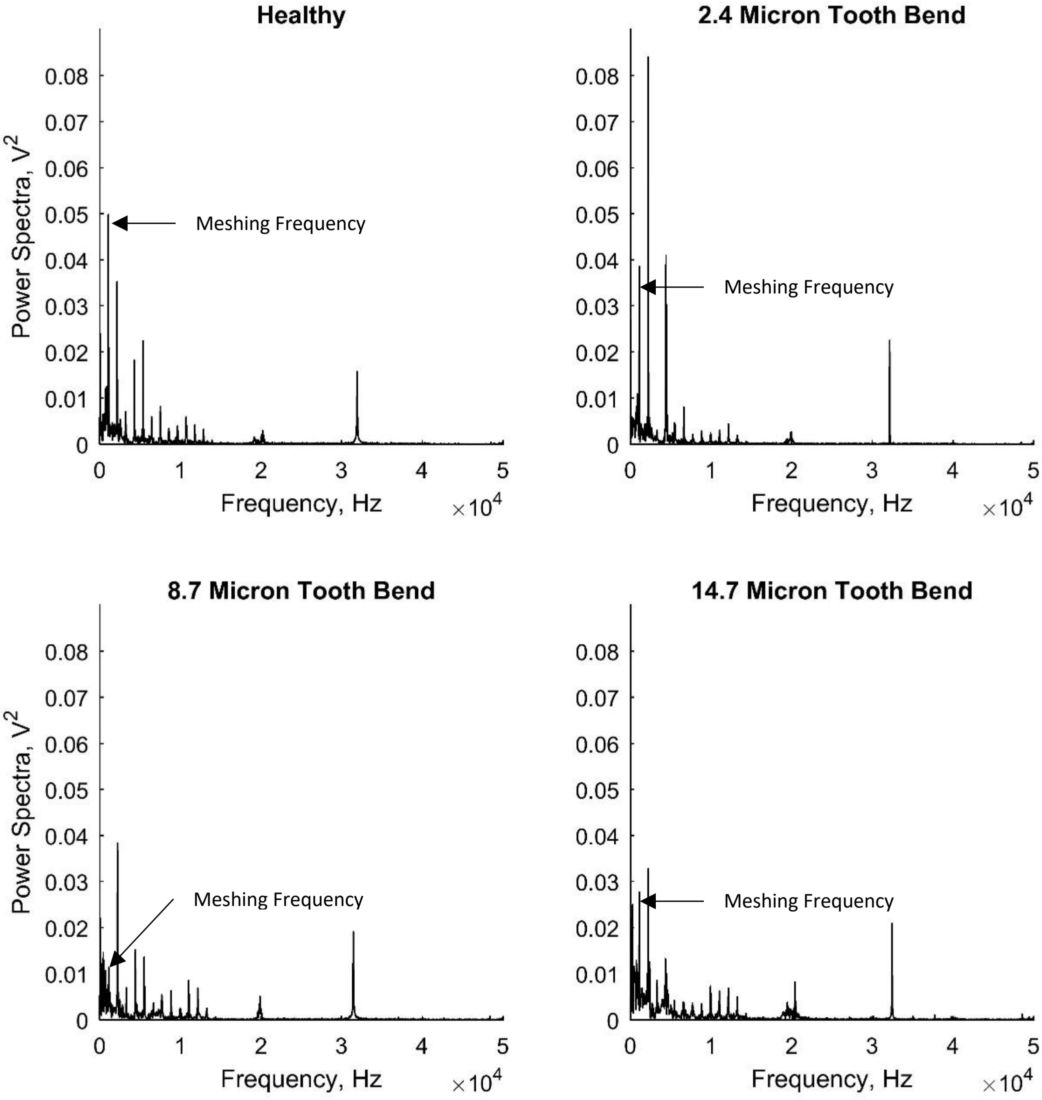

Figure 5-4 – Comparison of frequency spectra for healthy and damaged specimens at 100Nm torque and 3000 RPM.

While the amount of noise in Figure 5-4 is largely minimal, two regions of high amplitude noise are present within all waveforms captured from the new rig. The first is present at approximately 20 kHz and is of similar amplitude to the latter meshing harmonics i.e. the 8th and beyond. The second region is present at approximately 32 kHz and is consistently of an approximate amplitude of 0.02 V^2. While the sources of this noise have at this time not been able to be confirmed, use of a low pass filter set with a passband of 15 kHz and stopband of 15.5 kHz provides a much cleaner overall signal with significantly less noise as shown in Figure 5-5.

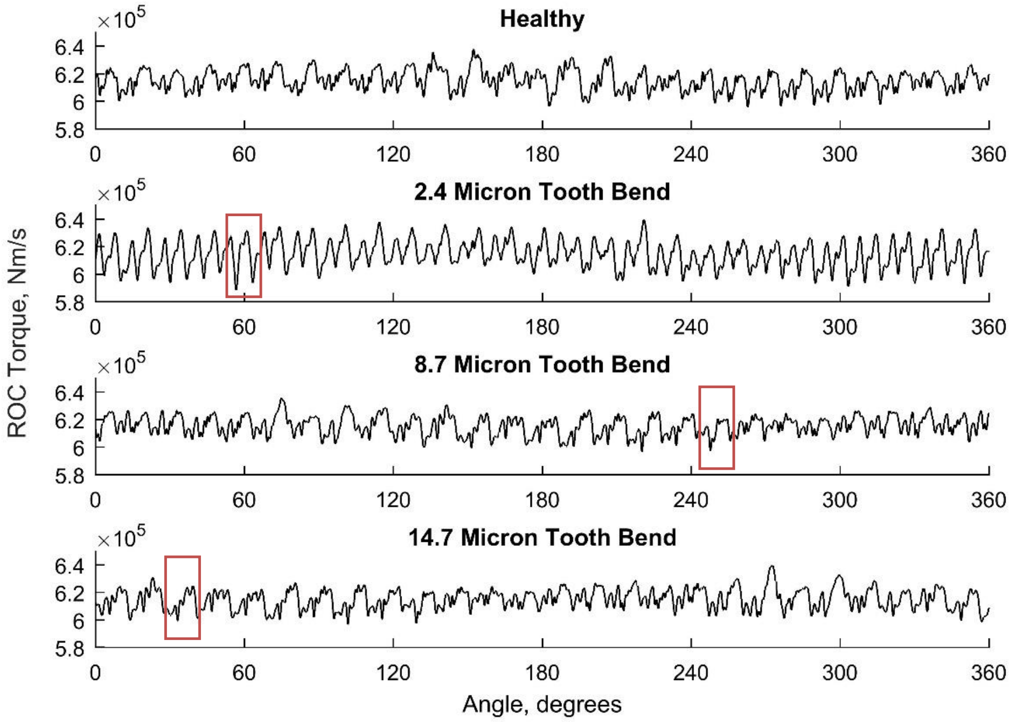

Figure 5-5 –Comparison of the low pass filtered signals at 100 Nm torque and 3000 RPM.

Although clarity is greatly improved with each tooth interaction now visible in every waveform, the damage in the 8.7 and 14.7 micron is not. Whilst amplitude modulation was present in Figure 5-2, the amount was minimal, however the filter appears to have exasperated this effect, which has likely contributed to a noticeable decline in the presence of the damage. It may also be that frequencies associated with tooth dynamics as the damaged tooth passes through the mesh are of similar order to the frequencies being filtered.

Examining the sub 15 kHz spectrum, shown in Figure 5-6, it can be seen that there is very little noise. Most of the noise that is present is low level and exists within the first 5000 Hz. The highest amplitude region exists between the upper shaft rotational frequency and the meshing frequency. The major peaks within this region were found to be harmonics of the rotational frequency ranging from as low as the 5th harmonic up to the 21st harmonic. It is notable however that the spectra for the distinct damage levels contain different harmonics, this is possibly due to how the size of the damage changes how the gears mesh once per revolution, however this is just conjecture. One trend of note is that of the meshing frequency and its first harmonic. As seen in Figure 5-6, when damage is present the first harmonic is always of greater amplitude than the meshing frequency itself. Although the difference in amplitudes is not consistent enough for characterisation this trend does appear to be a simple and effective method of confirming damage in ROC signals.

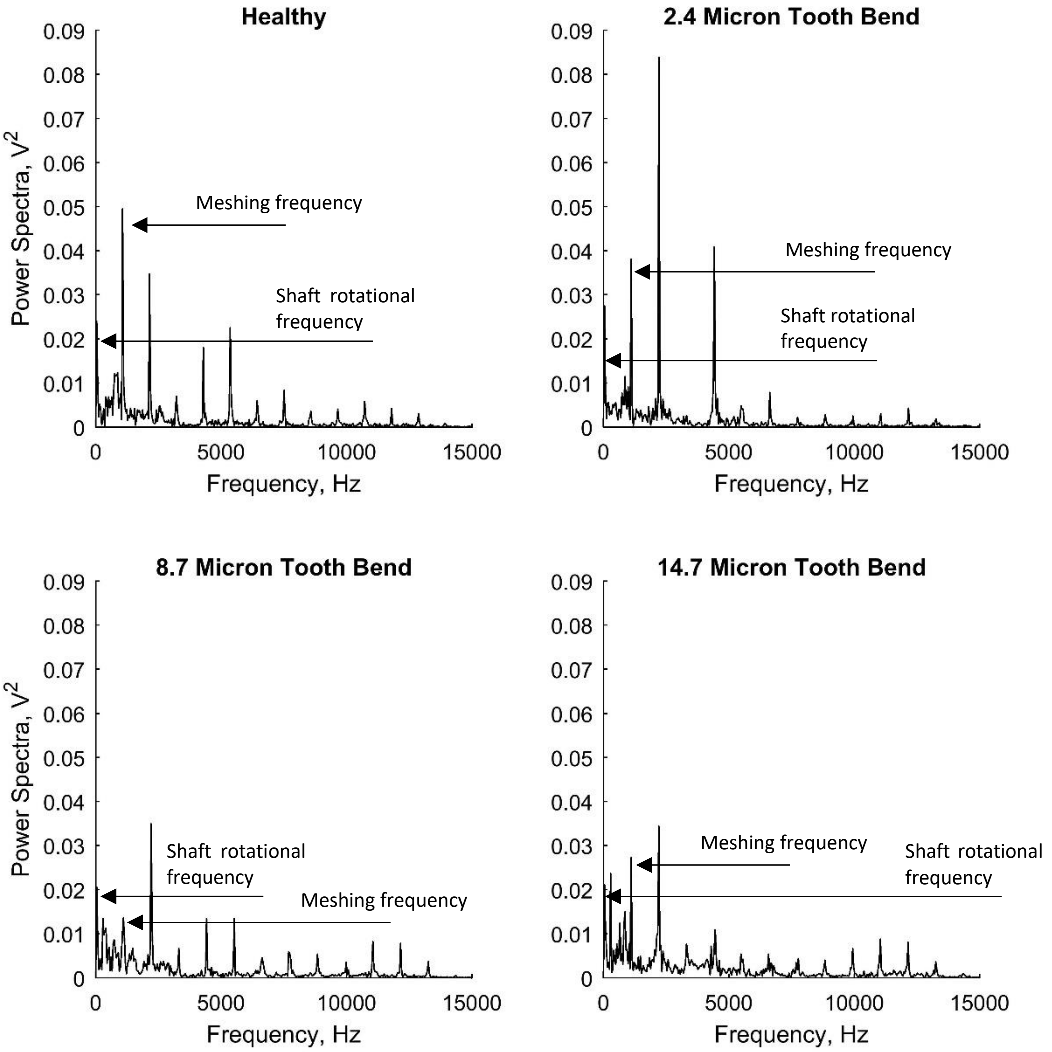

Figure 5-6 – Comparison of the first 15 kHz of Figure 5-4 i.e. all damage levels at 100 Nm torque and 3000 RPM.

5.2.2 Time Synchronous Averaging

Due to the amplitude modulation and loss of information caused by the use of the low pass filter, a different method of averaging was required to improve the signal clarity. To this end, time synchronous averaging (TSA) was performed. By using a once per revolution pulse the time signal was deconstructed into a set of rotations, and these rotations were then averaged removing any non-stationary information.

Examples of the effectiveness of this method can be seen in Figure 5-7, where a significant boost to clarity is visible. Figure 5-7 demonstrates that not only is the high frequency noise eliminated from the time series, but there are no signs of amplitude modulation or damage transient reduction as observed in Figure 5-5.

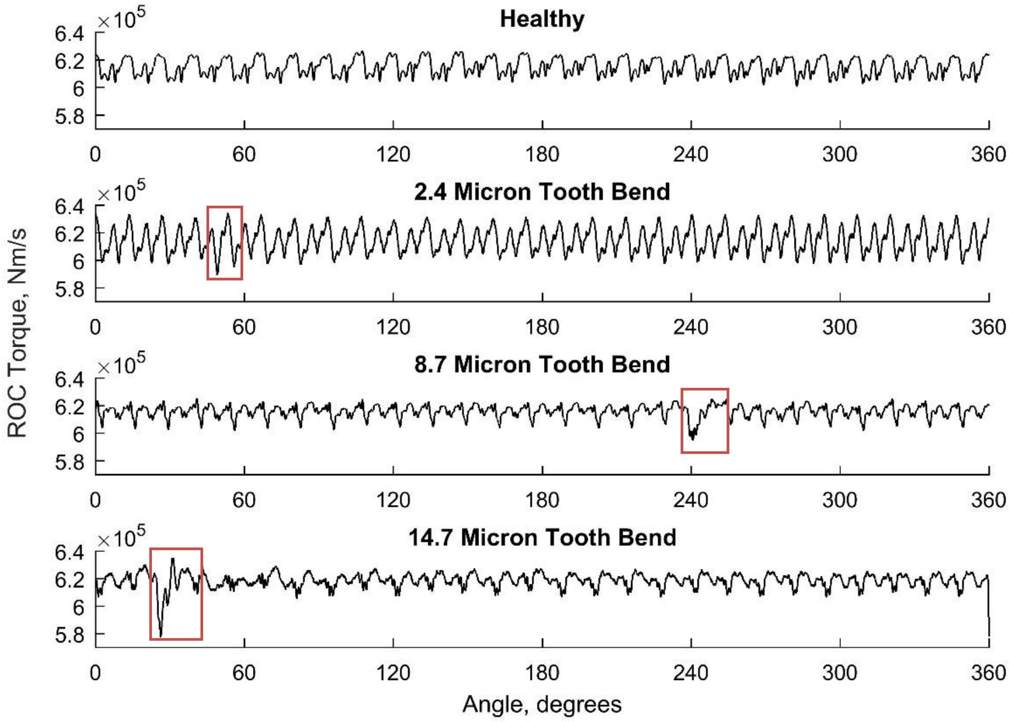

Figure 5-7 – TSA Comparison at 100 Nm Torque and 3000 RPM.

Importantly, TSA provides an unparalleled image as to the torque fluctuations occurring within the meshing cycle of the Cardiff test rig, with each time series now containing 27 distinct and repeating waveforms that represent the meshing of each tooth of the test gear.

The shape of these waveforms are quite distinct and can be loosely compared to a deformed ‘M’. The nature for this shape was initially thought to be caused by the change points in the meshing cycle, however this was quickly refuted however as the nature of the meshing cycle could not result in the twin peaks format seen here. Analysis of an integrated ROC signal i.e. a torque signal showed that this pattern is caused by the meshing cycles of the two gear housings being out of phase. As Figure 5-8 shows, whilst the major peaks in the ROC signal are much closer to parity, the torque signal shows a much greater difference. This is attributed to the distance along the torque path from the sensor to the gear pairs, causing a reduction in amplitude. The test housing gear pair is located directly along the torque path to the ROC sensor, however the slave pair located in the rear housing has a less direct path as it must pass through the torque head first. This longer path means, more components and in effect more torsional springs reducing the amplitude of what is seen at the sensor. From this, it can be assumed that the difference in shapes of the ROC signals is due to different amount of phase shift between the two housings, with the lesser peak being associated with the meshing cycle of the rear housing.

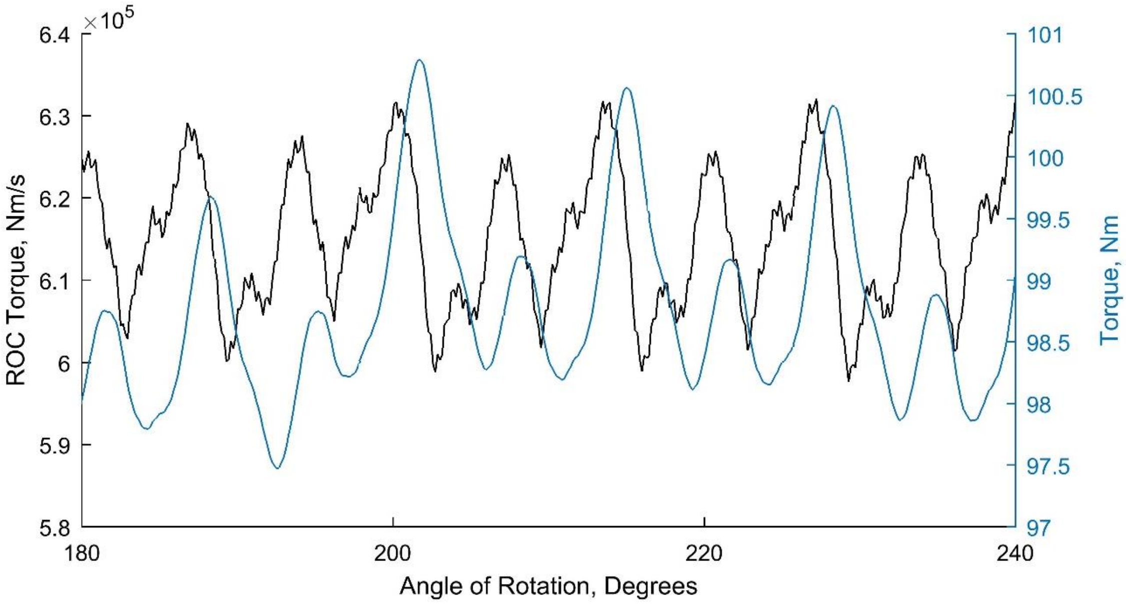

Figure 5-8 – Comparison of torque and ROC signals for 2.4 Micron Tooth Bend at 3000 RPM and 100 Nm.

Looking at the spectra of the TSA waveforms in Figure 5-9, a reduction in both low and high-end noise is evident. While the high-end noise has been reduced however, with the 20 kHz area nearly entirely eliminated, the 32 kHz noise is still present. Despite a reduction in amplitude from its previous 0.02 V^2, the noise is still clearly present. The consistent amplitude and frequency previously observed have thus far suggested that this noise is not stationary, and it was expected that the use of TSA would eliminate it entirely. Although it can be argued that TSA has eliminated any non-stationary components: the static frequency range and the changing amplitude regardless of speed, torque or the size of damage would suggest that this is not the case. The reasons for this are likely related to the slight changes in speed present due to the inverter control being unable to hold a perfectly constant speed. This change would cause frequency shifts, meaning that while most non-stationary noise is eliminated smaller elements may persist through the TSA, resulting in the present but much reduced noise.

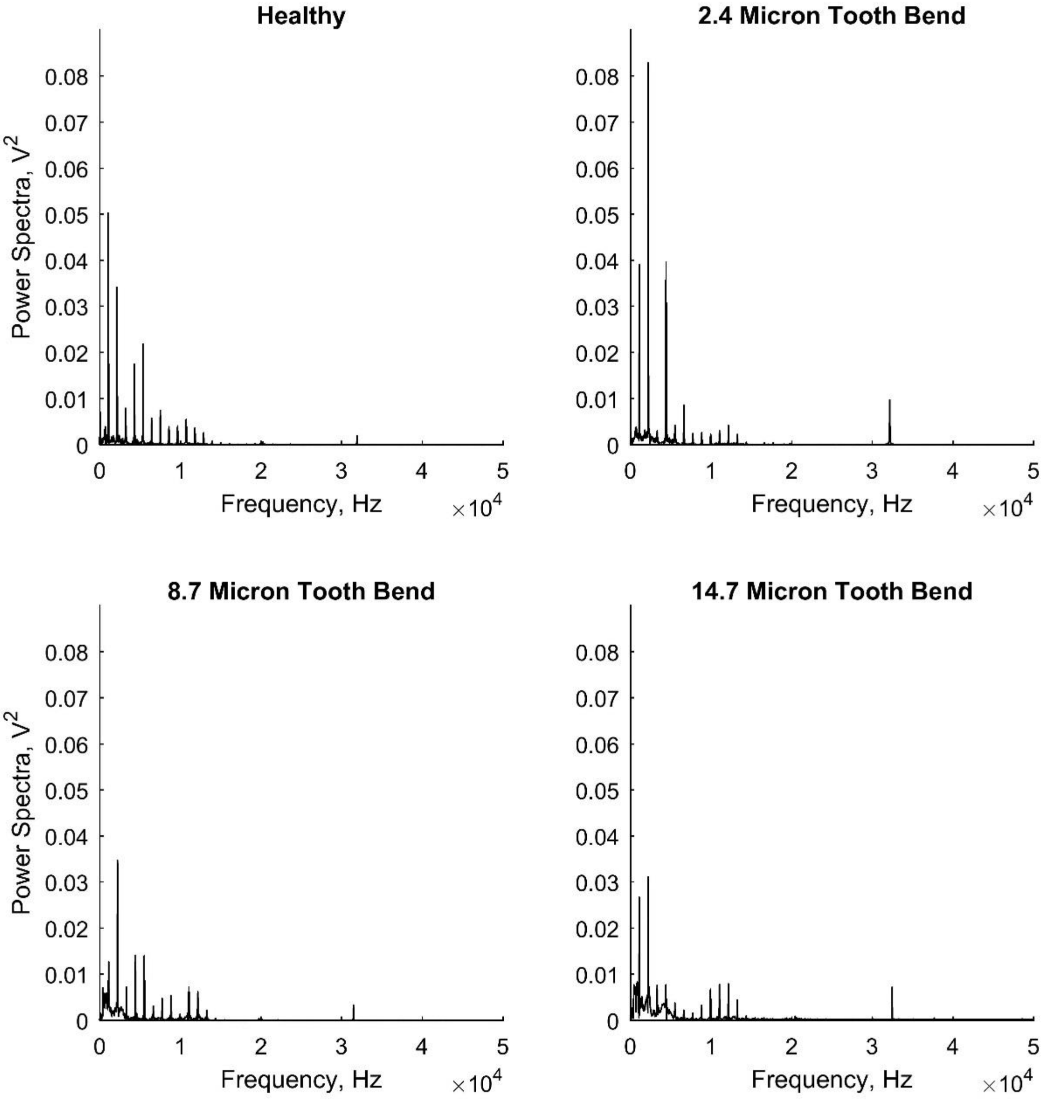

Figure 5-9 – Comparison of frequency spectra for healthy and damaged specimens at 150 Nm torque and 7500 RPM.

Moving away from the high-end of the spectrum, Figure 5-10 provides more detail of the first 15 kHz of the spectrum. It is clear from this figure that the low end of the spectrum is nearly entirely dominated by the meshing frequency and its harmonics. Whilst the shaft rotational frequency and its harmonics are still present there has been a noticeable reduction in their amplitude. This amplitude is not fixed however as with that of the background noise it can be seen to grow proportionally with the damage. The increase in noise is most likely related to frequency shifts caused by speed changes due to the alterations to the meshing cycle, preventing the TSA from eliminating them. The increase in the shaft rotational frequency and its harmonics is presumably caused by the once per revolution interaction of the damaged tooth. A feature of note is that the amplitude of the rotational frequency itself decreases while that of its harmonics increases as the damage progresses. Whilst a similar feature has been observed in the meshing harmonics, with the rotational harmonics there does not appear to be a trend in which harmonics are accentuated by the increase in damage with the first prominent harmonic varying from test to test.

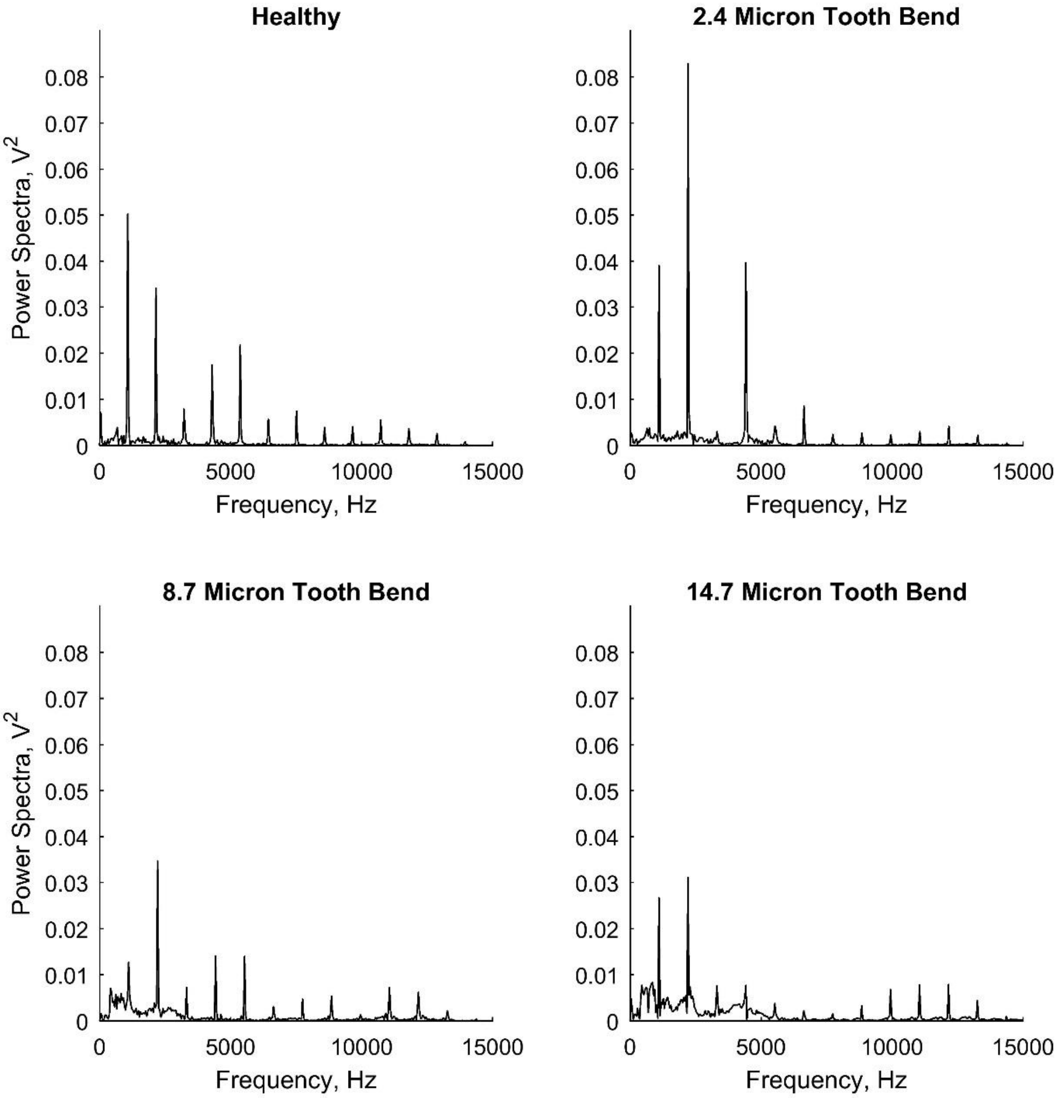

Figure 5-10 – Enhanced look at the first 15 kHz of Figure 5-9, i.e. all damage specimens at 150 Nm torque and 7500 RPM.

This is shown in Figure 5-11 where the amplitude of the shaft frequency can be seen to be declining, while the amplitude of the first dominant harmonic is seen increasing. At first it appears that the first prominent harmonic is decreasing in number i.e. from the 17th to 16th harmonic, however comparison with other tests shows that this is not consistent. As which harmonics react to the damage changes with speed and torque, with no regularity or consistency as well as which the amplitude of these harmonics does not necessarily follow the trend shown in Figure 5-11.

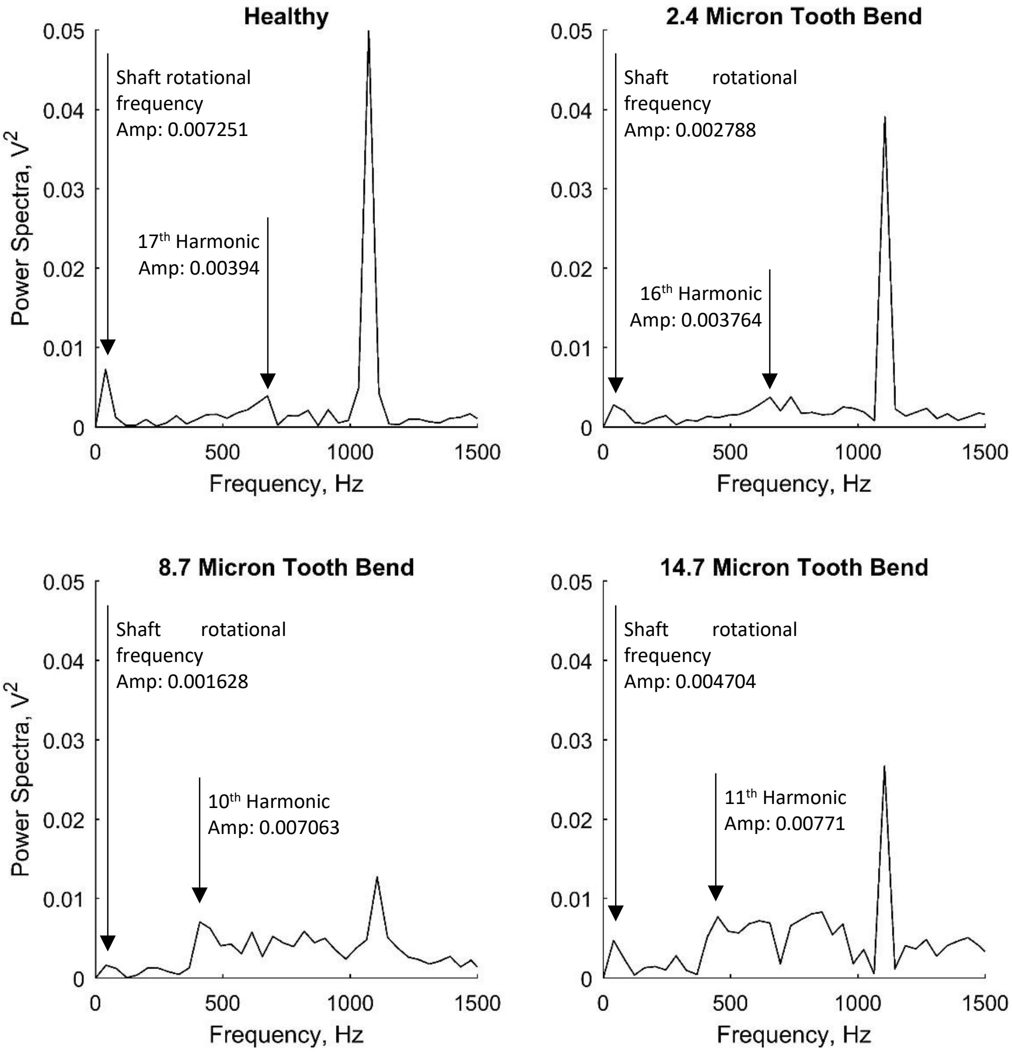

Figure 5-11 – Comparison of the first 1500 Hz of Figure 5-9 i.e. all damage specimens at 150 Nm torque and 7500 RPM.

It has previously been proposed that torque and speed have an effect on the signal clarity and the damage. To quantify this, comparison of TSA waveforms at different torques and the same speed and different speeds and the same torque were made. As presented in Figure 5-12, an obvious correlation between the amount of torque in the system and the peak-to-peak amplitude of the waveform can be seen. Despite the noticeable increase in amplitude across the figure, the damage appears to not suffer from any mal-effects due to the torque and is clearly visible at 240° in all the waveforms, bar 0 Nm.

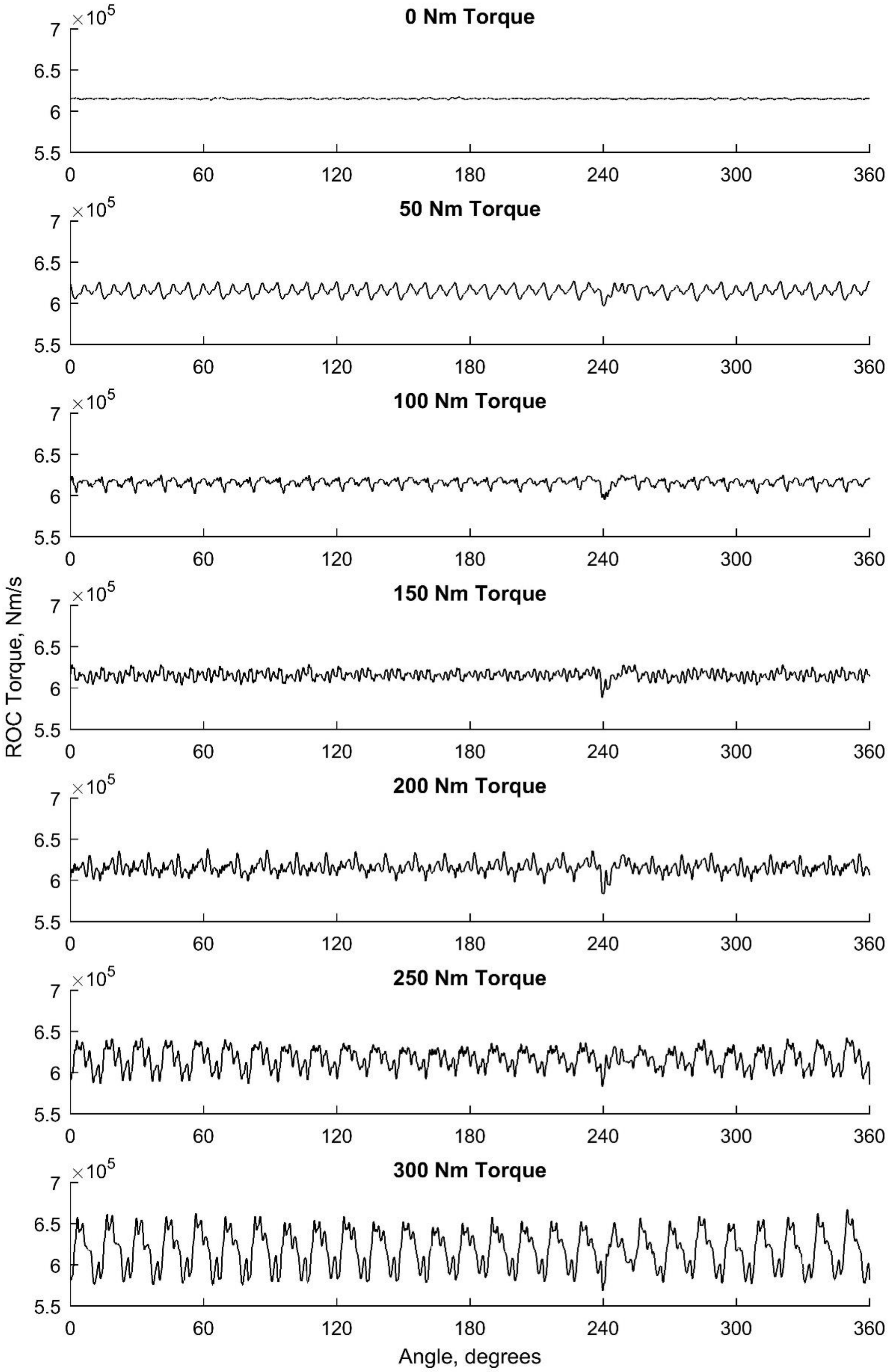

Figure 5-12 – Observing the effect of increasing torque applied to an 8.7 micron tooth bend at 3000 RPM.

Figure 5-12 demonstrates the most noticeable difference in waveform amplitude is between 0 and 50 Nm. This effect was seen across all the data captured with 0 Nm always possessing an amplitude so minimal that comparison to other data on the same axis was not possible. It was also noted that waveforms captured at 0 Nm were found to not have the characteristics of other data. This will be due to insufficient torque in the system for a magnetic field of the minimum required size to be generated, thusly the ROC sensor cannot consistently detect and monitor the axial flux leading to low amplitude erratic results. Due to this reason and that in reality no rotating machinery will operate under no load, after the initial data set was collected 0 Nm was removed from the test plan.

Observing Figure 5-13, the effect of increasing speed can be shown to also indicate an increase in amplitude however not to the same degree as torque. Given that higher speeds would lead to more sudden changes in torque over the meshing cycle, the increase in ROC is not unwarranted. This effect appears to be limited, with increasing amplitude observed in between 3000 and 9000 RPM but it does not increase after this. More noticeable is that the 15000 RPM waveform develops sinusoidal tendencies however, with this being seen in all waveforms captured at speeds over 12000 RPM, leading the author to suspect that an aliasing effect is occurring. Whilst this could not be verified however as the maximum sample rate of 100 kHz was already in use, the effect is certainly either a physical effect or the sampling rate as previous testing by the sponsor at these speeds has not reported the same effect. Though which of the two possibilities will require expansion of the DAQ and further testing to verify which is the cause.

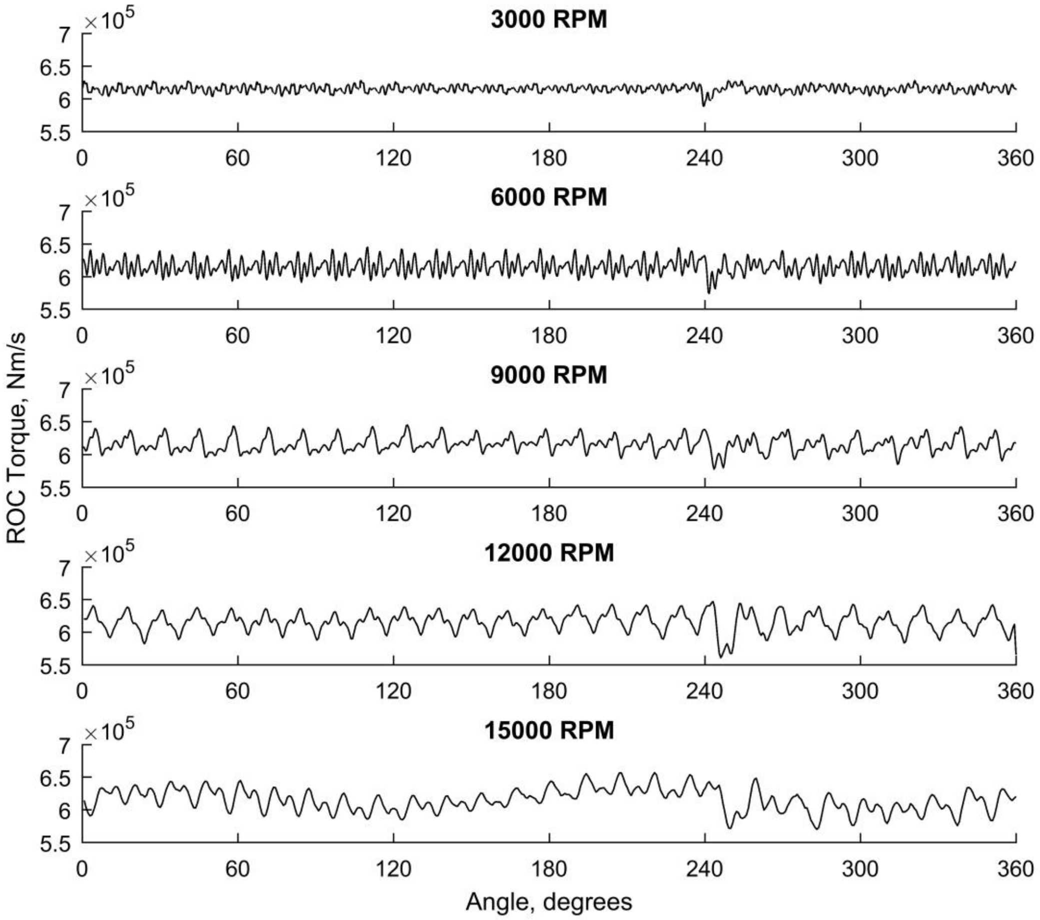

Figure 5-13 – The effect of increasing speed at 150 Nm with an 8.7 micron tooth bend.

5.3 Statistical Metrics

In order to have the metrics generate the most accurate description of the waveform, a short study of the difference between running the metrics on the raw data and TSA waveforms was made. By comparing the single values generated by the root mean square (RMS) for all speeds and torque levels, the effects of the two data sets could be measured. For this study, the healthy data set was used to remove any influence that the damage may have, so that the difference between raw and TSA data is not obscured.

Figure 5-14 shows the single value averaged metrics, this is to say that an RMS value was generated for each rotation of a test, and the resulting values for rotations at the same test conditions were then averaged to produce the values seen here. To begin there are obvious effects caused by the speed and torque, the effect of increased torque is to be expected as more torque in the system will generate larger rates of change of torque. The speed meanwhile clearly gives the different series a positive trend, again this is not unexpected as the faster speeds will see quicker changes in torque increasing the rate of change.

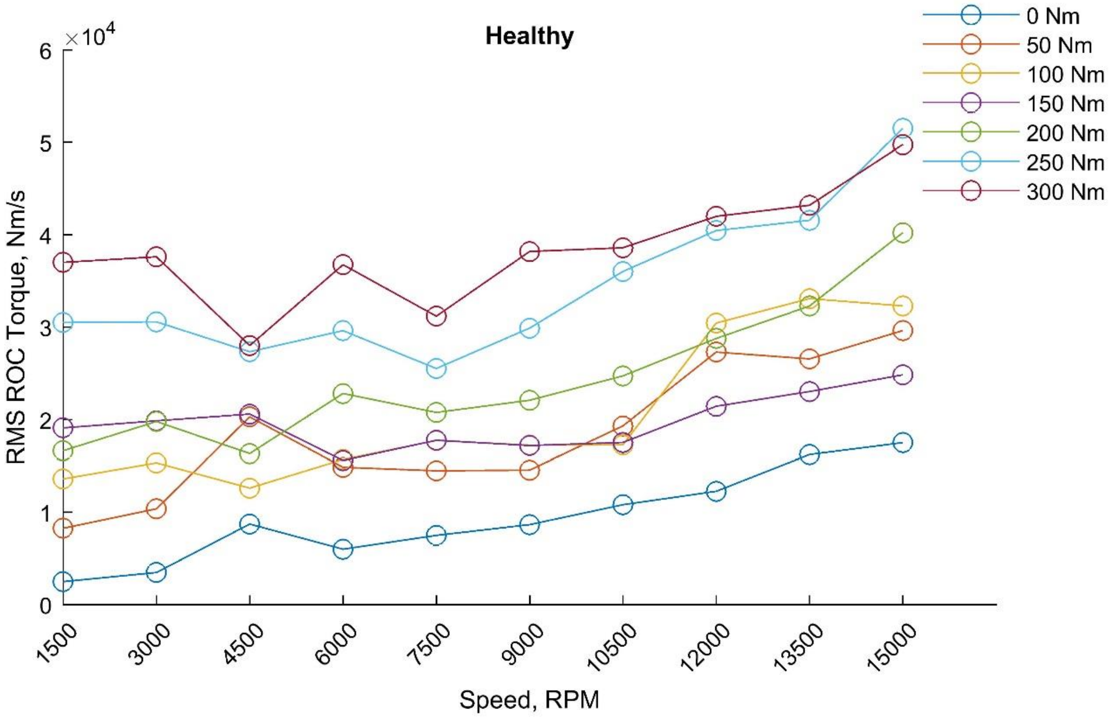

Figure 5-14 – Single value average RMS for raw data of the healthy specimen.

Although both test conditions clearly have an effect on the RMS, the reaction to the torque is inconsistent. A clear distinction between the individual levels was expected, however what occurs is a mixed reaction with 50 – 200 Nm shifting in amplitude between each other and only the highest and lowest torques acting as predicted. This is in contrast to the TSA data however, where, as shown in Figure 5-15, the different torque level are more distinct. While it can be argued that 50-200 Nm are nearly as mired as the raw data, the author proposes that without the 12000 RPM outliers the distinction is far clearer albeit the offset between the different torque levels being reduced.

The TSA also appears to have reduced the effect of the increasing speed as, while the trend remains positive, the gradient has been reduced. This appears to come at the cost of stability however, with the RMS values fluctuating more point-to-point as torque is increased.

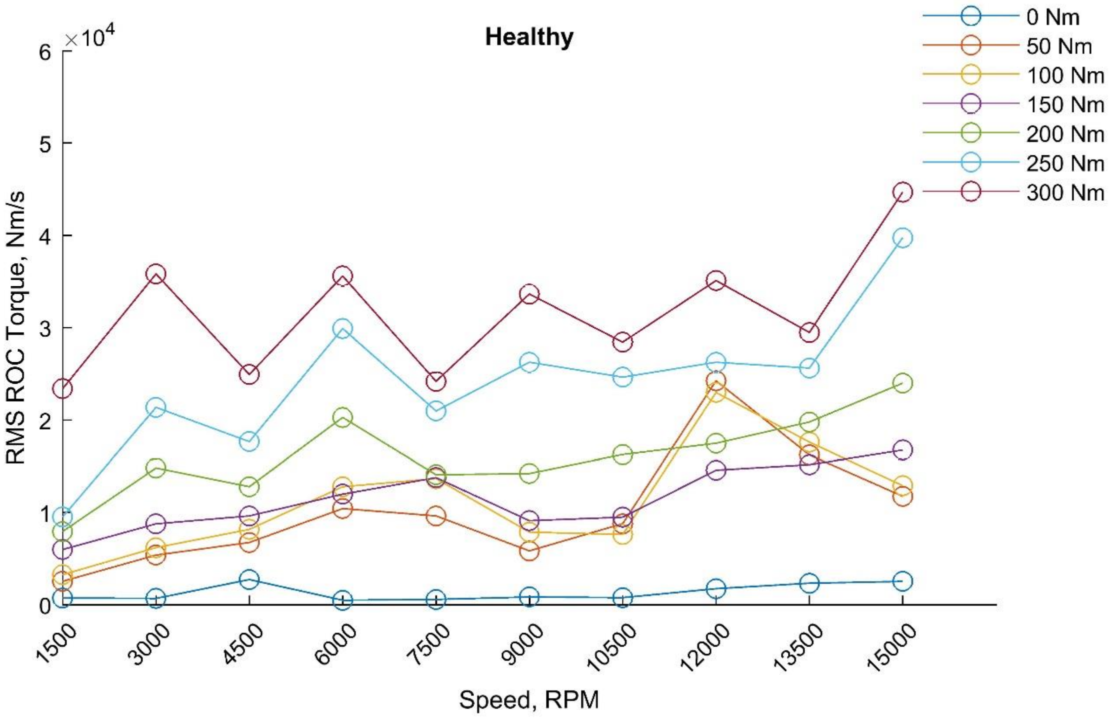

Figure 5-15 – Single value RMS for TSA data of the healthy specimen.

Following this study, it became clear that there are no clear advantages of using just the TSA or raw data, at least not with single value metrics (SVM). As shown previously in Chapter 3, SVM have been found to be unreliable when applied to parasitic ROC data. This was further confirmed with the initial analysis using the new in-loop data, where single values were found to be inconsistent and provide little to no discernible indication of damage, as presented in Figure 5-16 and Figure 5-17, where examples of the kurtosis and FM0 can be seen applied to both healthy and damaged data in both raw and TSA form. These figures demonstrate the instability in single value metrics where there is clearly no consistent trend between torque, speed, or damage. Whilst Figure 5-16 roughly maintains the torque levels in order of magnitude, it deviates easily from this and any major distinction between the healthy and damaged data is not visible, with TSA providing no additional clarity.

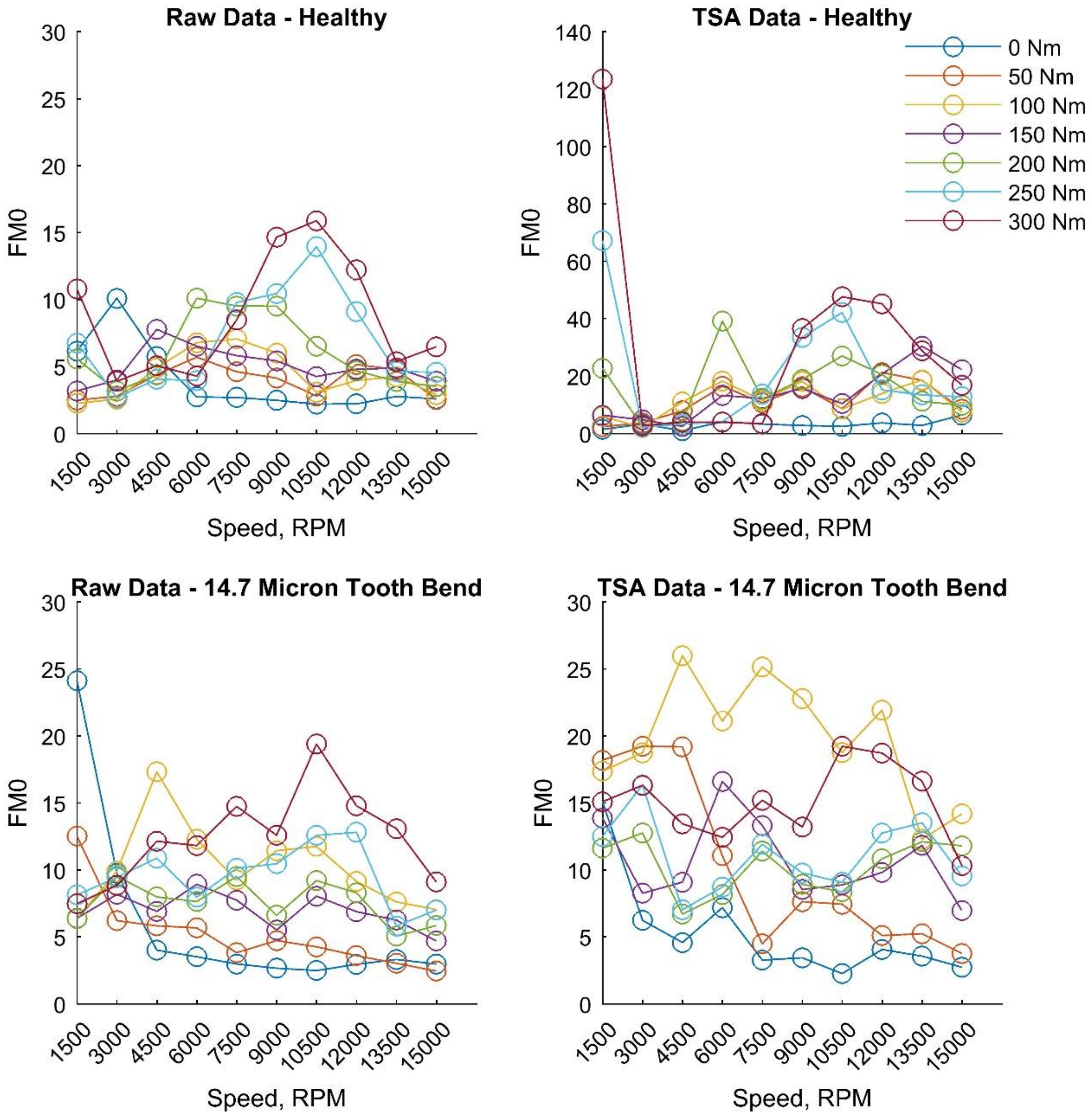

Figure 5-16 – Comparison of FM0 values for both raw and TSA data of healthy and 14.7 micron tooth bend gear pairs.

Figure 5-17 suffers from many of the same problems, but with the addition of high amplitude outliers. These outliers are not uncommon with this particular metric as it responds to ‘tails’ in the probability distribution of the signal. This makes it very easy for a single abnormal value to significantly raise the overall kurtosis, causing anomalies as seen in Figure 5-17.

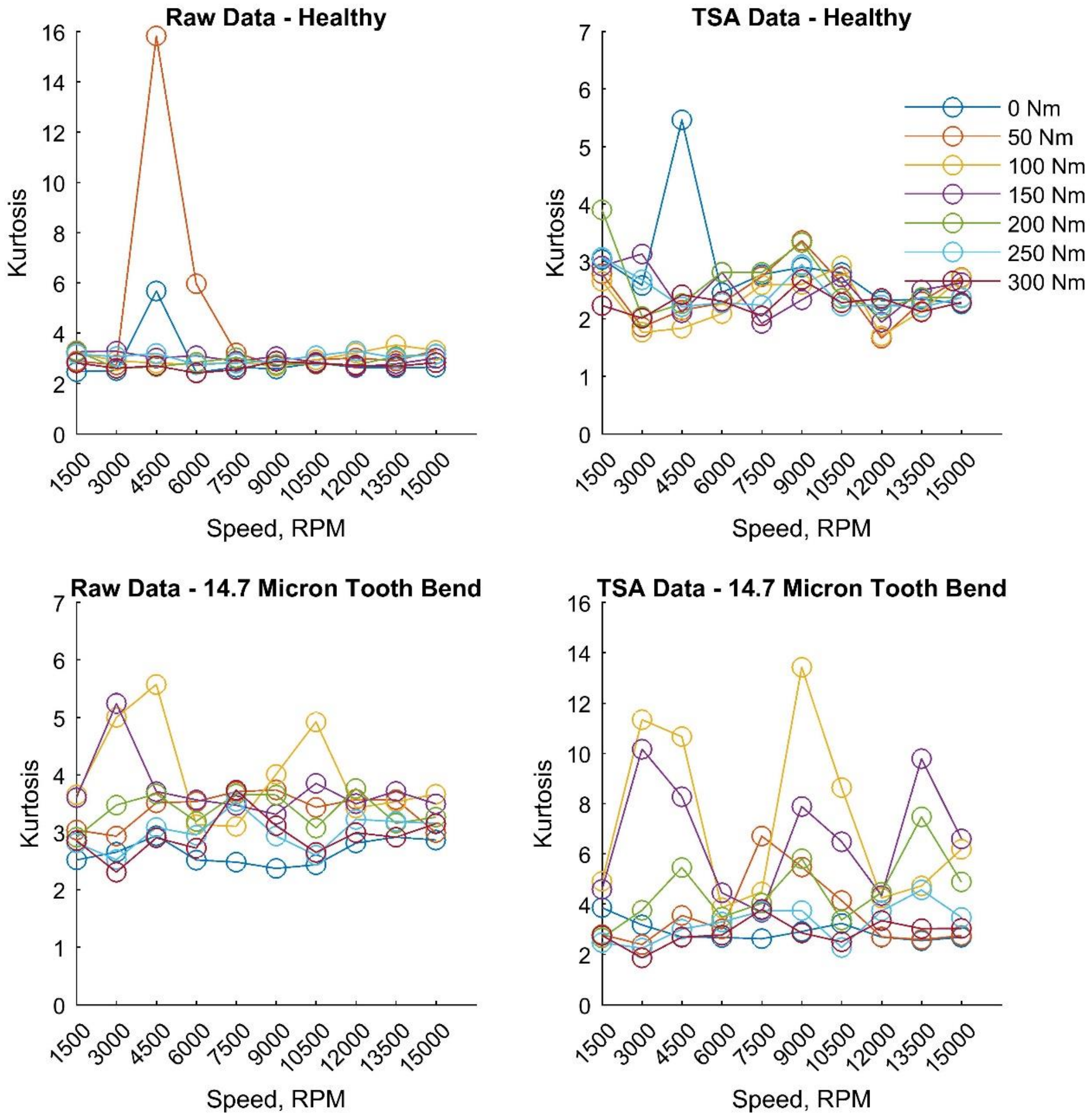

Figure 5-17 – Comparison of kurtosis values for both raw and TSA data of healthy and 14.7 micron tooth bend gear pairs.

The reason for this unreliability is likely due to fact that many of the metrics presented in this thesis were designed for use with vibration data and vibration difference signals. Due to the nature of these signals, these metrics are often designed to react to changes in the signal caused by high energy side bands of the meshing frequency and its harmonics which are normally indicative of damage within a vibration signal. As can be seen in the FFTs presented in this chapter, ROC data does appear to possess the distinctive high energy sidebands that occur within vibration signals. This does not mean that these methods are completely ineffective however, but instead must be applied in a different way to allow them to react to changes in the signal. For this purpose, a rolling square window that encompassed the equivalent of 3 teeth with a 75% overlap was employed. As in Chapter 3, the metrics were applied to this window, to generate a series of values across a rotation.

5.3.1 Root Mean Square

This action of applying the window and calculating the desired metric was two-fold. First the window was applied to each subsequent rotation of the raw data, and then the singular TSA rotation generated from this raw data. Figure 5-18 shows the results of this process for the 14.7 micron tooth bend at 1500 RPM and 50 Nm torque. Whilst the TSA provides a rotational overview, allowing the damage to clearly be identified at 30°, this not clearly in every rotation in the raw data. Although the highest amplitude peaks do appear at 30°, they occur only every 5 rotations and appear to 'fade' in and out over this duration. This is accompanied by a noticeable 'diagonal' pattern of areas of medium to high amplitude.

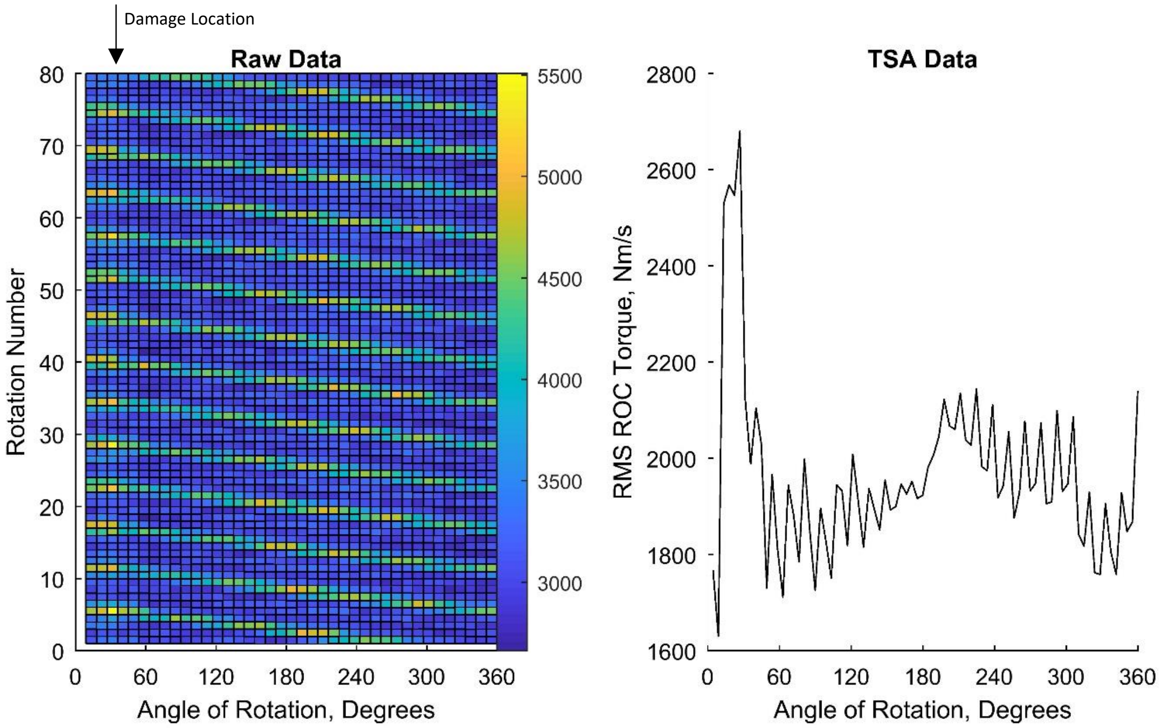

Figure 5-18 – Windowed RMS for a 14.7 micron tooth bend at 1500 RPM and 50 Nm torque.

Initially these areas along with the diminishing damaged were thought to be caused by misalignment of the rotations leading to shifts in the data, analysis of the individual waveforms disproved this however, as seen in Figure 5-19. The red highlights indicate the damage which can be seen to remain stationary, implying that the rotations are being identified correctly. The green highlights indicate the area causing abnormally high RMS values, while the cause of this phenomena is currently unknown with further testing required. The shift per rotation is approximately 60°, this corresponds to the difference in shaft speed indicating that this transient is being caused once per rotation on the layshaft.

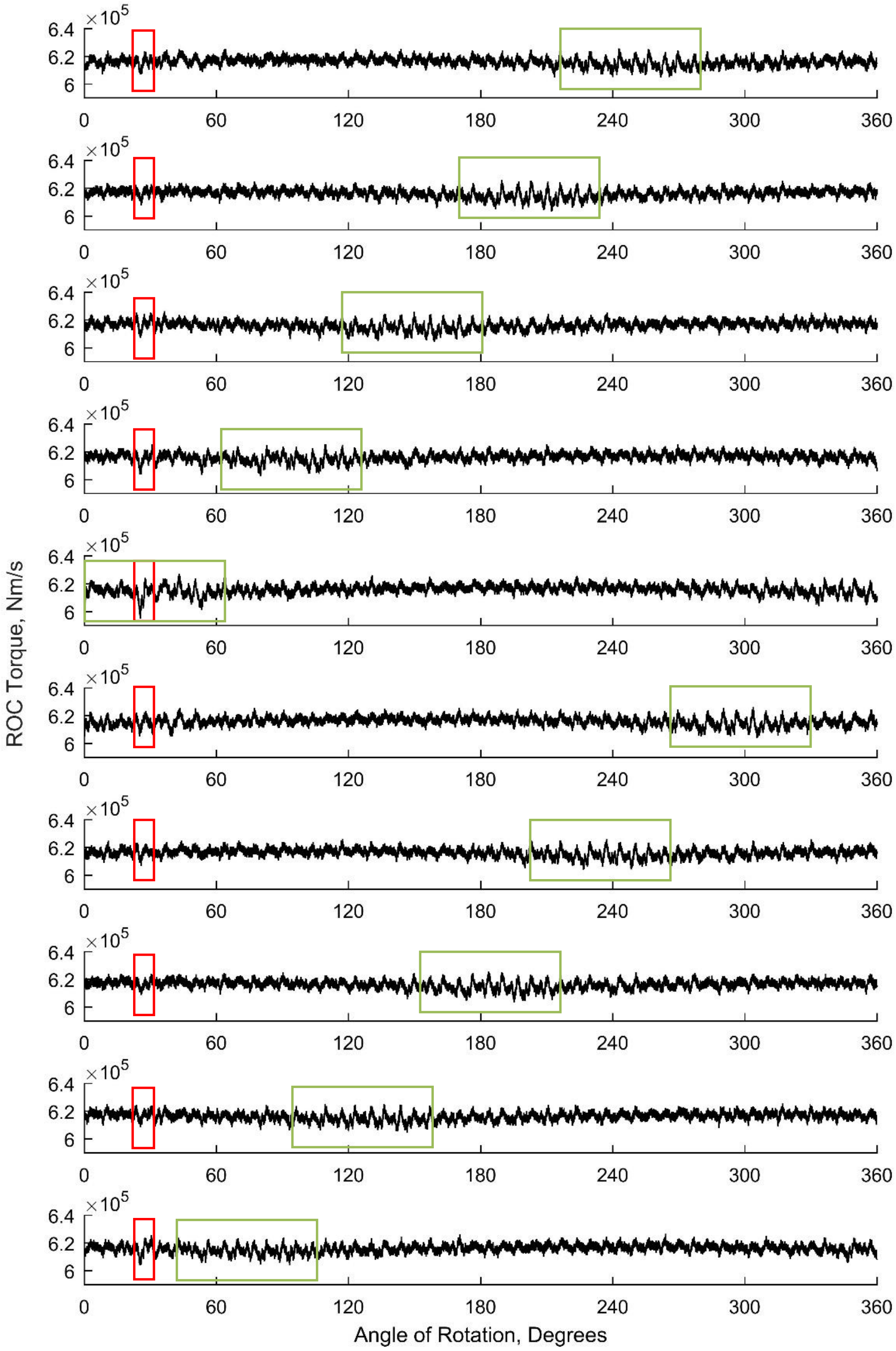

Figure 5-19 – Raw waveforms for the first 10 rotations of the 14.7 micron tooth bend at 3000 RPM and 50 Nm torque.

This pattern is diminished with speed however as demonstrated in Figure 5-20 and Figure 5-21 where the pattern remains slightly visible, but clarity has been significantly reduced. This also true for the damage however, indicated by the white dotted line, which while still clearly visible in the TSA is now diminished in the raw data.

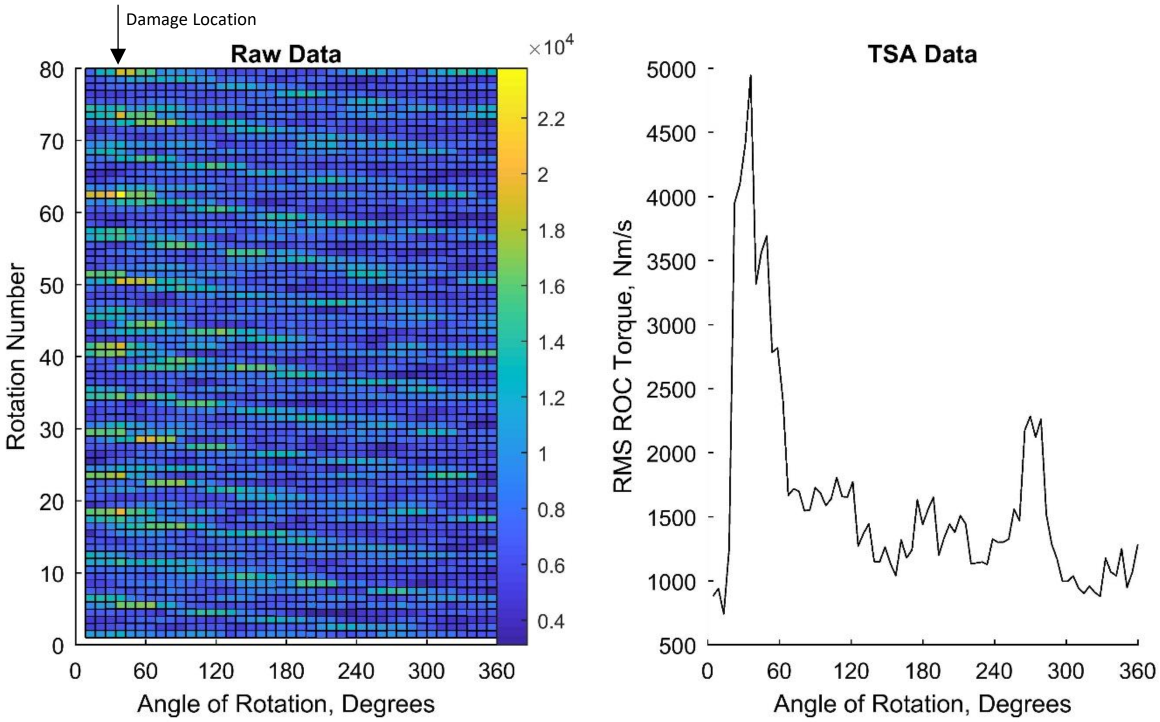

Figure 5-20 – Windowed RMS for a 14.7 micron tooth bend at 7500 RPM and 50 Nm torque.

This effect continues to escalate as the speed is further increased as witnessed in Figure 5-21, where the test was at its maximum speed of 15,000 RPM. At this point neither the shifting layshaft transient nor the damage are visible in the raw data. Whilst still visible in the TSA, the overall amplitude of the waveform has increased meaning that the damage was only identifiable within the TSA waveform. This may be related to the sinusoidal effect witnessed earlier in Figure 5-13. Without a consistent baseline amplitude and the natural fluctuations of the ROC signal, the damage may no longer generate the largest amplitude RMS, causing the reduction in clarity that is seen here.

Another possible explanation however is that the amount of torque in the system is not actually 50 Nm. The manual method of torqueing is by no means exact and while a torque sensor is equipped to provide a measure of the torque in the system over the course of testing it was found to be unreliable. It is also possible that a drop in the torque is due to the uncompensated backlash, where the shafts are independent during the loading process backlash can be introduced if precautions are not taken. Whilst checks were in place to prevent this, it is difficult to say how effective they are without an effective torque measurement.

This lack of precise torque measurement in the system, and initial issues with successfully locking-in the torque, leads the author to believe that the most reasonable explanation is that the amount of torque is insufficient to counter the effects of the speed, i.e. increased amplitude across the signal, making the detection of the damage vastly inferior. It is worth addressing that although an alternative method was unable to be implemented during the course of this project, one will be required for future work as accurately measuring the torque in the system will help be an invaluable tool. One possible solution is a strain gauge-based method, strain gauges would provide a parallel to the non-contact systems. It is also possible that a strain gauge method could be built into one of the connections of the rig circumventing the need for slip-rings and helping prevent a potential increase in electrical noise, although a direct measurement on the quill shaft would be preferable.

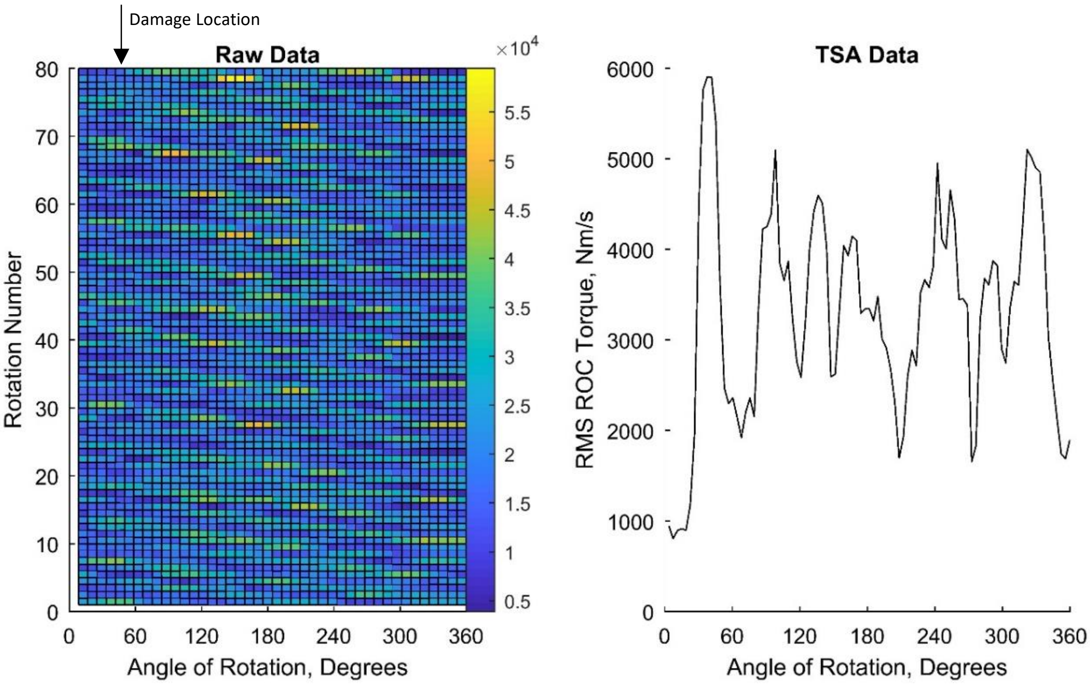

Figure 5-21 – Windowed RMS for a 14.7 micron tooth bend at 15000 RPM and 50 Nm torque.

This theory is further supported by Figure 5-22, which is a later test of the same gear at the same conditions as Figure 5-21. As can be seen the damage is a lot clearer despite the relatively high amplitude area between 180° and 240°, the layshaft transient is still present as well though notably to a lesser degree as discussed.

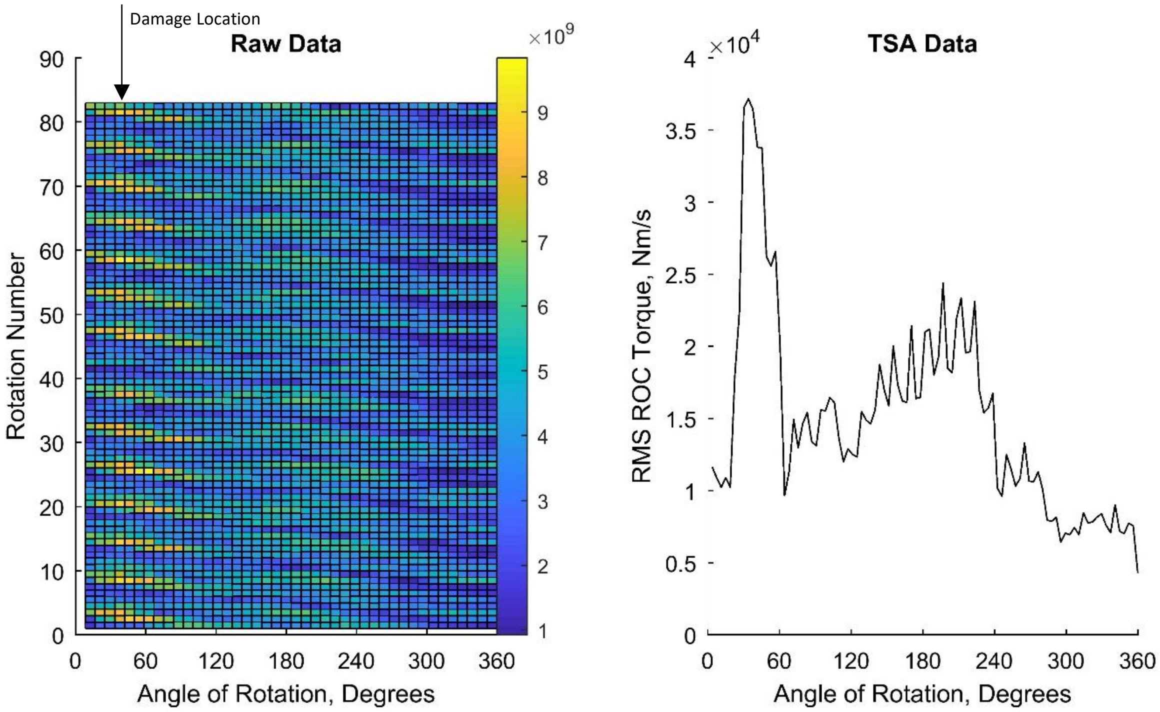

Figure 5-22 - Windowed RMS for a re-test of the 14.7 micron tooth bend at 15000 RPM and 50 Nm torque.

These issues are immediately negated when the same technique is applied to the same gear at higher torques as seen in Figure 5-23 and 4.11. Here even if the same losses that occurred at 50 Nm were applied, the amount of torque in the system can easily be seen to compensate and provides a clear and accurate image of the damage and its location. This occurs in both the raw and TSA data, despite an increase in background noise in the raw data.

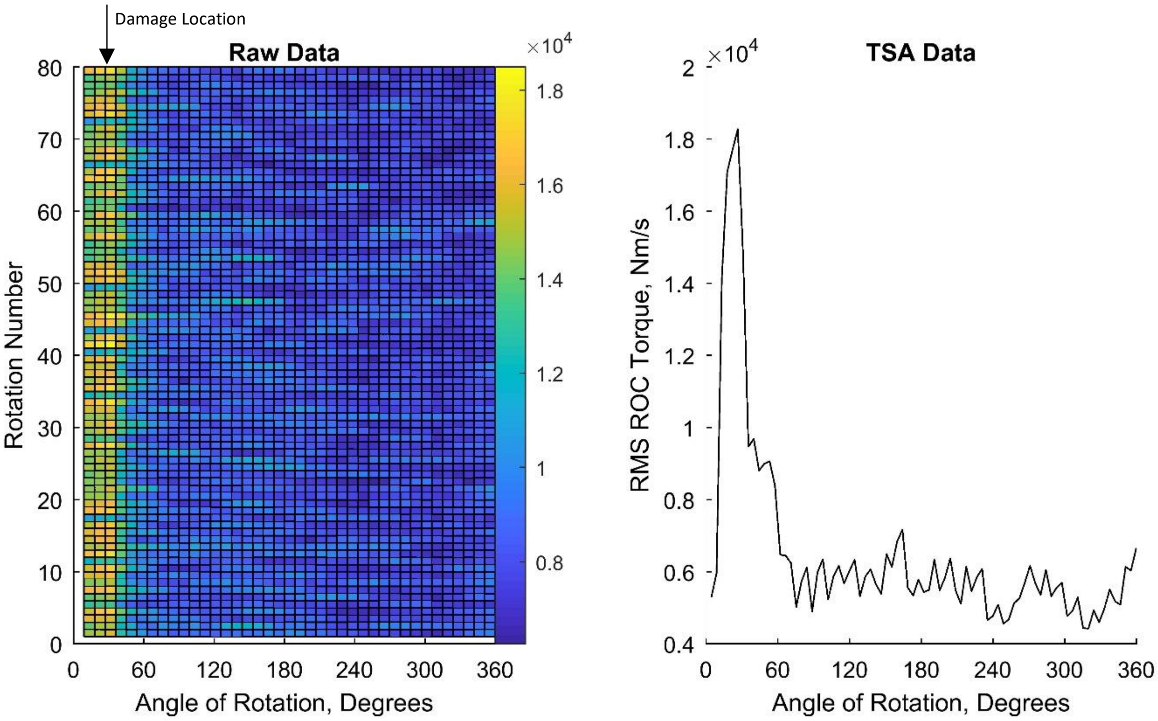

Figure 5-23 - Windowed RMS for a 14.7 micron tooth bend at 3000 RPM and 150 Nm torque.

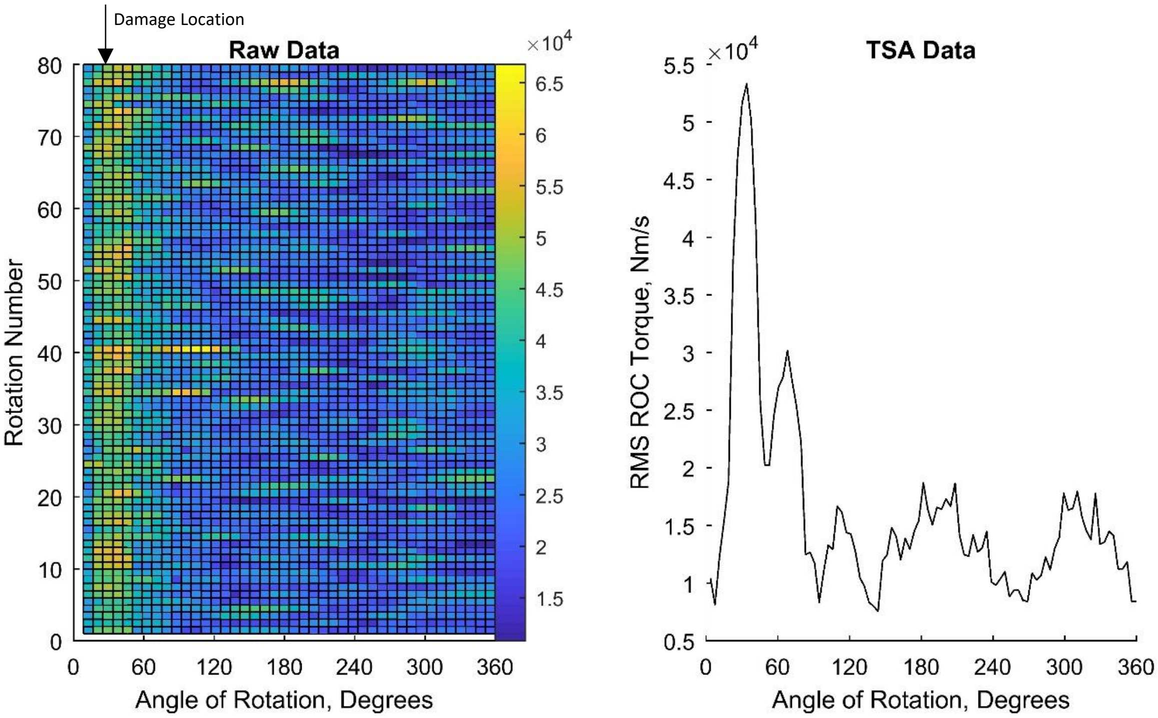

Figure 5-24 – Windowed RMS for a 14.7 micron tooth bend at 15000 RPM and 150 Nm torque.

Moving away from the 14.7 micron tooth bend, Figure 5-25 shows the waveform for a healthy gear at mid torque and speed. Comparison of the figure scales shows that the healthy gear has a substantially lower maximum than those already presented with a 14.7 micron tooth bend. There are also traces of the layshaft transient as well, though clarity is reduced as is expected due to the increased speed and torque. Its presence within a healthy gear test does however suggest that it may not be a gear related issue, however further testing would be required to confirm this.

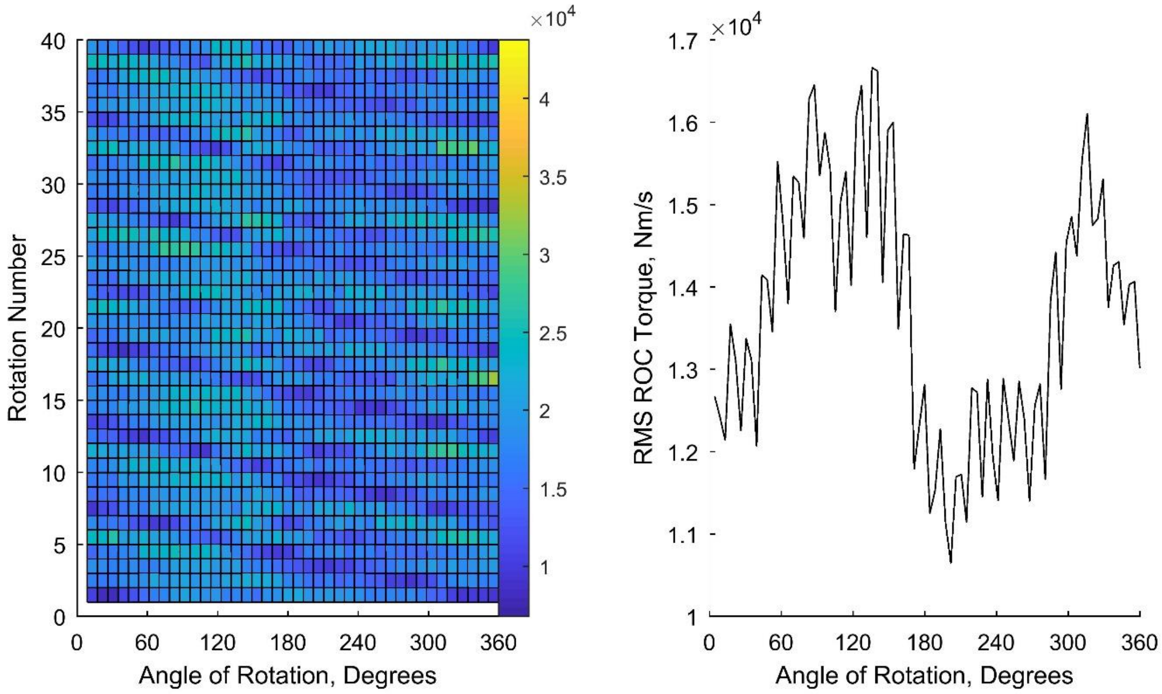

Figure 5-25 – Windowed RMS for the healthy gear pair at 7500 RPM and 150 Nm torque.

A feature that was not anticipated however was the sinusoidal trend clearly present across the TSA RMS. Whilst this has not been present in other waveforms examination of data at the same conditions shows similar behaviour with a trough clearly present at approximately 200°. Expanding on this with Figure 5-26 and Figure 5-27, while the damage is clearly indicated at 60° and 240° respectively, both possess the same trough. This is accompanied by an apparent loss of the reduction in amplitude at 30° and 330° displayed in Figure 5-25. It is possible that the nature of the damaged gears reduces this sinusoidal effect, however if this was the case, the trough would be expected to be reduced as well. Given the information presented here, it is clear that the trough must be occurring once a rotation for it not to have been eliminated by the TSA. While the origin of this phenomenon is uncertain, its effect on detecting the 2.4 micron tooth bend within the raw data is evident.

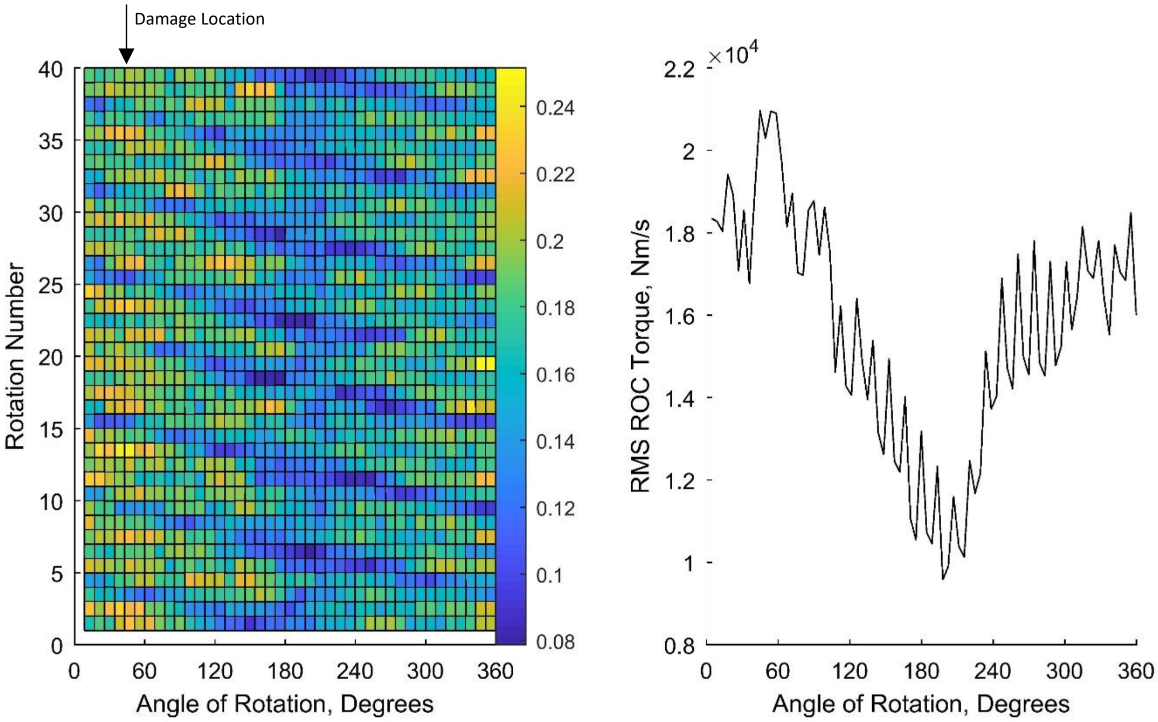

Figure 5-26 –Windowed RMS for the 2.4 micron tooth bend at 7500 RPM and 150 Nm torque.

Fortunately, the 8.7 micron tooth bend present in Figure 5-27 generates a large enough presence that it is still easily perceptible in both the raw and TSA data.

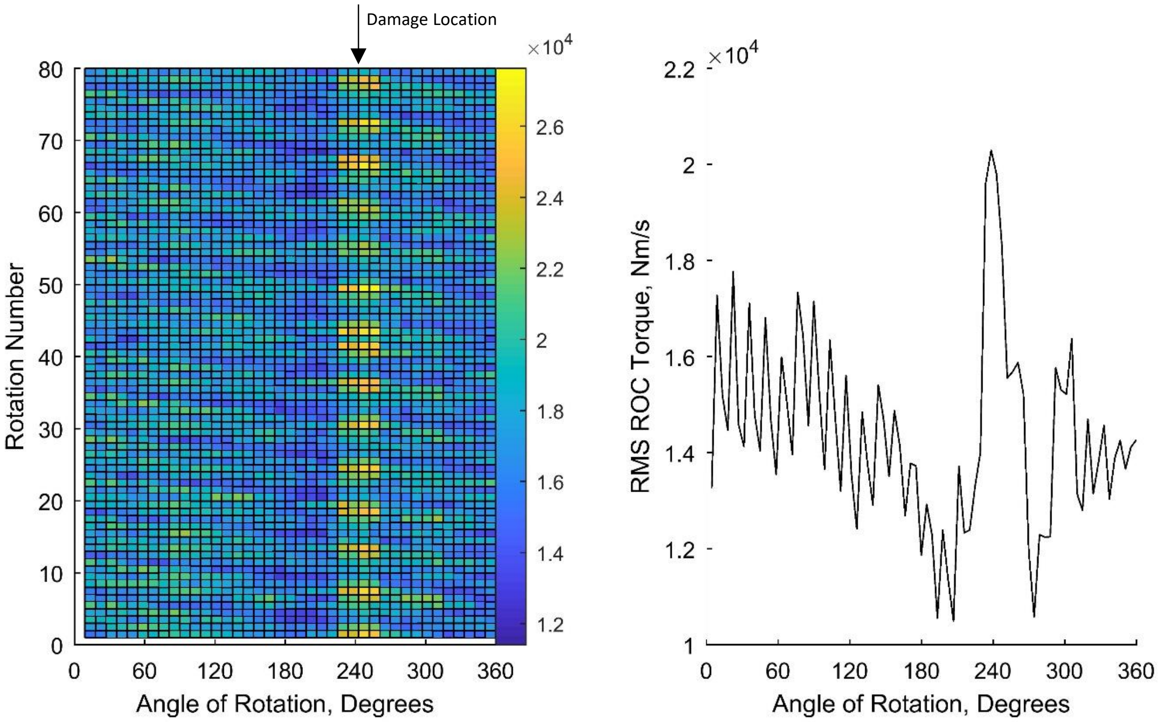

Figure 5-27 – Windowed RMS for the 8.7 micron tooth bend at 7500 RPM and 150 Nm torque.

This phenomenon is not seen in other waveforms at different settings suggesting that this may be caused by a unique resonance at this speed and torque. Whilst a human operator can still clearly identify the damage within the TSA waveforms, phenomena like this present a problem for automated algorithms. Where unexpected changes in the waveform could mask the true extent of the damage or cause false alarms, this clearly indicates that neither of these approaches are ideally suited for dealing with ROC technology, but the results are promising. Looking at a signal comparison of the various damage levels, in Figure 5-28, shows that the differences between the 4 levels can be determined with relative ease, despite the trough at 200°. This is to say the damaged tooth is still identifiable at 30°, 60° and 240° for 14.7, 2.4 and 8.7 micron tooth bends respectively with the healthy waveform showing cleaner and lower level results.

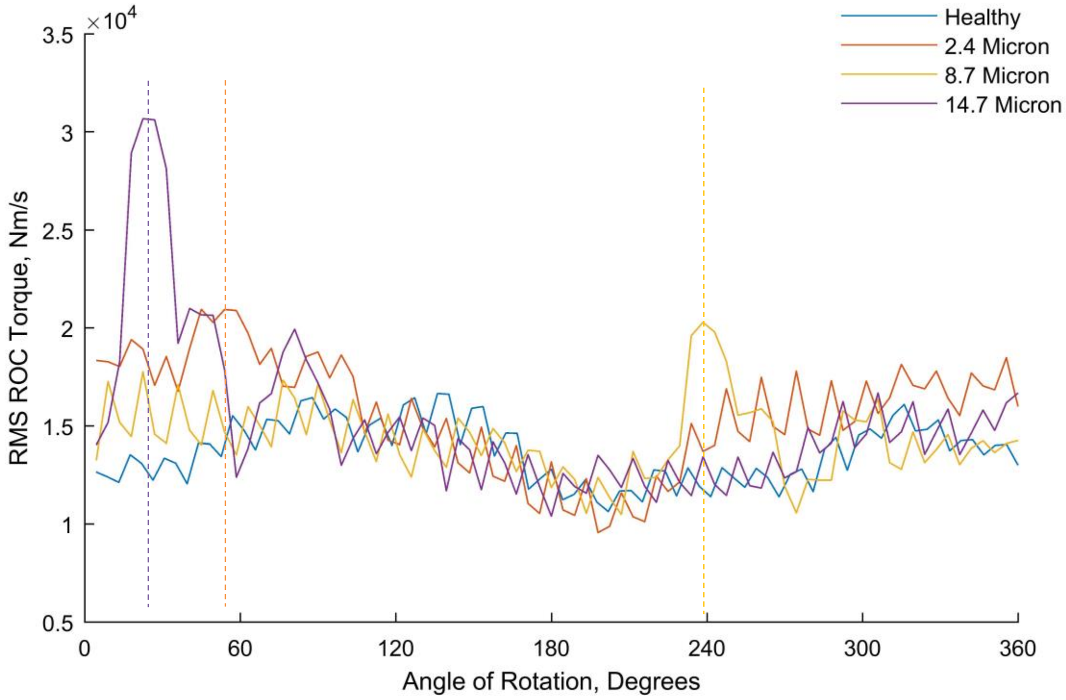

Figure 5-28 – Comparison of windowed RMS results for all degrees of damage at 150 Nm and 3000 RPM with damage positions indicated by the vertical dotted lines.

Whilst the peak amplitude caused by the 8.7 and 2.4 micron damage are roughly equal, due to the fluctuating levels average amplitude. It is possible that an automated method may overcome this by comparing each value to its surroundings. While a full examination of this was proposal was not possible within the timespan of this work, using the same data that generated Figure 5-28, Figure 5-29 was created.

By comparing each value to its direct neighbours, the difference between them was calculated using the simple formula extracted from the energy operator:

$$x_i{}^2 - (x_{i+1} \times x_{i-1}) \tag{5-1}$$

Where *x* is the time series and *i* is the index. Applying this formula eliminated any fluctuations in the results but didn't have the desired effect of accentuating the damage and increased the amplitude of areas of non-interest. Whilst the 14.7 micron tooth bend is still clearly visible, the 2.4 micron is no longer detectable and could now mistakenly be interpreted as existing at approximately 270°. The 8.7 micron tooth bend is still visible but only through prior knowledge of the location of the damaged tooth within the rotation. Without this knowledge the large peaks within the first 60° could easily be misinterpreted as the location of this damage.

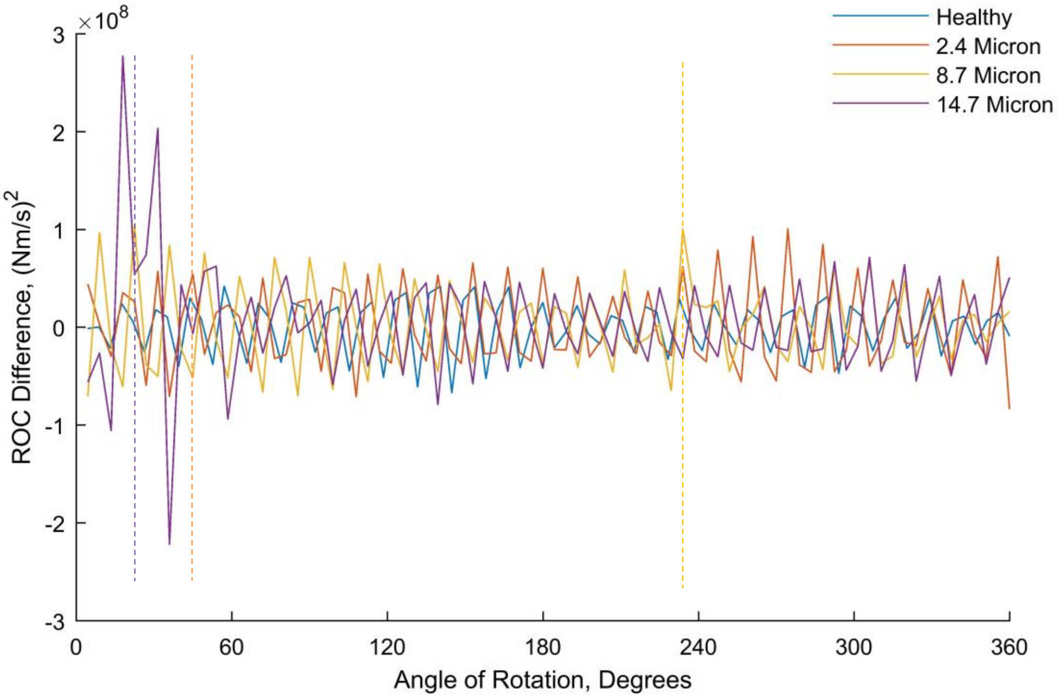

Figure 5-29 – Comparison of singular data points to the surrounding data points based on the data presented in Figure 5-28 with damage positions indicated by vertical dotted lines.

The major failing of this method is that it only compares a value to its closest neighbours, so damage without an immediate jump in amplitude is reduced in visibility. Broader, more advanced methods of point comparison may yield better results, but this extends beyond the scope of this project.

5.3.2 Kurtosis

As previously discussed, kurtosis is the 4th statistical moment and is a measure of 'tailedness' i.e. a measure of outliers in the signal or the chance of outliers in a probability distribution. It is calculated by:

$$Kurtosis = \frac{N\sum_{i=1}^{N}(x_i - \bar{x})^4}{[\sum_{i=1}^{N}(x_i - \bar{x})^2]^2} \tag{5-2}$$

Application of the kurtosis to ROC signals has been attempted before as seen in Chapter 3, with limited effectiveness. Utilizing the clarity of the in-loop data, it was hoped that the kurtosis would react better to the damage as an outlier and due to the greater consistency in the waveforms. Examining Figure 5-30, the initial results appear quite promising with kurtosis with reacting consistently with kurtosis values below 3 implying that there are few extreme outliers, which is seen for the majority of the raw and TSA data. There is however the singular anomaly present at the end of the TSA data, examination of the waveform gives no indication of the cause however with no clear outliers present that would cause a sudden jump in the kurtosis.

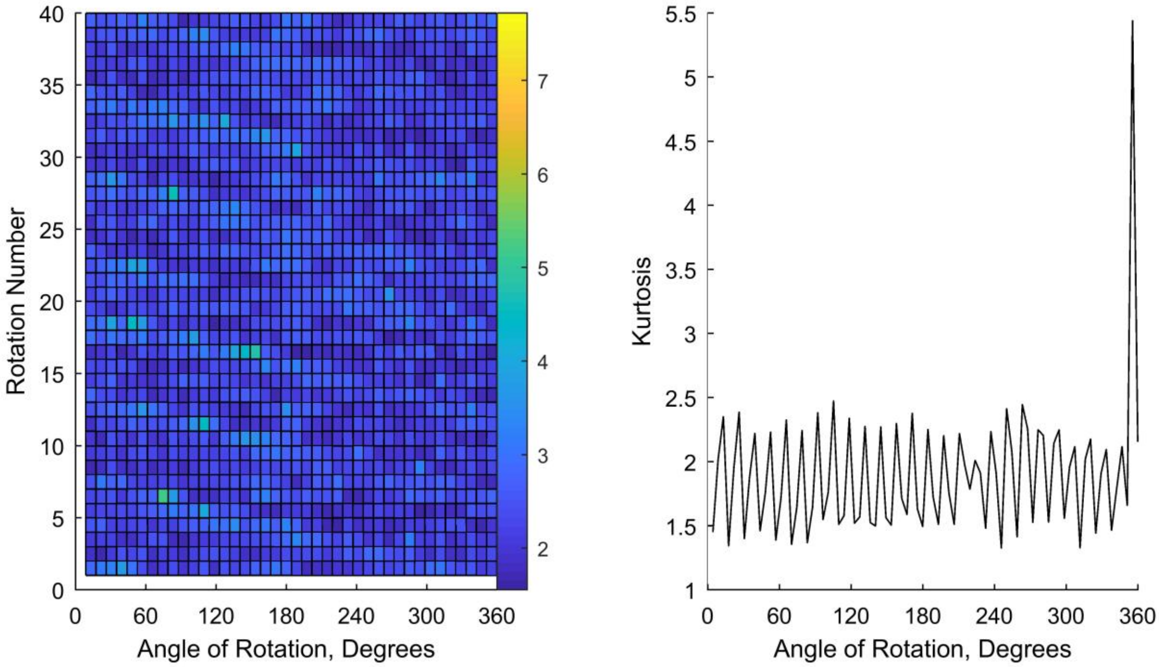

Figure 5-30 – Windowed kurtosis for the healthy gear pair at 7500 RPM and 150 Nm torque, where raw data is on the left and TSA data is on the right.

This represents one of the key problems with the application of kurtosis to ROC data that has been witnessed thus far. As the measure is designed to react to outliers, a windowed application is not necessary a beneficial solution over a single value. By segmenting the data, the criteria for an outlier becomes relative and will change depending on the data contained within the window. This can cause instability in the results as the kurtosis reacts to values that would have a lesser effect normally, given more data.

Unlike the parasitic loss data, Figure 5-31 demonstrates a lack of extreme amplitude anomalies in the data. An increase in the average kurtosis is noted but cannot be attributed to the damage, as comparison to other data sets has shown that this value is inconsistent and can vary from waveform to waveform. No indication of the damage is visible in the raw data and nothing is immediately clear with regards to amplitude in the TSA. A singular peak found between 30° and 60° in the TSA has a distinctly wider base width. This is in contrast to the rest of the TSA data which comprises of short, sharp peaks and troughs. Given that this region is known to possess the damage it is clear that the kurtosis is not reacting as anticipated. Instead of a greatly increased kurtosis value forming an outlier indicating the damage, a series of more consistent kurtosis values are generated over the movement of the window appearing to cause a slight delay in response with regards to the angle at which it is seen.

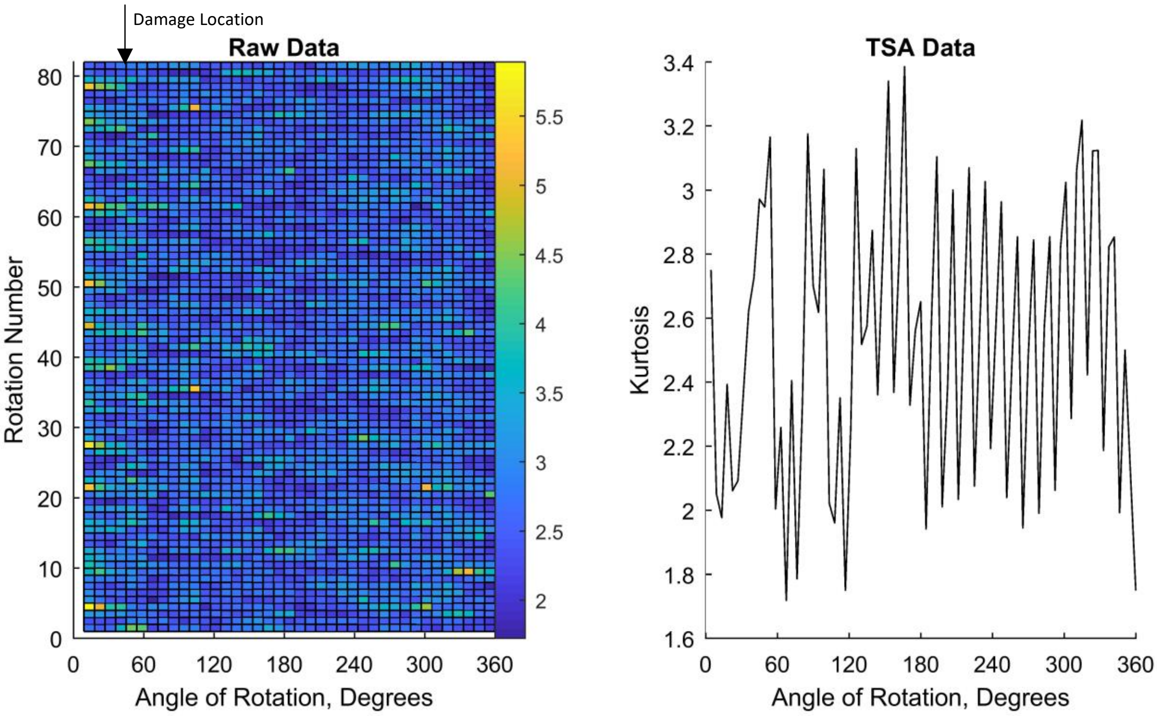

Figure 5-31 – Windowed kurtosis for the 14.7 micron tooth bend at 7500 RPM and 150 Nm torque.

This effect can be seen further in Figure 5-32 where the 8.7 micron tooth bend generates a similar effect with another wider based peak starting at 240° (the damage location) to 270° in the TSA data, with no discernible indication in the raw data. Again, this peak is offset from the damage location but stands out from the rest of the waveform. This effect is unfortunately not consistent enough for accurate damage detection as not only was no indication present for the 2.4 micron tooth bend but it requires a minimum of 150 Nm torque to be present before the effect is discernible. The speed only aggravates the situation by increasing how erratic the resulting kurtosis values are preventing consistent results.

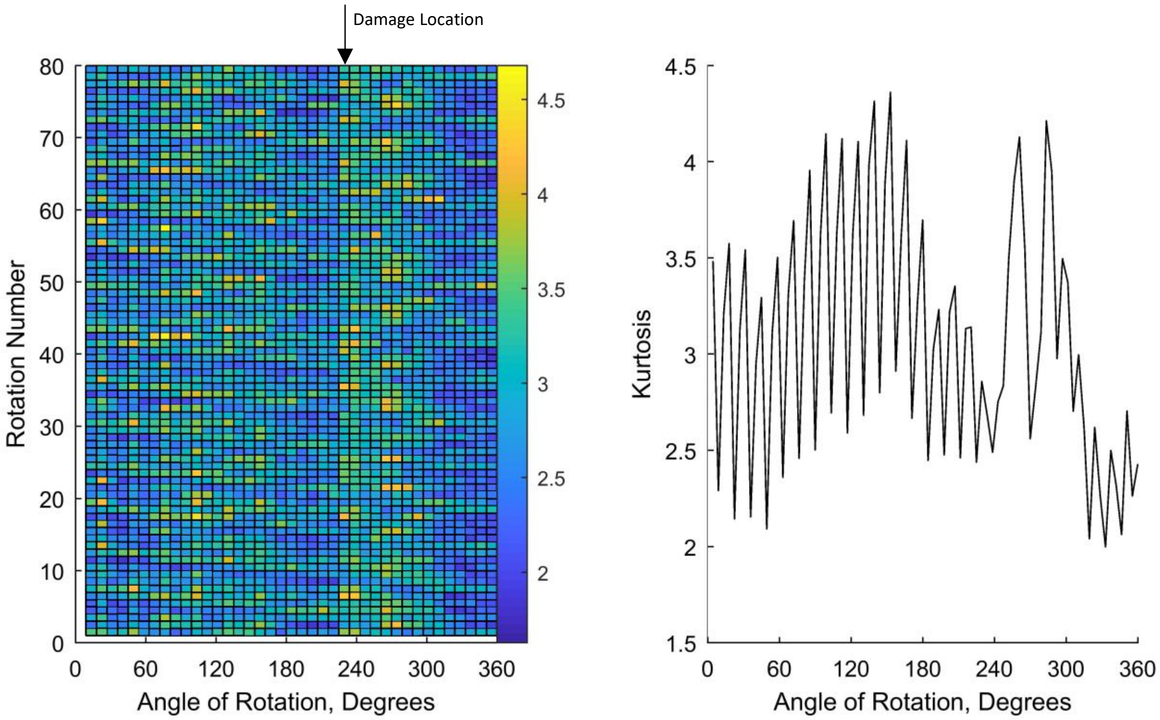

Figure 5-32 – Windowed kurtosis for the 8.7 micron tooth bend at 7500 RPM and 150 Nm torque, where raw data is on the left and TSA data is on the right.

5.3.3 Energy Operator

The energy operator (EO) is an extension to the kurtosis. Just as was applied to the RMS to try to detect sudden changes in the wave form the EO evaluates each value of the signal in relation to its neighbours via:

$$x_i{}^2 - (x_{i+1} \times x_{i-1}) \tag{5-3}$$

Where *x* is the signal value and *i* is the index, any outliers are hoped to be accentuated before calculating the kurtosis. Due to the nature of the kurtosis, the technique should respond better to these outliers and create a better indication of the level and nature of the damage. Unfortunately application of this method to both the raw and TSA waveforms did not provide any such clarity as can be seen in Figure 5-33, Figure 5-34, Figure 5-35, and Figure 5-36. No consistency was able to be found across any results from the EO, this is due to the results seen from the kurtosis, where the damage is presented as a slow increase in value, forming a wide based peak. The extension offered by the EO would eliminate these values due to their closer nature than the rest of the signal which varies wildly, resulting in incoherent results with no discernible information.

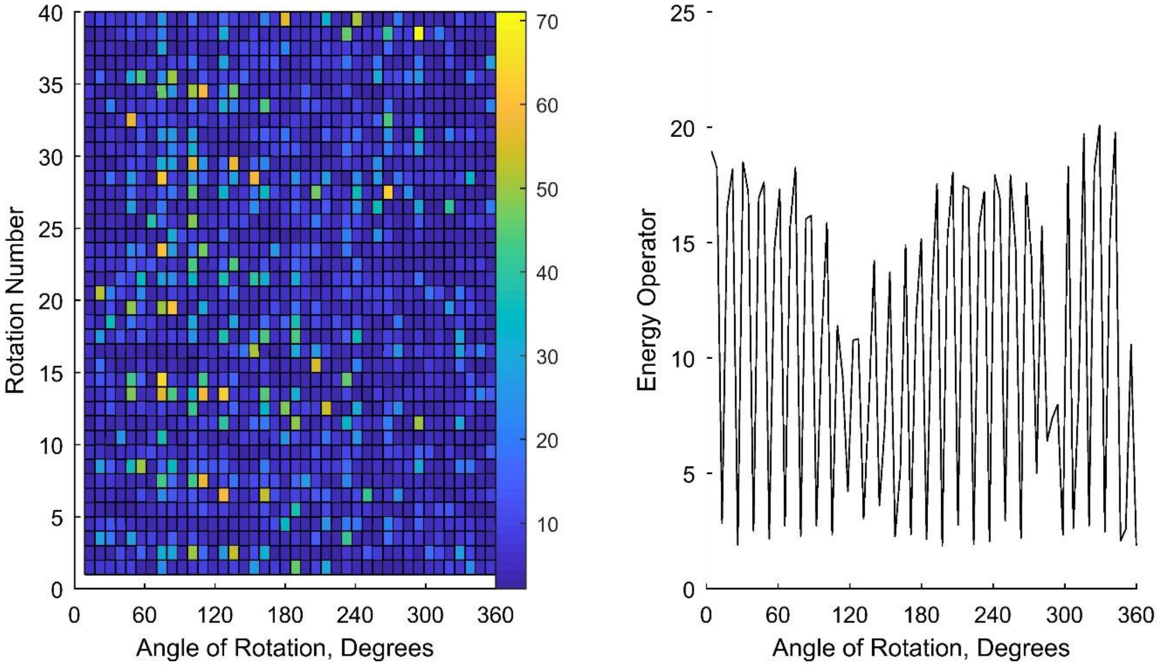

Figure 5-33 – Windowed EO for the healthy gear pair at 7500 RPM and 150 Nm torque, where raw data is on the left and TSA data is on the right.

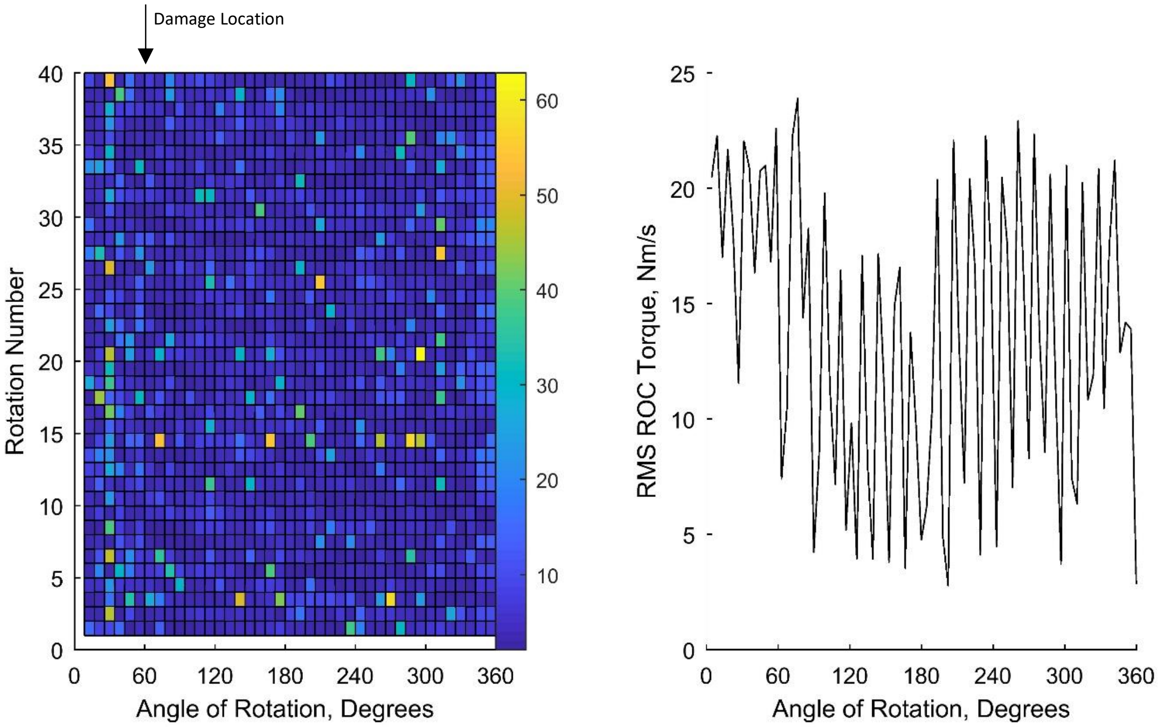

Figure 5-34 – Windowed EO for the 2.4 micron tooth bend at 7500 RPM and 150 Nm torque, where raw data is on the left and TSA data is on the right.

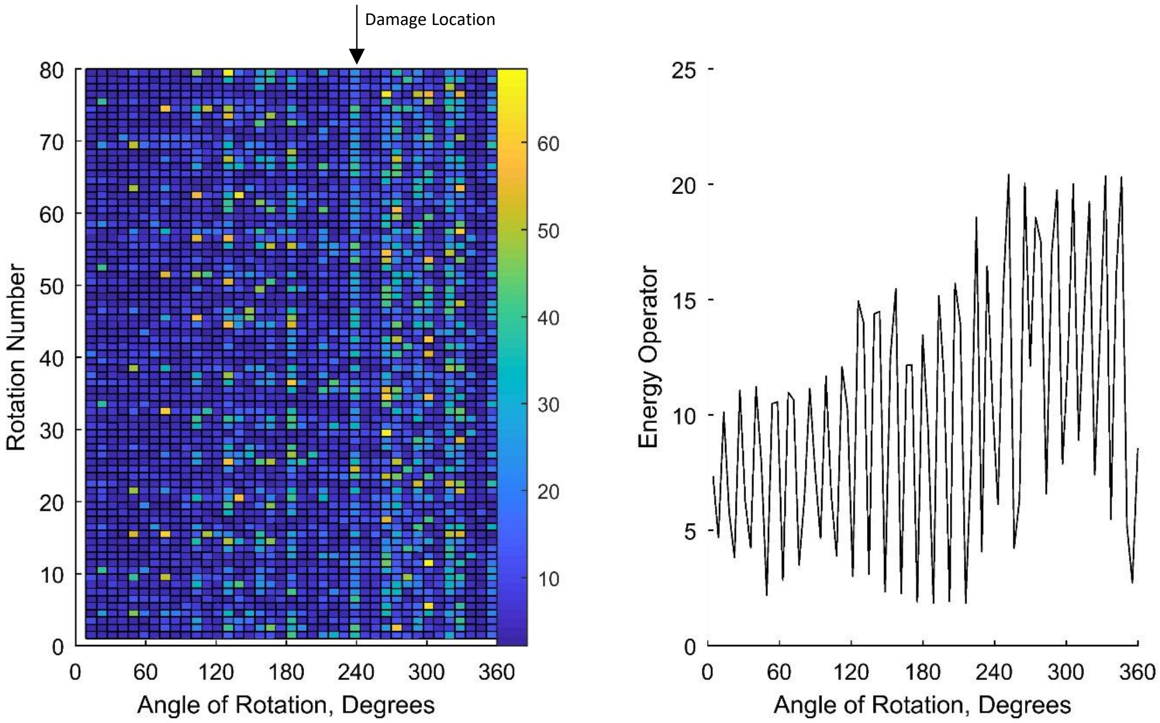

Figure 5-35 – Windowed EO for the 8.7 micron tooth bend at 7500 RPM and 150 Nm torque, where raw data is on the left and TSA data is on the right.

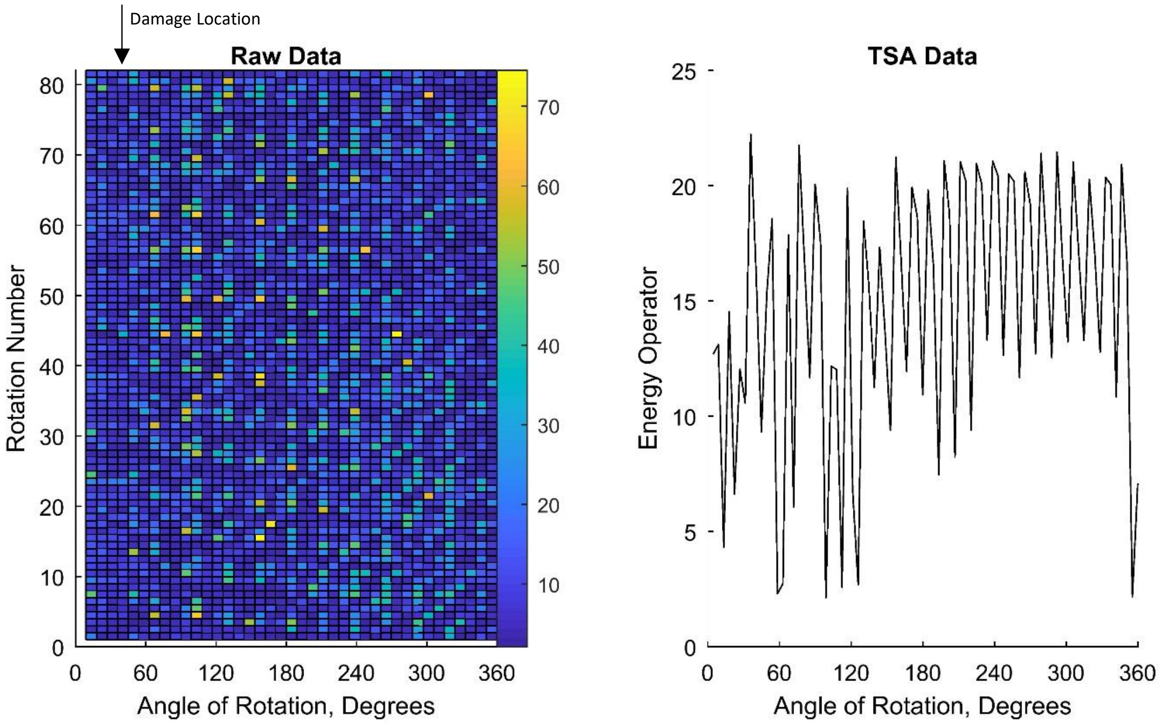

Figure 5-36 – Windowed EO for the 14.7 micron tooth bend at 7500 RPM and 150 Nm torque, where raw data is on the left and TSA data is on the right.

5.3.4 M6A & M8A

M6A and M8A are expansions of the kurtosis created by Martin (1989) to have different degrees of sensitivity to outlier peaks, with both more sensitive than the original formula. Experience has shown that these do not have this effect when applied to ROC signals and simply increase the amplitude of the signal and cause any outliers to be accentuated to an unnecessary level. This was found to be the case in Chapter 3 and again here as demonstrated in Figure 5-37 and Figure 5-38, where the results are found to be identical to those of the kurtosis albeit with higher peak values.

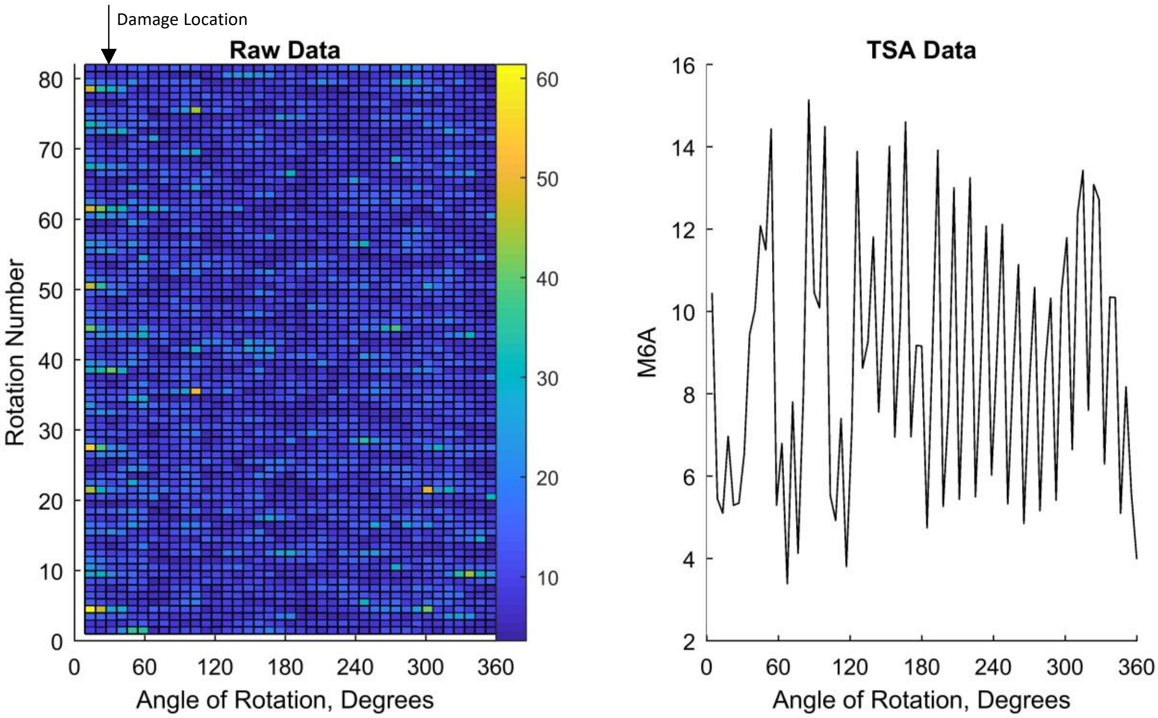

Figure 5-37 – Windowed M6A for the 14.7 micron tooth bend at 7500 RPM and 150 Nm torque.

Although the graphs do provide the same indication of damage as the kurtosis due to their near identical nature the increased powers of the formula do little in improve sensitivity or clarity in the either the raw or TSA data.

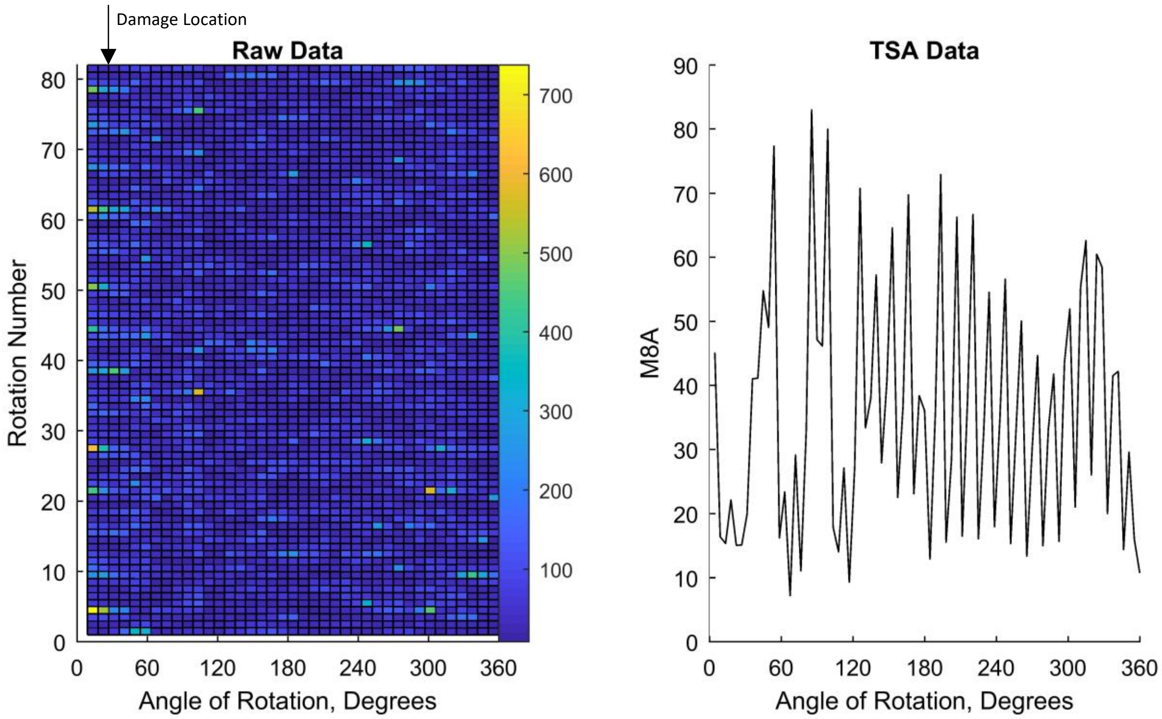

Figure 5-38 – Windowed M8A for the 14.7 micron tooth bend at 7500 RPM and 150 Nm torque.

5.3.5 NA4 & NB4

NA4 is a vibration fault indicator designed to detect the onset and track the progression of damage developed by Zakrajsek, Townsend, and Decker (1993). As with the majority of gear fault indicators NA4 is a modified variation of the 4th statistical moment: kurtosis. The main difference between NA4 and kurtosis is that NA4 is designed to run over a number of different time series signals. The similarities and differences between the two can easily be seen in the formula which is described mathematically as:

$$NA4 = \frac{N \sum_{i=1}^{N} (x_{iM} - \bar{x}_M)^4}{\left\{ \frac{1}{M} \sum_{j=1}^{M} \left[\sum_{i=1}^{N} (x_{ij} - \bar{x}_j) \right]^2 \right\}} \tag{5-4}$$

Here $\bar{x}$ is the mean of the time series, N is the total number of data points in the time series, M is the current time series, and j is the index of the time signal. The unique nature of NA4 meant that to effectively test its capabilities, a separate set of data files were constructed from both the raw and TSA data. This was done by stitching rotations from the different damage levels at the same torque and speed together to create a signal with damage onset and growth. The nature of NA4 meant that applying it to a single value across these new data sets was done in two methods to produce both singular values and multiple values using a rolling window.

Figure 5-39, demonstrates the results for the NA4 for the windowed raw data at 150 Nm. These results are the most coherent with increasing activity correlating with the increasing damage at multiple speeds. Most notably there are 5 major peaks present in the 14.7 micron region, the equal spacing between the peaks indicates that they likely represent the damage occurring in the 5 rotations that make up this portion of the signal. Although the highest amplitude results, on average, are 12000 and 15000 RPM, this is not always the case with 6000 RPM clearly showing prominence at the far end of the 14.7 micron. Despite this however the 3000 and 9000 RPM are not to be seen, with very low amplitudes throughout the signal. This most likely due to the relation between NA4 and kurtosis, with certain waveforms being more uniform leading to the less outliers and a smaller response this can be seen from the NA4 values in Figure 5-39. Given that NA4 has a nominal value of 3, most of the signals are quite low level implying the visible peaks are caused by greater than average outliers when normalised by the increasing denominator.

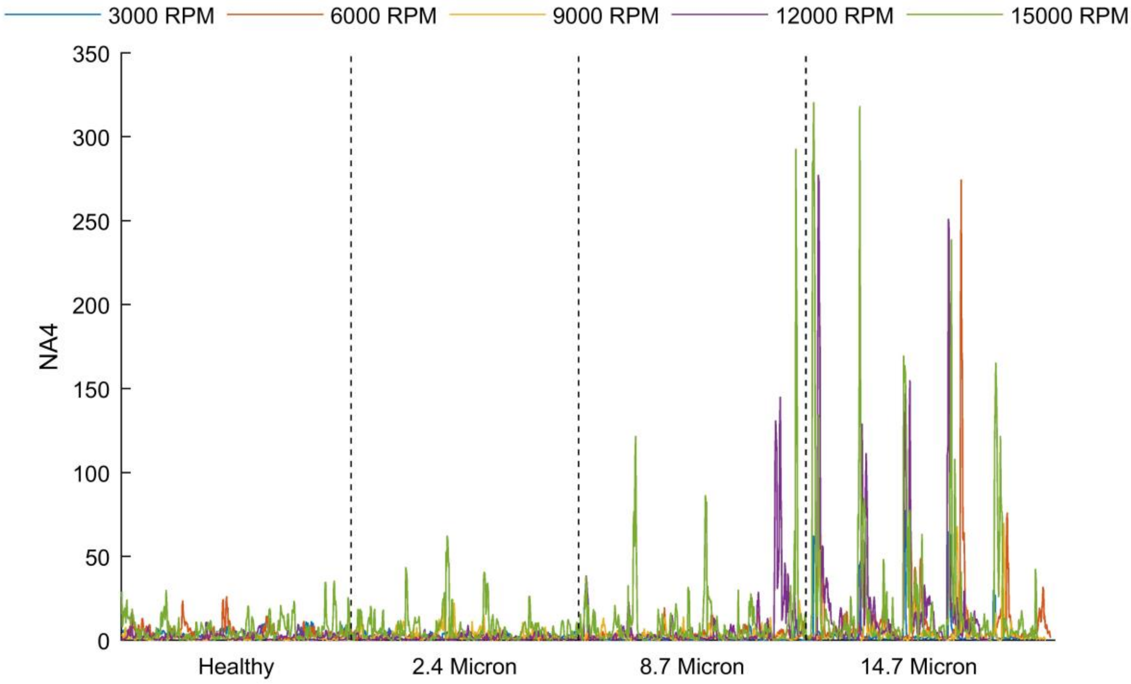

Figure 5-39 – Windowed NA4 for the total captured rotations (approx. 1600) of the raw data for all degrees of damage at 150 Nm torque.

This trend isn’t consistent however with results varying wildly with high amplitude outliers and non-consistent trends, example of which can be seen in Figure 5-40 and Figure 5-41. Here extreme outliers can be observed to reduce all other values to obscurity and no significant trends can be determined.

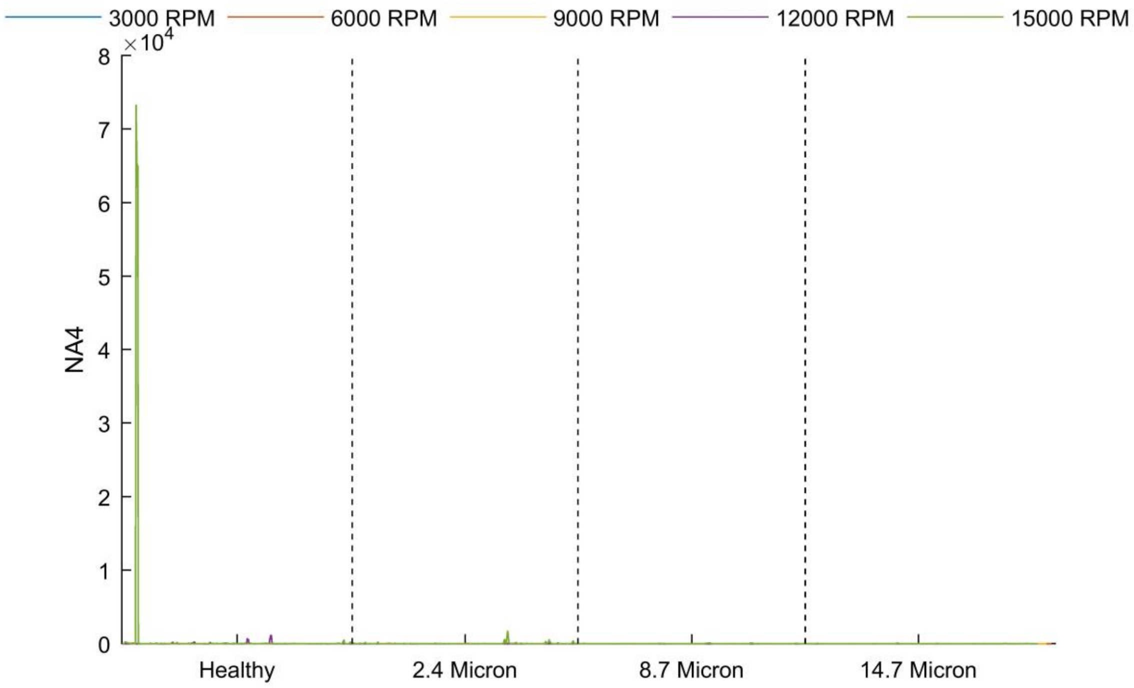

Figure 5-40 – Windowed NA4 for the total captured rotations (approx. 1600) of the raw data for all degrees of damage at 50 Nm torque.

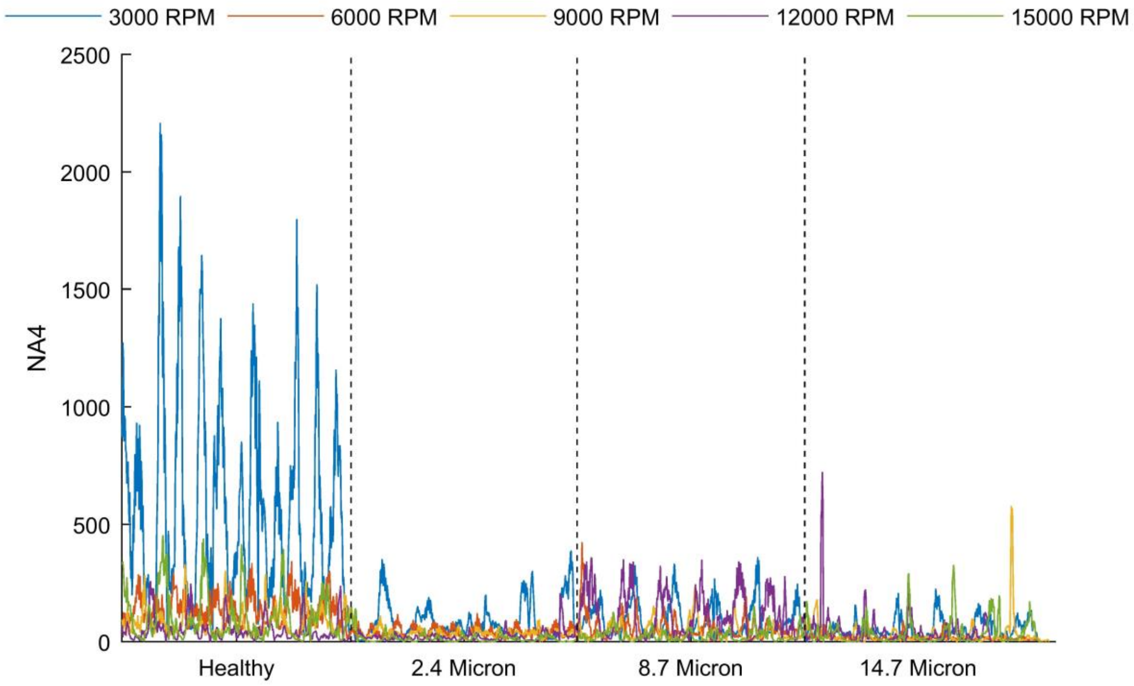

Figure 5-41 – Windowed NA4 for the total captured rotations (approx. 1600) of the raw data for all degrees of damage at 300 Nm

The same application to the time synchronous averaged data produced no benefit as can be seen in Figure 5-42, where amplitudes between the different speeds are erratic and no clear trend is observable between the different damage levels.

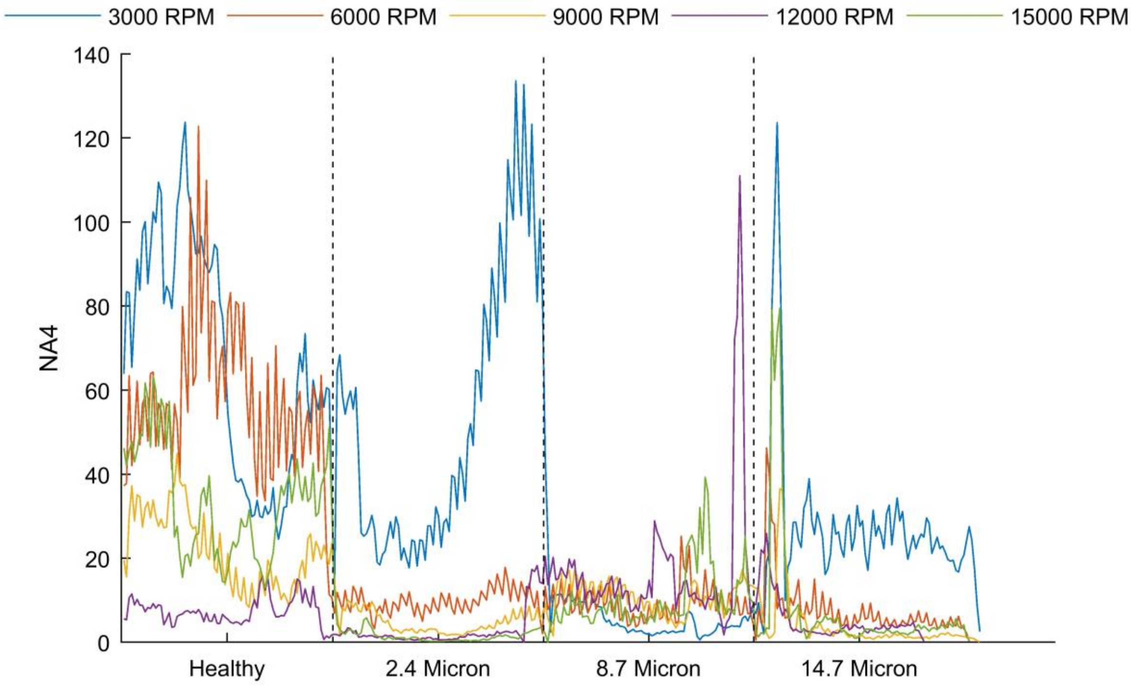

Figure 5-42 – Windowed NA4 the total captured rotations (approx. 1600) of the TSA data for all degrees of damage at 250 Nm.

Removing the window and calculating a single NA4 for each rotation proved to be a more fruitful pursuit with much more controlled values and the removal of any high amplitude outliers. Whilst the raw data still proved to be plagued by anomalous results, on the whole most results showed a much more controlled approach that given more time may be refined into a more usable measure. Currently, as seen in Figure 5-43, this method is not reliable enough where although all speeds display an upward trend they also display a downwards trend as well at non-consistent points. The order of amplitude also goes against what would be expected with the higher speed found at the bottom of the figure. This is not consistent however and the amplitudes jump around wildly with no pattern or apparent reason.

Figure 5-42

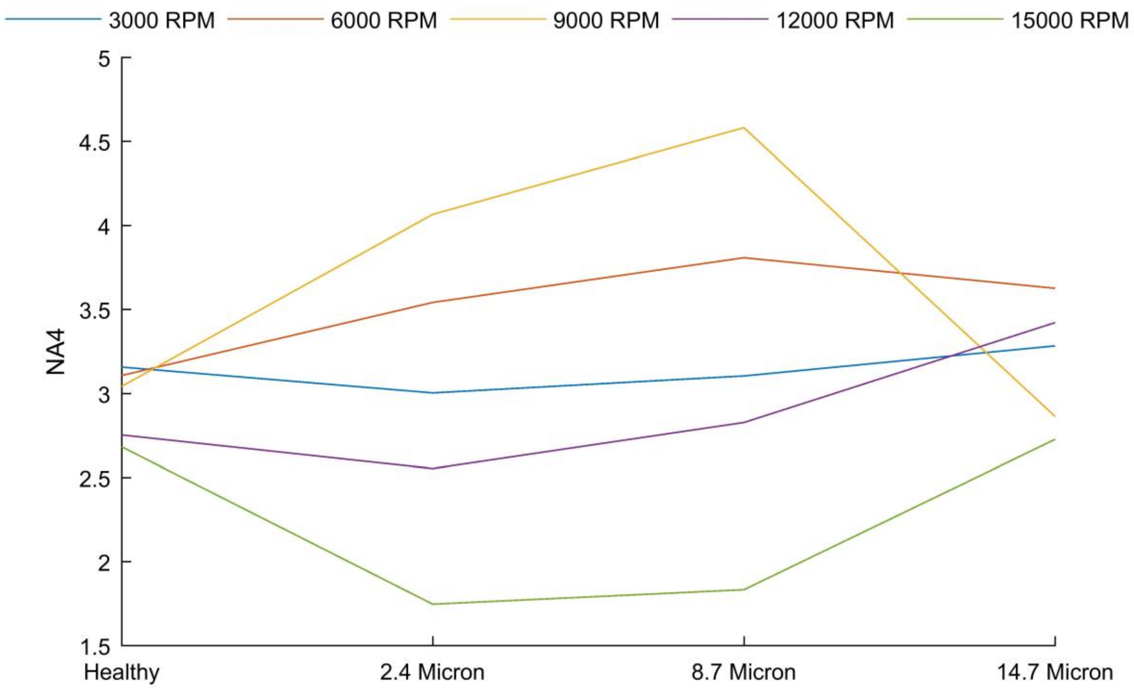

Figure 5-43 – Single value NA4 calculated from raw data at 150 Nm.

Whilst little difference is found with application to the TSA data, some results stand out. One such is Figure 5-44, where a despite a sight abnormal response at 8.7 microns for 3000 and 6000 RPM all figure show a clear upward trend with damage level, with a significant increase at 14.7 microns.

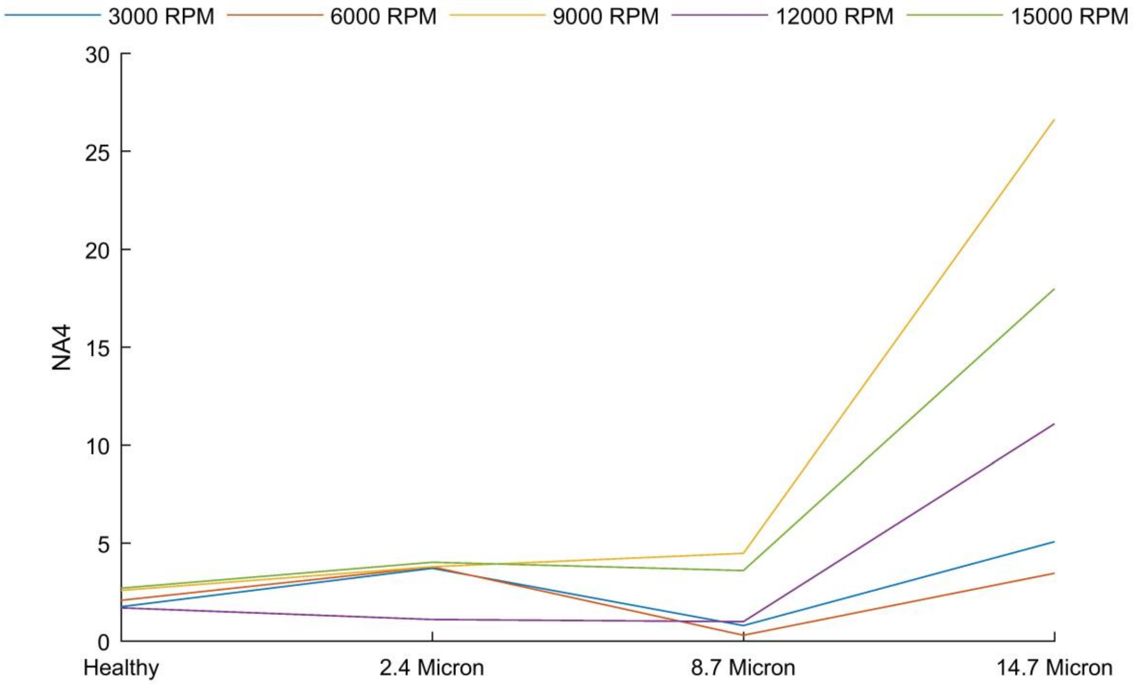

Figure 5-44 – Single value NA4 calculated from TSA data at 150 Nm.

There are notable flaws with NA4 and for this reason the expansion NB4 was also investigated. NB4 differs from NA4 via its use of the Hilbert transform to calculate the envelope of the signal before the application of the standard NA4 formula. Whilst application of NB4 to the raw data wrought much the same results, despite some analogous results remaining NB4 showed a greater ability to detect the damage as demonstrated by Figure 5-45. NB4 displayed a capacity to detect the 14.7 micron tooth bend consistently given the right circumstances and the 8.7 micron at times, however this detection is few and far between and is only seen to be present in the higher speeds i.e. 9000 to 15000 RPM.

While currently the results are unreliable and prone to errors, with speed having a clear effect on the results for both methods. This is inherently due to the method by which the waveforms are being processed. While TSA clearly has a great effect on ROC signals, it is possible that a more targeted averaging/weighting method designed for specifically for ROC signals may allow greater clarity and increase the regularity with which detection of the damage occurs. If possible, the increase in clarity and reliability would allow these techniques to be used as an indicator for increasing damage trends. Of the two NB4 seems the more promising however due to its higher stability when processing data at different torque levels and its ability to detect the 8.7 micron tooth bend, if only intermittent.

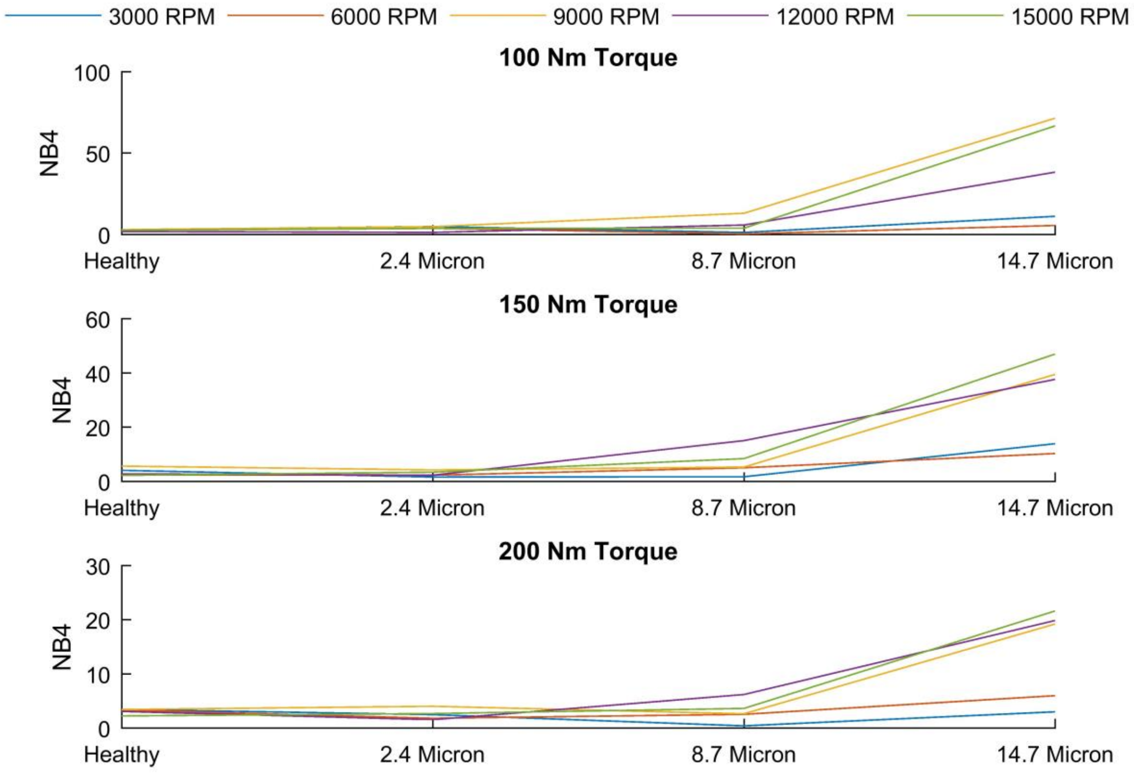

Figure 5-45 – Single value NB4 of TSA data for 100, 150, and 200 Nm of torque.

5.4 Advanced Computational Methods

In additional to the statistical metrics, more advanced techniques were investigated. Unlike the statistics these methods were more involved with purpose designed applications of specific or multiple branches of mathematics. These methods can provide unique ways of interpreting time and frequency data or provide non-trivial applications of well-established methods. Techniques such as these are the result of the availability of computing power in the modern era and are often too time consuming to be performed by hand. The focus of the investigation into the methods presented here was to review alternative approaches to those already applied, namely: moving statistics and frequency analysis.

5.4.1 Multiscale Local Statistics

Developed by Loutridis, S. J. (2008), multiscale local statistics (MLS) were created in response to localised, early stage gear damage e.g. tooth crack initiation, often having little effect on global indicators (i.e. single value metrics) that examine a time-series in its entirety. Presenting a possible solution to this, Loutridis created a combined application of local and multiscale statistics for the four statistical moments: mean, variance, skewness and kurtosis.

From his previous work with wavelets (S. Loutridis, 2004), it was known that a defect maybe more apparent in a certain range of scales (frequencies), due both to the nature of the damage and that the signal-to noise ratio (SNR) may be higher in a range of signals due to the energy involved. Multiscale statistics are part of a branch of mathematics known as multiscale mathematics that focuses on the solving of problems with features on different scales. It therefore allows control over the scale used providing a more robust measure as the method can be tuned to the individual application with local statistics being used to control the region of application via weighting functions.

The first of the multiscale local statistics is the local mean at scale σ of time series *x(t)* and is defined as:

$$\mu(t|\sigma) = m_1(t|\sigma) = g(t|\sigma) \otimes x(t)$$

$$= \int_{-\infty}^{\infty} g(t-\tau|\sigma)\, x(\tau)\, d\tau \qquad \text{(5-5)}$$

Where the multiscale mean is the convolution of *x(t)* and a weighting function *g(t|σ)* with *t* as time and *τ* as a dummy variable. Which weighting function is used is not of consequence so long as it integrates to unity. For the purposes of this work a gaussian weighting function was used:

$$g(t|\sigma) = \frac{1}{\sigma\sqrt{2\pi}} e^{-\frac{t^2}{2\sigma^2}} \qquad \text{(5-6)}$$

An example of the effect of the scale on the response of this weighing function can be seen in Figure 5-46. Where it can be seen as that as the scale value approaches 1, the weighting response becomes much broader as it approaches parity with the x-axis. Opposed to this as σ approaches 0 the weighting becomes infinitely tall and thin. The difference in response shape allows for different frequency ranges to be analysed with the larger scales providing a broadness that allows for the full wavelength of low frequency data to be captured and a smoother result from the moment. Lower values in comparison mean that only higher frequency components are captured in their entirety providing a more localised estimation of the statistics.

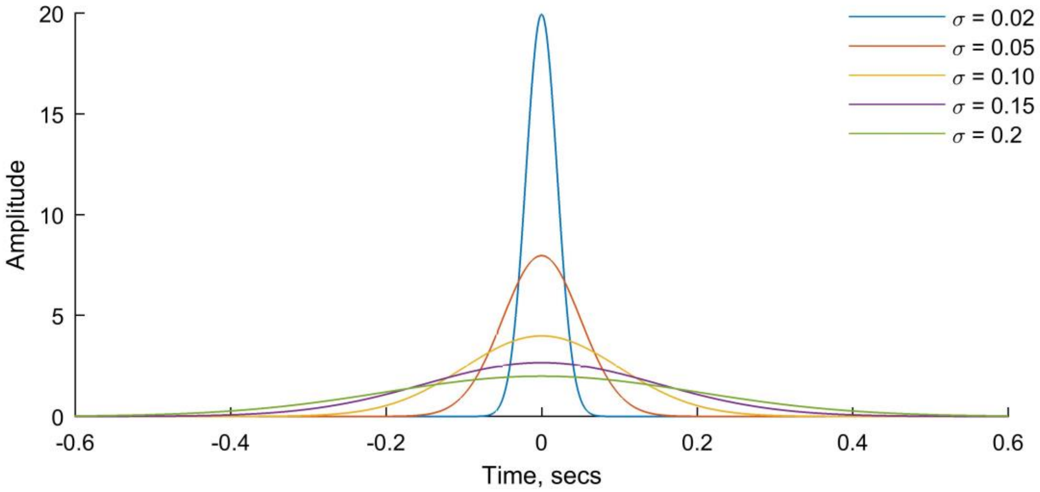

Figure 5-46 – The response of the gaussian weighting function at a range of scales.

Following the definition of the multiscale local mean, the second order moment or multiscale local variance is defined similarly as:

$$m_2(t|\sigma) = g(t|\sigma) \otimes [x(t) - \mu(t|\sigma)]^2$$

$$= \int_{-\infty}^{\infty} g(t-\tau|\sigma)[x(\tau) - \mu(\tau|\sigma)]^2 \, d\tau \tag{5-7}$$

Using equation 5-3 it is possible to define the nth order moment at scale σ as

$$m_n(t|\sigma) = g(t|\sigma) \otimes [x(t) - \mu(t|\sigma)]^n$$

$$= \int_{-\infty}^{\infty} g(t-\tau|\sigma)[x(\tau) - \mu(\tau|\sigma)]^n \, d\tau \tag{5-8}$$

The higher-order moments can then be normalised using powers of the square root of the multiscale local variance meaning the skewness and kurtosis can be defined respectively as:

$$\gamma_3(t|\sigma) = \frac{m_3(t|\sigma)}{\left(\sqrt{m_2(t|\sigma)}\right)^3} \tag{5-9}$$

$$\gamma_4(t|\sigma) = \frac{m_4(t|\sigma)}{\left(m_2(t|\sigma)\right)^2} \tag{5-10}$$

Application of the MLS to the in-loop ROC data was found to not be as straight forward as initially thought. The nature of MLS means that it requires a large amount of memory, and so whilst initially the functions were to be applied to both raw and TSA data it soon became apparent that the computational time and memory required to run the raw data were beyond that of what was available to the author. For this reason, the results presented here are solely generated from the TSA data.

Before analysis could begin the selection of an appropriate scale had to be made. Due to the fixed sample rate, the number of samples per rotation decreases as the speed increases. This means that a singular scale value will have a range of responses dependant on the speed it is applied to as seen in Figure 5-47. Here the scale value has been tuned to provide a reasonable degree of detail at 1500 RPM, but as the speed increases the effect is the same as increasing the scale value, where the waveforms are 'smeared' becoming smoother with a decrease in resolution. There is also a shift of the damage presence by approximately 20° between 1500 and 15000 RPM, this is due to weighting function becoming more broad due to the reduction in samples available caused by the increase in speed and as such the function adjusts the weighting of the samples captured, resulting in a shift. Experimenting, it was found 1x10^5 provided a good balance between too much and too little information at 1500 RPM (visible in Figure 5-47), in order to try and keep the resolution the same for all speeds a ratio was calculated from the number of samples in the desired speed and that of 1500 RPM. Using this ratio, the scale value was altered for each speed to maintain the resolution, while this method was not perfect the results provided were more than adequate for the analysis.

Using the aforementioned scale value and ratio, plots were generated of all four multiscale statistics at single damage level, torque and speed. The results were varied but showed considerable promise with the multiscale local mean and variance successfully detecting the damage in nearly every scenario presented to it.

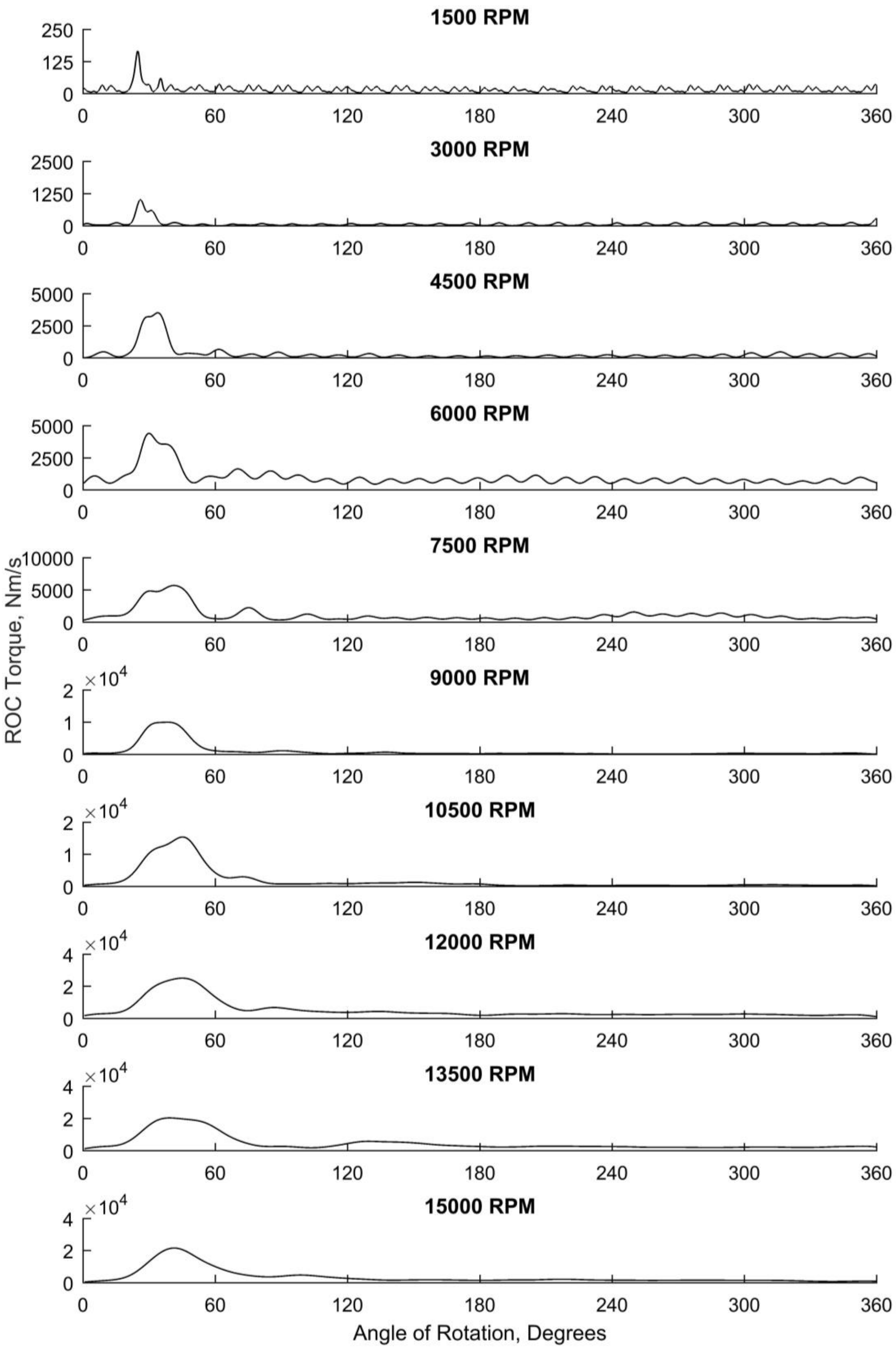

Figure 5-47 – The effect of scale on the multiscale local variance as the speed increases for the TSA data of the 14.7 micron tooth bend at 100 Nm.

Examining Figure 5-48, each method generates a signal that can be broken down into 27 near identical components. A clear response by the mean and variance at 30 degrees, disrupts this pattern momentarily indicating the 14.7 micron tooth bend. Though not as clear as the mean and variance the multiscale local skewness and kurtosis both demonstrate a variation in their respective patterns at around 30 degrees. The standard representation of each tooth in the skewness can be seen to be comprised of 3 peaks - 2 outer larger peaks of similar amplitude forming a 'valley' shaped feature and a smaller increase during the decent of the first peak. The disruption to this pattern comes in the form of an additional peak during the decent of the first peak. Whilst this could easy be dismissed as a random fluctuation, its location and its existence being the only occurrence of this feature implies that it is a small but valid detection of the damage.

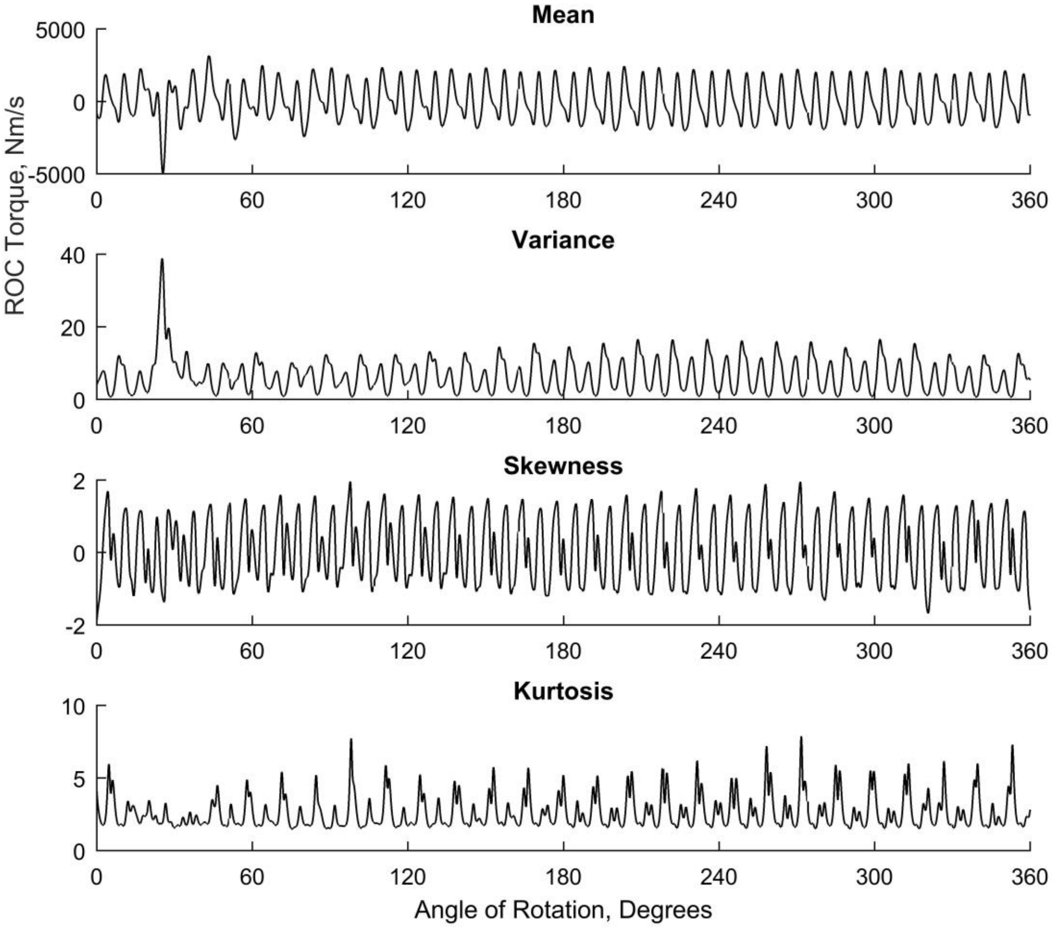

Figure 5-48 – Comparison of the four multiscale local statistics for the TSA data of the 14.7 micron tooth bend at 1500 RPM and 50 Nm torque.

The kurtosis also shows some indication of the damage with a clear reduction in its value around 30 degrees. A reduction in the value of kurtosis is unusual as it implies a lack of outliers within the sample, given the reaction to the other teeth seen across the waveform is fairly consistent it is unclear as to why the damage might illicit a lower reaction than a higher one. Comparison of the multiscale local kurtosis across all the tests, as shown in Figure 5-49 shows that it is clearly the most inconsistent of the 4 moments producing a range of different results. At times it correctly identifies the damage such as in the first two subplots of Figure 5-49, but the identification isn't constant with examples here showing the damage identified by both a reduced and increased kurtosis value. The other examples demonstrate a lack of detection via singular extreme anomalies reducing the visibility of all other detail in the signal, or the damage doesn't generate enough presence to distinguish itself. When compared with the other applications of the kurtosis to in-loop ROC data this is not unusual and further confirms that the kurtosis is less than ideal for damage detection with ROC technology.

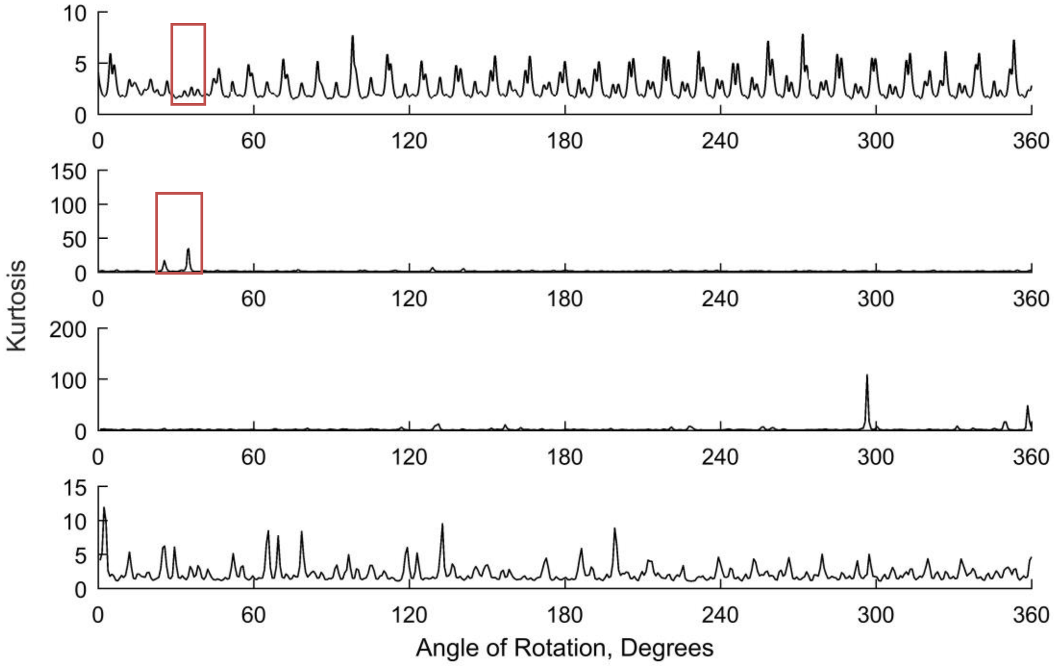

Figure 5-49 – Examples of the different reactions seen by the kurtosis to the TSA data of the 14.7 micron tooth bend.

The results for the mean and variance were largely unaffected by speed and torque as seen in Figure 5-50, which is at the highest speed and torque. A reaction at 30 degrees is clearly visible in the mean and variance signifying the 14.7 micron damage. Whilst the skewness and kurtosis had subtle reactions to the damage at the lower speed and torque present in Figure 5-48, there are no clear reactions that can be directly linked to the damaged tooth. There is a peak present in both statistics at approximately 20 degrees, but due to the location and that no shifts have been seen previously this highly unlikely to be the damage.

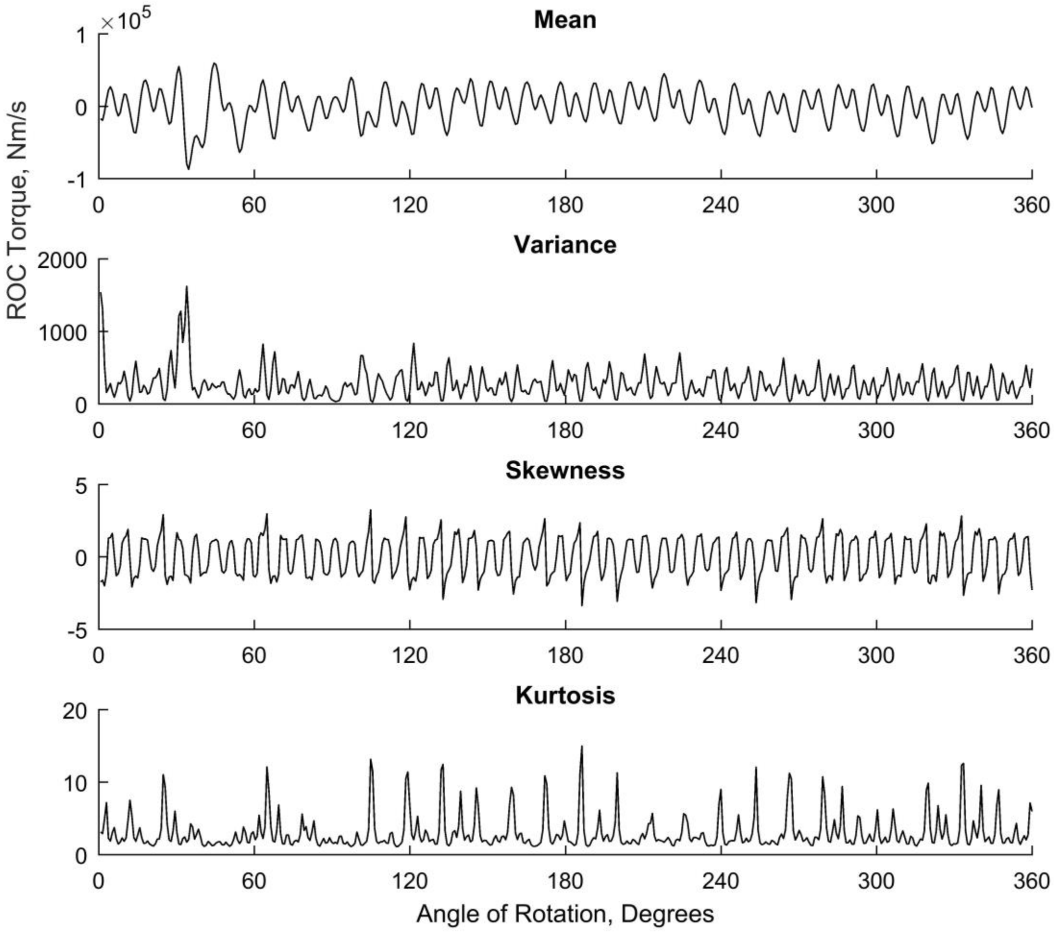

Figure 5-50 – MLS for the TSA data of the 14.7 micron tooth bend at 15000 RPM and 300 Nm torque.

Expanding the analysis, there is a clear decline in the frequency of detection in correlation with the size of the damage. Whilst signs of detection for the 14.7 micron tooth bend were present in nearly all variations of torque and speed, detection of the 8.7 micron tooth bend although still common are visibly less frequent as shown in Figure 5.6. As before there are distinct indications that the damage, previously identified at approximately 240°, is being detected across all 4 statistical moments. The mean and variance are again the prominent results of the 4 with skewness and kurtosis being more subtle, with features differing from an established pattern as opposed to the simple high amplitude peak/trough seen by the first 2 moments.

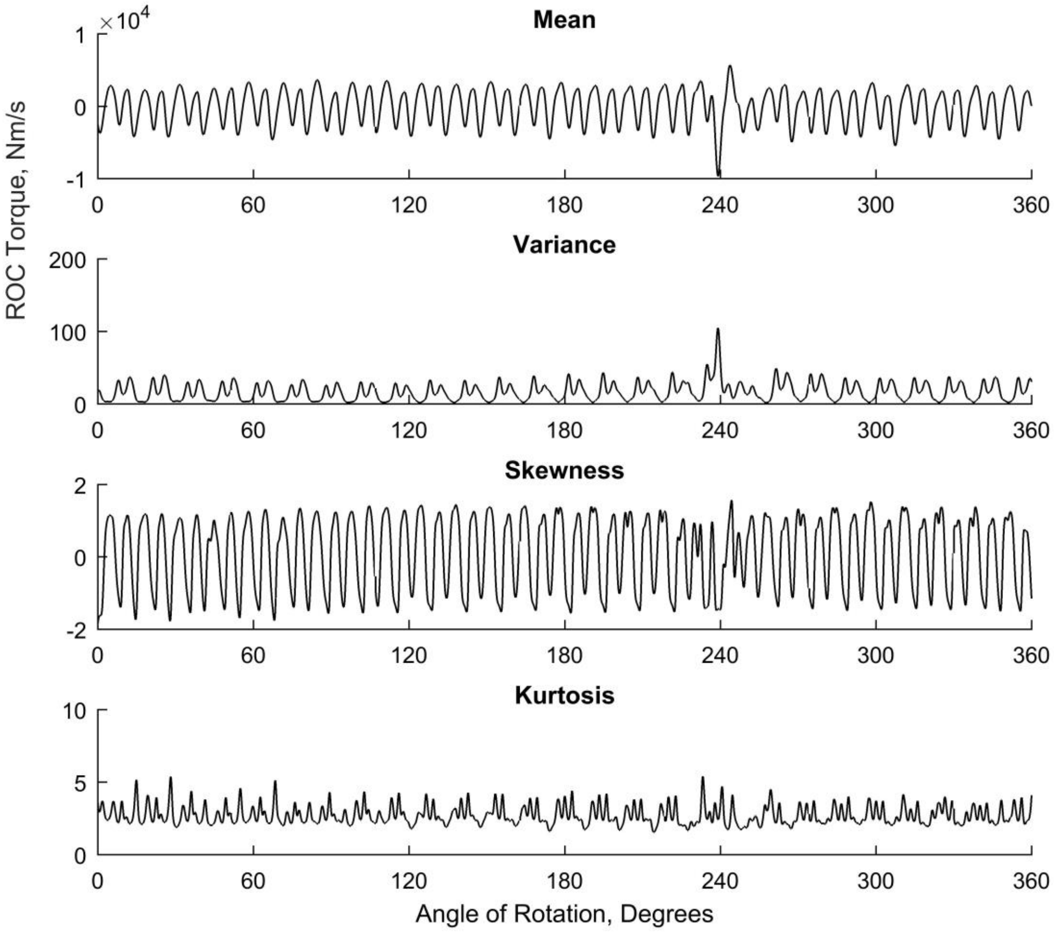

Figure 5-51 – MLS for the TSA data of the 8.7 micron tooth bend at 1500 RPM and 50 Nm torque.

The decline in detection frequency is observed further when the 2.4 micron tooth bend results are examined. At this point the detection rate was around 50% at the lowest torque and 0% at the highest. This is not uncommon however with the smallest tooth bend falling within manufacturers tolerances often making it indistinguishable from the heathy specimen, when the effects of torque and speed are included into this the chances of detecting the 2.4 micron tooth bend are low enough that detection is not expected. When the damage is detected however it is clearly defined against the rest of the signal as seen in Figure 5-52.

Figure 5-52 also demonstrates one of the disadvantages of MLS, specifically affecting the kurtosis and variance. As seen in the multiscale local variance that is a sudden high amplitude spike at the end of the waveform. During the analysis it became apparent that the variance and kurtosis are highly susceptible to end effects, whilst this was easily remedied by mirroring the last 100 data points and then cropping the waveform back to its original length after calculation of the statistical moment, it is an issue that users must be aware of.

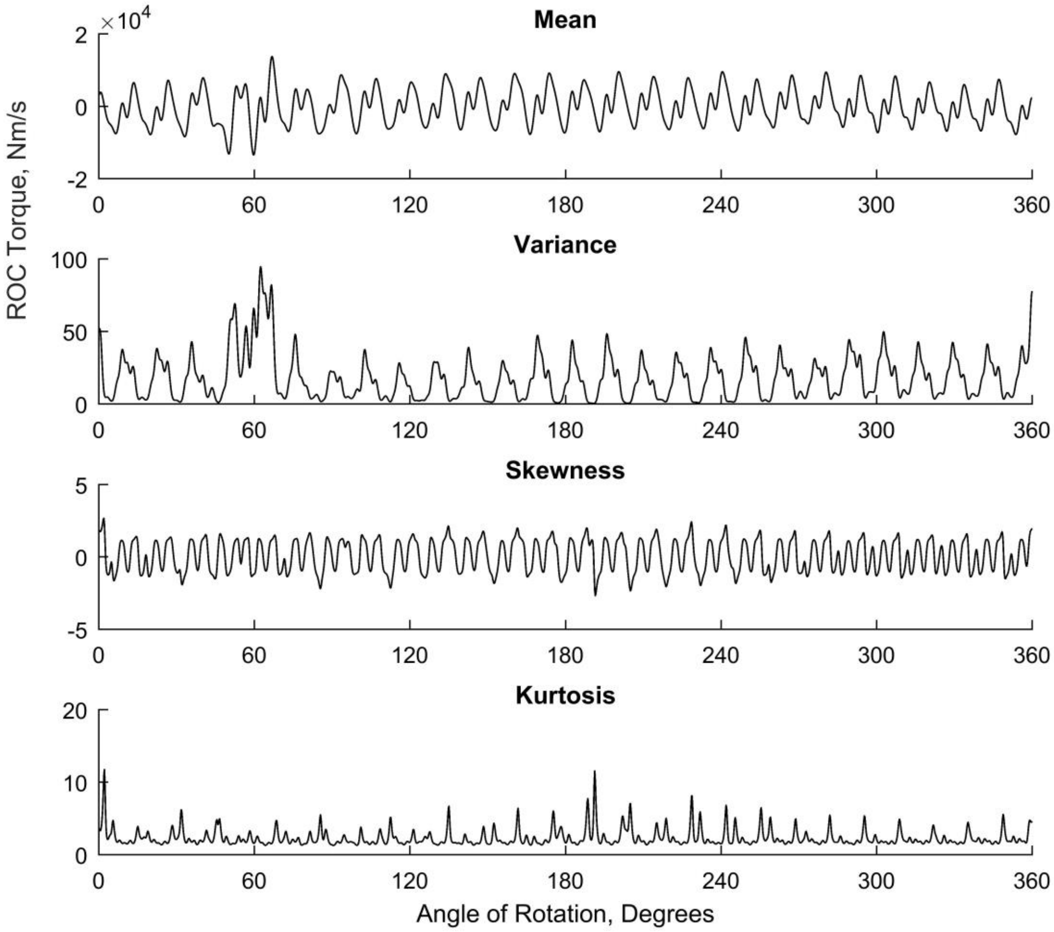

Figure 5-52 – MLS for the TSA data of a 2.4 micron tooth bend at 50 Nm torque and 4500 RPM.

Comparison of Figure 5-52 to Figure 5-48 and Figure 5-51, displays a serious disadvantage of the use of MLS for damage detection using ROC signals. As exemplified in Figure 5-53, it can be seen that there is no consistency in the maximum amplitude of the results. Whilst the overall peak-to-peak amplitude increases with torque and speed as expected, results at the same speed and torque for different damage levels have shown no correlation with respect to damage size. Despite Figure 5-53 showing the 14.7 micron as clearly the most prominent of all the damage, this lacks consistency with certain files producing results where the 14.7 damage would fall below the value of 8.7 and 2.4 micron tooth bends. The ratio of the damage to the signal average doesn't allow for characterisation either as this is as inconsistent as the peak-to-peak amplitude. This makes MLS highly unsuitable for characterisation as it is impossible to interpret the scale of the damage from the results without prior knowledge.

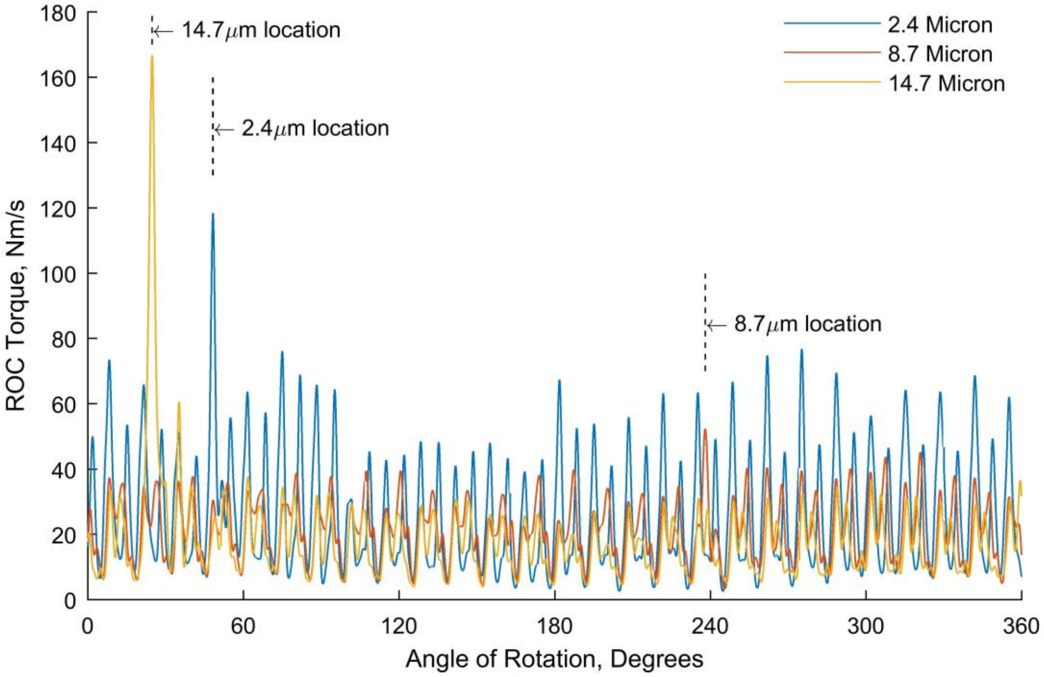

Figure 5-53 – Multiscale local variance amplitude comparison for all damage at 100 Nm torque and 1500 RPM.

Although characterisation is not possible, the multiscale mean and variance have displayed the ability to detect the 8.7 and 14.7 micron tooth bends regardless of speed and torque. It is also possible that the scale selected here by the author is not the most suitable with a higher scale value reducing the amount of information in the results reducing the chances of false positives. It is also possible that a broader area of analysis will increase the detection rate - as areas with more outliers are captured across the region it increases the average reducing the variance and kurtosis, allowing extreme outliers such as the damage to stand out further.

5.4.2 Hilbert Spectra

The Hilbert spectrum and its subsequent derivatives the marginal Hilbert spectrum and the instantaneous energy spectrum are alternatives to the Fourier based spectral analysis methods such as wavelets. Huang, developed the Hilbert spectrum as ‘a new method for analysis of nonlinear and non-stationary data’ (Huang *et al.*, 1998), using a newly created pre-processing method: empirical mode decomposition (EMD), to make the technique self-adaptive to the input data.

The general method for the Hilbert spectrum can be divided in to 2 steps, the first is pre-processing of the data via EMD, the second is the application of the Hilbert transform and calculation of the Hilbert spectra. The empirical mode decomposition was designed by Huang *et al.* (1998) to decompose a signal into intrinsic mode functions (IMFs). An IMF is a function of the original signal where the number of extrema and zero crossings are identical or differ only by one and at any point the mean value of the envelope is one, examples of which can be seen in Figure 5-54.

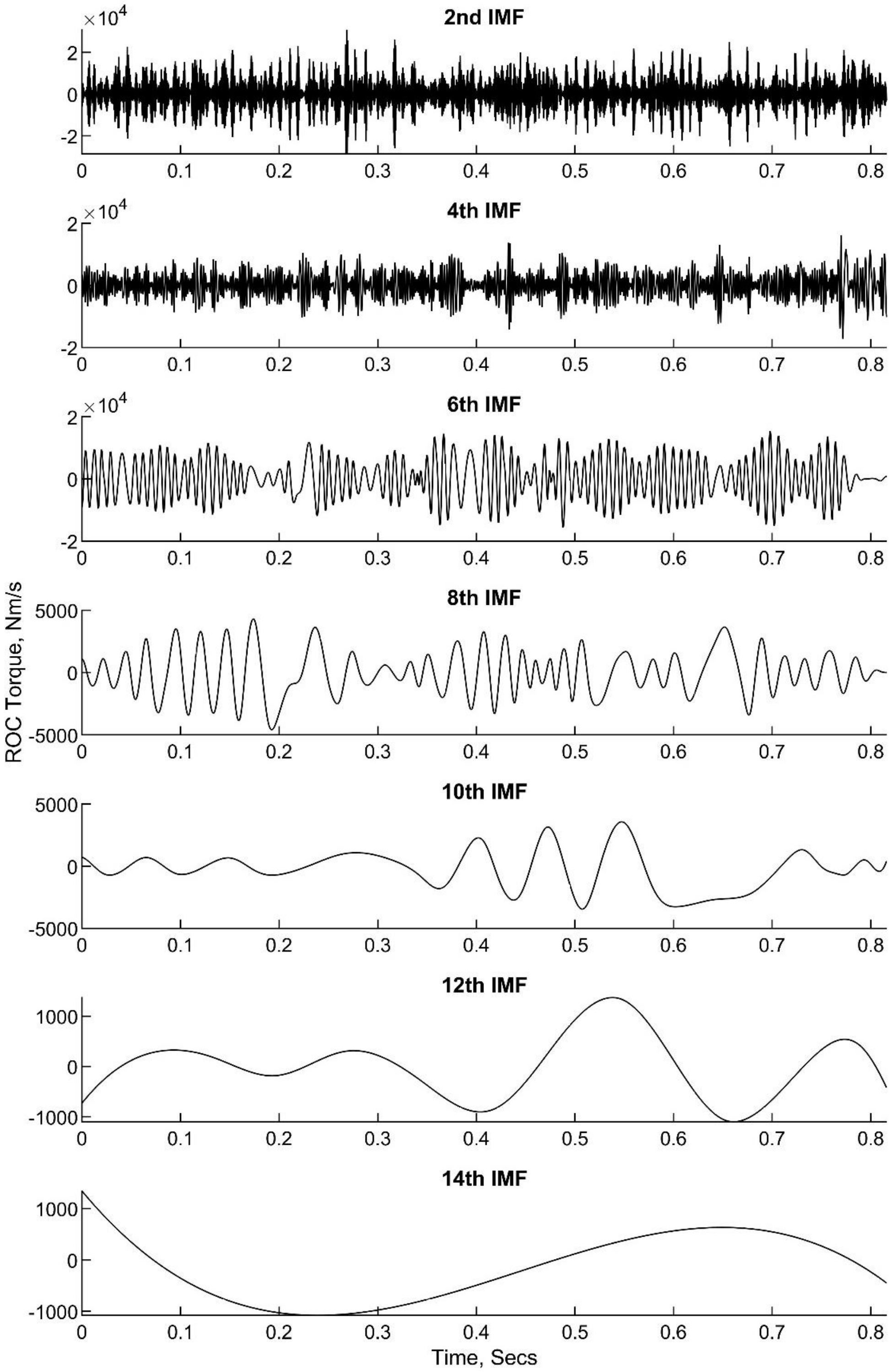

Figure 5-54 – Examples of IMFs generated by decomposing the raw data for the 14.7 micron tooth bend at 7500 RPM and 150 Nm Torque, demonstrating the removal of frequency bands until only the trend remains.

The process of identifying an IMF for a given data set is as follows: The maxima are identified and connected via a spline forming the upper envelope, with the process repeated then for the minima to form the lower envelope. The mean of these envelopes is calculated and designated $m_1(t)$, this mean is then subtracted from the original data:

$$x(t) - m_1(t) = h_1(t) \tag{5-11}$$

The resulting waveform $h_1(t)$ is then checked to see if it is an IMF using the aforementioned defining criteria. If these criteria are not satisfied, then the sifting process is repeated:

$$h_1(t) - m_{11}(t) = h_{11}(t) \tag{5-12}$$

Here $m_{11}(t)$ is the mean of the envelopes of $h_1(t)$. The results of this are checked and if the criteria are still not satisfied the process of sifting and checking repeated up until *n* times when an IMF is found. Where the IMF is then designated:

$$c_1(t) = h_{1n}(t) \tag{5-13}$$

This IMF is then subtracted from the original data with the resulting difference referred to as the residue $r_1(t)$:

$$x(t) - c_1(t) = r_1(t) \tag{5-14}$$

Using the residue as the original signal, the process is then repeated until the final IMF mode is found with the final residue being a constant or monotonic function. The original signal can then be defined as:

$$x(t) = \sum_{j}^{n} c_j(t) + r_n(t) \tag{5-15}$$

This completes the decomposition of the signal $x(t)$ into 'n-empirical IMF modes, plus a residue $r_n(t)$, which can be the mean trend or a constant' (Li *et al.*, 2006). With the IMFs defined the Hilbert spectrum (sometimes referred to as the Hilbert-Huang spectrum) can be calculated. Applying the Hilbert transform to each IMF an analytic signal $z_j(t)$ is defined:

$$z_j(t) = c_j(t) + iH[c_i(t)] \tag{5-16}$$

This is also expressed as:

$$z_j(t) = a_j(t)e^{-i\omega_j(t)} \tag{5-17}$$

Where $a_j(t)$ is the amplitude and $\omega_j(t)$ is the instantaneous frequency. These quantities can further be defined as such:

$$a_j(t) = \sqrt{c_j^2(t) + H^2[c_j(t)]} \tag{5-18}$$

$$\omega_j(t) = \frac{d\theta_j(t)}{dt} \tag{5-19}$$

Where phase $\Theta_j(t)$ is defined as:

$$\theta_j(t) = \tan^{-1}\left(\frac{H[c_j(t)]}{c_j(t)}\right) \tag{5-20}$$

Using equation (5-17, the amplitude and instantaneous frequency can be displayed in a 3D time-frequency plot designated as the Hilbert spectrum which is defined as:

$$H(\omega, t) = \sum_{j=1}^{n} a_i(t) e^{-i \int \omega_j(t)} \tag{5-21}$$

The Hilbert spectrum provides information on the amount of energy per frequency with respect to time. This can be simplified into the marginal Hilbert spectrum (or simply marginal spectrum) and the instantaneous energy spectrum that display the total energy per frequency and the total energy per unit of time and are expressed as:

$$\begin{gathered} h(\omega) = \int_0^T H(\omega, t)\, dt \\ E(t) = \int_{-\infty}^{+\infty} H^2(\omega, t)\, d\omega \end{gathered} \tag{5-22}$$

From this the local marginal spectrum and instantaneous energy spectrum can be defined. These provide information on the contribution of each IMF with regards to the total amplitude contribution per frequency and energy with respect to time respectively. These are therefore defined as:

$$h_j(\omega) = \int_0^T H_j(\omega, t)\, dt \tag{5-23}$$

$$E_j(t) = \int_{-\infty}^{+\infty} H_j^2(\omega, t)\, d\omega \tag{5-24}$$

The nature of this process, with regards specially to EMD is quite time consuming, sometimes with the with the sifting process being over-decomposing due to the end criteria not always being met. For this reason, the end conditions for EMD are heavily debated in the literature with many different approaches being taken to optimise the process such as Rilling *et al.* (2003) Sun *et al.* (2010) and Li *et al.* (2017). The time-consuming processing associated with this technique meant that there was not sufficient time to process the local spectra as well as the complete spectra, however, as will be demonstrated later it is unlikely that these additional spectra would have provided anything further.

Hilbert Spectrum

Examining the Hilbert spectrum for the 14.7 micron damage (Figure 5-55), there is nothing that indicates the presence of the damage. From examining Figure 5-55, it is clear that there are no regular patterns or consistent areas of increased amplitude that may be linked to the presence of the damage.

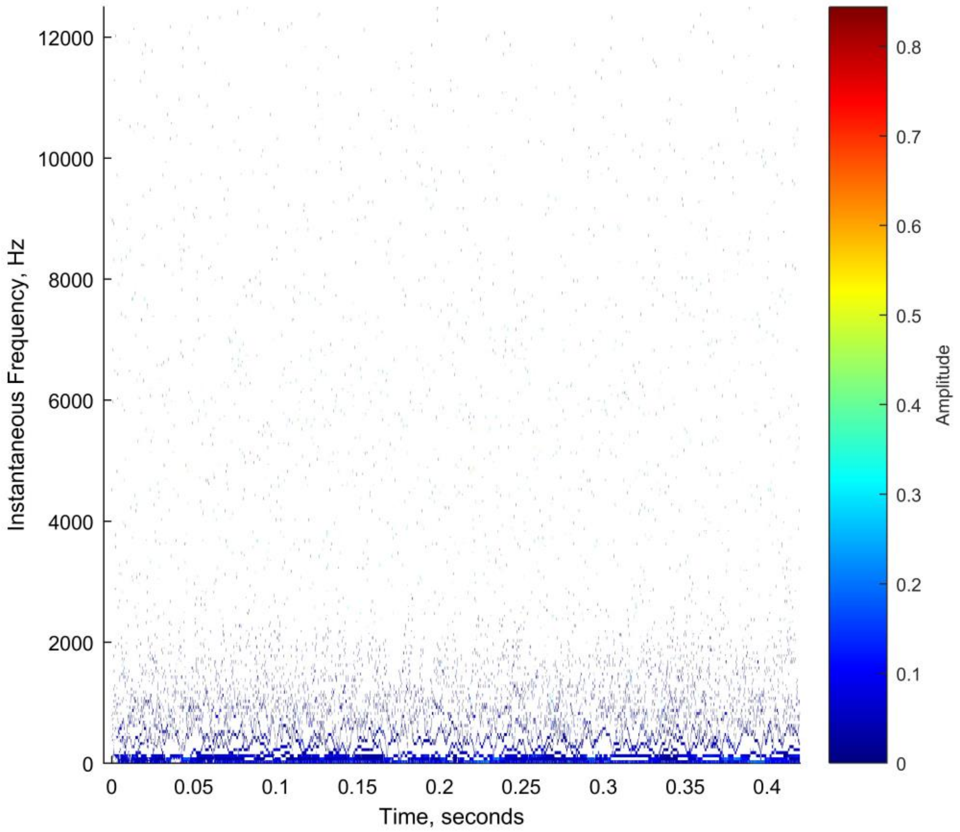

Figure 5-55 – Hilbert spectrum for the raw data of the 14.7 micron tooth bend at 150 Nm and 7500 RPM

Comparison to the healthy data sets saw a reduction in the maximum amplitude as well as a general decline in the amount of sub-2000 Hz noise. As Figure 5-56 demonstrates, the healthy specimen contains a band on frequencies roughly centring around 1000 Hz with boundaries ranging approximately from 250 to 1500 Hz. This region is densely populated with a majority of the activity being present in this region, this is excluding the sub 100 Hz bands where the rotational frequencies and noise occur. This region is of interest as comparison to the damaged specimen, shows that the 14.7 micron tooth bend has a higher upper boundary to this region of approximately 2000 Hz. Above this region it was found that no information could be determined with sporadic low-level noise being seen throughout the both healthy and damaged time series. With no determinable effect, the focus of the rest of the analysis of the Hilbert spectrum was directed at the 0-3000 Hz area.

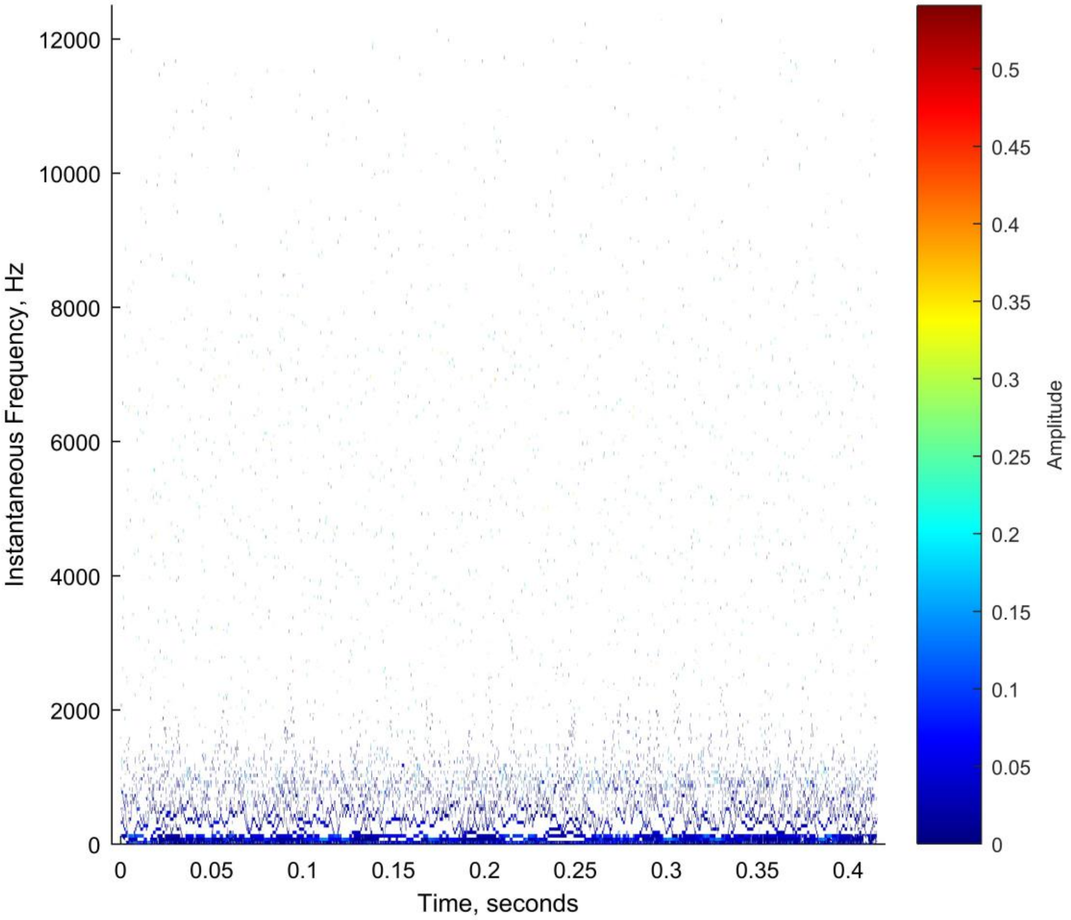

Figure 5-56 – Hilbert spectrum of the raw data for the healthy specimen at 150 Nm torque and 7500 RPM

The aforementioned band was best highlighted at 1500 RPM and 100 Nm torque (Figure 5-57), where it can clearly be distinguished from the rest of the figure and seen to possess a higher amplitude. From Figure 5-57 it was also established that another band of frequencies is continuously present around 500 Hz, however it is less well defined than the higher frequency band. This band was initially thought to represent the meshing frequency given its position and continuous presence throughout the signal. Examination of higher speeds however brought this into doubt as the band did not shift as would be expected but instead expanded covering a larger range of frequencies making it less distinct and harder to distinguish resulting in the difference between Figure 5-56 and Figure 5-57.

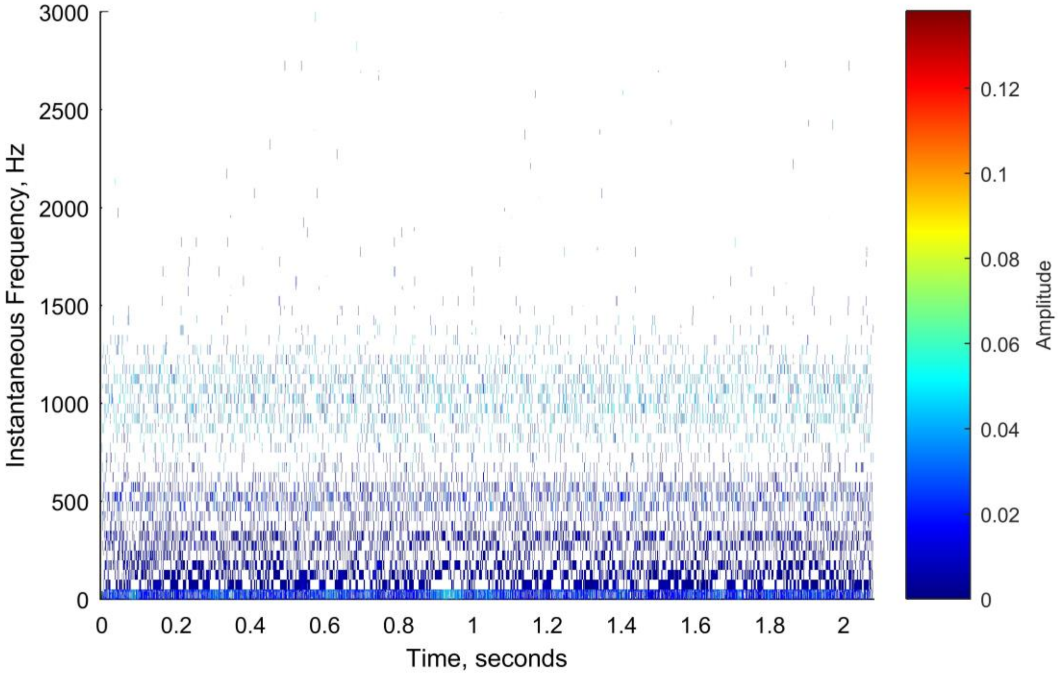

Figure 5-57 – Hilbert spectrum for the raw data of the healthy specimen at 1500 RPM and 100 Nm.

Comparing the Hilbert spectrum of the different damage levels showed that these different bands increase in energy as well as in range. Whilst the 2.4 micron tooth bend exhibited no significant changes from the healthy, the 8.7 micron lacks the distinct band at 500 Hz, with instead the region being merged with the lower frequencies present, making it nearly indistinguishable. The upper band extends to higher frequencies than the healthy with it reaching 1500 Hz as opposed to the approximately 1250 Hz maximum reached by the healthy specimen.

The 14.7 micron tooth bend displays very similar results to the 8.7 micron but with the bands better defined and with higher overall energy. The upper band has decreased density of the frequencies appearing between and 1000 and 1500 Hz, but increased frequencies between 1500 and 2000 Hz. The difference between these two regions for the two damage levels is marginal. The differences are so slight it is impossible to say that these changes are due to the increase in tooth deviation or changes in testing conditions. The increasing levels of amplitude present in these bands across the healthy specimen, 8.7 and 14.7 micron damage is thought to be a result of the increasing size of the damage. Given the propensity of these bands in the Hilbert spectrum to disperse with additional speed, even if such a trend is true it is irrelevant as any information would be lost above the lowest speeds.

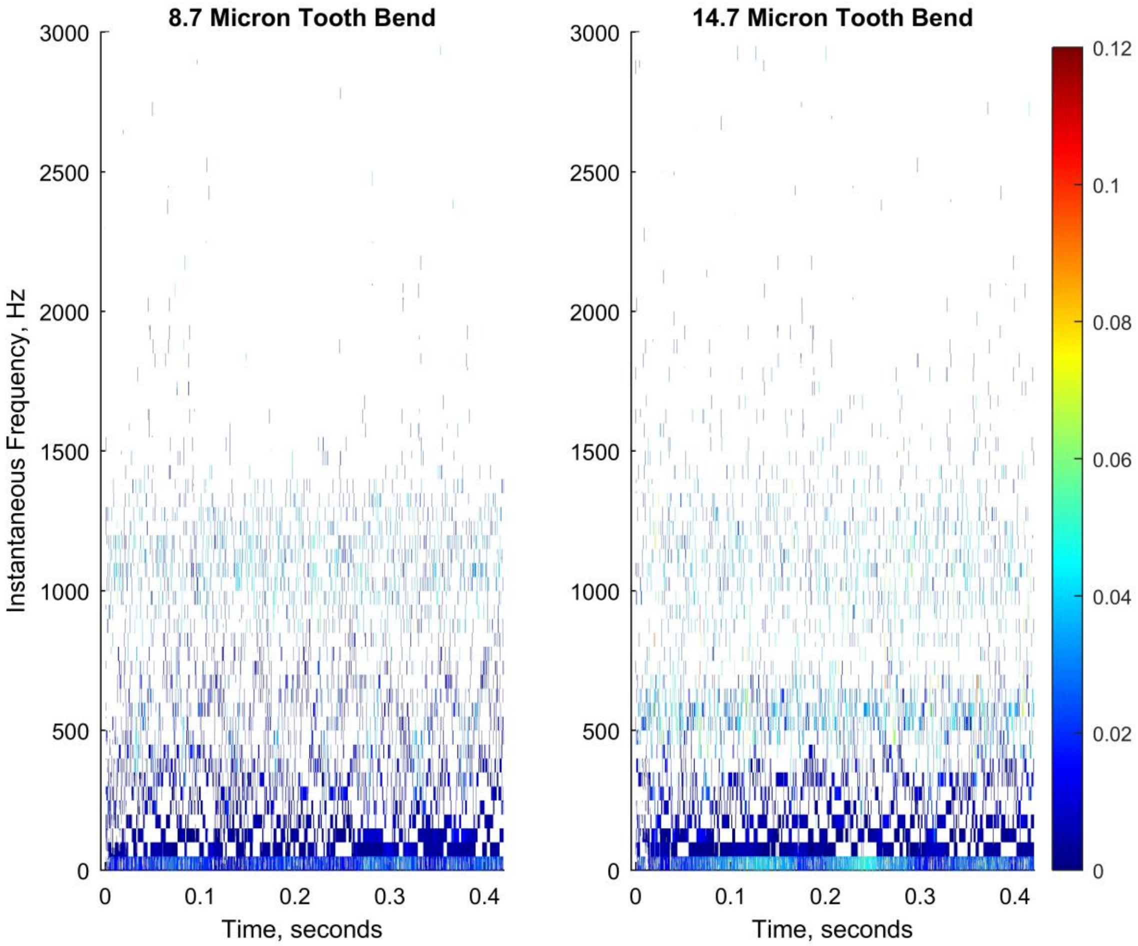

Figure 5-58 – Comparison of the Hilbert spectra for the raw data of the 8.7 and 14.7 micron tooth bends at 1500 RPM and 100 Nm torque.

In an attempt to rectify this issue, non-stationary frequencies were removed from the spectrum by processing the TSA data. Examining the same speed and torque resulted in higher clarity as presented in Figure 5-59. Here the individual contribution of each IMF can be loosely seen. Little information can be drawn from this however, with no trends being easily identified and all traces present appearing to be erratic and non-sensical. The only discernible difference between the spectra in Figure 5-59 is the lack of frequency content around 750 Hz after 60° in the 14.7 micron tooth bend spectrum. Whether this is an indication of the damage is difficult to say, but it is in the author’s opinion that it is unlikely to be so as whilst there is frequency content before 60°, the transient indicating the tooth bend only exists for a short duration at 60°. It is highly unlikely for this transient to cause a shift in frequency over a wider area and given that there is no direct evidence of the tooth bend at its known location.

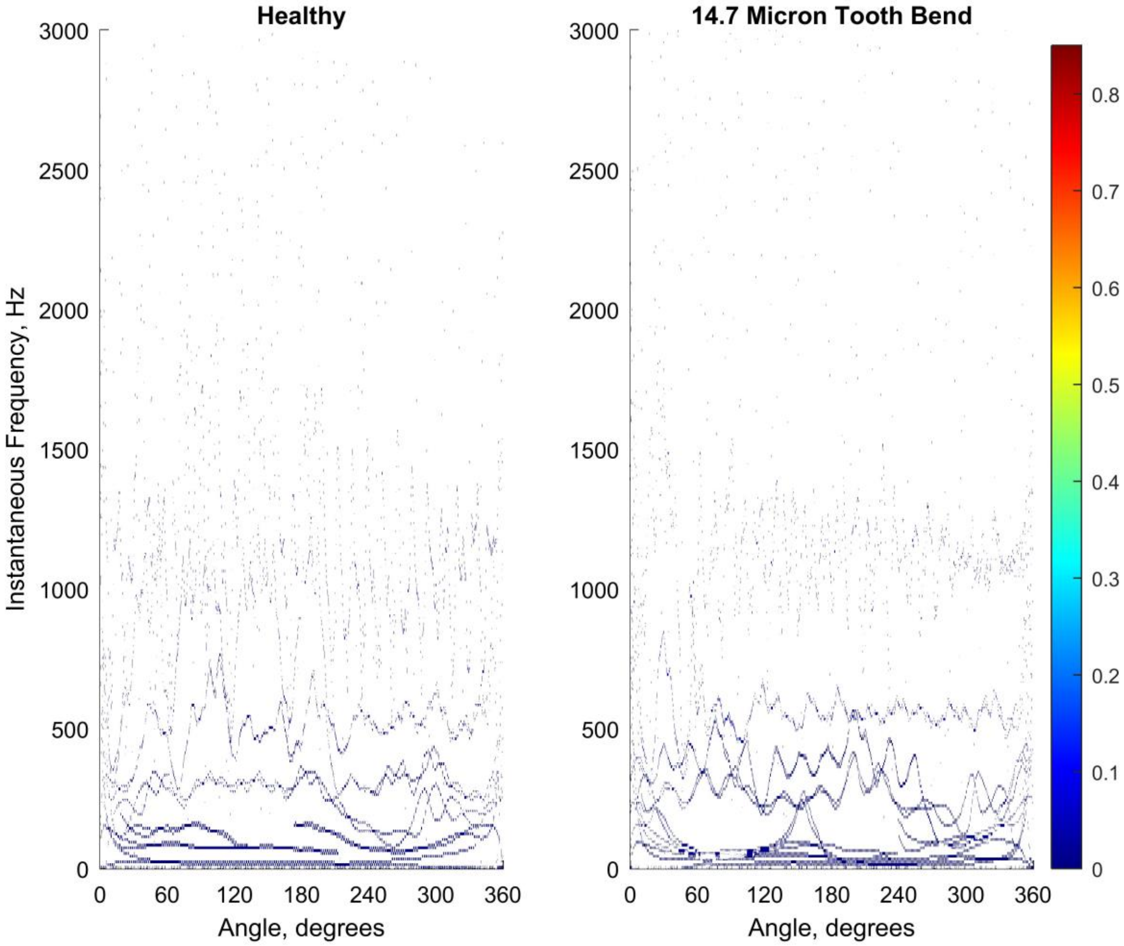

Figure 5-59 – Comparison of Hilbert spectra for the TSA of the healthy gear pair and 14.7 micron tooth bend at 100 Nm torque and 1500 RPM.

Marginal Spectrum

The marginal spectrum which shows the total amplitude contribution per frequency of the HHS, provided more clarity as to the overall frequency content of the Hilbert spectra, allowing for better identification of the frequencies with high intensity. Despite this, it was clear that very little additional information was available, and the ineffectiveness of the technique was made further apparent. Figure 5-60 shows that the two previously identified bands were centred closer to 600 and 1100 Hz, with the 14.7 micron having the greatest amplitude. Whilst it was previously thought that the 8.7 micron damage had a higher amplitude than the healthy spectrum in these regions, the marginal spectrum shows that this is not the case with the 8.7 micron damage having either similar or lower amplitude than the healthy results. If the marginal spectrum for the healthy gears is taken as a baseline, then it quickly becomes apparent that the only damage that could be consistently identified is the largest i.e. the 14.7 micron tooth bend.

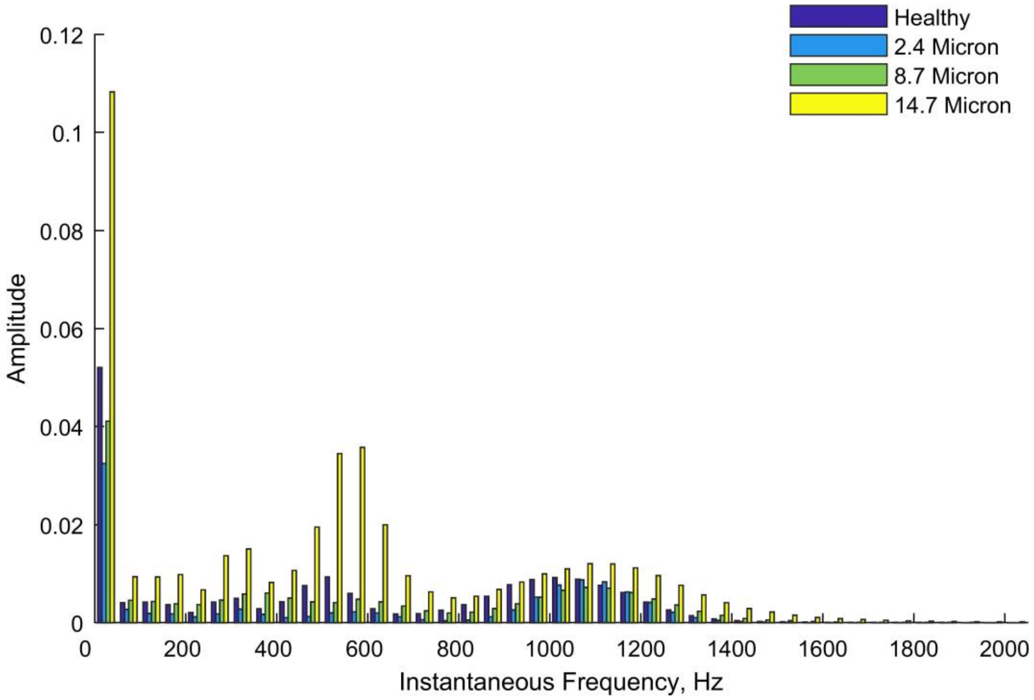

Figure 5-60 – Marginal spectrum for the raw data of all gear pairs at 1500 RPM and 100 Nm.

Increasing the amplitude and torque provided further clarity in certain circumstances, such as in Figure 5-61 where the 8.7 and 2.4 micron tooth bends do exhibit higher average amplitudes for the first 400 Hz after which the amplitudes of the damage excluding the 14.7 micron damage settle to similar or lower levels than the healthy results. In these conditions using the healthy marginal spectrum as a baseline and comparison of the frequencies over the first 400-600 Hz would allow for the damage to be successfully identified, however these results are circumstantial and are not repeatable as demonstrated by Figure 5-62

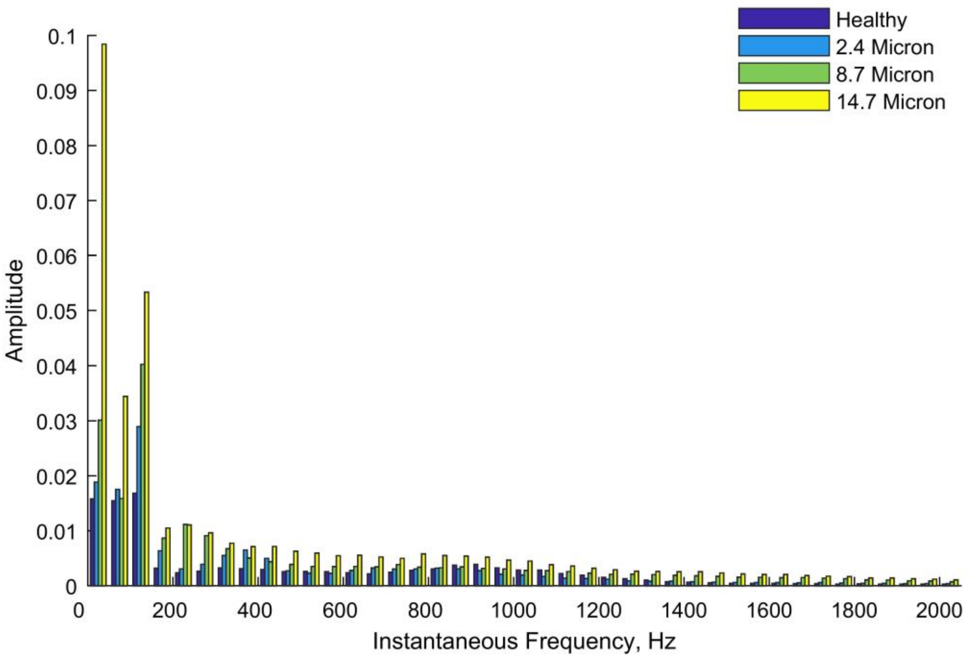

Figure 5-61 - Marginal spectrum for the raw data of all gear pairs at 7500 RPM and 150 Nm.

Figure 5-62 further confirms the instability of the use of EMD to access damage in ROC signals, where yet again the results differ from those previously seen. Here with the 14.7 micron 50 Hz bin possesses an exaggerated amplitude that causes a lack of clarity in the other frequencies, although an automated method comparing frequencies to a baseline would not be hindered by this. Examination of the other frequencies sees that there is little that represents the trend seen in Figure 5-61 with frequency amplitudes often being lower than those of the healthy spectrum or close enough that a blind test would make identification near impossible.

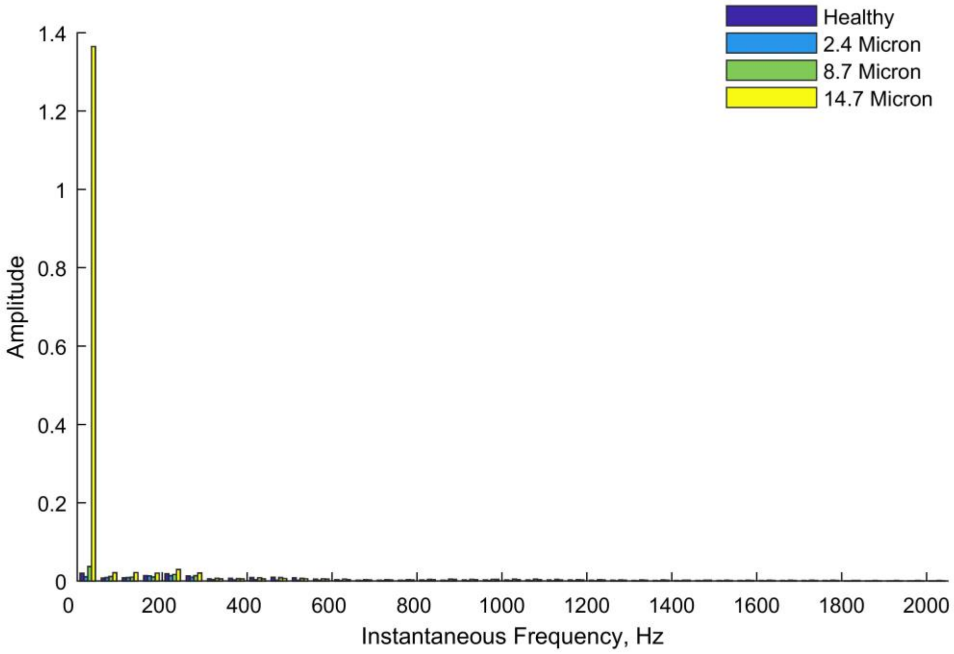

Figure 5-62 – Marginal spectrum for the raw data of all gear pairs at 15000 RPM and 300 Nm.

Instantaneous Energy Spectrum

With the lack of success of the preceding two spectra and the mathematical relationship between the instantaneous energy spectrum (IES) and Hilbert spectrum, it was unlikely that it would be able to provide any significant improvement. The results from the raw data were, as expected, erratic with changes to the spectra being seen with every speed and load change with no comparative indication of the damage possible. Application to the TSA data was more promising however, while the reaction would be too inconsistent for the basis of a condition monitoring system, areas of high energy correlating with the damage in the TSA waveform were successfully detected for all three damage specimens.

Figure 5-63 shows the clearest IES for each of the three damage levels, with visible indications of the damage present at 60°, 240°, and 30°. The maximum amplitudes of the three waveforms can be seen to increase with the scale of the damage but due to the infrequency of clear results, examples of which can be seen in Figure 5-64, it is impossible to tell if this is due to the size of the tooth bend or the effects of the speed and load of the test. Notably the results for the 2.4 and 8.7 micron tooth bends can be seen to show a count of 27 repeated patterns suggesting that they are in fact capable of reacting to the meshing cycle within the ROC signal.

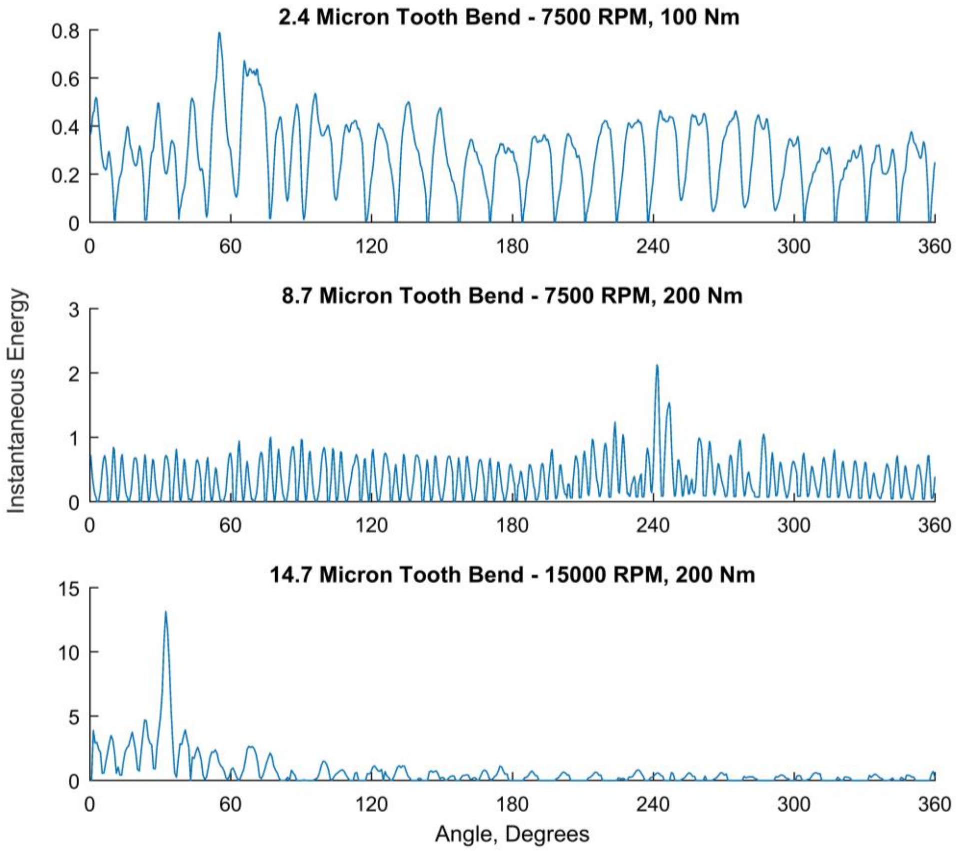

Figure 5-63 – Instantaneous energy spectra for the clearest examples of successful detection for all damages using TSA data.

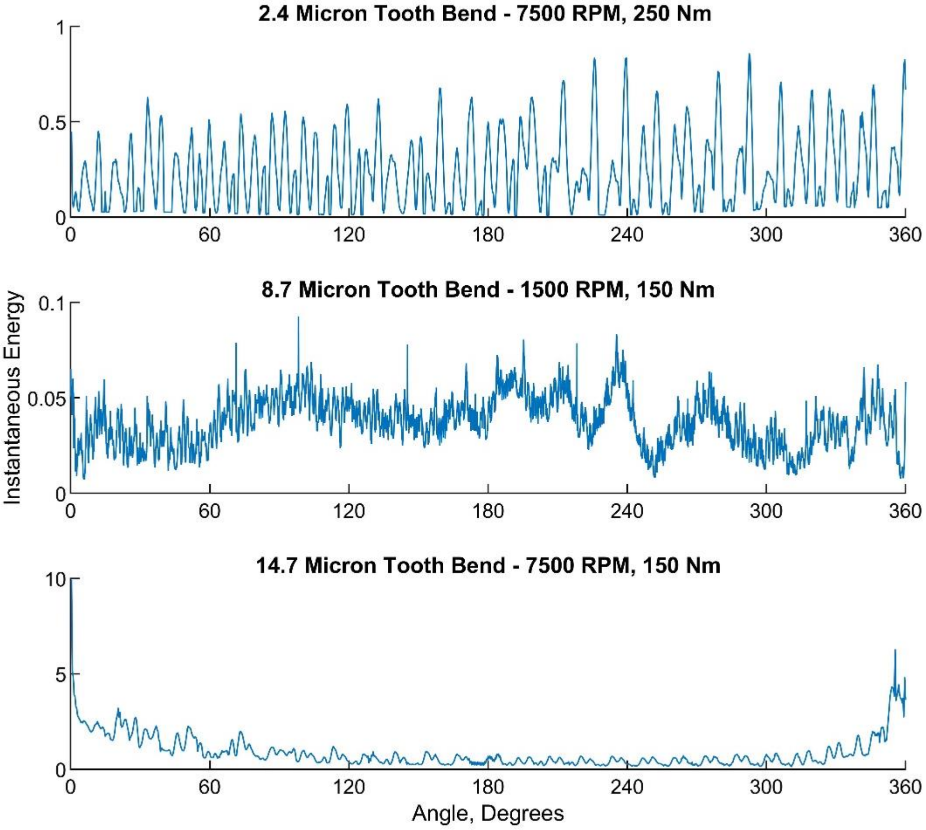

Figure 5-64 – Instantaneous energy spectrum of TSA data where no detection was possible for all damage levels.

It is then unclear as to why the reaction is so inconsistent, given the regularity of the original ROC signals. The largest factor in the process is likely responsible i.e. EMD, it is possible that the method by which EMD decomposes a signal is simply not suited to ROC technology and a different decomposition method such as wavelets or local mean, may produce more consistent results. This is entirely speculation however as the timescale of this project did not allow for these additional decompositions to be tested. There is clearly potential with IES, however more work is required to ascertain the true level of its abilities.

5.5 Bearing Failure

During a repeat of the initial set of tests, the high-speed rig suffered from a catastrophic failure of the rear bearing of the pulley support block. While the data at the exact moment of the failure was lost due to the emergency stop being activated, the data preceding this point was captured. Data captured directly after the bearing replacement provided the opportunity to for a preliminary study to determine the abilities of ROC technology to detect bearing damage.

Given that the core focus of this project is the application to gears, this study was not as extensive as the gear investigations. ROC technology has been previous applied to rolling element bearings by Kari (2011), using frequency analysis to detect damage in a simulated helicopter transmission. There are some key differences between this failure and Kari's work however, the first is that the Cardiff rig is significantly more complex than the setup than that used in Kari's work with 14 bearings present in the test head across both shafts. Secondly, the failure occurred in a bearing which is external to the torque loop. Experience dictates that this will have a negative effect on the amplitude of the bearing failure, suggesting that detection of the initial stages of the failure would be difficult to detect. Given that the bearing failed due to gross overloading because of misalignment and considering the severely damaged condition of it upon inspection proceeding the failure, it is unlikely that this will have a significant effect towards the end of the bearings life. For this study frequency analysis was performed alongside examination of the raw/TSA waveforms. As the main focus is on gears, bearing specific metrics and damage detection methods have not been covered within the literature review.

From a comparison of the raw waveforms, a decrease in peak-to-peak amplitude after the replacement bearing has been fitted can be witnessed. As Figure 5-65 displays however, this initial pre-failure amplitude is related to the meshing cycle with the largest presence being the 54 distinct peaks indicating the 27 teeth present on the mainshaft gear across the 2 rotations. The difference in the presence of the meshing cycle before and after the bearing failure would imply that the cause of this decrease is a difference in torque caused by the manual loading system being imprecise. The post-failure rotation indicates that less torque has been locked into the system resulting in a lower amplitude reaction from the meshing cycle. Despite this amplitude change there appears to be a little evidence of the bearing failure in the signal, whilst a transient is also visible in the signal it is present both before and after the bearing failure, suggesting a different cause, which may relate to another damaged component.

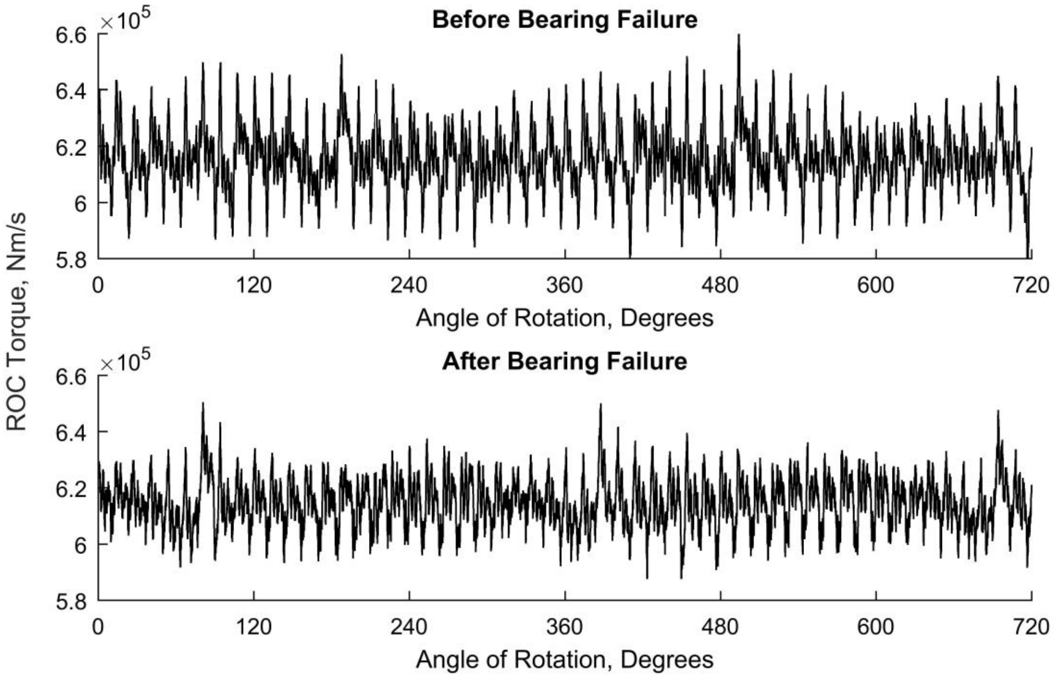

Figure 5-65 – Two rotations of raw data for the 2.4 micron tooth bend approximately two hours before the bearing failure compared to data after the replacement at 3000 RPM and 100 Nm torque.

Through simple calculations this transient was seen to appear once a rotation for the layshaft, because of this the data was plotted with respect to the layshaft instead of the main, as shown in Figure 6.2. Plotting each rotation stacked over the others highlighted the trend with it being seen at roughly 350° before the failure and 250° afterwards (note that the rig was disassembled after the failure). Notably this abnormal transient was not present in every set of data, with the healthy and the 14.7 micron tooth bend specimens showing no signs of the transient after the bearing failure, the reason for this is not yet understood and more testing is required for confirmation. This is also true for higher torques, however this is likely related to the change in peak-to-peak amplitude of the meshing cycle caused by increasing load masking this transient.

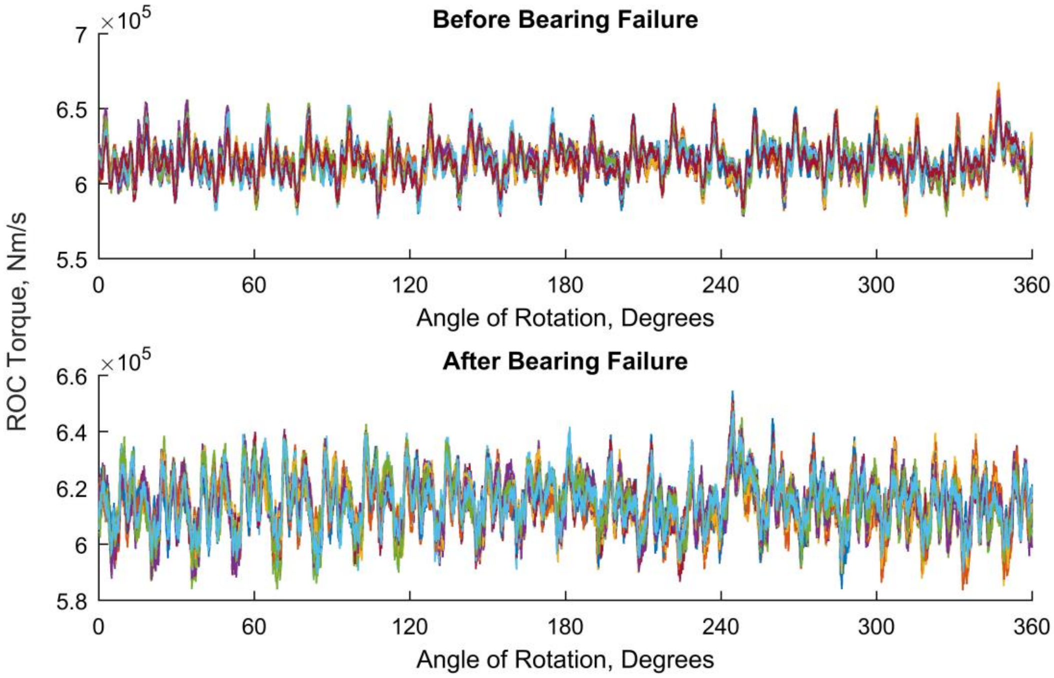

Figure 5-66 – Rotations of the 2.4 micron tooth bend before and after the bearing failure aligned with respect to the layshaft.

Using TSA to clarify the signals (Figure 5-67) it became apparent that this transient is affecting a single gear tooth or rotational position on the layshaft. The nature of this transient indicates it is not affecting the meshing cycle in the same manner as the tooth bends, instead the form of the data around that particular tooth is altered and resembling a bell curve. While this does little to narrow the range of possible defects responsible, the fact it inconsistently appears across multiple tests indicates that it is likely related to either the test gears or the setup of the test rig. Even with an intimate knowledge of the test rig design it is difficult to say what component or aspect of the setup would cause such a transient as it's alignment with the meshing cycle is too consistent to be related to a majority of the components. As such it is in the author's opinion that this transient may be the result of a defect specific to a singular tooth on the 2.4 and 8.7 micron tooth bend specimens. Examining the initial test data for these gears shows no sign of this transient suggesting that this is a defect that has manifested over the course of the test plan.

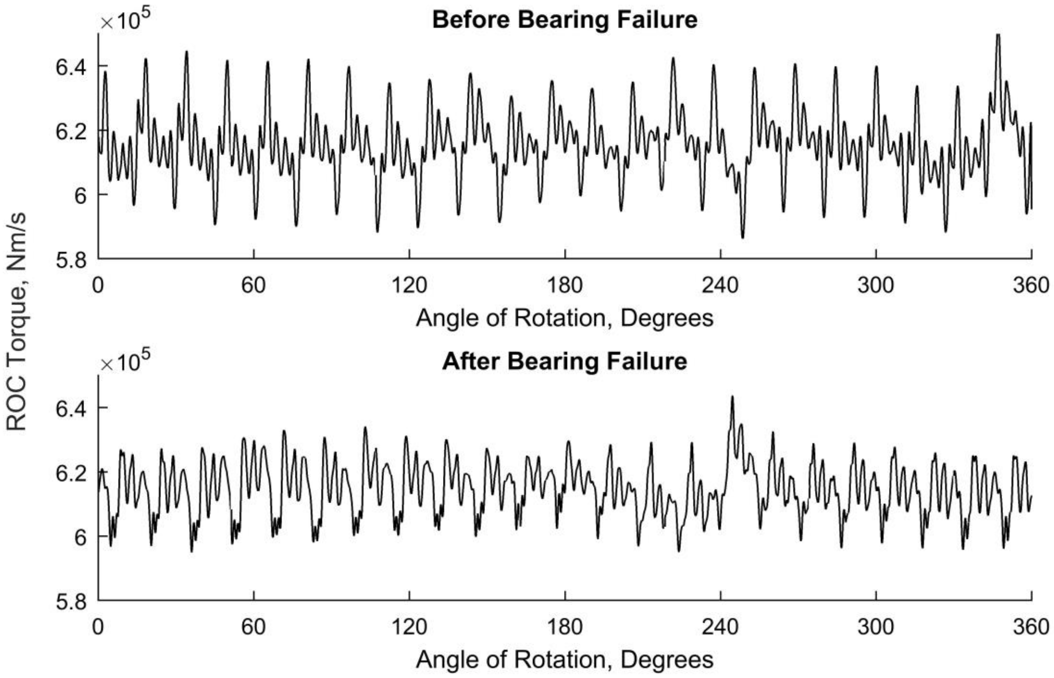

Figure 5-67 – TSA waveforms for the 2.4 micron tooth bend before the bearing failure and after the replacement at 3000 RPM and 100 Nm torque.

Whilst this is only conjecture as testing to confirm this hypothesis is not possible at this stage of the project, in the author's opinion this transient has a high chance of being caused by a surface defect. As surface defects will alter the surface finish of the gear changing the nature of the contact patch through either a reduction of the lubrication film or reduction of size of the contact area, due to material loss. This could result in more concentrated torque transfer leading to the bell curve shape over the course of the singular tooth while the meshing cycle has not been affected. Whether this is truly the cause or not, the sensitivity of the technique is clearly visible with it clearly responding to something affecting torque transfer while the tooth is engaged in the gear mesh.

The data presented in Figure 5-65 and Figure 5-66, was captured a couple of hours before the failure and shows no indications of anything amiss. This can be compared to Figure 5-68, which displays the last data recorded before the bearing failure and the same gears at the same conditions during the initial testing and after the bearing replacement. There is an undeniable difference in the waveforms directly before and after the bearing failure with the data from after the bearing replacement exhibiting more stability with little to no sinusoidal oscillations and relatively distinct peaks indicating tooth interactions although this is not true for the entirety of the data. This is in contrast to before the bearing failure with the data evidently being dominated by sinusoidal oscillations and the large regions where any sign of the meshing cycle is indeterminable such as between 240° and 360°. Notably these oscillations are present in the initial testing as well but to far lesser degree, it’s unclear as to whether these are preliminary signs of a bearing defect.

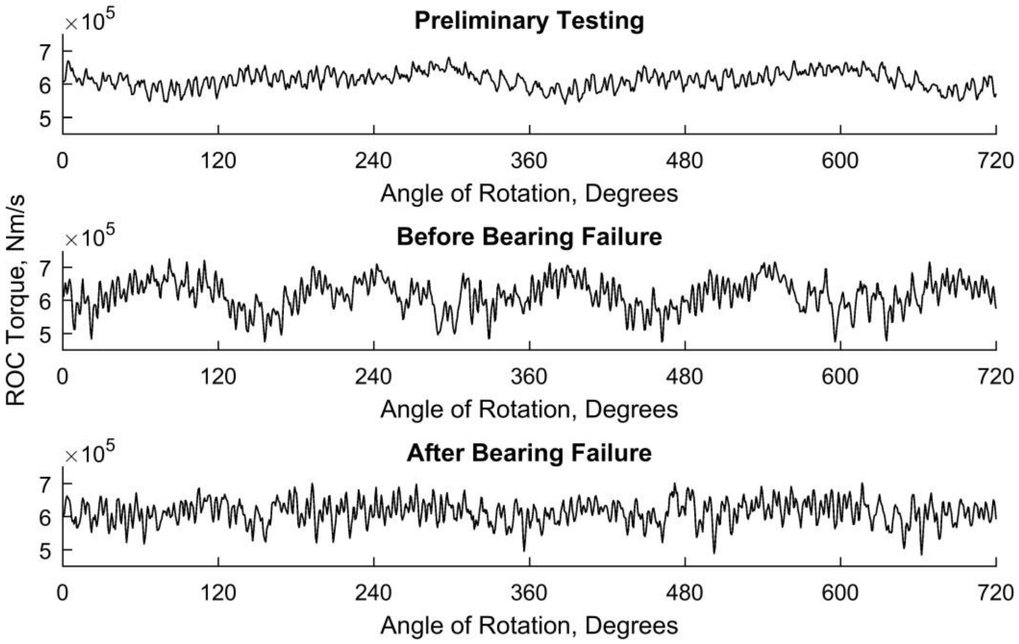

Figure 5-68 – Comparison of the last data captured before failure and the same conditions after a bearing replacement: 2.4 micron tooth bend at 13500 RPM and 250 Nm torque.

Observing the difference between the various sets of data it is possible these oscillations are caused by the motion of the bearing as it approached failure with its motion being inhibited by faulty elements causing a knock-on effect to the torque. From the authors knowledge of the state of the bearing at failure; this appears unlikely as the effect is too regular and with a consistency unbecoming of the scale of the damage found upon inspection. Examining the data captured from the various data sets this seems unlikely however with a slight oscillation being visible after the bearing has been replaced. Due to the amplitude differences between the preliminary tests and those after the bearing replacement, it is possible that these oscillations are of comparable size, but it is masked by the increased amplitude of the fluctuations of the meshing cycle. If this is the case, then it is not inconceivable that this effect is a symptom of a healthy bearing and is exaggerated as they proceed towards failure.

Aside from this there is little indication within the raw and TSA waveforms that something is amiss, an examining the frequency spectra provided little additional insight. Figure 5-69 can be seen to show the frequency spectra of the same test but when the bearing was known to be healthy and damaged. By highlighting the fundamental bearing frequencies, it was hoped that that any frequency shifts caused by the damage could be quantified. This did not matter however as no indication of the bearing frequencies could be found at or around the expected frequencies in either the healthy or damaged spectra. It is possible that fundamental train frequency and the ball spin frequency are simply not visible due to their proximity to the meshing frequency and it's 4th harmonic respectively but given the complete lack of presence of the ball pass frequencies for both raceways, the author believes this is unlikely and that they are simply not present.

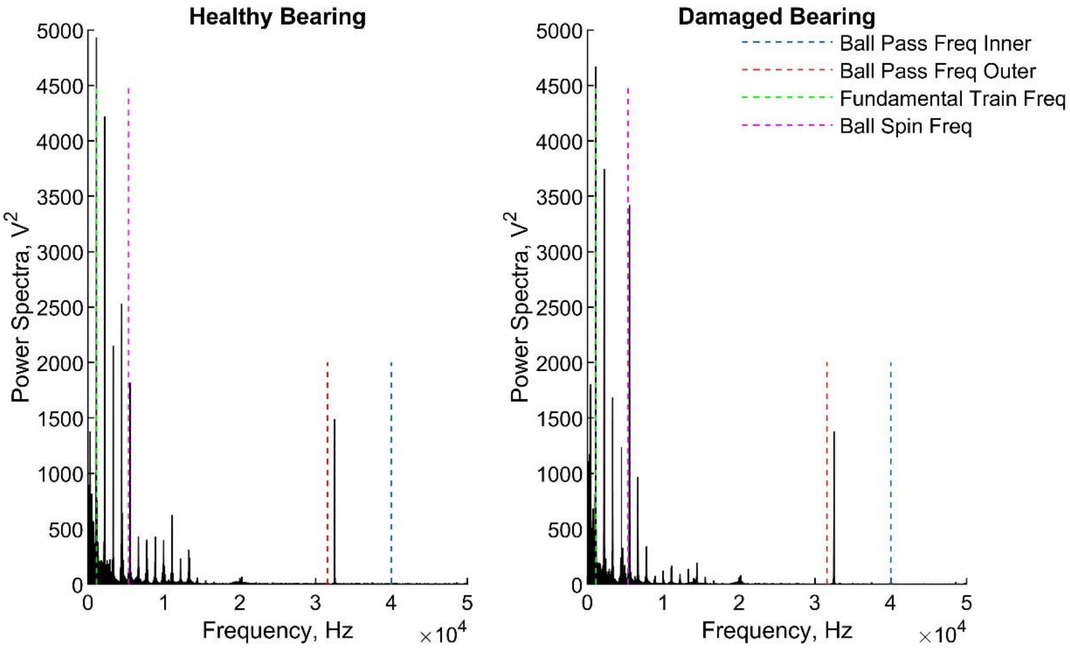

Figure 5-69 – Frequency spectra of 2.4 micron tooth bend at 3000 RPM and 100 Nm at known healthy and damaged bearing conditions with the fundamental bearing frequencies indicated.

Examination of the spectra of final data captured before the bearing failure and its healthy counterpart again showed no presence of the bearing frequencies (Figure 5-70), with the ball spin frequency now being confirmed as not present due to no longer being within proximity of a mesh harmonic. This is not entirely unexpected however, as it has already been established that the new in-loop ROC data is heavily dominated by the meshing frequency and its harmonics with few other frequencies present. As the bearing that failed was external to the torque loop, it would have only affected the 'input torque' i.e. the torque entering the system to compensate for the parasitic losses. This torque will be minimal in comparison to that within the torque loop and could easily be overshadowed as result obscuring any indication of the damage.

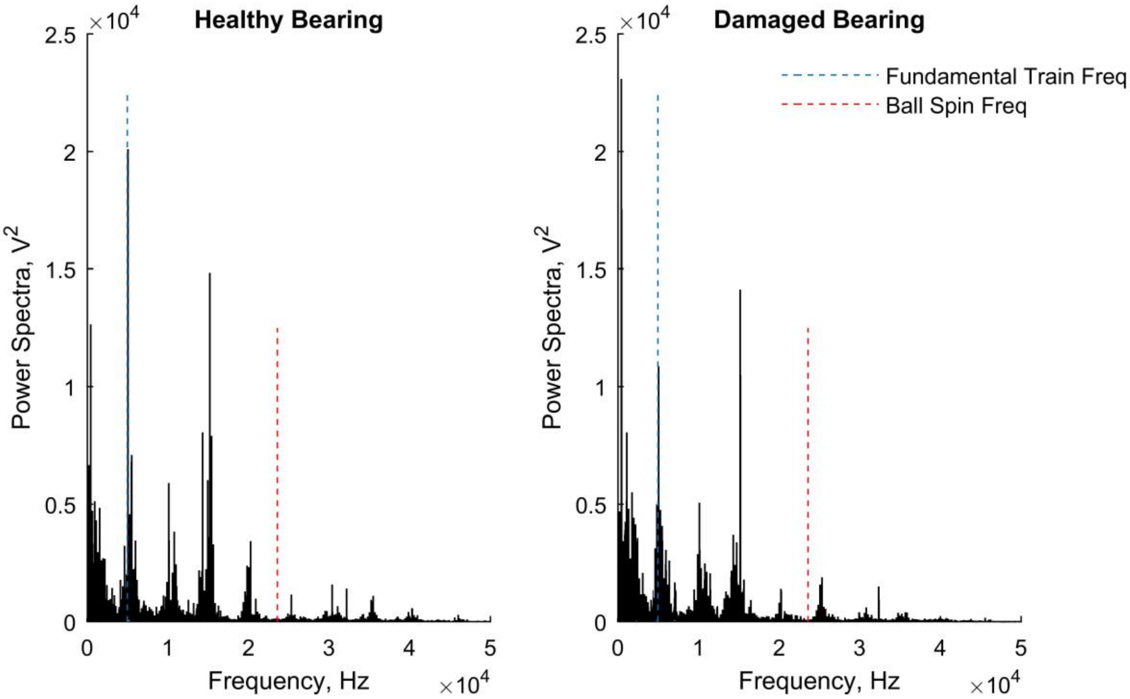

Figure 5-70 – Frequency spectra of 2.4 micron tooth bend at 13500 RPM and 250 Nm at known healthy and damaged bearing conditions with the fundamental bearing frequencies indicated.

The lack of detection of this bearing has little effect on the application of ROC technology as a potential industrial candidate, as real systems do not have an 'out-of-loop' region. It does however mean that for continued operation of the test rig, the bearing of the forward assembly of the Cardiff high speed gear rig will require periodic inspection to prevent a similar failure happening in the future.

5.6 Discussion and Conclusions

The new in-loop data displayed immediate superiority over the previously acquired frictional loss data. Where the previous data had allowed for detection of 8 and 16 micron tooth bends within the raw signal, the in-loop data saw visible transients for all 3 damage levels. Special attention was given to the 2.4 micron tooth bend, the smallest tooth bend to have been detected thus far with ROC technology and an indication of the inherent sensitivity of the technique. This sensitivity was further displayed with individual tooth interactions present in each rotation of the waveform.

Despite this evident improvement, the signals could often be hard to read due to noise. In order to eliminate any non-stationary frequencies, time synchronous averaging was employed. This provided a far cleaner and more repeatable signal with each tooth interaction clearly defined, allowing for even easier identification of the various damage levels. Using this newly averaged data and the raw signals a series of methods were employed in an attempt to consistently identify and allow for characterisation. To this end, single value damage indicators or metrics were used.

These indicators, having been specifically designed for damage detection via vibration signals from gearboxes, were found to provide little or no information when applied to the signals in their entirety. To improve this a moving average-style format was introduced with the metrics calculated over a controlled area of the signal which was repeated along the length of the waveform. Despite this change in approach the best results were found to be provided by the only non-gear specific metric: the root mean square. The RMS provided good results with a consistent detection of all 3 damage levels using both data sets so long as sufficient torque was present in the system. This required torque level or around 50 Nm was of no concern as it highly unlikely that any real system where this sensor is likely to operate would ever operate at torque levels as low as this. If a ROC sensor were to be integrated into a system with torque levels as low as this, it would be possible to counter this issue in the design stage with the magnetised shaft design.

After the results by the RMS, little more was offered by the other metrics with: kurtosis, energy operator, M6A and M8A providing no signs of detection at any speed or load level with either data set. This is thought to be because of the nature of the design of these metrics. Nearly all vibration-based gear metrics are designed to be used with a difference or residual signal, a signal with the meshing frequency and harmonics removed and in the case of the difference: the first order sidebands as well. The purpose of this is to remove the dominant frequencies to allow examination and detection of shifts and changes in the high energy side bands that exists in vibration signals. These sidebands simply do not exist in ROC signals with the signal constructed nearly exclusively of the shaft frequency, the meshing frequency and their respective harmonics. This makes the generation of difference or residual signals impossible for ROC data as any attempt to do so will remove much of the signal often leaving nothing but the filter response in its wake. This and the lack of any high energy sidebands in ROC signals is thought to be the reason that the vibration metrics are not as effective when applied to ROC data. Ideally the author suggests that research is undertaken into new meshing frequency-dependant metrics if something similar is to be repeated with ROC technology.

The final metrics studied provided better results than the others however they still under-performed in comparison to the RMS. NA4 and its modification NB4 examined growing damage across time for which a special set of data waveforms were constructed for this purpose. Whilst the moving window application was erratic and provided little of substance, calculating a single value for each file present in the constructed signal provided consistent detection of the largest, 14.7 micron, tooth bend. Although NA4 was unable to improve upon this, NB4 fared better with detection of the 8.7 micron tooth bend being more regular than not. This clearly indicated that NA4 and primarily NB4 are capable of responding to the amplitude change caused by the damaged tooth suggesting that if the damaged tooth transient could be exaggerated using signal processing then these methods may provide a good basis for a live data damage detection method.

Looking beyond statistical based metrics, more computationally advanced methods were examined. These methods were multiscale local statistics and the Hilbert spectra which, due to the computational requirements, are far more suited for post-processing analysis than that of live data analysis. The MLS provided good results with its weighting function allowing it act in a similar but more comprehensive way to the sliding window used in conjunction with the metrics. The length of the time required for computation of the MLS was a considerable hinderance with the only data set capable of being processed being the TSA. The processing time aside, the results were impressive with detection of all 3 damage levels. Of the 4 multiscale local techniques, the mean and variance were substantially more consistent with their rate of detection than the skewness and kurtosis which often were mired by outliers that made the damage impossible to distinguish from the rest of the waveform. The mean and variance had their own issues however as although the response to the damage tooth could clearly be distinguished the amplitude of the results for the different damage levels was erratic. Even when processed at the same speed and torque levels the results when compared against each other gave no indication of the correct scale of the damage, which in a blind test would cause misidentification. Whilst characterisation would not be possible using MLS as a post processing detection method it is would be useful for confirmation of suspected damage.

The Hilbert spectra fared less well than the MLS with the Hilbert and marginal spectrum providing no results with any indication caused by the damage. The results were often erratic, and no correlation could be found between either speed or torque. It was a surprise then to find that the instantaneous energy spectrum did provide successful detection of all levels of the damage. Given the increasing size of the results with scale of damage it is possible that this spectrum could be used for characterisation of the damage, although this is conjecture as the results generated were far too unreliable to confirm this with successful detection only being made a handful of times across all the data analysed. Given the reliance on these spectra on the decomposition process which is the mainstay of the Hilbert spectrum, it is almost certain that the instability of the results is due to the self-regulating nature of the decomposition. It is in the author's opinion that greater clarity and regularity could be brought to the results using a different decomposition method. Examples of which are the wavelet decomposition which is more controlled and not self-regulating or local mean decomposition that whilst also self-regulating has shown greater promise with rotational applications in the literature as seen in Wang *et al.* (2010), Deng and Zhao (2013) and Liu *et al.* (2017)

Finally, a short analysis was performed to see if it was possible to detect the bearing failure that occurred during the testing process. Analysis was performed of the raw waveforms and the Fourier spectrum of known tests where the bearing was damaged and healthy, and it quickly became clear that there was no visible or frequency content related to the damage bearing in any of the tests. As the failed bearing was external to the torque loop, the current hypothesis is that the amplitude of components external to the torque loop are simply too low in comparison to the components internal to the loop. This means that while frequency content may be within the spectrum it is simple too low due to it being swamped by the higher amplitude meshing-related signals inside the torque loop. Thus, ROC data requires more specialised detection and characterisation methods centred on the nature of ROC signals.

To provide a comparison of the sensitivity and the effectiveness of some of the methods presented here, the following chapter demonstrates the application of some of these metrics to vibration data captured alongside the ROC data on the Cardiff high speed gear test rig.

CHAPTER 6

Comparison of Vibration-Based Condition Monitoring to the Rate of Change of Torque

The novelty of ROC technology has meant that, to date, few published materials concerning it exist. As can be seen in chapter 2 where the available literature is reviewed, most research is concerned with application of the technology and its response to simple, easily modelled applications e.g. monitoring of the condition of a milling cutter. This has meant that little comparison has been performed between ROC and existing condition monitoring techniques. As discussed in Chapter 2, vibration monitoring is a well-established form of condition monitoring currently in use across a broad range of industries. Kari *et al.* (2011) had previously compared the effectiveness of both ROC and vibration monitoring of bearing defects in a simulated helicopter transmission, however thus far there are currently no published works on the comparative applications of both technologies to gear systems.

In order for a comparison of both methods to be performed, a set of vibration data was obtained during routine testing alongside a set of ROC data. This data was captured in Cardiff on the high-speed test rig described in Chapter 4 so as to maintain comparability between the testing conditions.

6.1 Data Acquisition

Three sets of data were acquired in total. These sets consist of the standard speed and torque combinations found in the main ROC testing but only covered the healthy, 2.4 and 8.7 micron tooth bend gear pairs due to time constraints. Data acquisition was made by single-direction PicoCoulomB (PCB) Piezotronics M320C18 accelerometers mounted on the end plate of the test head, the positions of which can be seen in Figure 6-1. The specifications for these accelerometers are as follows:

- Measurement Range: ±4900 m/s^2 peak
- Frequency Range:
    - Optimal: 1 – 10000 Hz (± 5%)
    - Maximum: 0.35 – 30000 Hz (± 3dB)
- Sensitivity: 1.02 $mV/(m/s^2)$

These accelerometers were connected to a DEWESoft Sirius mini-system capturing at 200 kHz with the acquisition triggered by the layshaft speed sensor. This sample rate reflected the initial desire to have the Sirius mini-system to simultaneously capture ROC data in order to clarify aliasing issues associated with the highest speeds. Unexpected incompatibilities between the wiring loom of the Cardiff high speed rig and the Sirius mini-system meant that this was sadly not possible given the required time to rectify the issue and as such the ROC data was acquired by the rig's own system at 100 kHz, using the same configuration as that used for the tests in Chapter 5.

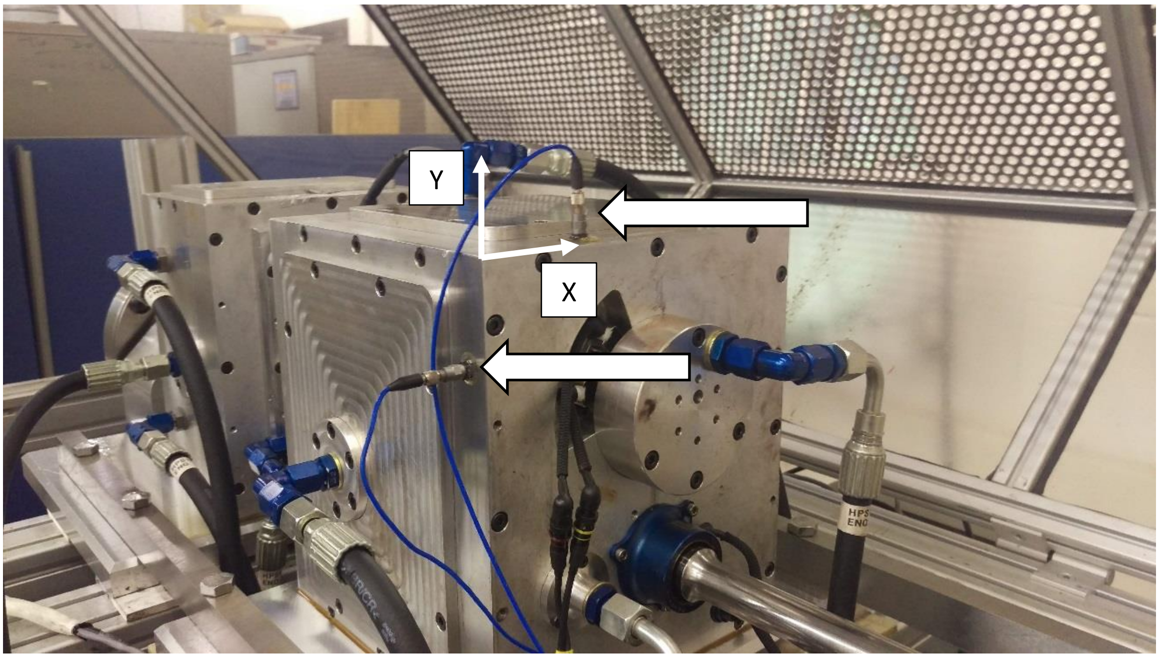

Figure 6-1 – Placement of accelerometers on the Cardiff Gear Test Rig.

6.2 Results

6.2.1 Difference Signal Generation

In order to effectively determine the ability of the vibration metrics in comparison to ROC technology, the metrics must be applied correctly. For this purpose, a bandpass filter was used to generate a residual signal. Using the layshaft speed sensor to accurately calculate the speed, the meshing frequency and the first 12 harmonics were removed to ensure that they would have no influence on the metrics. Special attention was made to leave any sidebands untouched by the filtering process, as per the requirements of the signal. This signal was then processed using a number of metrics already examined in the previous chapter, namely: RMS, FM4 (Kurtosis), M6A and M8A.

Initial examination of the frequency spectrum before the creation of the residual signal, reveals a much noisier spectrum than that of the ROC data. The ROC data presented a relatively clean spectrum dominated by the meshing frequency and its harmonics and with all the relevant frequency data located in the first 15 kHz. In contrast to this, the vibration spectrum extends much further with frequency content being found as high as 90 kHz as seen in the spectrum of the healthy gear pair in Figure 6-2.

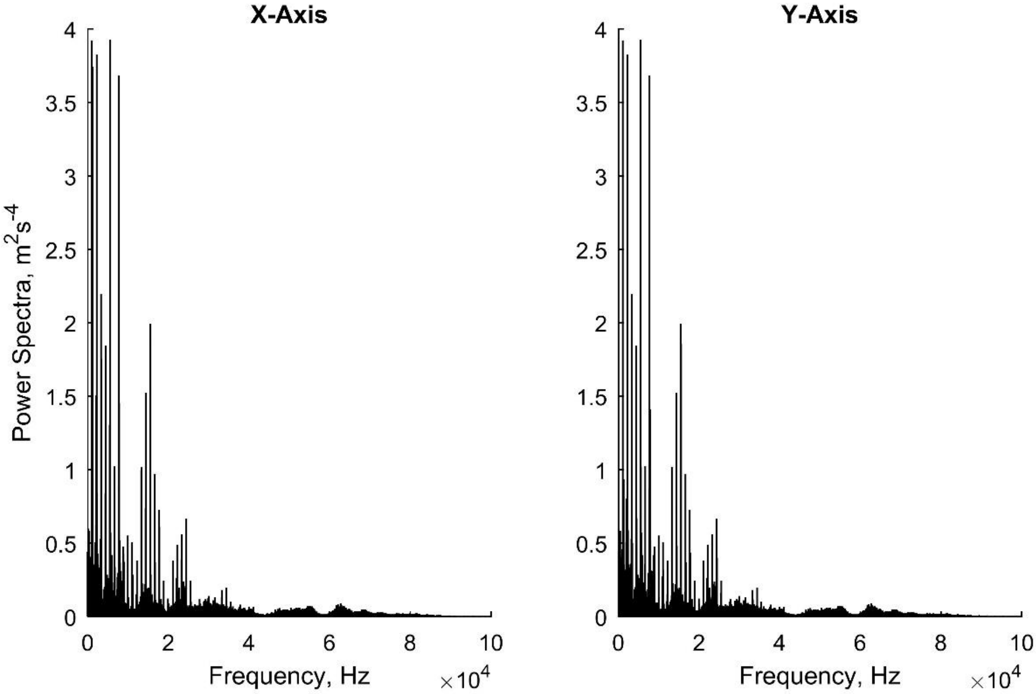

Figure 6-2 – Frequency spectra for both axes of the raw vibration data for the healthy test gear pair at 3000 RPM and 100 Nm torque.

There is a notably higher degree of low level noise present in the vibration spectrum relative to that of the ROC signals, which is not unexpected given the nature of the vibration signals. This low level noise is also accompanied by many harmonics of the meshing frequency. Despite the ROC signal being heavily dominated by the meshing frequency and its harmonics, they only extend as far as the first 15 kHz, while the vibration signal was found to have a total of 21 harmonics, all appearing within the first 30 kHz as can be seen in Figure 6-3. As expected, the meshing frequency and its harmonics are all accompanied by high energy side bands that often have 70-80% of the amplitude of the frequency it is attached to. In order to preserve these side bands during the creation of the residual signal, the spectrum before and after the band stop filter were plotted as in Figure 6-4. The results of this were then used to tailor the filter specifications until the author was able to confirm that the first-order sidebands were still present with minimal changes to their amplitude caused by the filter.

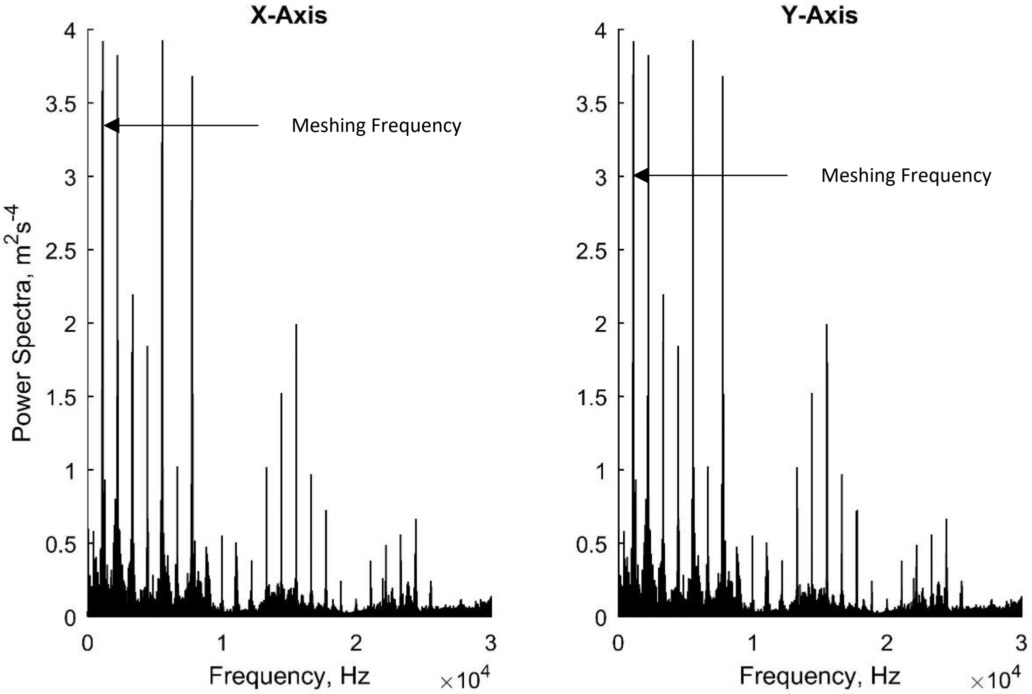

Figure 6-3 – A closer inspection of the first 30 kHz of Figure 6-2.

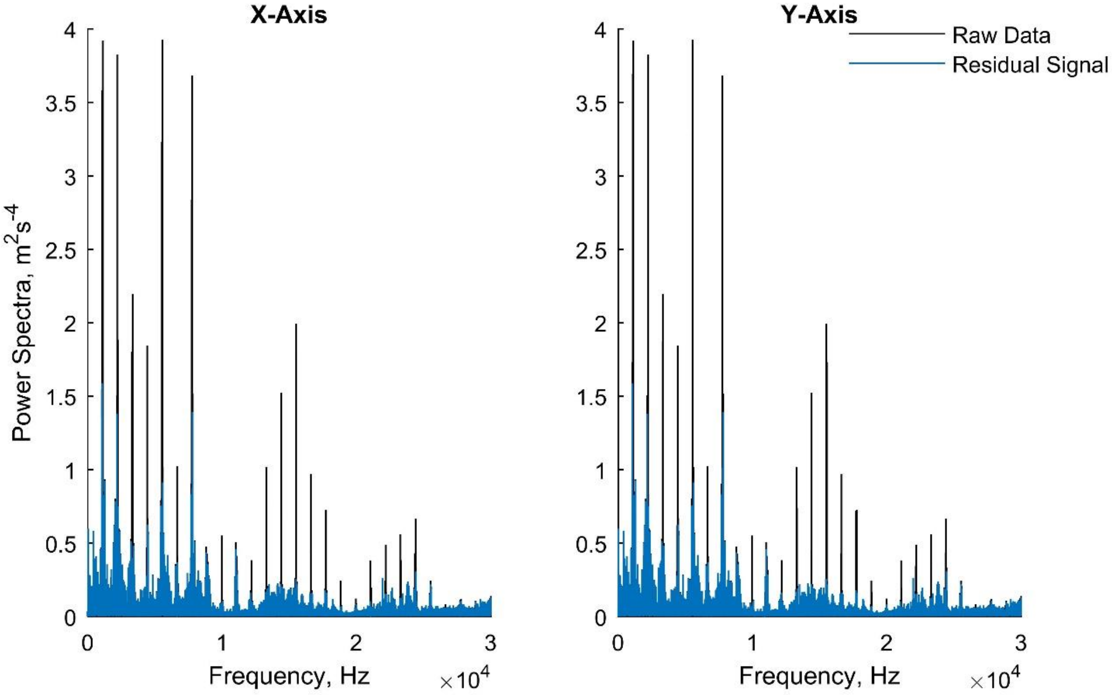

Figure 6-4 – The first 30 kHz of the residual signal spectrum mapped over that of the raw data to confirm correct frequency removal.

6.2.2 Root Mean Square

Application of the RMS was straight forward and immediately a clear increase in vibration could be seen from the increasing speed and levels of torque. As demonstrated by Figure 6-5, each torque has its own distinct level with an increasing trend with speed. A slight anomaly can be seen at 15000 RPM and 200 Nm torque, what is of interest is that anomalies such as this only occurred in the x-axis data whilst the y-axis data for all 3 tests remained free of any errors. The first major difference between ROC and vibration can be observed as the clarity with which these trends are presented is of a far greater level than that which was seen in the ROC data. Whilst showing similar trends ROC suffered from far more anomalies and less well-defined trends. This is too be expected however as the energy in the system is increased through higher loads and speeds, the imperfections that cause the losses resulting in vibration will be directly affected giving a greater acceleration value.

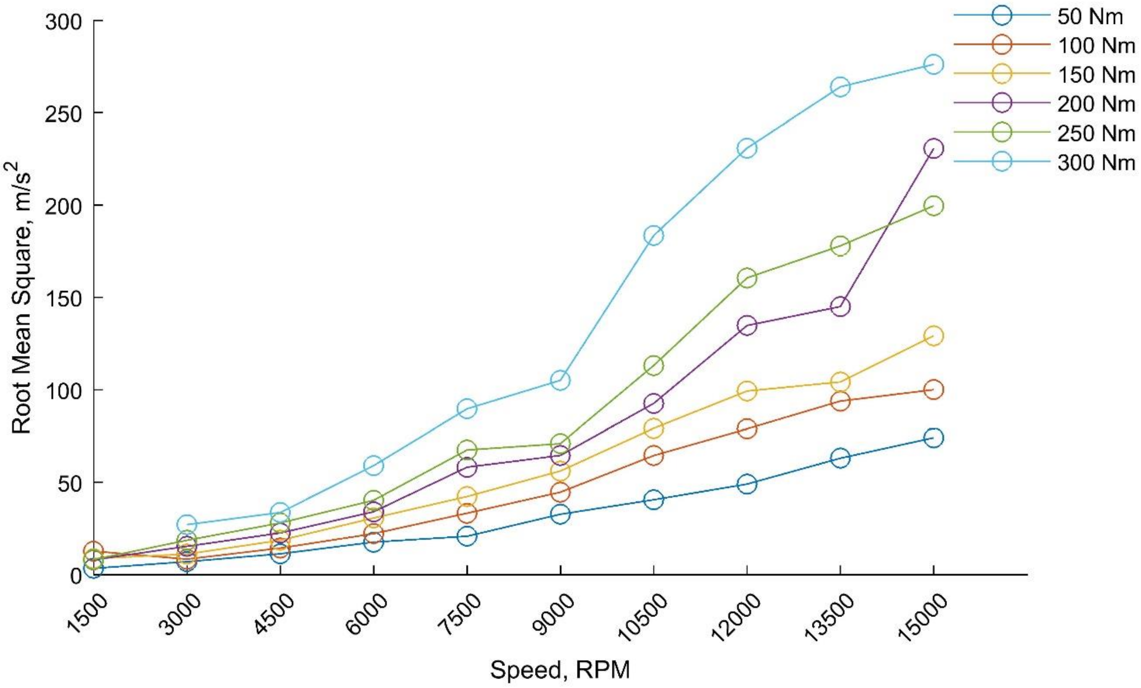

Figure 6-5 – Single value RMS for the x-axis healthy vibration data at all speeds and torque levels.

Following this, comparison of the different damage levels at the same torque (Figure 6-6) saw little difference between the 3 traces below 9000 RPM. After this point the traces can be seen to disperse, if only slightly. This dispersion is often too slight for any conclusions to be drawn, especially when considered from the perspective of a blind test, where it would be impossible to distinguish the different gears from each other. As Figure 6-6 demonstrates, the dispersion is often muddled with the y-axis data showing little to no separation and with the 2.4 micron tooth bend showing the lowest results with the healthy gear pair producing nearly identical values to the pair with 8.7 micron damage. Whilst the x-axis shows the 8.7 micron maintaining the highest values for all but one speed, there simply is not enough information here to allow successful identification of the damage let alone characterisation.

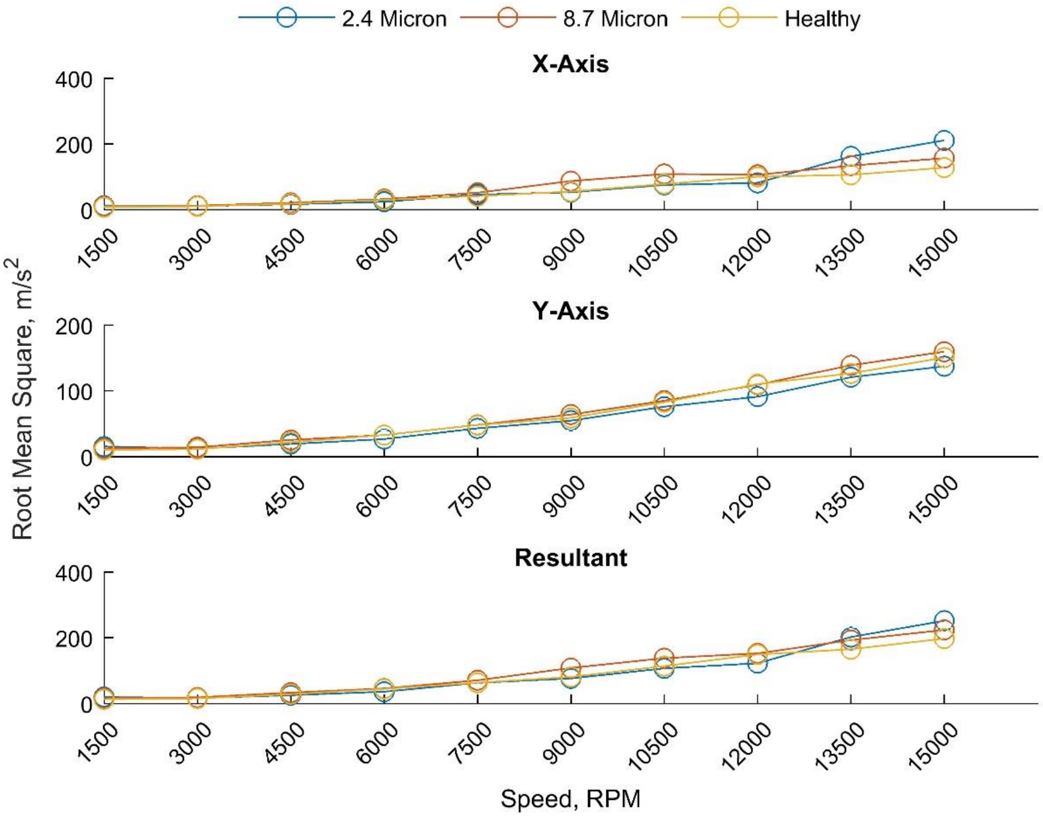

Figure 6-6 – Comparison of the different damage levels for all 3 vibration tests at 150 Nm.

This isn't a singular occurrence either, with each torque level being similarly obtuse albeit with the exception that is the x-axis at 50 Nm which can be seen in Figure 6-7, where the divergence following 9000 RPM clearly separates to levels accurately distinguishing the damage correctly. This is of little use however when even the y-axis data for the same test does not provide a supporting result, with the 2.4 micron tooth bend producing near identical results to the healthy gears.

Between Figure 6-6 and Figure 6-7, it is clear that single value RMS calculations do not present a consistent or indeed successful method of detecting the damage within the vibration data. This is consistent with the findings when single value RMS calculations were applied to ROC data. Single value RMS vibration results clearly display more consistency than their ROC counterparts, but still do not provide a useful method of damage detection. As has been previously discussed, RMS is simply a statistical measure and not a vibration specific metric, as such it can be argued that the results of single value calculations for the RMS do not reflect those of the other purpose-designed metrics and as such they may provide a more reliable method of detection even as a single value.

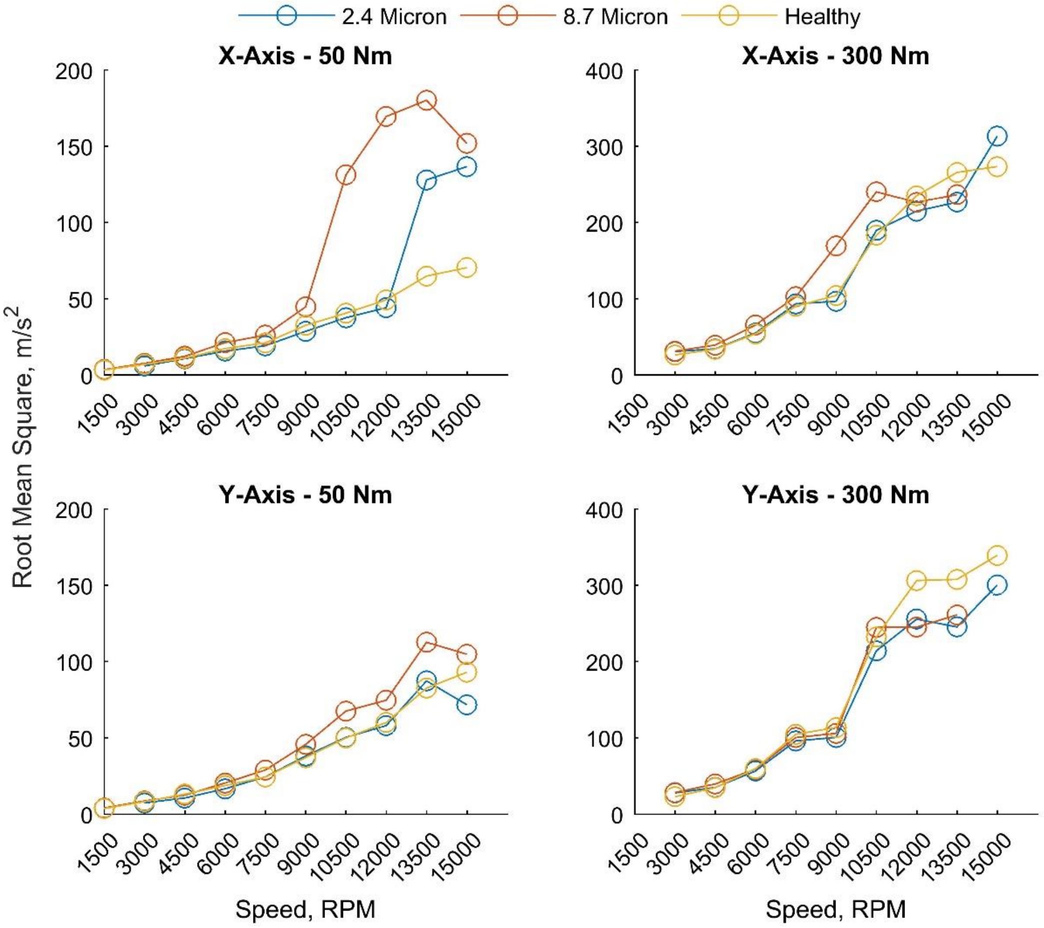

Figure 6-7 – Comparison of the SVM RMS for all damage levels at 50 Nm and 300 Nm torque.

Application of the RMS in moving-windowed form saw an improvement with consistent damage detection of the 8 micron tooth bend as is presented in Figure 6-8, where the results for the individual rotations are overlaid, with a different colour assigned to each rotation to allow for identification. The window was set to the length of two pulses from the layshaft sensor that triggered the acquisition, there are 17 pulses per rotation on the layshaft but scaling this to the main shaft makes approximately 20 pulses per rotation making each window roughly 18° or one and half teeth. The shift of the window is then set to a quarter of the window length, this was to provide enough results that the changes in the RMS could be captured but not so many that the results become cluttered.

A clear indication of the tooth bend can be seen around 300°. Although the stacked rotations make it easy to distinguish the damage there are noticeable fluctuations in the amplitude of the damage ranging from approximately 80 to 100 ms^{-2}. With the inclusion of high amplitude outliers seen at 10° and 240°, it is possible that these outliers would inhibit detection when observing a single rotation or continuous waveform as it may be impossible to distinguish the damage from these outliers. Another concern is that if these fluctuations occur constantly it may lead to false positives with an automated system.

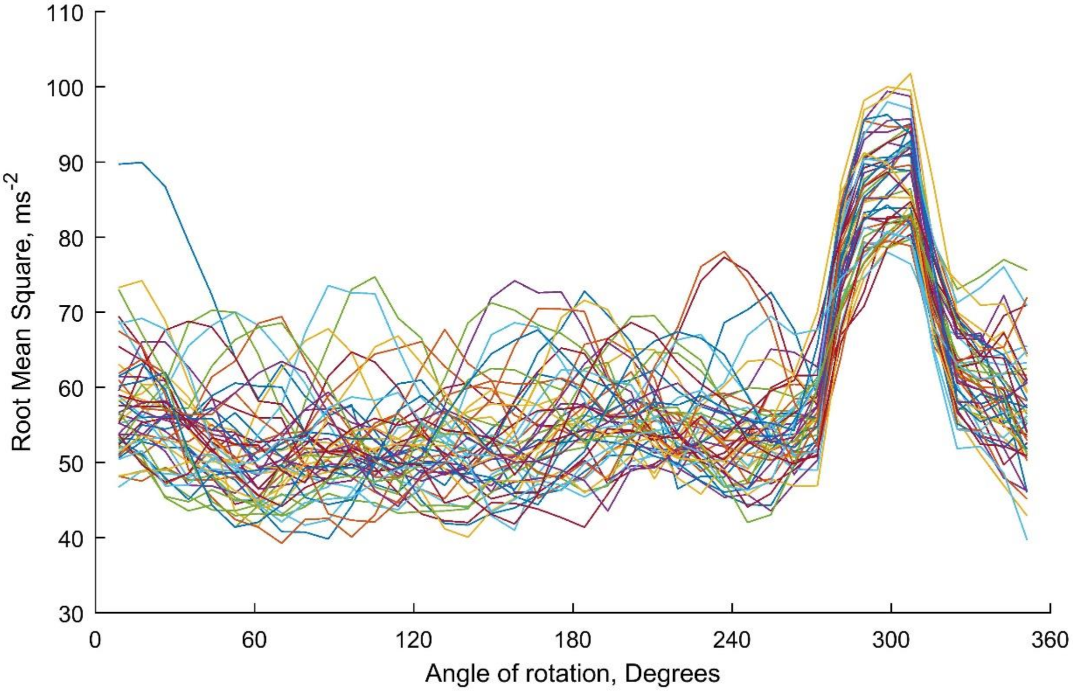

Figure 6-8 – Overlaid RMS results per rotation for 8.7 micron tooth bend at 200 Nm torque and 7500 RPM.

Comparison of the results of the 8.7 micron damage to those of the healthy and 2.4 micron tooth bend, as seen in Figure 6-9, shows that there no clear indication of the damage within the 2.4 micron tooth bend within the RMS results, with it appearing very similar to the healthy specimen, a characteristic that has been seen before with the frictional loss ROC data due to the small nature of the tooth bend. Whilst at first it appears that there is an increase in the RMS acceleration present within the signals when damage is present, examination of the average levels of these signals shows that this not the case however with the average amplitudes for the 3 plots as shown in Table 6-1.

Table 6-1 – Comparison of average RMS values for the different damage levels.

Healthy: 57.7269 2.4 Micron: 72.1136 8.7 Micron: 58.1017

Even with the inclusion of the high amplitude area resulting from the damage it is clear that the 8.7 micron tooth bend does not follow this trend with the mean healthy value being within 0.65% of the 8.7 micron average. As more results were inspected it quickly became clear that there was no basis for this trend with the average of the results being predominantly close and no trend between what little separated them.

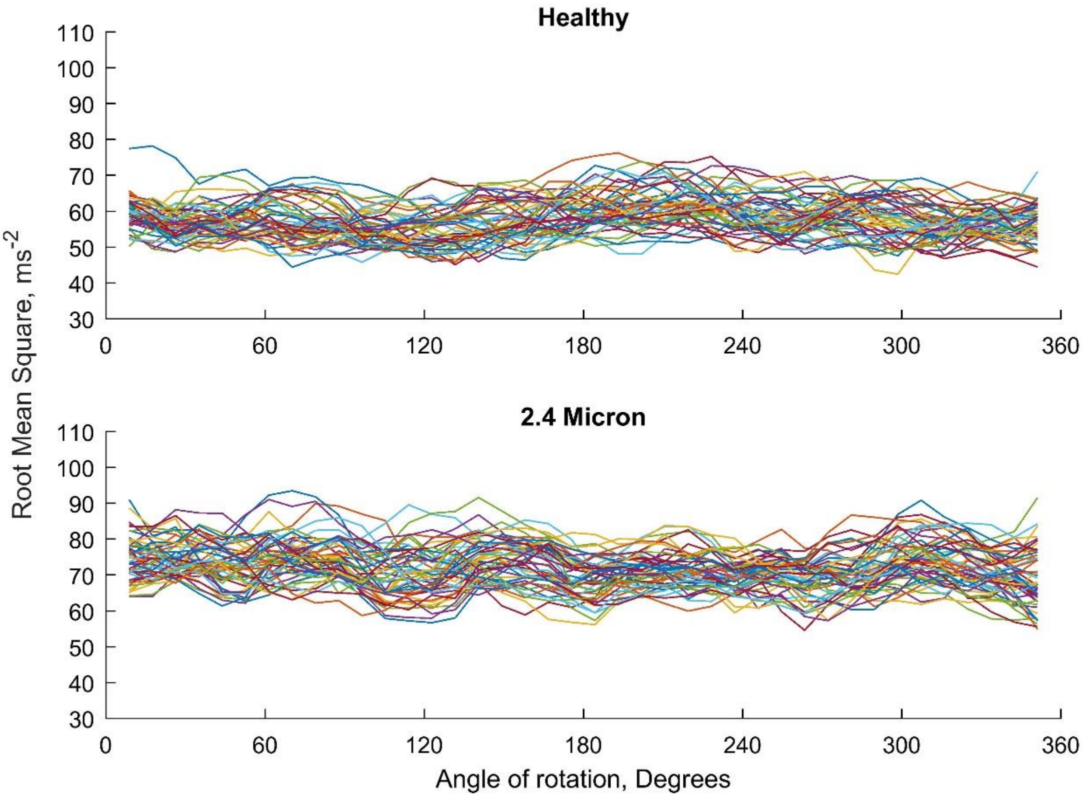

Figure 6-9 – Rolling RMS results for the healthy and 2.4 micron damage specimens

Examination of the results at other speeds and torques to establish if there were any trends that provided an indication of the 2.4 micron tooth bend showed that a similar effect to the divergence in the single value results appears to happen above 9000 RPM. Whilst no indication of the 2.4 micron damage could be located in any of the results, the peak indicating the 8.7 micron tooth bend becomes mired as the speed exceeds 9000 RPM with the results becoming more unstable with increasing speed. An example of this can be seen in Figure 6-10, where the results are dominated by high amplitude 'arches' that mask any indications of the damage at all. These 'arches' can also be found in the 2.4 micron damage with a similar consistency to those in the 8.7 micron damage, but are noticeably less common within the results for the healthy specimen. Initially, it was thought that these 'arches' maybe the indication of the damage being shifted but examination of the analysis code and raw data shows that this is not the case and as such the cause of these outliers is currently unknown. It is to be noted however that this effect is reduced with torque as can be observed in Figure 6-11, where an indication of the 8.7 micron damage can still be seen at approximately 70°. Although the arches are still present, they are mostly limited to the first 30° and the last 100°.

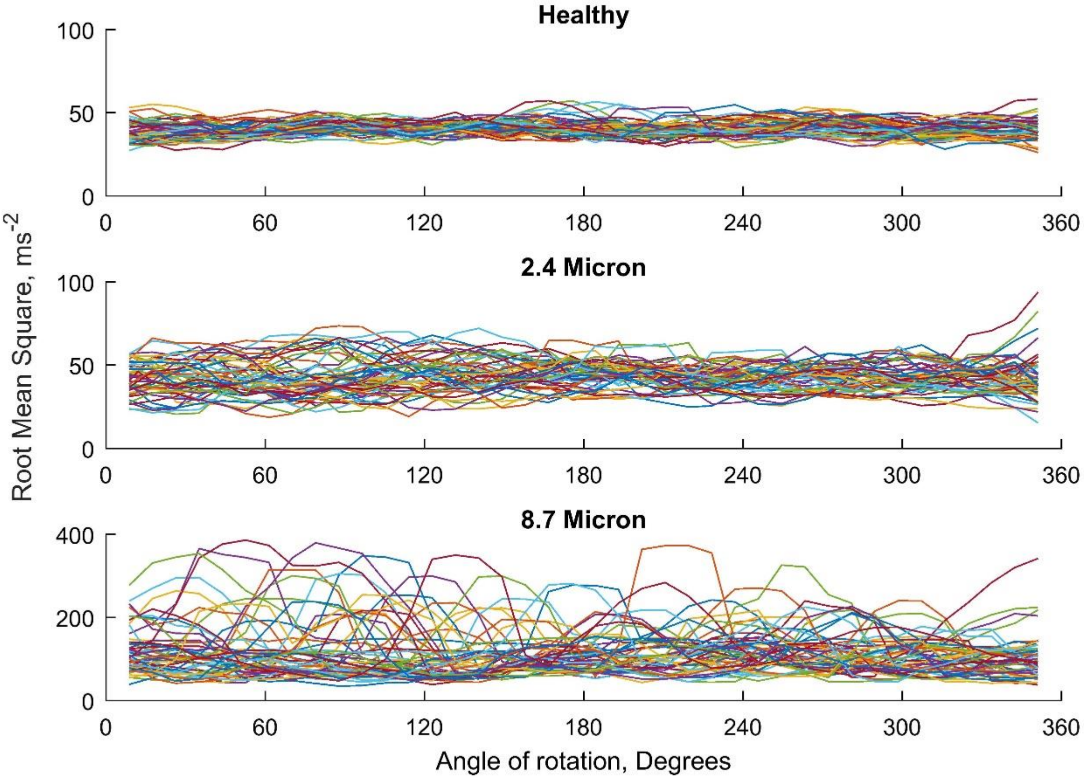

Figure 6-10 – Rolling RMS results for all pairs of test gears at 50 Nm and 10500 RPM.

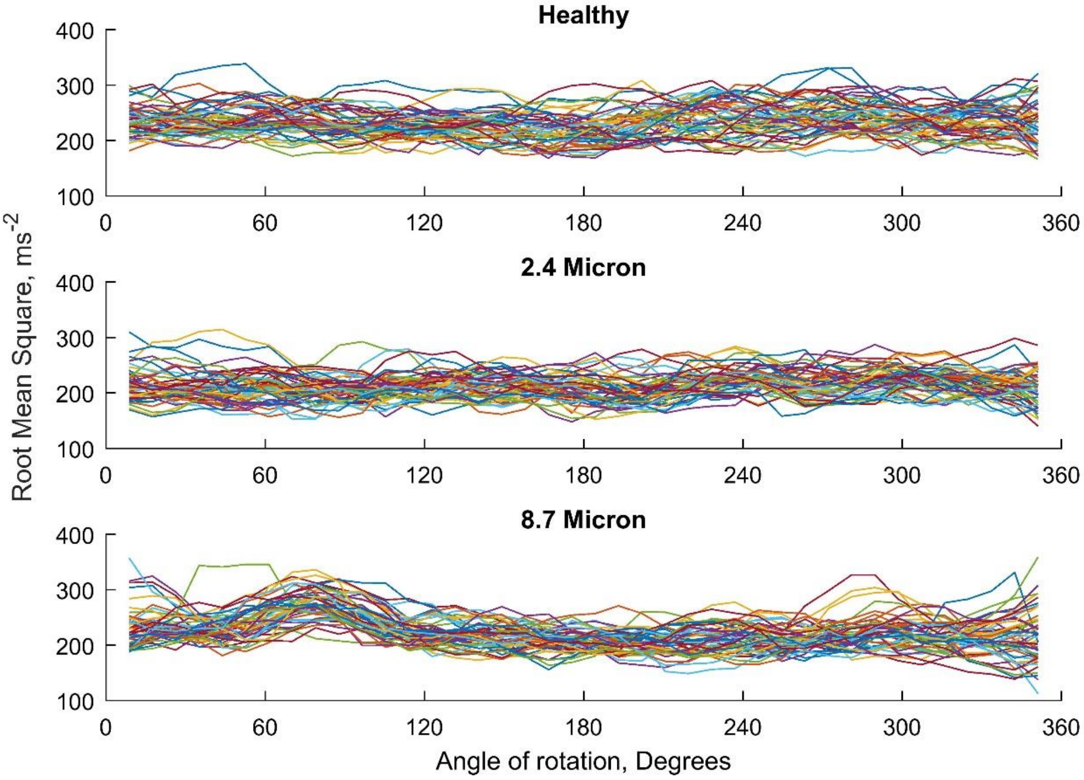

Figure 6-11 – Rolling RMS results for all pairs of test gears at 300 Nm and 12000 RPM.

These anomalies make damage detection difficult using RMS within the vibration data by limiting the range of speeds at which detection is possible based on the level of torque. This is an issue that the ROC data does not have as can be seen in Figure 6-12, where application to the raw data without any filtering still poses a baseline increase can be observed in all 3 plots at approximately 260° which indicates the presence of the damage. Even if this increase is slight and difficult to observe as with the 300 Nm and 1200 RPM plot.

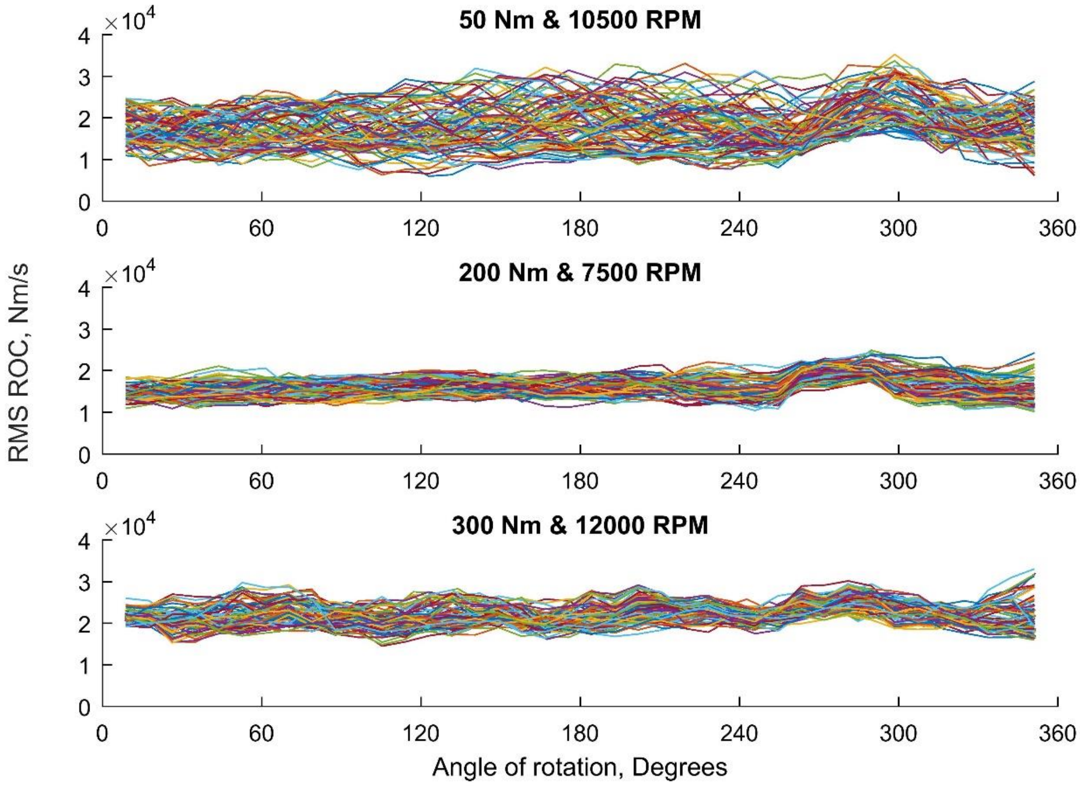

Figure 6-12 – The 8.7 micron damage RMS ROC results of the raw data at the same conditions as Figure 6-8, Figure 6-10, and Figure 6-11.

This is greatly improved when applied to the TSA data instead of the raw data, as just as the use of the residual signal is the primary from of vibration data within condition monitoring, it is in the authors opinion that TSA will become the primary from of ROC data. Examining Figure 6-13, it is obvious that the ROC data provides a much clearer indication of the damage at different speeds and torques than the vibration data. With clear indications of the damage at approximately 260°, however again this is much harder to discern in the third subplot. It is possible this is due to the reduction in available sample numbers though as this is the highest speed of the 3, thus the TSA has less data available per rotation, which may be leading to the decrease in visibility.

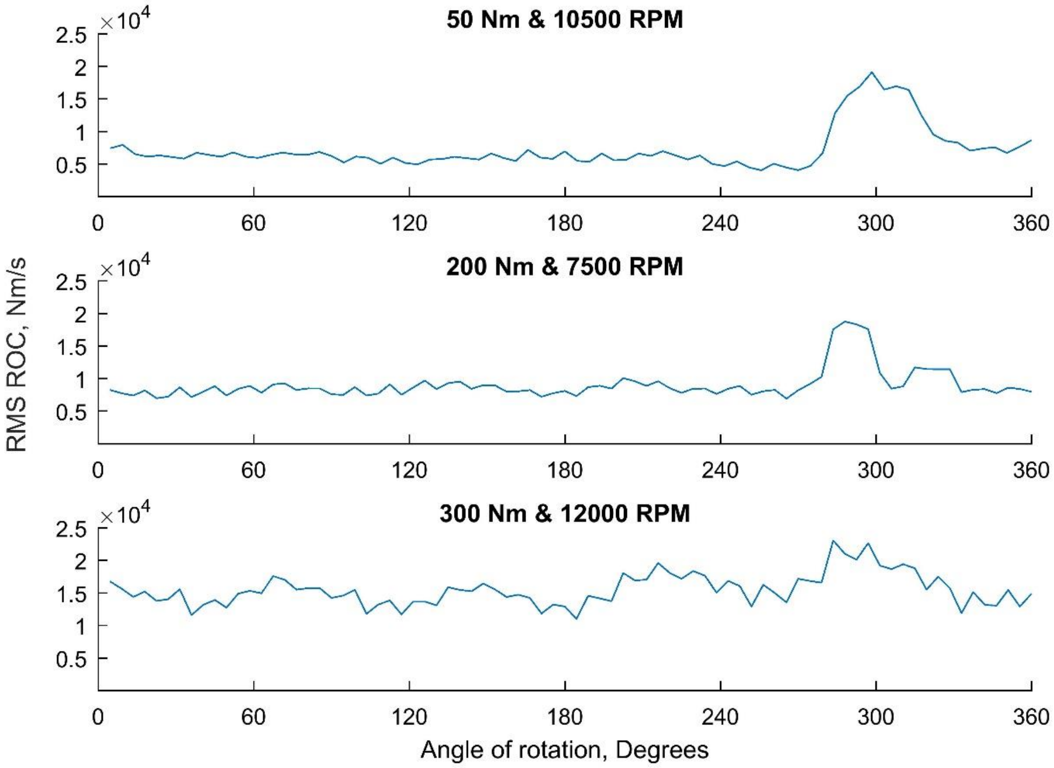

Figure 6-13 – The 8.7 micron damage RMS ROC results of the TSA data at the same conditions as Figure 6-8, Figure 6-10, and Figure 6-11.

It should also be noted that the results of the RMS on the ROC data also had difficulty detecting the 2.4 micron tooth bend. Whilst a small indication was found at times, this would often fall away and no disenable change in the rotation of the results could be found even when applied to the TSA signal. This detection, however intermittent, provides an example of the increased sensitivity of ROC technology when compared to vibration. Whilst the use of ROC data is still in its infancy, the application of the RMS already displays an increase in reliability over vibration with detection being more straightforward and consistent over a range of speeds and torques, something that will likely only improve as the technology is investigated further.

6.2.3 FM4

FM4 is the designation given to the application of the kurtosis to a difference or residual signal and was first used by Stewart (1977). Single value application of FM4 to the vibration data was far more promising that its in-loop ROC counterpart with the 8.7 micron tooth bend being consistently offset from the healthy and 2.4 micron results. An example of this can be seen in Figure 6-14, where although the amplitudes of FM4 appear to fluctuate randomly with speed, the 8.7 micron data can be seen to maintain an offset apart from the discrepancy at the start of the x-axis plot. In contrast to this the ROC data shows no consistent trends that allow for distinction between the different test gears. FM4 of the ROC data is clearly less stable with one high amplitude outlier per gear pair with no apparent reason for this.

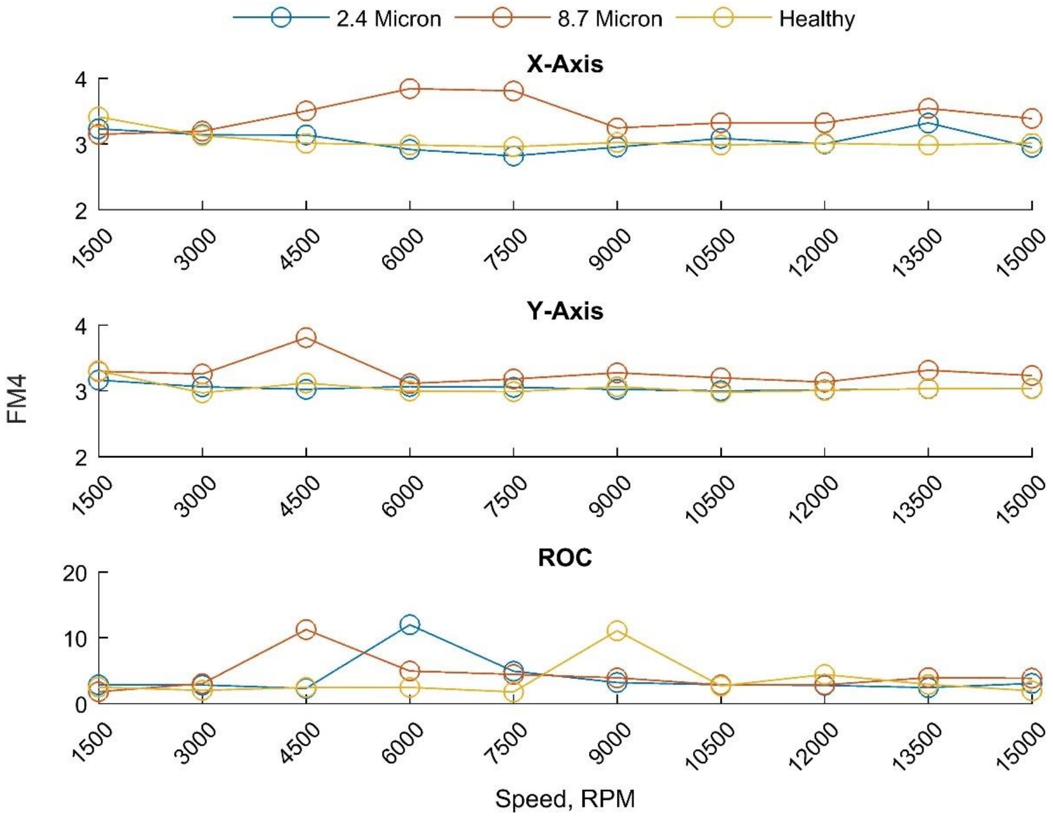

Figure 6-14 – Comparison of single value FM4 results for vibration and ROC data at 200 Nm torque.

Whilst the vibration data in Figure 6-14 is a particularly clear example, there are a number of cases where this offset isn't consistent and detection of the 8.7 micron bend is simply not possible. The best example of this is at 50 Nm, as displayed by Figure 6-15. Here the results of the different gear pairs are not distinct from each other in either axis. Whilst the 8.7 micron damage does appear to start developing an offset at the higher speeds in the x-axis plot, the increase at 13500 RPM from the 2.4 micron damage would make this impossible to decipher in a blind test. Despite providing an indication of the damage, the vibration data yet again shows sign of instability, despite this it still out performs the ROC data which can be observed to be erratic and provide no information of any significance.

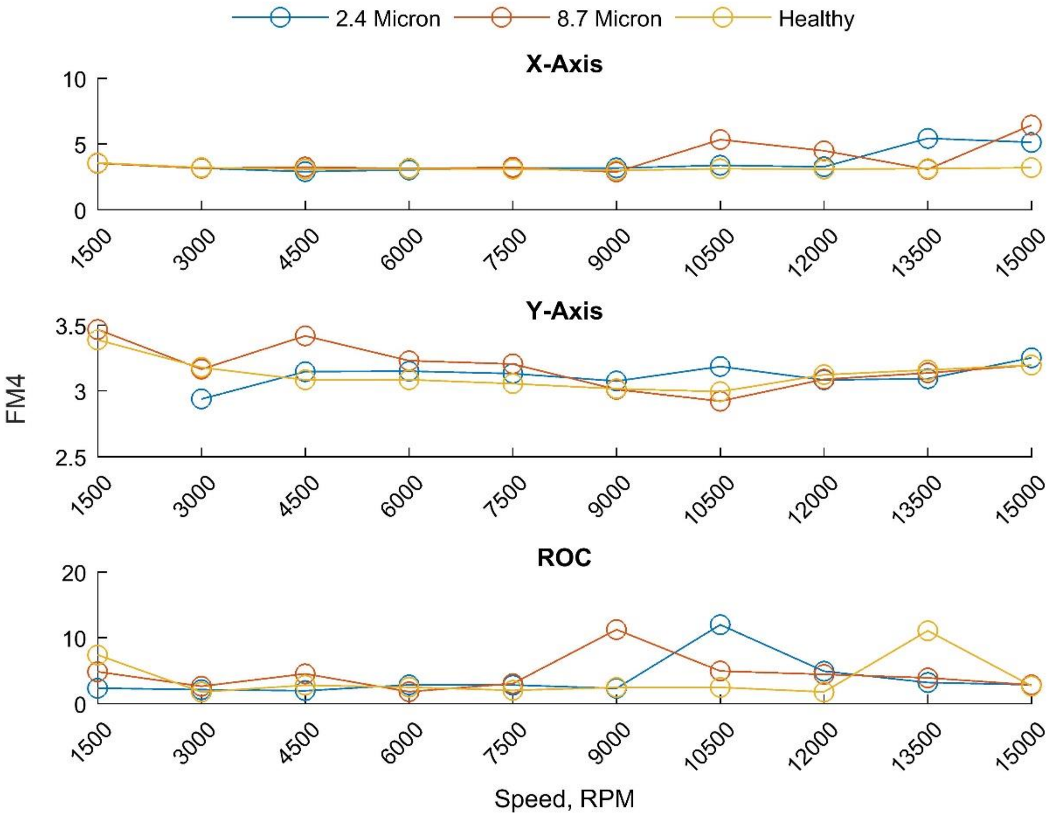

Figure 6-15 – Comparison of single value FM4 results for vibration and ROC data at 50 Nm torque.

Showing a similar level of consistency as the single value results, the application of FM4 to a rolling window did provide a measure of detection for the 8.7 micron tooth bend. This detection rarely extended beyond 6000 RPM with the level of torque in the system appearing to have no effect on whether detection was possible or not. Figure 6-16 provides the clearest depiction of the damage, with a region of greater than average amplitude starting at 120° in both axes. Detection of the damage through the use of FM4 indicates a serious difference in signal content between vibration and ROC data. As was seen in previously in Chapter 5, application of the kurtosis to ROC was underwhelming with damage detection being uncommon and the response when detected often being difficult to identify amongst the other results. Something similar can be seen again in Figure 6-17, where using the RMS as confirmation is it known that the damage occurs at approximately 260°. The largest peak in the TSA kurtosis appears at 240°, yet the damage doesn't appear for another 20°, with the correct position of the damage being seen in the results of the application to the raw data, although even here it is barely distinguishable from the rest of the signal. Issues such as this were what plagued the previous examples of the use of kurtosis with ROC data. This often led to situations where without prior knowledge the damage was completely undetectable. It should be noted that the difference in the position of the damage between the vibration and ROC data is due to the breakdown of rotations, as they were captured on 2 isolated systems, there is sensor input between the 2 systems that would allow for accurate alignment of both sets of data.

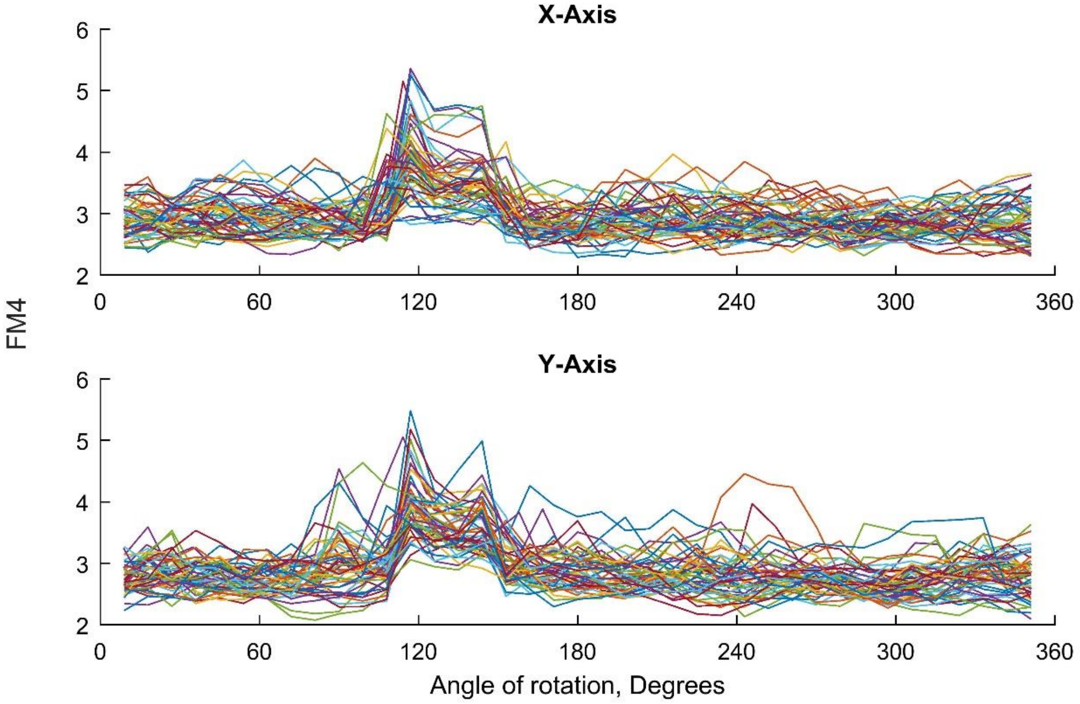

Figure 6-16 – Results for the application of FM4 to a rolling window at 4500 RPM and 200 Nm torque.

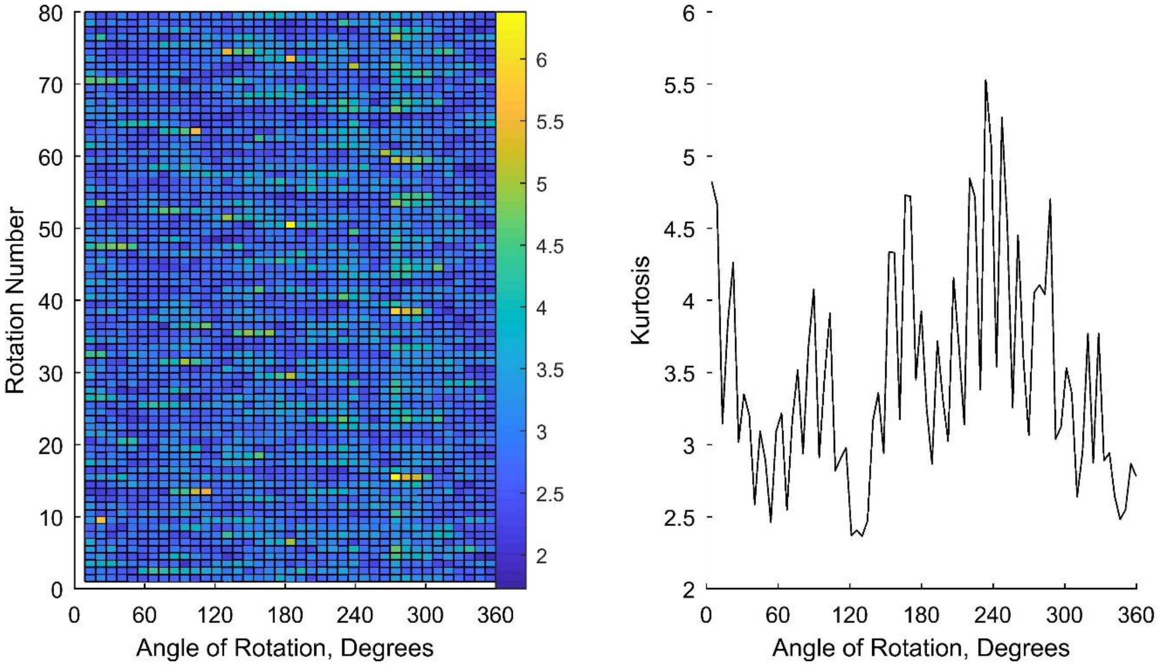

Figure 6-17 – Windowed Kurtosis for raw and TSA ROC data at 4500 RPM and 200 Nm torque.

The difference in damage detection ability through application of the kurtosis to both the vibration residual signal and the ROC data, both raw and averaged, highlights a difference in signal content. As it has been seen previously the damage is often visible in the ROC waveforms while vibration mostly appears as gaussian noise. It is possible that the larger noise content of a vibration signal means that the damage is more often relegated to the tail ends of the probability distribution for the signal allowing for better detection as opposed to the 'clean' signal that is received from ROC, especially once averaged. The cleaner signal may restrict ROC in this sense with the damage not differing from the general signal content enough to allow for accurate or consistent detection via kurtosis.

Finally, once again no sign of the 2.4 micron damage could be found within the vibration signals from either sensor. The 2.4 micron results appear strikingly similar to those of the healthy gear as can be seen by comparing Figure 6-18 and Figure 6-19. It would be unlikely though that such a small gear would cause any abnormal vibration during the operation of the gears however given that its size falls within the manufacturer's tolerances.

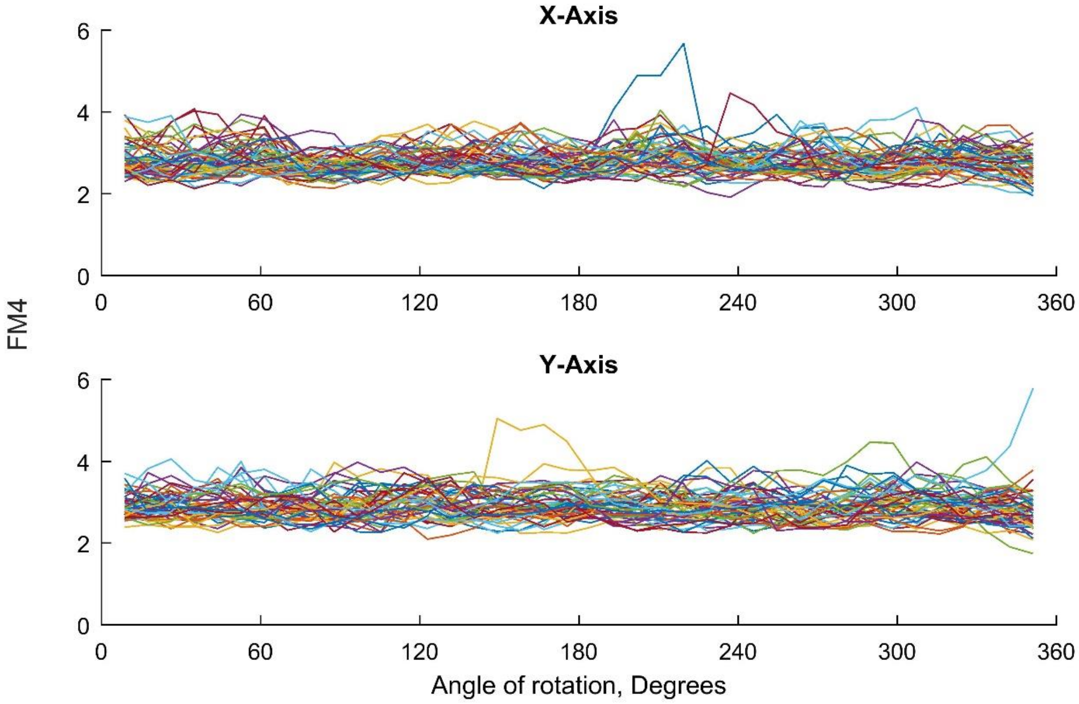

Figure 6-18 – Rolling window FM4 for 2.4 micron damage vibration data at 100 Nm torque and 7500 RPM.

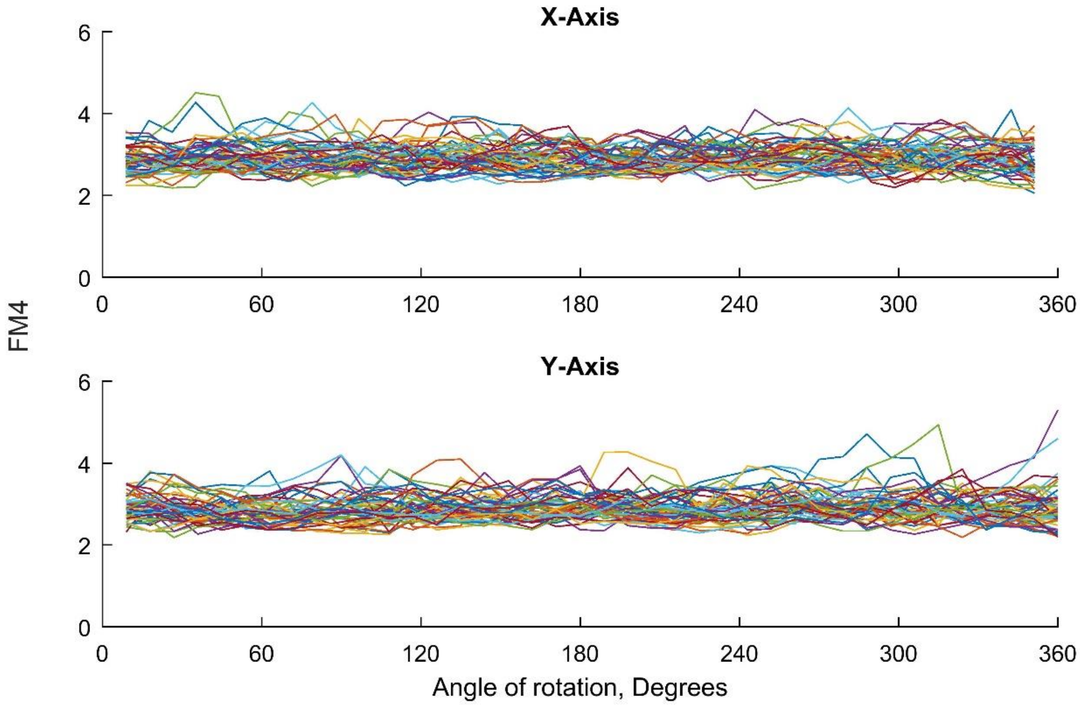

Figure 6-19 – Rolling window FM4 for healthy vibration data at 100 Nm torque and 7500 RPM.

6.2.4 M6A & M8A

M6A and M8A are modifications of FM4 that use higher powers (6 and 8 respectively) to amplify the sensitivity to outliers within the signal. Applications of these metrics thus far shown that these modifications do manage to achieve this but has so far caused anomalies to be amplified to the point where any other characteristics of the results for a signal are lost. It was thought that the application of these methods to the type of data it was designed to process (e.g. vibration signals) would yield better results but as can be seen in Figure 6-20 and Figure 6-21, this is not necessarily the case. It is clear from the scales of the two figures that all the points have been amplified, but comparison of the two shows that some points such as the 9000 and 3000 RPM points for the 8.7 micron damage on the x and y axes respectively have been particularly affected by the higher power metric. The reason for the increased reaction by these particular points is unclear, however with these singular points increasing it better highlights the 8.7 micron damage at certain speeds. Overall this adds very little to the FM4 results other than larger scales. These scales can be a hinderance as well as, whilst this increase can allow for the 8.7 micron damage to better highlighted, there is the possibility that this would cause areas that are not amplified by the same amount to fall behind and be relatively indistinguishable from the healthy results. M6A and M8A did little to help the detection of the 2.4 micron tooth bend with the results effectively mirroring those of the healthy specimen, with the occasional anomaly which can be seen at 13500 RPM in the x-axis data for both metrics. This anomaly makes the vibration results for 2.4 micron damage similar to those of the ROC for all 3 test gears where the results are relatively low level with a singular large scale anomaly present for each gear.

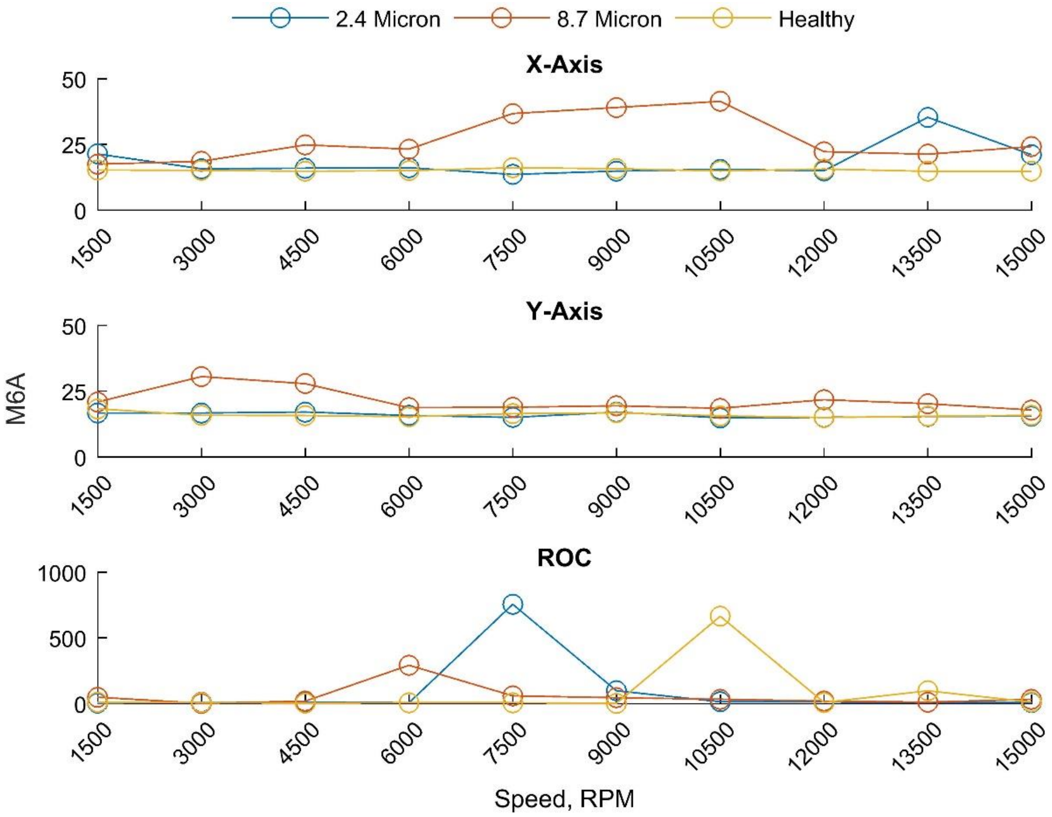

Figure 6-20 – Single value results for M6A on all test specimens at 150 Nm.

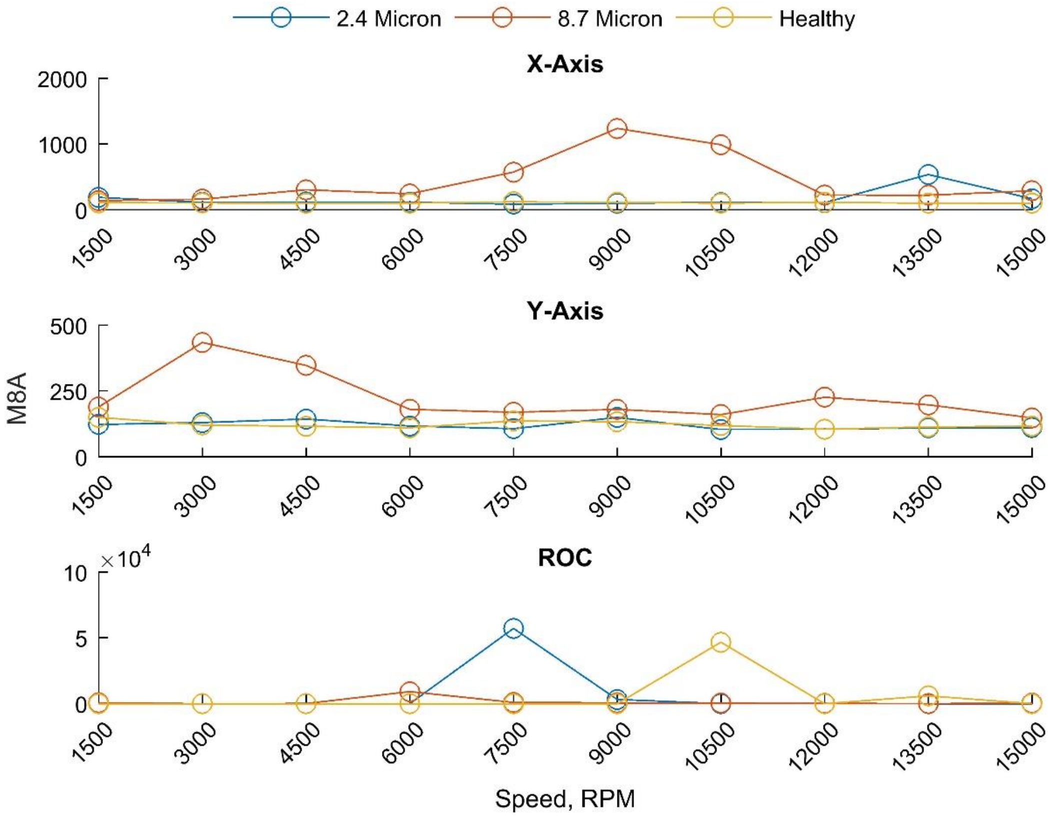

Figure 6-21 – Single value results for M8A on all test specimens at 150 Nm.

As with the single value metrics, application of M6A and M8A to a rolling window was found to add little to the analysis. Figure 6-22 and Figure 6-23 show an example of these results for M6A and M8A at the same conditions as those present in Figure 6-16, overall the figures are very similar with transients akin to one another indicating the presence of the damage around 120°. Aside from the increase the scales it worth noting that the presence of the damage, whilst still easily identifiable in M6A and M8A, was more obscured with the x-axis data seeing a decrease in the offset that distinguishes the damage in FM4 from the baseline of the results. In both M6A and M8A this offset is largely reduced to be close to or matching this baseline across multiple rotations, while this had little effect on visibly identifying the damage when examining all the rotations simultaneously. It is unclear as to what would cause this change and reduction in amplitude given the consistent speed and torque across these rotations. It is likely that this could lead to complications in the damage detection if the higher amplitude results were not present which is plausible given the inconsistency with which FM4, M6A and M8A are able to accurately detect the damage. The y-axis data on the other hand is subject to more anomalies across the rotation of the results than that of the FM4. This will be due to the increased sensitivity of the metrics amplifying the results of features in the waveform that previously had little weighting on the FM4 values. These anomalies add further unreliability to already unstable methods as these anomalies could easily be mistaken for the damage upon examination of a single rotation.

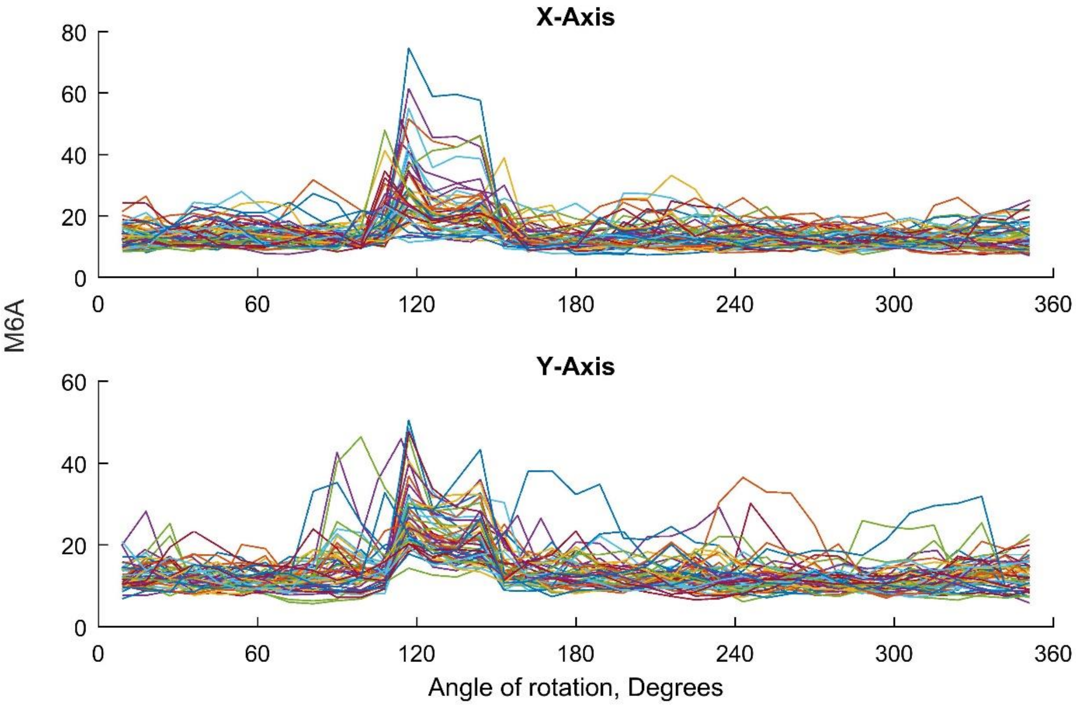

Figure 6-22 – Application of the metric M6A to a rolling window for the 8.7 micron defect vibration data captured at 4500 RPM and 200 Nm torque.

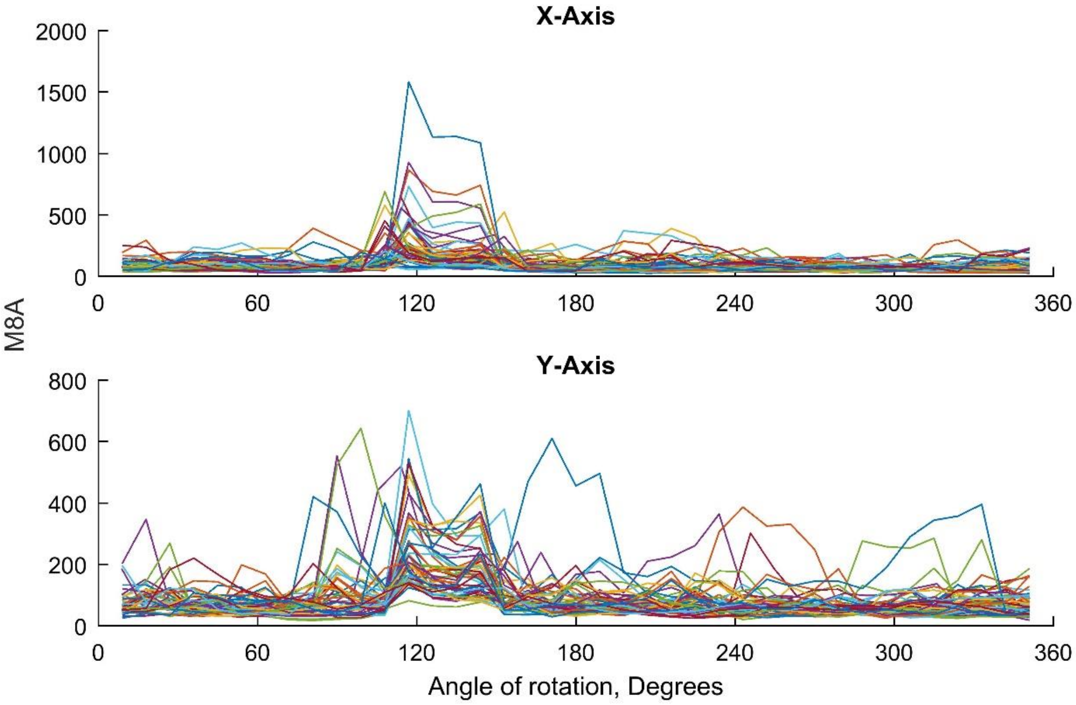

Figure 6-23 – Application of the metric M8A to a rolling window for the 8.7 micron defect vibration data captured at 4500 RPM and 200 Nm torque.

It was clear at this point that whilst the application of the M6A and M8A to vibration data was significantly better than its application to ROC data, the metrics add little to the results already provided by FM4. With the increased sensitivity failing also to detect the 2.4 micron tooth bend and adding more anomalous results across each rotation it is unclear as to how these metrics can provide any advantage over the application of their progenitor: FM4.

6.3 Discussion and conclusions

Analysis of the vibration data and comparison of results of the same techniques when applied to ROC data has shown that not only is there is difference in the ability of the techniques depending on the signal content to which they are applied, but a difference in sensitivity and reliability as well. Whilst the RMS did provide detection of the larger 8.7 micron damage in the residual vibration signal, the results were inferior to those seen from its application to ROC data with no detection of the 2.4 micron damage and only intermittent detection of the 8.7 micron damage. This detection was found to suffer over 9000 RPM where the transient indicating the damaged tooth disappeared, although increasing torque appeared to help reduce this effect allowing detection up to 12,000 RPM it was still insufficient for detection across the full spectrum of tests. In contrast the ROC data successfully showed signs of detection for both levels of damage, consistently with the 8.7 micron damage and intermittently for the 2.4 micron damage.

This situation changed with the application of FM4 however, whilst detection of the 2.4 micron damage was not possible with either data set, the results of the vibration data did provide some measure of detection of the 8.7 micron tooth bend, unlike the ROC data. Detection using the vibration data was again intermittent, but this was still more promising than the ROC for which the results were erratic and showed no signs of detection for any of the damage levels. It is currently thought that this is related to the frequency content of the signals with the amount of frequencies present changing the probability distribution of the signal meaning the damage is more likely to fall in the tails of the distribution and therefore be detected.

Use of the more sensitive modifications of FM4: M6A and M8A, provided little extra to the analysis, with the results often being near identical copies of the FM4 results but at higher amplitudes due to their amplification factor. Whilst in areas of the single value results these methods did better highlight the 8.7 micron tooth bend, areas that were not made more distinct were reduced in visible offset from the increase in scale. Even less use came from application to a rolling window where M6A and M8A were seen to be only detrimental to the detection process by adding nothing but introducing more high amplitude outliers in certain rotations and the new scale making the damage less defined in others.

Overall, it has been seen from this relatively brief analysis that clearly vibration metrics do have merit, with successful identification of the damage, if not consistently. Whilst it is possible that the lack of consistency in the detection is due to unoptimized positions of the sensors and the resultant attenuation, it is unlikely that vibration signals and its associated metrics will be able to match ROC with regards to sensitivity simple due to the quantity they are measuring, this said however this comparison has also made it clear that application of vibration metrics to ROC signals do not behave as intended. This suggests to the author that for truly consistent and accurate detection using ROC technology, a new set of metrics and techniques must be devised which are specifically designed for the frequency content found within a ROC signal, just as has been done before with both vibration and AE.

CHAPTER 7

Conclusions and Future Work

Over the course of this thesis four studies have been made that advance the knowledge and understanding of ROC technology, its abilities and applications. Using experimental data, out-of-loop parasitic loss data, in-loop data, and comparative vibration data have all been examined with the purpose of detecting seeded form defects at realistic gear system operating conditions.

7.1 Conclusions

The work presented in this thesis has demonstrated that ROC technology is a viable condition monitoring technology for use with rotating machinery. It has been shown that ROC technology possesses a high degree of sensitivity with the detection of a 2.7 µm form defect. This detection however did require prior knowledge and is unlikely to have occurred outside of a laboratory setting, however it demonstrates the potential of the technology given that it is the subject of more work.

7.1.1 Parasitic Losses

Despite being external to the torque loop with little energy being lost to friction due to the high efficiency of spur gears, it was still concluded that the presence of tooth bends specifically those of 8 µm or greater can be successfully detected by monitoring parasitic torque losses. This detection took the form of a sudden drop in ROC followed by a sharp increase, with both extrema occurring outside of the standard deviation of the signal. This transient indicated sudden changes in the torque transference within the meshing cycle as the form defect entered the gear mesh confirming that the damage was being detected.

A range of statistical measures and metrics (originally developed for use with vibration signals) were used to provide a numerical measure of the transient seen in raw waveform. Using a simple high-pass filter to remove low end noise, the performance of these various metrics was analysed where it was concluded that the RMS provided the most robust measure of damage detection. Whilst characterisation would not be possible, by monitoring the activity beyond a threshold, a simple go/no go gauge could be used to determine whether damage was present in the gear system. The effectiveness of this method is limited however, as it was found that increasing the torque present within the system reduced the size of the damage transient in the parasitic losses until it echoed the healthy specimen results. Despite this it was clear that ROC technology possessed a fundamental ability to respond to form defects as they enter the gear mesh even from outside of the torque loop. Monitoring of parasitic losses outside a torque loop would only occur on a back to back gear testing rig, and so this lent validity to the prospect that ROC would be just, as if not more, effective under real world conditions when used to monitor in-loop torque fluctuations.

7.1.2 In-loop

Expanding on the previous study, data was collected from a newly designed novel test rig that allowed tests to occur under realistic conditions. The new design also placed the new ROC probe sensor within the torque loop meaning data collected would better replicate that acquired from an industrial gear system. As predicted it was found that in-loop data was vastly superior to its parasitic counterpart. Clarity within the raw signal provided a new level of detection with tooth bends of 2.4 µm, generating a noticeable transient within the raw waveforms. Beyond this, individual tooth interactions were now visible giving the potential to isolate the exact tooth the damage had occurred on given sufficient rotational position information. Moving the sensor inside the loop was also found to introduce more noise generated from the increased number of components now acting upon the torque flow. By applying TSA to the signals an even greater level of clarity could be achieved once non-stationary signals were removed, with the results being a highly repeatable waveform, which key points such as the change points within the meshing cycle could be mapped to.

Analysing the frequency spectrum of the new ROC data showed that the signal was nearly entirely comprised of the meshing frequency and its harmonics. Whilst overall this had little effect on the analysis a simple method of determining the presence of damage was found. By comparing the difference in amplitudes of the meshing frequency and the first harmonic, it can be seen that damage is present if the amplitude of the first harmonic is greater than that of the meshing frequency. Examination of the difference at various test conditions found that this relationship was not stable enough for characterisation but indicated the reliance of ROC signals on the mesh frequency.

Application of statistical measures and vibration metrics provided similar outcomes to that of the forerunner study where it was found that, again, only the RMS provided a robust and consistent detection method. The vibration metric NA4 and its descendant NB4 did also provide a degree of detection. These techniques provided consistent detection of the largest defect (14.7 µm) and intermittent detection of the 8.7 µm damage, but overall were unable to match the results of the RMS at this time. It was concluded however that with the correct signal processing methods, NA4 and NB4 may be able to provide a method of detecting damage growth and even allowing for characterisation.

Despite this no other methods showed any signs of detection of the damage despite its notable presence in the ROC signals. This inability to detect damage in ROC signals is concluded to be due to the difference in signal content between ROC and vibration, that for which the metrics were designed. With a noticeable lack of high amplitude sidebands and the reliance on the meshing frequency which is removed before vibration analysis it was becoming clear that the use of vibration metrics would not allow adequate detection with this new technology and as such newer and more advanced methods must be explored.

These more advanced methods would take the form of MLS and the Hilbert spectra. Application of these methods would see that computational time was a significant drawback with MLS being heavily restricted by the length of data it can process in a reasonable time. Despite this it provided clear, consistent results with visible detection of all levels of damage within two of its four techniques. Further tests were undertaken to identify the capacity to which these results could be used for characterisation. Disappointingly the amplitudes of the different results were erratic with identification of which result related to which damage only being possible with prior knowledge. Disregarding this though, the use of the multiscale mean and variance provided another robust method of confirming damage within gear systems, especially that which is only suspected and not yet confirmed by a live system.

The Hilbert spectra performed poorly when compared to the results of the MLS with only one of the three spectra, namely the instantaneous energy spectrum providing any results of substance. This spectrum provided promise with regards to characterisation with a relative increase in the size of the transient with damage. The detection was not frequent enough however for this to be truly tested, a flaw that is undoubtedly down to the decomposition process used within the generation of these spectra. The reliance of these spectra on the decomposition process makes it likely that a different process would provide better results depending on its suitability to the data.

7.1.3 Bearing Failure

Due to unforeseen reasons a bearing failure occurred midway through the testing process. With the data available a small study into the ability of ROC to detect bearing failures was undertaken. During this study only, frequency analysis was used as it was quickly found that none of the principle bearing frequencies could be located with the data, even that which was captured directly before failure. It was concluded that the position of the bearing being external to the torque loop, meant any indications of the oncoming failure were too low energy to generate a notable presence within the signal given the relative amplitude to the components situated within the loop.

7.1.4 Vibration

By capturing vibration data alongside ROC, it allowed the first comparison of the technologies' application to gear systems. Processing this data across a range of vibration metrics solidified the belief that other methodologies are required for detection in ROC technology, as while detection using vibration was unstable it yielded results which, when the same metrics were applied to ROC, had not been seen. This was best displayed by FM4, a method that had previously shown limited effectiveness with parasitic loss data and gave no viable results using the in-loop data. Despite this it performed reasonably well when applied to vibration data with detection of the 8.7 micron damage being found with relative regularity. In contrast, the RMS suffered when applied to vibration data with detection similar to FM4, a noticeable downgrade in performance compared to what had been seen previously. Comparison of the vibration results to those of the ROC showed that it was evident that ROC had the upper hand with more consistent detection as well as a higher sensitivity towards with the defects, as the vibration analysis showed no evidence of detection of the 2.4 micron bend. The inconsistency in the vibration results is thought to be due to the position of the sensors and not being optimised meaning attenuation may have affected the results. It is of course possible that, the 8.7 micron bend was simply not large enough to generate a consistent reaction within the vibration data. More data would be required to confirm this however, with ROC prevailing as the more reliable technology despite the use of vibration metrics on the correct data.

Over the course of these studies, the benefits and potential that ROC technology possesses have been observed. Form defects at a range of sizes from the minimal at 2.7 µm to the overtly large 16 µm have been successfully detected over a set of realistic test conditions. This has shown that ROC technology has the capacity for detection of early onset damage and the possibility of tracking progression, if a suitable method for characterisation can be found. Despite this success, no ability to characterise the damage has as of yet been possible with the results showing that currently the condition of a gear can only be described as damaged or healthy. It is likely that this lack of both successful characterisation and detection by many of the applied methods is due to the initial approach of borrowing methods from other fields of condition monitoring, most notably vibration monitoring. Whilst this was done only due to the novelty of the technology, it is clear that future techniques must be tailored to the ROC signals and their frequency content to allow for the expansion of this technology into a fully-fledged condition monitoring system.

Of course, these results have been collected in laboratory conditions using a back-to-back test rig. Whilst there is clearly promise of ROC technology it is, it would be remiss to think that the same results would be produced from installing the sensor into a vehicle. There are likely to be complications with the use of the sensor outside of an isolated system. The greater complexity observed in, for example, an F1 powertrain will likely introduce unforeseen complications in the signal, while results have shown that objects subjected to no torque generate little to no presence in a ROC signal. The cumulation of these parts as well support elements such as bearings will likely add noise to the signal that has thus far not been witnessed. It is also likely that the power source will have an effect on the signal, with the test rig using a highly repeatable electric motor the signals were comparatively similar. An engine subject to a race, will be far less repeatable and could introduce new issues with the detection and characterisation of ROC signals.

7.2 Future Work

Although the work in this thesis has examined many aspects of the foundations for ROC based condition monitoring, this can be regarded simply as the overture with more yet to follow. There are still many aspects of this technology that require investigation to allow ROC technology to become an established rival to the current rotating machinery monitoring techniques.

The study undertaken here has managed to successfully detect a range of damage but was unable to differentiate the results to allow for characterisation of the scale of the damage. This is something that should be investigated as it will allow not only allow for identification of the damage scale but will also allow for damage progression to be monitored, a key feature that will be required for a complete condition monitoring system. Due to the regularity of TSA ROC signals it is possible that this may be achieved through wavelets and pattern recognition methods such as Chebyshev coefficients.

With regards to the testing undertaken in this project, work should be undertaken to expand the test set up beyond that of a singular gear pair. Through the introduction of idle gears to the test housing, replication of the conditions of a working gearbox will be more accurate. This will allow for identification of the level of background noise under realistic conditions and its effect on the detection ability of the ROC sensors within. With the current study having focussed entirely on tooth bends, it will be of interest as to know how ROC signals react to other forms of damage, such as root cracks and even surface defects like pitting. The ability to detect and differentiate between these various damage types will allow for better characterisation as well determine the true limits as to the detection capabilities of this technology. This expansion should not just be limited to other defect types, as a number of different components make up a power system it should be investigated as to the potential for ROC to detect damage in other rotational components such as bearings.

It was seen in the literature how McFadden's generation of a set of equations that mathematically describe a vibration signal was of use for both understanding the nature of the signals being processed as well as how damage effected the frequency content. Therefore, it is believed that a similar undertaking would be beneficial for ROC signals, where the understanding of the nature of signals is still in its infancy but such an undertaking could allow for ROC specific metrics to be developed allowing for greater condition monitoring potential.

References

Anon 2005. Managing the wind: Reducing kilowatt-hour costs with condition monitoring. *Refocus* 6(3) 1 May, pp. 48–51. Available at: https://www.sciencedirect.com/science/article/pii/S1471084605704029 [Accessed: 28 March 2018].

Barrueto Novoa, A. and Molina Vicuña, C. 2016. New aspects concerning the generation of acoustic emissions in spur gears, the influence of operating conditions and gear defects in planetary gearboxes. *Insight: Non-Destructive Testing and Condition Monitoring* 58(1), pp. 18–27. doi: 10.1784/insi.2016.58.1.18.

Clarke, A. et al. 2015. Understanding micropitting in gears. *Proceedings of the Institution of Mechanical Engineers, Part C: Journal of Mechanical Engineering Science* 230(7–8), pp. 1276–1289. doi: 10.1177/0954406215606934.

Clarke, A. et al. 2017. Effects of profile errors on lubrication performance of helical gears. *Tribology International* 111(February), pp. 184–191. doi: 10.1016/j.triboint.2017.02.034.

Clarke, A. 2017. Gearbox Schematic. In: *EN3607 Automotive Power Transmission Module Notes*. Cardiff University, p. 11.

Crivelli, D. et al. 2017. Gear tooth root fatigue test monitoring with continuous acoustic emission: Advanced signal processing techniques for detection of incipient failure. *Structural Health Monitoring* , pp. 1–11. Available at: http://journals.sagepub.com/doi/10.1177/1475921717700567.

D'Antona, G. and Ferrero, A. 2006. *Digital signal processing for measurement systems: theory and applications*. Available at: http://books.google.com/books?hl=en&lr=&id=7rRx1tHUob4C&oi=fnd&pg=PR10&dq=Digital+Signal+Processing+for+measurment+systems:+theory+and+applications&ots=CvO8AJF1AY&sig=LboorwM7ogbtn3oVoYYDnVcezHY.

Decker, H.J. and Lewicki, D.G. 2003. Spiral Bevel Pinion Crack Detection in a Helicopter Gearbox. *Nasa Tm-2003-212327 Arl-Tr-2958* (June), p. 16.

Deng, L. and Zhao, R. 2013. A vibration analysis method based on hybrid techniques and its application to rotating machinery. *Measurement* 46(9), pp. 3671–3682. Available at: http://linkinghub.elsevier.com/retrieve/pii/S0263224113003138 [Accessed: 22 June 2014].

Doebelin, E. 2004a. Piezoelectric Transducers. In: *Measurement Systems: Application & Design*. 5th ed. McGraw-Hill, pp. 284–292.

Doebelin, E. 2004b. Seisemic- (absolute-) acceleration pickups (accelerometers). In: *Measurement Systems: Application & Design*. 5th ed. McGraw-Hill, pp. 357–375.

FIA 2017. *2018 Formula One Technical Regulations*.

FIA 2018. *2018 Formula One Sporting Regulations*.

Freeth, T. et al. 2006. Decoding the Antikythera Mechanism : Investigation of an Ancient Astronomical Calculator. *Notes* 444(7119), pp. 587–591.

García Márquez, F.P. et al. 2012. Condition monitoring of wind turbines: Techniques and methods. *Renewable Energy* 46, pp. 169–178. Available at: http://linkinghub.elsevier.com/retrieve/pii/S0960148112001899 [Accessed: 9 July 2014].

Garshelis, I.J. 1992. A torque transducer utilizing a circularly polarized ring. *IEEE Transactions on Magnetics* 28(5), pp. 2202–2204. doi: 10.1109/20.179443.

Garshelis, I.J. et al. 2007. A Rate of Change of Torque Sensor. *IEEE Transactions on Magnetics* 43(6), pp. 2388–2390. Available at: http://ieeexplore.ieee.org/lpdocs/epic03/wrapper.htm?arnumber=4202729.

Garshelis, I.J. et al. 2008. Monitoring cutting tool operation and condition with a magnetoelastic rate of change of torque sensor. *Journal of Applied Physics* 103(7), p. 07E908. Available at: http://scitation.aip.org/content/aip/journal/jap/103/7/10.1063/1.2833316 [Accessed: 2 July 2014].

Garshelis, I.J. and Jones, C.A. 1999. A torque transducer based on local bands of naturally stabilized remanent circumferential magnetization. *Journal of Applied Physics* 85(8), pp. 5468–5470. doi: 10.1063/1.369978.

Hase, A. et al. 2016. Fundamental study on early detection of seizure in journal bearing by using acoustic emission technique. *Wear* 346–347, pp. 132–139. Available at: http://dx.doi.org/10.1016/j.wear.2015.11.012.

Howard, I. 1994. *A Review of Rolling Element Bearing Vibration 'Detection, Diagnosis and Prognosis'*.

Huang, N.E. et al. 1998. The empirical mode decomposition and the Hilbert spectrum for nonlinear and non-stationary time series analysis. *Proceedings of the Royal Society A: Mathematical, Physical and Engineering Sciences* 454(1971), pp. 903–995. Available at: http://rspa.royalsocietypublishing.org/cgi/doi/10.1098/rspa.1998.0193 [Accessed: 9 July 2014].

Inalpolat, M. et al. 2015. Influence of indexing errors on dynamic response of spur gear pairs. *Mechanical Systems and Signal Processing* 60–61, pp. 391–405. Available at: http://dx.doi.org/10.1016/j.ymssp.2014.11.017.

Institute of Machine Elements 2016. FZG: Technical Equipment. Available at: https://www.fzg.mw.tum.de/en/research/technical-equipment/ [Accessed: 4 June 2018].

Jardine, A.K.S. et al. 2006. A review on machinery diagnostics and prognostics implementing condition-based maintenance. *Mechanical Systems and Signal Processing* 20(7), pp. 1483–1510. Available at: https://www.sciencedirect.com/science/article/pii/S0888327005001512 [Accessed: 28 March 2018].

Kari, R.J. et al. 2011. Magnetoelastic Rate of Change of Torque Sensor-Based Health Monitoring System for Bearings in Helicopter Powertrains. In: *American Helicopter Society 67th Annual Forum*. Virginia Beach

Kattelus, J. et al. 2018. Detection of gear pitting failure progression with on-line particle monitoring. *Tribology International* 118, pp. 458–464. Available at: https://www.sciencedirect.com/science/article/pii/S0301679X17301056 [Accessed: 10 May 2018].

Lewicki, D.G. et al. 1995. *Transmission Diagnostic Research at NASA Lewis Research Centre*.

Li, H. et al. 2006. Wear Detection in Gear System Using Hilbert-Huang Transform. *Journal of Mechanical Science and Technology* 20(11), pp. 1781–1789.

Li, H. et al. 2017. Succinct and fast empirical mode decomposition. *Mechanical Systems and Signal Processing* 85, pp. 879–895. Available at: http://linkinghub.elsevier.com/retrieve/pii/S0888327016303697 [Accessed: 28 August 2018].

Li, S. 2007a. Effects of machining errors, assembly errors and tooth modifications on loading capacity, load-sharing ratio and transmission error of a pair of spur gears. *Mechanism and Machine Theory* 42(6), pp. 698–726. Available at: https://www.sciencedirect.com/science/article/pii/S0094114X06001133?via%3Dihub [Accessed: 17 April 2018].

Li, S. 2007b. Finite element analyses for contact strength and bending strength of a pair of spur gears with machining errors, assembly errors and tooth modifications. *Mechanism and Machine Theory* 42(1), pp. 88–114. Available at: https://www.sciencedirect.com/science/article/pii/S0094114X06000280?via%3Dihub [Accessed: 18 April 2018].

Liu, Z. et al. 2017. Improved local mean decomposition for modulation information mining and its application to machinery fault diagnosis. *Journal of Sound and Vibration* . Available at: http://linkinghub.elsevier.com/retrieve/pii/S0022460X17302006.

Loutas, T.H. et al. 2011. The combined use of vibration, acoustic emission and oil debris on-line monitoring towards a more effective condition monitoring of rotating machinery. *Mechanical Systems and Signal Processing* 25(4), pp. 1339–1352. Available at: http://dx.doi.org/10.1016/j.ymssp.2010.11.007.

Loutridis, S. 2004. A local energy density methodology for monitoring the evolution of gear faults. *NDT & E International* 37(6), pp. 447–453. Available at: https://www.sciencedirect.com/science/article/pii/S0963869503001725 [Accessed: 1 August 2018].

Loutridis, S.J. 2004. Damage detection in gear systems using empirical mode decomposition. *Engineering Structures* 26(12), pp. 1833–1841. Available at: https://www.sciencedirect.com/science/article/pii/S0141029604002238 [Accessed: 5 April 2018].

Loutridis, S.J. 2008. Gear failure prediction using multiscale local statistics. *Engineering Structures* 30(5), pp. 1214–1223. Available at: http://www.sciencedirect.com/science/article/pii/S0141029607002891 [Accessed: 16 July 2014].

Markovic, K. and Franulovic, M. 2011. Contact Stresses in Gear Teeth Due to Tip Relief Profile Modification. *Engineering Review* 31(1), pp. 19–26.

Martin-del-Campo, S. and Sandin, F. 2017. Online feature learning for condition monitoring of rotating machinery. *Engineering Applications of Artificial Intelligence* 64, pp. 187–196. Available at: https://www.sciencedirect.com/science/article/pii/S0952197617301318#b12 [Accessed: 28 March 2018].

Martin, H.R. 1989. Statistical moment analysis as a means of surface damage detection. In: *Proceedings of the Seventh International Modal Analysis Conference*. New York: Society for Experimental Mechanics, pp. 1016–1021.

MathWorks 2018. FIR Filter Design - FIR vs. IIR Filters. Available at: https://uk.mathworks.com/help/signal/ug/fir-filter-design.html [Accessed: 12 June 2018].

McFadden, P.D. 1986. Detecting Fatigue Cracks in Gears by Amplitude and Phase Demodulation of the Meshing Vibration. *Journal of vibration, acoustics, stress, and reliability in design* 108(2), pp. 165–170. Available at: http://www.scopus.com/inward/record.url?eid=2-s2.0-0022695238&partnerID=40&md5=65f08c8ec0d19b7885dea0db58c38c9e.

McFadden, P.D. 1987. Examination of a technique for the early detection of failure in gears by signal processing of the time domain average of the meshing vibration. *Mechanical Systems and Signal Processing* 1(2), pp. 173–183.

McFadden, P.D. and Smith, J.D. 1985. A signal processing technique for detecting local defects in a gear from the signal average of the vibration. *Proceedings of the Institution of Mechanical Engineers, Part C: Journal of Mechanical Engineering Science* 199(4), pp. 287–292. doi: 10.1243/PIME_PROC_1985_199_125_02.

Miettinen, J. and Siekkinen, V. 1995. Acoustic Emission in Monitoring Sliding Contact Behaviour. *Wear* 183, pp. 897–900.

Miller, R.K. and McIntire, P. 1987. *Nondestructive testing handbook. Vol. 5, Acoustic emission testing*. 2nd ed. Columbus, OH: American Society for Nondestructive Testing.

Mitchell, J.S. 2007. From Vibration Measurements to Condition Based Maintenance. *Sound & Vibration* 41(1), pp. 62–78.

Mohanty, A.R. and Fatima, S. 2015. Shaft misalignment detection by thermal imaging of support bearings. *IFAC-PapersOnLine* 48(21), pp. 554–559. Available at: https://www.sciencedirect.com/science/article/pii/S2405896315017139 [Accessed: 16 May 2018].

Molina Vicuña, C. 2014. Effects of operating conditions on the Acoustic Emissions (AE) from planetary gearboxes. *Applied Acoustics* 77, pp. 150–158. doi: 10.1016/j.apacoust.2013.04.017.

Munro, R.G. 1990. A review of the theory and measurement of gear transmission error. In: *Proceedings of the 1st IMechE Conference of Gearbox Noise and Vibration*., pp. 3–10.

National Instruments 2019. Measuring Vibration with Accelerometers. Available at: https://www.ni.com/en-gb/innovations/white-papers/06/measuring-vibration-with-accelerometers.html.

Ottewill, J.R. et al. 2009. Intermittent gear rattle due to interactions between forcing and manufacturing errors. *Journal of Sound and Vibration* 321(3–5), pp. 913–935. Available at: https://www.sciencedirect.com/science/article/pii/S0022460X08008250 [Accessed: 17 April 2018].

Ottewill, J.R. et al. 2010. An investigation into the effect of tooth profile errors on gear rattle. *Journal of Sound and Vibration* 329(17), pp. 3495–3506. Available at: https://www.sciencedirect.com/science/article/pii/S0022460X10001872?via%3Dihub [Accessed: 17 April 2018].

Padmasolala, G. et al. 2000. Influence of Tooth With and Without Spacing Error on Gears Profile Modifications. *NASA TM-2000-210061*

Peng, Z. and Kessissoglou, N. 2003. An integrated approach to fault diagnosis of machinery using wear debris and vibration analysis. *Wear* 255(7–12), pp. 1221–1232. Available at: https://www.sciencedirect.com/science/article/pii/S004316480300098X?via%3Dihub [Accessed: 26 March 2018].

Physical Acoustics 2019. R30a - 300 kHz General Purpose AE Sensor. Available at: https://www.physicalacoustics.com/by-product/sensors/R30a-300-kHz-General-Purpose-AE-Sensor [Accessed: 20 July 2019].

Rademacher, J. 1968. Einfluss von Flankenrichtungsfehlern und Breitenballigkeiten auf die Tragfähikeit von Stirnradgetrieben. *Ind. Anz.* 90, pp. 915–921.

Randall, R.B. 1987. *Frequency Analysis*. 3rd ed. Naerum: Bruel & Kjaer.

Rilling, G. et al. 2003. On empirical mode decomposition and its algorithms. *IEEE-EURASIP workshop on nonlinear signal and image processing* 3, pp. 8–11. Available at: http://citeseerx.ist.psu.edu/viewdoc/download?doi=10.1.1.586.812&rep=rep1&type=pdf [Accessed: 28 August 2018].

Samuel, P.D. and Pines, D.J. 2005. A review of vibration-based techniques for helicopter transmission diagnostics. *Journal of Sound and Vibration* 282(1–2), pp. 475–508. Available at: http://www.sciencedirect.com/science/article/pii/S0022460X04003244 [Accessed: 15 July 2014].

Scheer, C. et al. 2007. Early fault detection at gear units by acoustic emission and wavelet analysis. *J. Acoust. Emission* 25, pp. 331–340. Available at: http://www.ndt.net/article/jae/papers/25-331.pdf%0Ahttp://212.8.206.21/article/jae/papers/25-331.pdf.

Sentoku, H. 1998. AE in tooth surface failure process of spur gears. *Journal of Acoustic Emission* 16(1–4), pp. S19–S24.

Shigley, J.E. and Mischke, C.R. 2001. *Mechanical Engineering Design*. Sixth Edit. McGraw-Hill.

Singh, A. et al. 1999. Detecting Gear Tooth Breakage Using Acoustic Emission: a Feasibility and Sensor Placement Study. *Journal of Mechanical Design* 121(4), p. 587. Available at: http://mechanicaldesign.asmedigitalcollection.asme.org/article.aspx?articleid=1445732.

SKF 2017. Bearing rating life. Available at: http://www.skf.com/group/products/bearings-units-housings/principles/bearing-selection-process/bearing-size/size-selection-based-on-rating-life/bearing-rating-life/index.html [Accessed: 6 June 2018].

Smith, J.S. 2005. The local mean decomposition and its application to EEG perception data. *Journal of the Royal Society, Interface / the Royal Society* 2(5), pp. 443–54. Available at: http://www.pubmedcentral.nih.gov/articlerender.fcgi?artid=1618495&tool=pmcentrez&rendertype=abstract [Accessed: 10 July 2014].

Snidle, R.W. and Evans, H.P. 2009. Some aspects of gear tribology. *Proceedings of the Institution of Mechanical Engineers, Part C: Journal of Mechanical Engineering Science* 223(1), pp. 103–141. doi: 10.1243/09544062JMES1168.

Stewart, R.M. 1977. Some useful data analysis techniques for gearbox diagnostics. In: *Applications of time series analysis*. University of Southampton, pp. 18.1-18.19.

Sun, H. et al. 2010. Research on the improved method of the endpoint wave extension of empirical mode decomposition. *Journal of Electronic Measurement and Instrument* 24(4), pp. 319–326. Available at: http://pub.chinasciencejournal.com/article/getArticleRedirect.action?doiCode=10.3724/SP.J.1187.2010.00319.

Tan, C.K. et al. 2007. A comparative experimental study on the diagnostic and prognostic capabilities of acoustics emission, vibration and spectrometric oil analysis for spur gears. *Mechanical Systems and Signal Processing* 21(1), pp. 208–233. doi: 10.1016/j.ymssp.2005.09.015.

Tharmakulasingam, R. 2009. *Transmission Error in Spur Gears: Static and Dynamic Finite-Element Modeling and Design Optimization*.

Touret, T. et al. 2018. On the use of temperature for online condition monitoring of geared systems – A review. *Mechanical Systems and Signal Processing* 101, pp. 197–210. Available at: https://www.sciencedirect.com/science/article/pii/S0888327017304089 [Accessed: 16 May

2018].

Toutountzakis, T. et al. 2005. Application of acoustic emission to seeded gear fault detection. *NDT and E International* 38(1), pp. 27–36. doi: 10.1016/j.ndteint.2004.06.008.

Toutountzakis, T. and Mba, D. 2003. Observations of acoustic emission activity during gear defect diagnosis. *NDT and E International* 36(7), pp. 471–477. Available at: http://www.sciencedirect.com/science/article/pii/S096386950300063X [Accessed: 18 May 2017].

Uicker, J.J. et al. 2003. *Theory of Machines and Mechanisms*. Third Edit. Oxford University Press.

Wang, W.J. and McFadden, P.D. 1993a. Early detection of gear failure by vibration analysis—I. calculation of the time-frequency distribution. *Mechanical Systems and Signal Processing* 7(3), pp. 193–203. doi: 10.1006/mssp.1993.1008.

Wang, W.J. and McFadden, P.D. 1993b. Early detection of gear failure by vibration analysis—II. Interpretation of the time-frequency distribution using image processing techniques. *Mechanical Systems and Signal Processing* 7(3), pp. 205–215. doi: 10.1006/mssp.1993.1009.

Wang, Y. et al. 2010. A Comparative Study on the Local Mean Decomposition and Empirical Mode Decomposition and Their Applications to Rotating Machinery Health Diagnosis. *Journal of Vibration and Acoustics* 132(2), p. 021010. Available at: http://vibrationacoustics.asmedigitalcollection.asme.org/article.aspx?articleid=1471458.

Waqar, T. and Demetgul, M. 2016. Thermal analysis MLP neural network based fault diagnosis on worm gears. *Measurement* 86, pp. 56–66. Available at: https://www.sciencedirect.com/science/article/pii/S0263224116001019 [Accessed: 16 May 2018].

Watson, H.J. 1970. *Modern Gear Production*. First. Oxford: Pergamon Press.

Wirtz, S.F. et al. 2016. Frequency-based damage detection of spur gear using wavelet analysis. *European Workshop On Structural Health Monitoring (EWSHM 2016)* (July), pp. 5–8.

Yang, W. et al. 2011. Bivariate empirical mode decomposition and its contribution to wind turbine condition monitoring. *Journal of Sound and Vibration* 330(15), pp. 3766–3782. Available at: https://www.sciencedirect.com/science/article/pii/S0022460X1100157X#bib1 [Accessed: 28 March 2018].

Zakarjsek, J.J. et al. 1993. An analysis of gear fault detection methods as applied to pitting.

Zakrajsek, J.J. 1994. A review of transmission diagnostic research at NASA Lewis research center. (December)